Electronic Theses and Dissertations

1995

The structure and spectroscopic properties of Langmuir-Blodgett films of perylene tetracarboxylic derivatives.

Eric G. Johnson
University of Windsor

Follow this and additional works at: http://scholar.uwindsor.ca/etd

NOTICE

AVIS

The quality of this microform is heavily dependent upon the quality of the original thesis submitted for microfilming. Every effort has been made to ensure the highest quality of reproduction possible.

La qualité de cette microforme dépend grandement de la qualité de la thèse soumise au microfilmage. Nous avons tout fait pour assurer une qualité supérieure de reproduction.

If pages are missing, contact the university which granted the degree.

S'il manque des pages, veuillez communiquer avec l'université qui a conféré le grade.

Some pages may have indistinct print especially if the original pages were typed with a poor typewriter ribbon or if the university sent us an inferior photocopy.

La qualité d'impression de certaines pages peut laisser à désirer, surtout si les pages originales ont été dactylographiées à l'aide d'un ruban usé ou si l'université nous a fait parvenir une photocopie de qualité inférieure.

Reproduction in full or in part of this microform is governed by the Canadian Copyright Act, R.S.C. 1970, c. C-30, and subsequent amendments.

La reproduction, même partielle, de cette microforme est soumise à la Loi canadienne sur le droit d'auteur, SRC 1970, c. C-30, et ses amendements subséquents.

Canada

The Structure and Spectroscopic Properties of Langmuir-Blodgett Films of Perylene Tetracarboxylic Derivatives

BY

ERIC G. JOHNSON

A Dissertation

Submitted to the Faculty of Graduate Studies through the Department of Chemistry and Biochemistry in partial fulfilment of the requirements for the Degree of Doctor of Philosophy at the University of Windsor

Windsor, Ontario, Canada

1994

THE AUTHOR HAS GRANTED AN
IRREVOCABLE NON-EXCLUSIVE
LICENCE ALLOWING THE NATIONAL
LIBRARY OF CANADA TO
REPRODUCE, LOAN, DISTRIBUTE OR
SELL COPIES OF HIS/HER THESIS BY
ANY MEANS AND IN ANY FORM OR
FORMAT, MAKING THIS THESIS
AVAILABLE TO INTERESTED
PERSONS.

L'AUTEUR A ACCORDE UNE LICENCE
IRREVOCABLE ET NON EXCLUSIVE
PERMETTANT A LA BIBLIOTHEQUE
NATIONALE DU CANADA DE
REPRODUIRE, PRETER, DISTRIBUER
OU VENDRE DES COPIES DE SA
THESE DE QUELQUE MANIERE ET
SOUS QUELQUE FORME QUE CE SOIT
POUR METTRE DES EXEMPLAIRES DE
CETTE THESE A LA DISPOSITION DES
PERSONNE INTERESSEES.

THE AUTHOR RETAINS OWNERSHIP
OF THE COPYRIGHT IN HIS/HER
THESIS. NEITHER THE THESIS NOR
SUBSTANTIAL EXTRACTS FROM IT
MAY BE PRINTED OR OTHERWISE
REPRODUCED WITHOUT HIS/HER
PERMISSION.

L'AUTEUR CONSERVE LA PROPRIETE
DU DROIT D'AUTEUR QUI PROTEGE
SA THESE. NI LA THESE NI DES
EXTRAITS SUBSTANTIELS DE CELLE-
CI NE DOIVENT ETRE IMPRIMES OU
AUTREMENT REPRODUITS SANS SON
AUTORISATION.

ISBN   0-612-01457-6

Canada

Name ERIC G. JOHNSON

Dissertation Abstracts International is arranged by broad, general subject categories. Please select the one subject which most nearly describes the content of your dissertation. Enter the corresponding four-digit code in the spaces provided.

PHYSICAL CHEMISTRY

SUBJECT TERM

0 4 9 4

SUBJECT CODE

U·M·I

Subject Categories

THE HUMANITIES AND SOCIAL SCIENCES

COMMUNICATIONS AND THE ARTS
Architecture 0729
Art History 0377
Cinema 0900
Dance 0378
Fine Arts 0357
Information Science 0723
Journalism 0391
Library Science 0399
Mass Communications 0708
Music 0413
Speech Communication 0459
Theater 0465

EDUCATION
General 0515
Administration 0514
Adult and Continuing 0516
Agricultural 0517
Art 0273
Bilingual and Multicultural 0282
Business 0688
Community College 0275
Curriculum and Instruction 0727
Early Childhood 0518
Elementary 0524
Finance 0277
Guidance and Counseling 0519
Health 0680
Higher 0745
History of 0520
Home Economics 0278
Industrial 0521
Language and Literature 0279
Mathematics 0280
Music 0522
Philosophy of 0998
Physical 0523

Psychology 0525
Reading 0535
Religious 0527
Sciences 0714
Secondary 0533
Social Sciences 0534
Sociology of 0340
Special 0529
Teacher Training 0530
Technology 0710
Tests and Measurements 0288
Vocational 0747

LANGUAGE, LITERATURE AND LINGUISTICS
Language
  General 0679
  Ancient 0289
  Linguistics 0290
  Modern 0291
Literature
  General 0401
  Classical 0294
  Comparative 0295
  Medieval 0297
  Modern 0298
  African 0316
  American 0591
  Asian 0305
  Canadian (English) 0352
  Canadian (French) 0355
  English 0593
  Germanic 0311
  Latin American 0312
  Middle Eastern 0315
  Romance 0313
  Slavic and East European 0314

PHILOSOPHY, RELIGION AND THEOLOGY
Philosophy 0422
Religion
  General 0318
  Biblical Studies 0321
  Clergy 0319
  History of 0320
  Philosophy of 0322
Theology 0469

SOCIAL SCIENCES
American Studies 0323
Anthropology
  Archaeology 0324
  Cultural 0326
  Physical 0327
Business Administration
  General 0310
  Accounting 0272
  Banking 0770
  Management 0454
  Marketing 0338
Canadian Studies 0385
Economics
  General 0501
  Agricultural 0503
  Commerce-Business 0505
  Finance 0508
  History 0509
  Labor 0510
  Theory 0511
Folklore 0358
Geography 0366
Gerontology 0351
History
  General 0578

Ancient 0579
Medieval 0581
Modern 0582
Black 0328
African 0331
Asia, Australia and Oceania 0332
Canadian 0334
European 0335
Latin American 0336
Middle Eastern 0333
United States 0337
History of Science 0585
Law 0398
Political Science
  General 0615
  International Law and
    Relations 0616
  Public Administration 0617
Recreation 0814
Social Work 0452
Sociology
  General 0626
  Criminology and Penology ... 0627
  Demography 0938
  Ethnic and Racial Studies 0631
  Individual and Family
    Studies 0628
  Industrial and Labor
    Relations 0629
  Public and Social Welfare 0630
  Social Structure and
    Development 0700
  Theory and Methods 0344
Transportation 0709
Urban and Regional Planning ... 0999
Women's Studies 0453

THE SCIENCES AND ENGINEERING

BIOLOGICAL SCIENCES
Agriculture
  General 0473
  Agronomy 0285
  Animal Culture and
    Nutrition 0475
  Animal Pathology 0476
  Food Science and
    Technology 0359
  Forestry and Wildlife 0478
  Plant Culture 0479
  Plant Pathology 0480
  Plant Physiology 0817
  Range Management 0777
  Wood Technology 0746
Biology
  General 0306
  Anatomy 0287
  Biostatistics 0308
  Botany 0309
  Cell 0379
  Ecology 0329
  Entomology 0353
  Genetics 0369
  Limnology 0793
  Microbiology 0410
  Molecular 0307
  Neuroscience 0317
  Oceanography 0416
  Physiology 0433
  Radiation 0821
  Veterinary Science 0778
  Zoology 0472
Biophysics
  General 0786
  Medical 0760

EARTH SCIENCES
Biogeochemistry 0425
Geochemistry 0996

Geodesy 0370
Geology 0372
Geophysics 0373
Hydrology 0388
Mineralogy 0411
Paleobotany 0345
Paleoecology 0426
Paleontology 0418
Paleozoology 0985
Palynology 0427
Physical Geography 0368
Physical Oceanography 0415

HEALTH AND ENVIRONMENTAL SCIENCES
Environmental Sciences 0768
Health Sciences
  General 0566
  Audiology 0300
  Chemotherapy 0992
  Dentistry 0567
  Education 0350
  Hospital Management 0769
  Human Development 0758
  Immunology 0982
  Medicine and Surgery 0564
  Mental Health 0347
  Nursing 0569
  Nutrition 0570
  Obstetrics and Gynecology .. 0380
  Occupational Health and
    Therapy 0354
  Ophthalmology 0381
  Pathology 0571
  Pharmacology 0419
  Pharmacy 0572
  Physical Therapy 0382
  Public Health 0573
  Radiology 0574
  Recreation 0575

Speech Pathology 0460
Toxicology 0383
Home Economics 0386

PHYSICAL SCIENCES
Pure Sciences
Chemistry
  General 0485
  Agricultural 0749
  Analytical 0486
  Biochemistry 0487
  Inorganic 0488
  Nuclear 0738
  Organic 0490
  Pharmaceutical 0491
  Physical 0494
  Polymer 0495
  Radiation 0754
Mathematics 0405
Physics
  General 0605
  Acoustics 0986
  Astronomy and
    Astrophysics 0606
  Atmospheric Science 0608
  Atomic 0748
  Electronics and Electricity 0607
  Elementary Particles and
    High Energy 0798
  Fluid and Plasma 0759
  Molecular 0609
  Nuclear 0610
  Optics 0752
  Radiation 0756
  Solid State 0611
Statistics 0463

Applied Sciences
Applied Mechanics 0346
Computer Science 0984
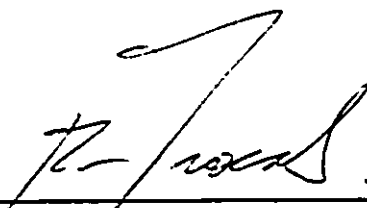
Engineering
  General 0537
  Aerospace 0538
  Agricultural 0539
  Automotive 0540
  Biomedical 0541
  Chemical 0542
  Civil 0543
  Electronics and Electrical 0544
  Heat and Thermodynamics ... 0348
  Hydraulic 0545
  Industrial 0546
  Marine 0547
  Materials Science 0794
  Mechanical 0548
  Metallurgy 0743
  Mining 0551
  Nuclear 0552
  Packaging 0549
  Petroleum 0765
  Sanitary and Municipal 0554
  System Science 0790
Geotechnology 0428
Operations Research 0796
Plastics Technology 0795
Textile Technology 0994

PSYCHOLOGY
General 0621
Behavioral 0384
Clinical 0622
Developmental 0620
Experimental 0623
Industrial 0624
Personality 0625
Physiological 0989
Psychobiology 0349
Psychometrics 0632
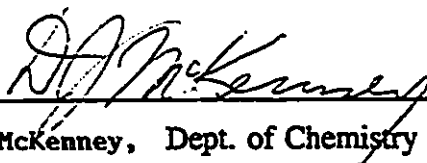Social 0451

This dissertation was examined and approved by:

R. Aroca, Dept. of Chemistry and Biochemistry

B. McGarvey, Dept. of Chemistry and Biochemistry

D. McKenney, Dept. of Chemistry and Biochemistry

J. B. Atkinson, Dept. of Physics

S. Asher
(External Examiner, University of Pittsburg)

Abstract

A series of perylene tetracarboxylic diimides and monoimides have been fabricated into Langmuir and Langmuir-Blodgett films. These films have been spectroscopically characterized through UV-visible absorption, steady state fluorescence, infrared and Raman techniques. Molecular exciton and excimer formation have been observed for these films. The average molecular orientation of the chromophore was deduced through infrared transmisson and reflection/absorption techniques. Electronic spectroscopy revealed the nature of the packing of the materials. The role of subphase/molecule and molecule/molecule interactions in the structure of the film were discussed, as well as the role of the imide substitution. These materials were successfully incorporated, as donors, into energy transfer systems with lutetium diphthalocyanine as an acceptor. These monolayers were used to investigate surface enhanced infrared and surface enhanced infrared reflection/absorption. The distance dependence and angle dependence of the enhancement in the infrared was simulated by using the Maxwell-Garnett composite layer model.

DEDICATION

To the loving memory of my father, Glen Raymond Johnson, whose guidance and encouragement laid the foundation for this work

Acknowledgements

Table of Contents

x

List of Tables

List of Figures

xiv

List of Abbreviations

A	area per molecule
AA	arachidic acid
AFM	atomic force microscopy
A_R	absorption, reflection geometry
A_T	absorption, transmission geometry
CCD	charge coupled device
d	distance between donour and acceptor layers
ΔE	monomer transition energy
$\Delta E'$	dimer transition energy
E_x	x-component of electric field vector
E_y	y-component of electric field vector
F	packing factor
f	oscillator strength
FFT	fast Fourier transform
FT	Fourier transform
FWHH	full width at half height
HOMO	highest occupied molecular orbital
HPLC	high pressure liquid chromatography
IR	infrared
l	dipole length
$2J_{12}$	interaction integral between two monomers
LB	Langmuir-Blodgett
LUMO	lowest unoccupied molecular orbital
$LuPc_2$	Lutetium diphthalocyanine
M	transition dipole moment, magnitude
m_x	enhancement factor, parallel to substrate surface
m_z	enhancement factor, perpendicular to substrate surface
n	refractive index
PTCD	perylene tetracarboxylic diimide

PTCO	perylene tetracarboxylic monoimide
q	quantum yield
Q	volume ratio
RAIRS	reflection/absorption infrared
RRS	resonance Raman scattering
SEIR	surface enhanced infrared
SEIRRA	surface enhanced infrared reflection/absorption
SERRS	surface enhanced resonance Raman scattering
SERS	surface enhanced Raman scattering
TFA	trifluoroacetic acid
TR	transfer ratio
UV	ultra-violet
α	polarizability
$+\epsilon$	partial positive charge
$-\epsilon$	partial negative charge
ϵ_d	dielectric constant of organic layer
ϵ_h	dielectric constant of host medium
ϵ_m	dielectric constant of metal particles
γ	surfaced tension
γ_0	reference surface tension (of water)
Π	surface pressure
π-A	surface pressure/area
μ_x	x-component of transition dipole
μ_y	y-component of transition dipole
ϕ	tilt angle
τ	relaxation time
ω	angular frequency
ω_p	plasma frequency

Chapter 1: Introduction

Perylene tetracarboxylic compounds represent a very interesting class of organic compounds. *Figure 1.1* illustrates the basic structure of perylene tetracarboxylic monoimides (PTCOs, a) and diimides (PTCDs, b). There is growing interest in the potential applicability of these materials in a wide range of technological applications. Before presenting an overview of applications, a brief history and description of the title compounds is presented.

History

The oldest member of the perylene family of chromophores is the parent perylene compound itself, described as early as 1912 *[1.1]*. The perylene compounds are bright orange to deep violet in colour and found their first use as colorants, initially as dyes, then later as pigments. Dyes are solutions that impart colouration through absorption into the host medium. Pigments are particle dispersions that provide colouration through adsorption of the particles onto the surface of the host medium. Compounds, such as the perylenes, can be either called dyes or pigments, depending on whether they are delivered in solution (dyes) or as suspended particles (pigments). The dimethyl PTCD was the first to be used as a vat dye in 1913. The diimides found application as pigments in 1950. Commercial perylene pigments have excellent lightfastness, weatherability and thermal stability. This makes them excellent for use in high-grade industrial paints such as automotive finishes. Currently, there are slightly less than a dozen PTCD's produced on an industrial scale. Reference 1 is an excellent source regarding the industrial use of perylene compounds as colourants. The earliest diimides were symmetric in nature. In other words, there is identical substitution off the imide nitrogens. Much later, asymmetric derivatives *[1.2,3]* and monoimides *[1.4]* were prepared.
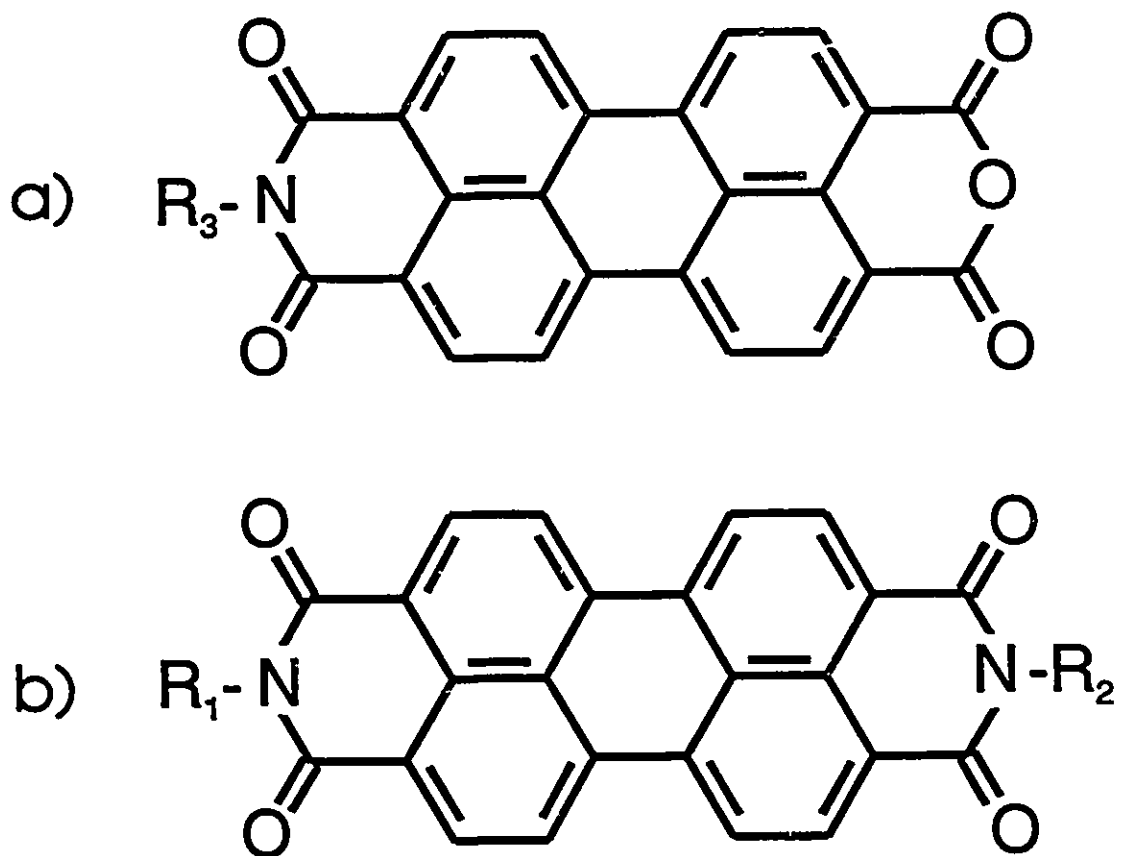
Figure 1.1: The basic structure of the perylene tetracarboxylic monoimides, PTCO's, a), and diimides, PTCD's, b).

Table 1.1: Abbreviations for the perylene derivatives studied.

PTCD:	R Groups:
PPTCDM	R_1 = pentyl, R_2 = methyl
PPTCDE	R_1 = pentyl, R_2 = ethyl
PPTCDPr	R_1 = pentyl, R_2 = propyl
HPTCDE	R_1 = hexyl, R_2 = ethyl
HPTCNH	R_1 = hexyl, R_2 = hydrogen
PTCO:	R Group:
PrPTCO	R_3 = propyl
PPTCO	R_3 = pentyl
HPTCO	R_3 = hexyl
PhPTCO	R_3 = 2-phenylethyl
HOPTCO	R_3 = 6-hydroxyhexyl

Applications

The PTCDs and PTCOs are an important class of electroactive and photoactive organic materials that may be applied as thin solid films in the development of new technologies [1.5]. A variety of diimides have potential use in tuneable dye lasing media [1.6,7]. Such systems have lasing ranges in the 555 to 587 nm range, depending on the choice of materials. These systems also experience very little, if any, photodegradation over a period of time. Xerographic applications [1.8] have also received significant attention in recent years. Several PTCD's were incorporated into photoreceptors and the photosensitivity of these systems has been measured in the 400 to 800 nm region. Electroluminescent display devices [1.9-11] have also been fabricated from thin films of perylene derivatives. These devices typically emit in the red spectral region and this emission is believed to arise from excimer emission. PTCD's and PTCO's have demonstrated their functionality as energy donors in energy transfer systems [1.12]. The PTCD's and PTCO's have a small band gap, making them potential organic semiconductors [1.13,14] and have been studied in diode systems [1.5,15-18].

Analytical applications have been explored with their use in chemical sensor systems [1.19-21]. Changes in the fluorescence of these materials due to different gases have been observed [1.19,20]. A more complicated system involved depositing a thin film of perylene onto a quartz crystal oscillator so changes in fluorescence and mass could be made during exposure to gases [1.21]. Moreover, the perylene diimide chromophore has been incorporated into a novel class of molecular recognition molecules [1.22].

As can be seen from this list, the range of applications is quite broad for PTCD and PTCO materials. Moreover, such devices can make use of the PTCD's and PTCO's as ultra-thin films. For application development, such miniaturization will result in smaller devices and improved cost since very small quantities of materials are required. One of the most successful techniques for fabrication of organized molecular structures as thin solid films is the Langmuir-Blodgett (LB) method [1.23,24]. These films are single monomolecular layers deposited onto solid substrates. A greater description of

these films can be found in *Chapter 2*. The structure of the film plays an important role in the potential application of the films. Therefore, there is strong motivation for studying the physical and spectroscopic properties of LB monolayers fabricated from perylene tetracarboxylics.

Synthesis

The synthesis of symmetric PTCDs has been reported in the literature *[1.1,25]*, as well as the asymmetric derivatives *[1.2,3]* and the monoimide derivatives *[1.4,26]*. A summary of the general synthetic methods is presented here for the sake of completeness. The typical starting material for the preparation of the diimides is perylene tetracarboxylic dianhyride (PTCDA), which is prepared by the fusion of napthalimide under basic conditions at elevated temperatures. The PTCDA is then reacted with primary amines (aromatic or aliphatic) in a high boiling solvent to yield the symmetric PTCDs. The route to the asymmetric PTCDs involves the preparation of a PTCO first, then reaction with the appropriate primary amine to yield the desired PTCD *[1.2,3]*.

There are two routes to the PTCO derivatives. The simplest involves reacting PTCDA (in large excess) with the desired primary amine, then purified appropriately. The second method involves synthesizing a symmetric PTCD and transforming it into a PTCO. The PTCOs and PTCDs used in this thesis were provided by Prof. Y. Nagao of the University of Tokyo and by Jim Duff at the Xerox Research Centre of Canada. The different materials studied and their abbreviations are given in *Table 1.1*. The R groups correspond to those in *Figure 1.1*.

Perylene and Perylene Tetracarboxylic Structure

The structure of these materials is very important. The PTCD and PTCO materials can have widely differing colours ranging from bright orange to dark violet, even though the parent chromophore is essentially the same for all the molecules in these classes. Therefore, their intermolecular structure must play a large role in their optical properties.

Structural characterizations of PTCDs and PTCOs are not common. The robustness of the PTCDs and PTCOs is a useful property for devices fabricated from these materials; but this same robustness makes them difficult to work with. Their solubility is marginal at best, and growing crystals of these materials has only been accomplished by two research groups *[1.27-31]*. The most successful crystals were recrystallized from nitrobenzene or *m*-cresol and were of very low quality. Typically, these crystals were needles about 1 mm in length. Scanning electron micrographs of 3000 Å thick evaporated films also show the formation of needle-like microcrystals *[1.32]*.

From the crystal studies, the perylene tetracaboxylic chromophore is planar. The nitrogen-nitrogen distance is between 1.134 and 1.143 nm. The width of the carbon skeleton of the chromophore is between 0.480 and 0.484 nm *[1.27-30]*.

On a molecular level, the chromophores are primarily arranged in parallel stacks, with one molecule slightly off-centre from its neighbour. The chromophores are plane-parallel to each other with separation distances between 0.341 and 0.348 nm. One molecule is displaced from its neighbour in the stack by about 0.09 to 0.32 nm along the length of the chromophore and by about 0.03 to 0.34 nm along the width of the chromophore, depending on the substituents off the imide nitrogens *[1.30]*. The larger separation distance corresponds with molecules that have hindered stacking due to bulky substituents. The *N, N'*-diethyl PTCD (EPTCDE) has an anomalous crystal structure, compared to the other PTCDs. The molecules are stacked, but they are twisted about a central axis, rather than laterally displaced *[1.30]*. The *N,N'*-di(2,6-xylyl) PTCD (XPTCDX) does not stack at all *[1.28,30]* since the phenyl ring is perpendicular to the perylene chromophore and the methyl groups interfere with effective stacking.

Typical crystals of the symmetric PTCDs are primarily triclinic or monoclinic *[1.27,28]*. When the substituents are ethers, such as ethoxyethyl or methoxypropyl, the crystals are triclinic with one molecule per unit cell. When the substituents are alkyl chains or branched alkyl chains, the crystals are monoclinic with 2 or 4 molecules per unit cell. The only exception is EPTCDE, which is orthorhombic and with 8 molecules per unit cell *[1.28]*. The *N,N'*-2-phenylethyl PTCO (PhPTCOPh) crystal is also monoclinic and is dimeric with four molecules per unit cell. The dimers are arranged in stacks.

It is believed that small differences in chromophore overlap are responsible for differences in observed colour. The greater the overlap, the darker the solid. It is the different *N* substituents that control this overlap. To date, no clear patterns have emerged that can be used to predict colour based on substituent effects.

It has been shown that the solubility of the materials in toluene, cyclohexanone or cyclohexane (depending on the PTCD) correlates well with melting points and is a function of substituent chain length (for single chain alkyl substituents) *[1.31]*. Solubility is highest and melting point is lowest for hexyl and pentyl substituents. For shorter chain lengths, π-stacking is believed to be the dominant driving force behind the molecular organization. For longer chains, the side-chain/side-chain interactions dominate and the crystals begin to behave like a paraffin-like material. Also, the addition of *t*-butyl groups to the *N*-substituents increases solubility by limiting the stacking abilities of the chromophores. Since physically studying the structure of PTCDs and PTCOs is extremely difficult, attempts are now being made to model structures using computer simulations *[1.33,34]*. Molecular stacking occurs almost universally for the perylenes simulated *[1.34]*.

Objective of Thesis Work

Perylene tetracarboxylics form an interesting class of materials with many potential applications in new technologies. The properties of these materials depends very strongly on the intermolecular geometry present. Space and cost requirements for PTCD or PTCO devices can be minimized by using these materials in ultra-thin film devices. Langmuir and Langmuir-Blodgett monolayers provide model systems for the characterization of these materials incorporated into a thin-film environment. Therefore, a study of the formation of floating layers and LB films of these materials was undertaken. The spectroscopic characterization of the bulk material, dispersed in KBr pellets, and that of the fabricated thin solid films was performed. The spectroscopic characteristics of these films was used to investigate their structure and film forming properties. These monolayers were used as probes to investigate surface enhanced infrared spectroscopy, and to explore energy transfer between monolayers.

Chapter 3 presents an overview of the observed spectroscopic characteristics of these films and materials. Moreover, LB films serve as model systems for structural determination through spectroscopic means. In *Chapters 4* and *5*, the average molecular orientation is determined via infrared spectroscopy. *Chapter 6* explores the intermolecular geometry of some PTCOs and PTCDs and compares them to the previously mentioned x-ray crystallography results. The roles of molecular amphilicity and *N*-substituents in monolayer structure and stability are also discussed in detail. *Chapter 7* investigates two compounds incorporated into energy transfer systems. The last chapter of this thesis is an investigation into surface enhanced infrared spectroscopy. The perylene tetracarboxylic that yielded the highest quality and most stable monolayers was used as a probe to investigate this interesting phenomenon.

Overall, the objective of this thesis is to prepare Langmuir and Langmuir-Blodgett films of perylene tetracarboxylic derivatives. Then the vibrational and electronic spectroscopic characterization of these films is performed with the intent to deduce film structure and stability. The functionality of these films is demonstrated via incorporation into energy transfer systems and as probe molecules to investigate surface enhanced

infrared spectroscopy.

References - Chapter 1

[1.1] Herbst, W.; Hunger, K., *Industrial Organic Pigments: Production, Properties, Applications*, VCH Publishers, NY, NY, 1993, p467-480.

[1.2] Nagao, Y; Misono, T., *Dyes and Pigments*, 1984, *5*, 171.

[1.3] Nagao, Y.; Abe, Y; Misono, T., *Dyes and Pigments*, 1985, *6*, 303.

[1.4] Nagao, Y; Misono, T., *Bull. Chem. Soc. Jpn.*, 1981, *54*, 1191.

[1.5] Forrest, S.R.; Kaplan, M.L., Schmidt, P.H.; Venkastesan, T.; Lovinger, A.; *Appl. Phys. Let.*, 1982, *41*, 708.

[1.6] Irvi, J.; Burshtein, Z.; Miron, E.; Resfeld, R.; Eyal, M.; *IEEE Journal of Quantum Electronics*, 1990, *26*, 1516.

[1.7] Lohmannsroben, H.G.; Langhals, H.; *Appl. Phys. B.*, 1989, *48*, 449.

[1.8] Duff, J.; Hor, A.M.; Melnyk, A.R.; Teney, D.; *SPIE Hard Copy and Printing Materials, Media and Process*, 1990, *1253*, 184.

[1.9] Hayashi, S.; Etoh, H,; Saito, S.; *Jap. J. Appl. Phys.*, 1986, *25*, L773.

[1.10] Adachi, C.; Tokito, S.; Tsutsui, T.; Saito, S., *Jap. J. Appl. Phys.*, 1988, *27*, L269.

[1.11] Tsutsui, T.; Adachi, C.; Saito, S. n *Photochemical Processes in Organized Molecular Systems*, Honda, K. ed., Elsevier Science Publishers, B.V., 1991, pp 437-450.

[1.12] Johnson, E.; Aroca, R.; *Can. J. Chem.*, 1991, *69*, 1728-1731.

[1.13] Danziger, J.; Dodelet, J.P.; Armstrong, N.R., *Chem. Mater.*, 1991, *3*, 812.

[1.14] Tanaka, K.; Nishio, S.; Matsuura, Y.; Yamabe, T., *Synthetic Metals*, 1993, *55-57*, 896.

[1.15] Forrest, S.R.; Kaplan, M.L. Schmidt, P.H.; Feldman, W.L.; Yanowski, E., *Appl. Phys. Let.*, 1982, *41*, 90.

[1.16] Forrest, S.R.; Kaplan, M.L.; Schmidt, P.H., *J. Appl. Phys.*, 1984, *55*, 1492.

[1.17] Lam, J.F.; Forrest, S.R., Tangonan, G.L.; *Phys. Rev. Let.*, 1991, *66*, 1614.

[1.18] So, F.F.; Forrest, S.R., *Phys. Rev. Let.*, 1986, *48*, 183.

[1.19] Aroca, R.; Maiti, A.K., Nagao, Y.; *J. Raman Spectrosc.*, 1993, *24*, 351.

[1.20] van Ewyk, R.L.; Chadwick, A.V.; Wright, J.D.; *J. Chem. Soc., Faraday Trans. 1*, **1981**, *77*, 73-79.

[1.21] Furuki, M.; Pu, L.S.; *Mol. Crystals Liq. Crystals*, **1993**, *227*, 325-337.

[1.22] Shimidzu, K.D., Dewey, T.M., Rebek, J., *J. Amer. Chem. Soc.*, **1994**, *116*, 5145.

[1.23] Ulman, A. *Ultrathin Organic Films*; Academic Press, Inc., New York, 1991.

[1.24] Roberts, G.G. in *Langmuir-Blodgett Films*, ed. G.G. Roberts, Plenum Press, New York, 1990 pp 317-412.

[1.25] Lukac, I.; Langhals, H., *Chem. Ber.*, **1983**, *116*, 3524.

[1.26] Kaiser, H.; Linder, J.; Langhals, H., *Chem. Ber.*, **1991**, *124*, 529.

[1.27] Hadicke, E.; Graser, F., *Acta Cryst.*, **1986**, *C42*, 189.

[1.28] Hadicke, E.; Graser, F., *Acta Cryst.*, **1986**, *C42*, 195.

[1.29] Graser, F.; Hadicke, E., *Liebigs Ann. Chem.*, **1980**, 1994.

[1.30] Graser, F.; Hadicke, E., *Liebigs Ann. Chem.*, **1984**, 483.

[1.31] Langhals, H.; Demmig, S.; Potrawa, T., *J. Prakt. Chem.*, **1991** *333*, 733.

[1.32] Tamizhmani, G., Dodelet, J.P., Cote, R., Gravel, D., *Chem. Mater.*, **1991**, *3*, 1046.

[1.33] McKerrow, A.J., Buncel, E., Kazmaier, P., *Can. J. Chem.*, **1993**, *71*, 390.

[1.34] Perlstein, J. *Chem. Mater.*, **1994**, *6*, 319.

Chapter 2 - Experimental and Instrumental Systems

The perylene derivatives studied differed in their physical properties. Hence, the conditions used to study them will also differ. More information pertaining to specific compounds and techniques are given in the appropriate chapters of this thesis. The primary focus of this chapter is to impart a general understanding of the instrumentation and techniques used for this thesis work.

Langmuir-Blodgett Film Concepts

The perylene derivatives studied were fabricated into Langmuir-Blodgett (LB) films. The LB technique permits the preparation of unimolecular layers that float at an air/liquid subphase interface. These layers may then be transferred to a solid subphase. Successive transfers can result in multilayer structures.

The pioneers, and the namesakes, of Langmuir-Blodgett films are Irving Langmuir and Catherine Blodgett. Langmuir designed and constructed the first LB trough *[2.1]*. The first report describing the transfer of monolayers to solid substrates *[2.2]* was read by Langmuir to the Faraday Society, but the first formal paper describing LB film preparation did not appear until 1935 *[2.3]*. It is very interesting that Langmuir described the size of fatty acids before the development of X-ray diffraction techniques *[2.1]*. The term "Langmuir Blodgett film" (LB) describes a monolayer or multilayer prepared after transfer to a solid substrate. Whereas the term "Langmuir film" refers to the monolayer floating on a liquid subphase.

The liquid subphase, usually high purity water, is contained in a teflon coated trough *(see Figure 2.1)*. At either end are two barriers, one floating and one moveable. In order to prepare LB layers, a solution containing the PTCD is spread dropwise over the aqueous subphase. The spreading solvent is allowed to evaporate, leaving behind PTCD molecules floating at the air/water interface. The moving barrier is shifted in order to decrease the spreading area and thereby compress the floating PTCD molecules. The floating barrier is fixed to a device that measures the surface pressure, Π, of the floating layer. The surface pressure is defined as the difference in surface tension
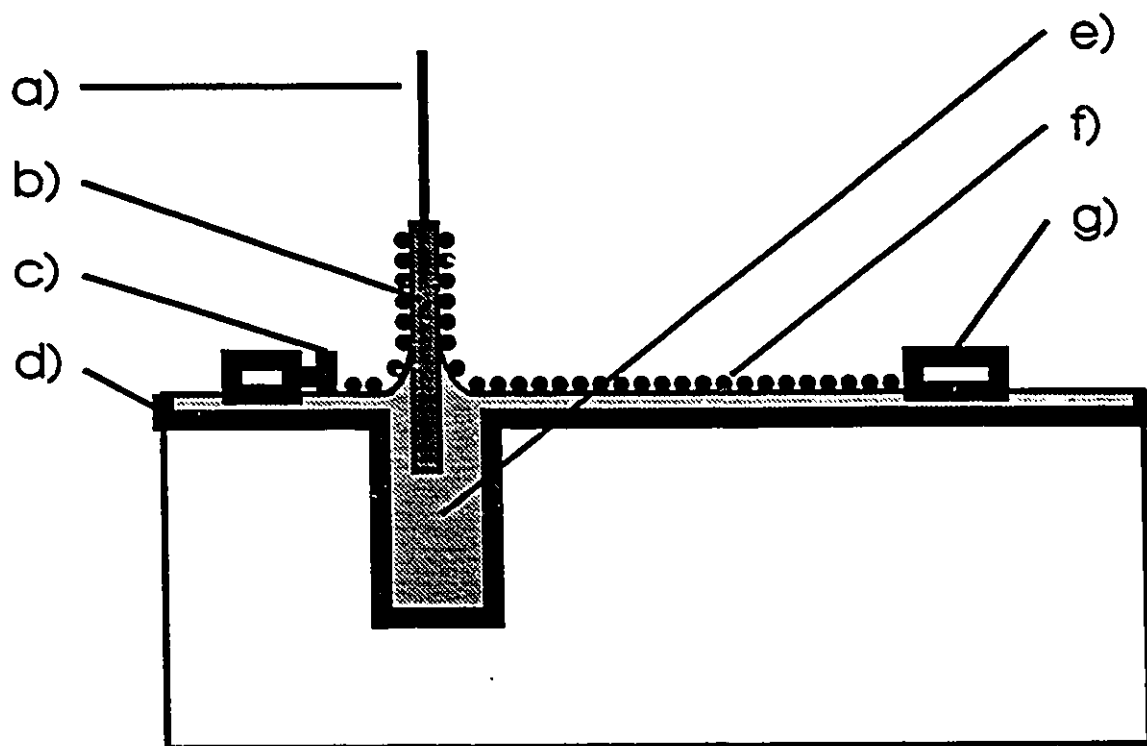
Figure 2.1:   Components of the LB trough: a) dipping arm, b) substrate, c) film
balance, d) teflon coated trough, e) aqueous subphase, f) floating
monolayer, g) moving barrier

between the monolayer covered surface and a clean, reference surface *[2.4]* and is given by equation 2.1

$$\Pi = \gamma - \gamma_o \qquad\qquad (2.1)$$

where γ is the surface tension of the subphase without the monolayer and γ_o is the surface tension in the presence of the floating monolayer. Water is the most common subphase due to its high surface tension of 73 mN/m and that most organic compounds are insoluble in water. For pure water, the maximum possible surface pressure would be 73 mN/m at 20°C. Non-aqueous subphases with even higher surface tensions have been used, such as mercury *[2.5]*.

By plotting the area per molecule, A, and the surface pressure at constant temperature, a pressure-area isotherm is recorded. This isotherm is the two dimensional analogue of a pressure-volume isotherm involving the compression of a gas in a cylinder. In this case, the floating PTCD molecules can be viewed as a two dimensional gas confined to the air/water interface. The compression of a monolayer can result in the formation of a variety of phases.

At very large surface areas, the spread molecules are far apart and interact primarily with the subphase. This is analogous to a two dimensional gas. As the surface area per molecule is diminished, the molecules begin to come into contact with each other and a liquid phase results. Continued decreases in area per molecule will result in a region of low compressibility. This is a solid phase, like a two dimensional crystal. *Figure* 2.2 illustrates how these different phases would appear in a surface pressure/area isotherm. This figure represents ideal features and does not represent one specific compound. Note that two types of liquid phases can exist. A liquid expanded phase, characterized by higher compressibility and non-linear region, and a liquid condensed phase, lower compressibility as the expanded phase, but not as low as a solid phase, exist. The linear portion of the isotherm related to the solid phase may be extrapolated to the x-axis of the isotherm plot. This intercept is known as the limiting area of the molecules spread. This value represents the area occupied by an uncompressed molecule in the floating layer.
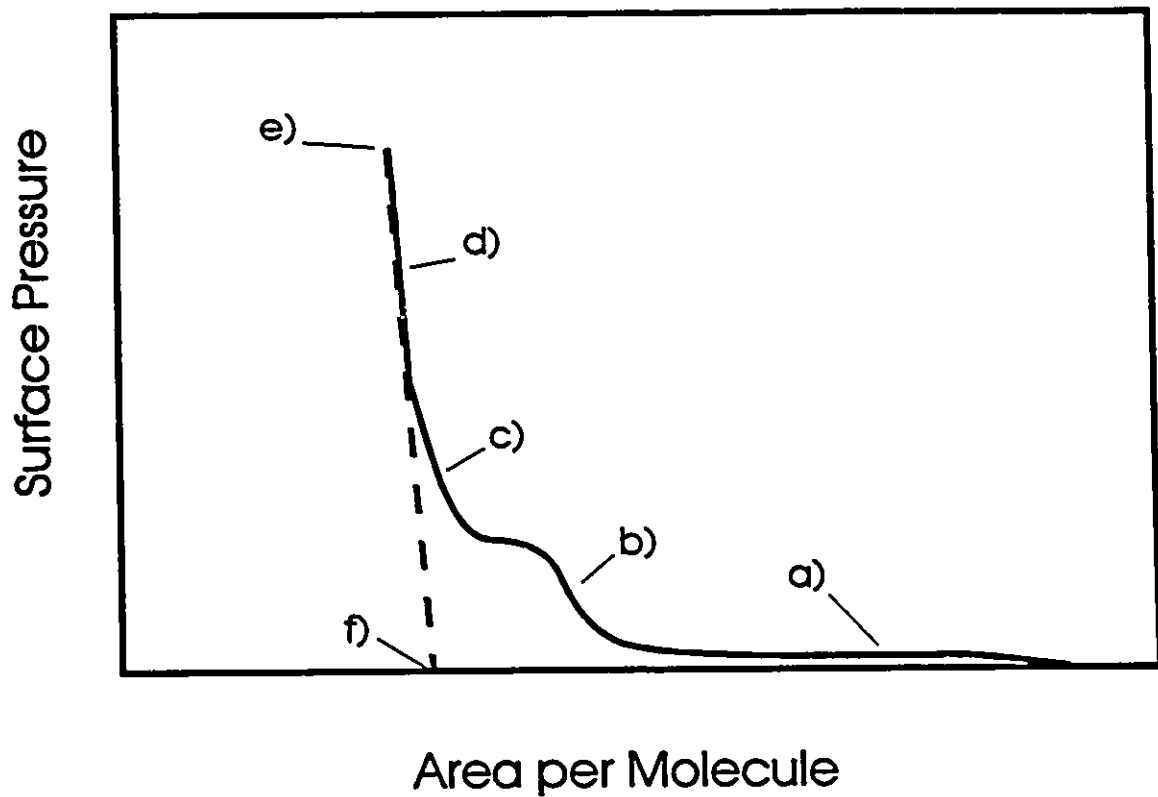
14

Figure 2.2: Appearance of phases in the surface pressure/area isotherm for a hypothetical monolayer. a) gas, b) liquid expanded, c) liquid condensed, d) solid, e) monolayer collapse, f) limiting area.

15

Careful choices must be made when selecting the materials used to prepare LB layers. First of all, the LB forming material needs to be soluble in the spreading solvent, yet must be insoluble in the subphase. Moreover, the spreading solvent needs to be volatile and also insoluble in water. The most common LB forming materials are amphiphiles, molecules with a hydrophobic portion and a hydrophilic portion. Classic examples are fatty acids such as arachidic and stearic acids. Amphiphiles will spread with the polar, hydrophilic end preferentially oriented toward the water subphase.

The PTCDs used in this work are of limited solubility. Chloroform (HPLC grade, BDH) was the initial solvent choice. If this did not provide adequate solubility, then a 10% by volume solution of trifluoroacetic acid (TFA, spectroscopic grade, Aldrich) in chloroform was used. The solid PTCDs appeared either reddish-brown or dark purple in colour. Upon solvation, a brilliant, yellow solution resulted that became orange at higher concentrations. *Table 1* summarizes the solutions used in the preparation of PTCD LBs. The only exception to this was HPTCNH. This material was the least soluble and its solutions were dark purple in colour.

Once the compressed, floating monolayer is formed, it may be transferred, at constant surface pressure, to a solid substrate for characterization. Transfer can be performed through one of several techniques, the choice of which depends upon the properties of the material spread and the substrate to which the film is to be transferred. *Figure 2.3* illustrates the four basic deposition techniques. Transfer resulting in X deposition results from the downward dipping of a hydrophobic substrate into the subphase. The hydrophobic end of the amphiphile interacts with a hydrophobic substrate and permits transfer. Z deposition occurs when a hydrophilic substrate is withdrawn from the subphase and the hydrophilic ends of the floating layer interact with the surface and permit transfer. Quite often, X deposition will result in a new, hydrophilic surface on the once hydrophobic substrate due to the fact that the polar ends of the amphiphile are now facing away from the substrate. When the substrate is withdrawn, transfer again takes place and a bilayer is formed. This forms an alternating LB bilayer structure and is known as Y deposition. The last form of transfer is horizontal deposition. This is similar to X deposition, except that the substrate surface is parallel to the floating layer. The

Table 2.1: Description of PTCDs used in monolayer fabrication

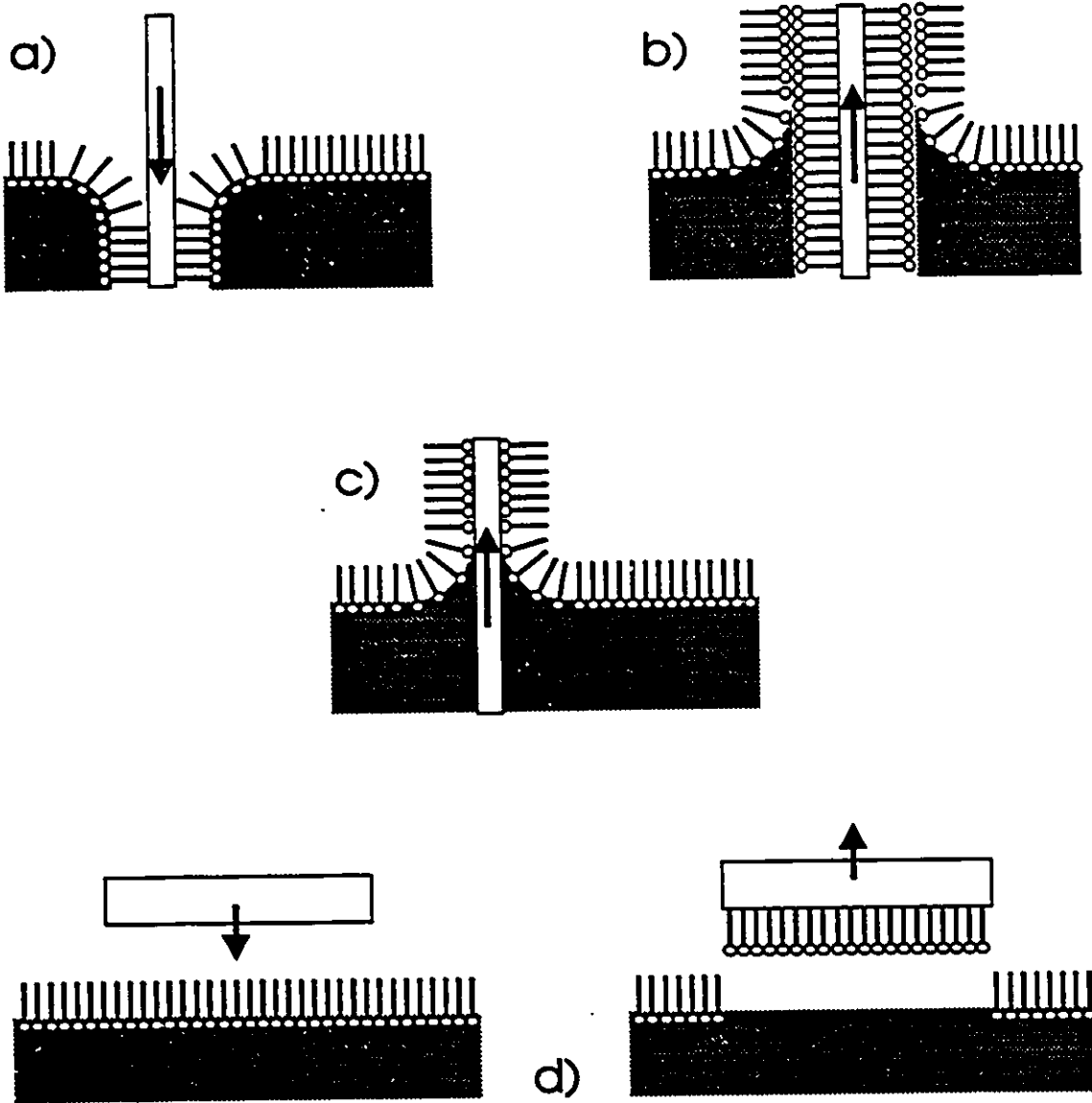| PTCD	F.W. (g/mol)	Colour of Solid	Solvent used	Spreading Temperature (°C)
PPTCDM	474.5	red	CHCl₃	25
PPTCDE	488.5	red	CHCl₃	25
PPTCDPr	502.6	red	CHCl₃	25
HPTCDE	502.6	red	CHCl₃	25
PrPTCO	433.4	red	10% TFA	15, 25
PPTCO	461.5	red	CHCl₃, 10% TFA	15, 25
HPTCO	476.5	red	CHCl₃, 10% TFA	15, 25
PhPTCO	495.5	brown/ red	10% TFA	15, 25
HOPTCO	491.5	brown/ red	10% TFA	15, 25
HPTCNH	475.5	dark purple	CHCl₃	25

17

Figure 2.3: The four deposition techniques. a) X, b) Y, c) Z, and d) horizontal.

substrate is lowered until it makes contact with the film and transfer takes place through hydrophobic-hydrophobic interactions. The primary difference between this and X deposition is that there is no change in direction of the film during the transfer process.

The choice of substrate depends on the characterization technique used. Mono and multilayers were transferred to Corning 7059 glass slides for electronic characterization. Infrared transparent windows such as CaF_2, Ge and ZnS (Wilmad) were used to characterize the LB films in the infrared. Metal island films on glass were used for surface enhanced Raman scattering (SERS), surface enhanced resonance Raman scattering (SERRS) and for surface enhanced infrared reflection/absorption (SEIRRA) spectroscopy. The details of monolayer transfer to different substrates is given in the appropriate chapters of this thesis. Details such as the type of deposition, observed transfer ratios and substrates used are also provided.

It is important to point out that most of the films could be transferred through Z deposition. However, the PTCDs dissolved in the 10% TFA were very difficult to transfer through vertical methods. Therefore, these films were transferred by horizontal deposition. Only PPTCO was transferred by both techniques and were studied to see the effects of the film deposition technique on the spectroscopy of the LB films.

Film quality was assessed from two methods. First of all, the transfer ratio for each film was measured. The transfer ratio, TR, for a film is defined as the ratio of area lost by the floating film during transfer to the area of the substrate that the film is transferred onto. If the transfer ratio is near unity, then a necessary, but not a sufficient, condition for good film transfer has been met. After transfer to solid substrates, the films were examined by optical microscopy. Overall, the films were fairly homogeneous on this scale.

Preparation of Langmuir Blodgett Films

The subphase used was double distilled water passed through a Milli-Q filtration system and had a measured resistivity of 18.2 MΩcm. The trough was a Lauda Langmuir film balance equipped with an electronically controlled dipping device, a Lauda Filmlift FL-1 and a temperature controlled circulating bath. Dipping speed was 0.06 mm/s and film compression was 10^{-3} $nm^2molecule^{-1}s^{-1}$. Typical transfer ratios were near unity. Deviations from this are mentioned in the appropriate chapters. Generally, the spreading solutions were in the $1x10^{-4}$ to $3x10^{-4}$ M range and spreading volumes were between 0.5 and 1.5 mL. The specific concentrations and volumes were carefully noted so the area per molecule could be calculated at a specific surface pressure and so the surface pressure/area isotherms could be appropriately calibrated. Before placing the subphase in the trough, the edges of the trough and the barriers were wiped clean with acetone and double rinsed with high purity water. The isotherms were recorded using an xy chart recorder and the data points were read from the chart paper and manually entered into Sigma Plot, a commercially available scientific graphing software package from Jandel Corporation. Glass slides and infrared windows were double cleaned ultrasonically in chloroform for 30 minutes and dried in a stream of high purity nitrogen prior to use. In order to render the glass hydrophilic, it was immersed in a 0.1 M NaOH solution for 30 minutes and rinsed in water. Hydrophobic slides were prepared from hydrophilic ones by immersing them in a 5% dichlorodimethylsilane (Aldrich) solution in chloroform for 5 minutes and rinsing in methanol, then water. Transfer was performed under constant surface pressure and the transfer ratio was measured for each film transferred.

Evaporated Films

This work makes use of a variety of surface enhancing substrates. Such substrates are typically noble metal island films on glass slides. In order to prepare surface enhancing substrates, the metal is evaporated, under high vacuum, to the desired substrate. Substrates used in reflection/absorption experiments were prepared in a similar manner. The most common material evaporated for SERRS work was silver. Gold, copper, tin, indium and aluminum were evaporated in order to study SEIRRA

spectroscopy. The specific choice of substrate is detailed in the appropriate chapters of this thesis.

The films were prepared by thermal evaporation onto Corning 7059 glass slides at 200°C and under pressures of 10^{-6} mbars. Island films were evaporated to a thickness of 6 nm and smooth film, used in reflectance measurements, were 110 nm. Evaporation rates were 0.05 nm/s for island films and 0.5 nm/s for continuous films.

The evaporation apparatus was composed of commercial and home built components. The vacuum system consisted of an Edwards E2M2 rotary vacuum pump which functioned as the forepump for an Edwards diffusion pump. A jacket filled with liquid nitrogen was used to reduce the pressure by an additional order of magnitude. Pressures were measured using a Balzers IKR 020 cold cathode gauge (for pressures $< 10^{-3}$ mbars) and a Balzers TPR 010 Pirani gauge (for pressures $> 10^{-3}$ mbars). The metals were thermally evaporated using a Balzers BSV 080 glow discharge/evaporation control unit. Film thickness (by mass) and evaporation rate was monitored by a XTC Inficon quartz crystal oscillator. *Figure 2.4* is a schematic diagram of the evaporation system used.

The same evaporation procedures were used to produce metal island films and smooth metal films. The structure of the film depends on the amount of metal evaporated *[2.6]*. When the metal first begins to condense on the substrate, isolated atoms exist. As the evaporation process continues, the metal atoms can migrate across the surface and form nucleation sites that continue to grow into islands structures. As the island structures grow, they begin to coalesce and eventually form a continuous film. The substrate is heated in order to impart more energy to the metal atoms. This allows greater diffusion across the surface and a more homogeneous particle distribution is obtained. This process is illustrated in *Figure 2.5*.

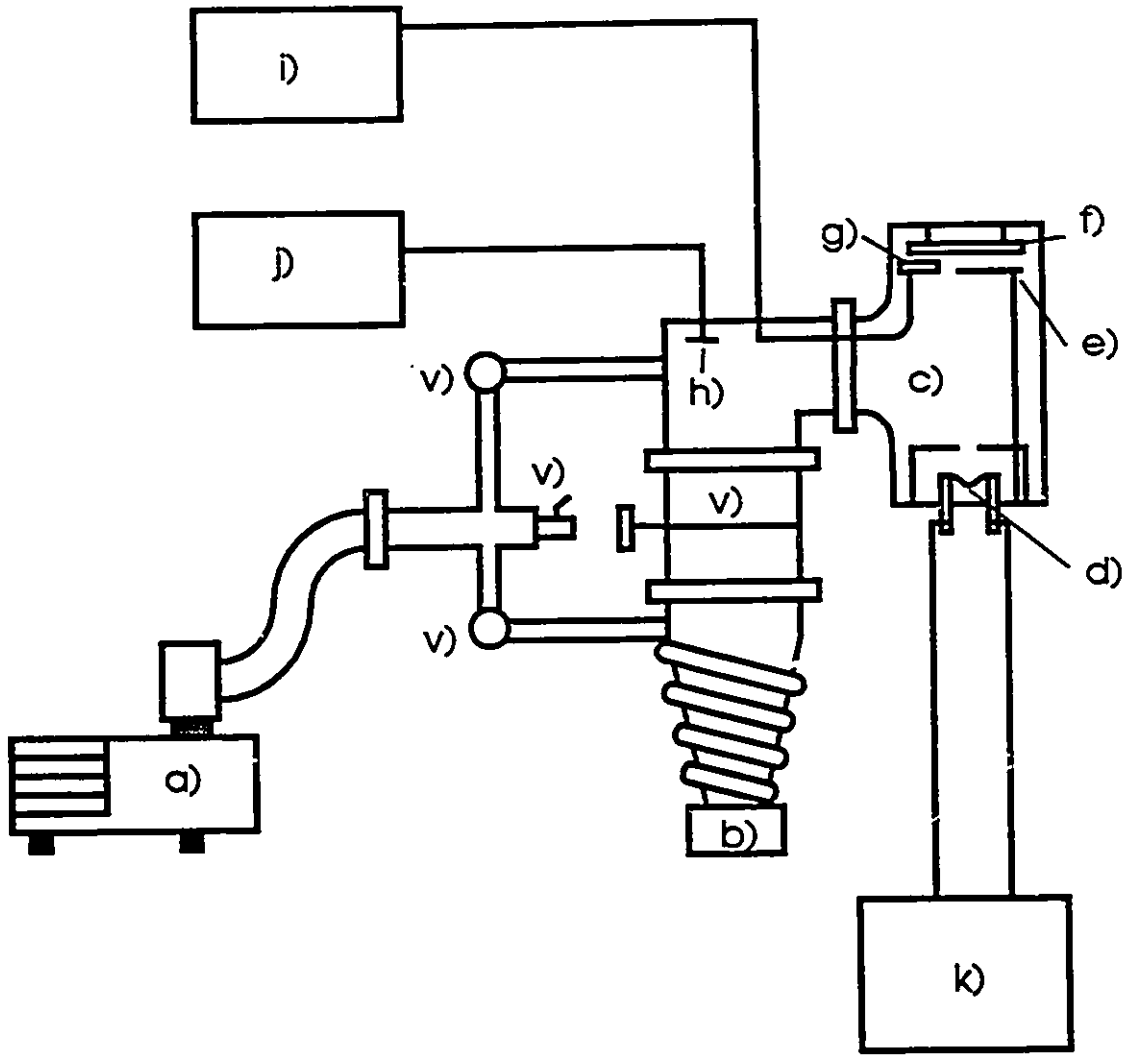Figure 2.4: Diagram of the evaporation system used. a) forepump, b) diffusion pump, c) evaporation chamber, d) source, e) shutter, f) substrate, g) crystal oscillator, h) pressure gauge, i) film thickness monitor, j) pressure monitor, k) evaporation current control, v) valves.
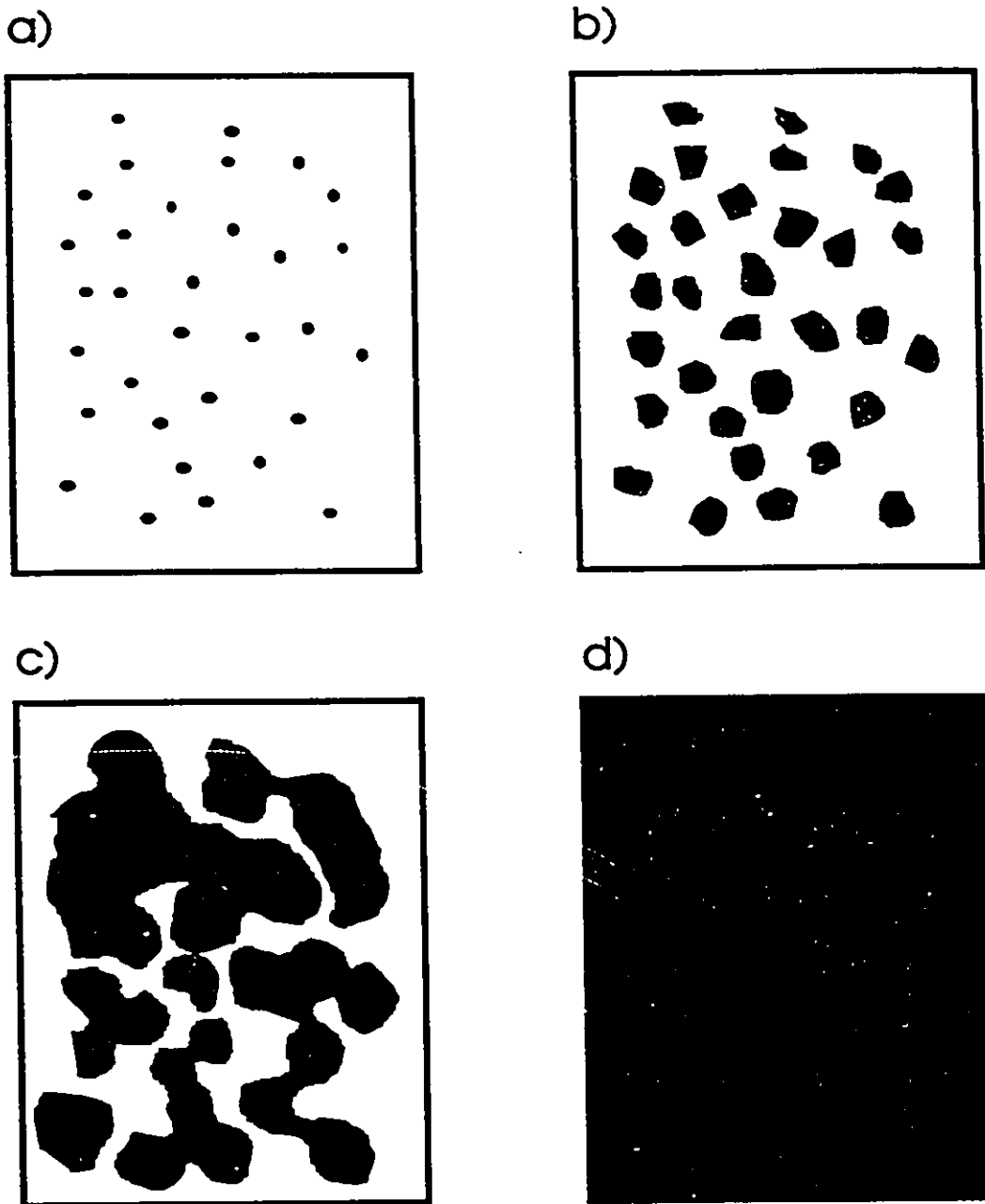
Figure 2.5:   Schematic representation of the formation of a thin metal film. a) nucleation, b) island growth, c) island coalescence, d) continuous film.

Spectroscopy - Instruments and Techniques

The primary goal of this research is to elucidate structure and properties of LB films of various perylene tetracarboxylic derivatives. This is being accomplished through spectroscopic means. Four fundamental forms of spectroscopy were used in this work: infrared absorption, UV-visible absorption, Raman scattering and steady state fluorescence. Each of these techniques can be used to characterize various aspects of the systems studied. The instrumentation and techniques are described in this chapter. Specific experimental details are left to the appropriate chapters of this thesis.

UV-Visible Absorption

The visible absorption of the PTCDs as LBs and in solutions were recorded using a Response single beam spectrophotometer. An IBM PC was interfaced to this instrument so spectra could be downloaded as ASCII files for import into Spectra-Calc, a commercially available spectral analysis software package. The ultraviolet portion of the spectrum was not investigated for two reasons. The glass slides are opaque below 300 nm and the interesting optical properties of these compounds are in the visible region of the spectrum.

Infrared Absorption

The most powerful structural tool used in this work is infrared absorption. Since molecular vibrations cause a change in dipole moment which can be represented as a vector, infrared spectroscopy can be used to determine molecular orientation. In particular, the orientation in LB films was probed by comparing reflection absorption (RAIR) spectra with transmission spectra. The surface selection rules for these systems are illustrated in *Figures 2.6 and 7.*

For RAIR spectroscopy, the sample LB is transferred to a 110 nm thick, smooth silver surface, prepared by vacuum evaporation. The unpolarized infrared beam makes a single reflection off the sample surface. The unpolarized beam can be broken into two components, a p polarized and an s polarized component. The p-polarized component lies in the plane of reflection and the s polarized component is perpendicular to the plane of
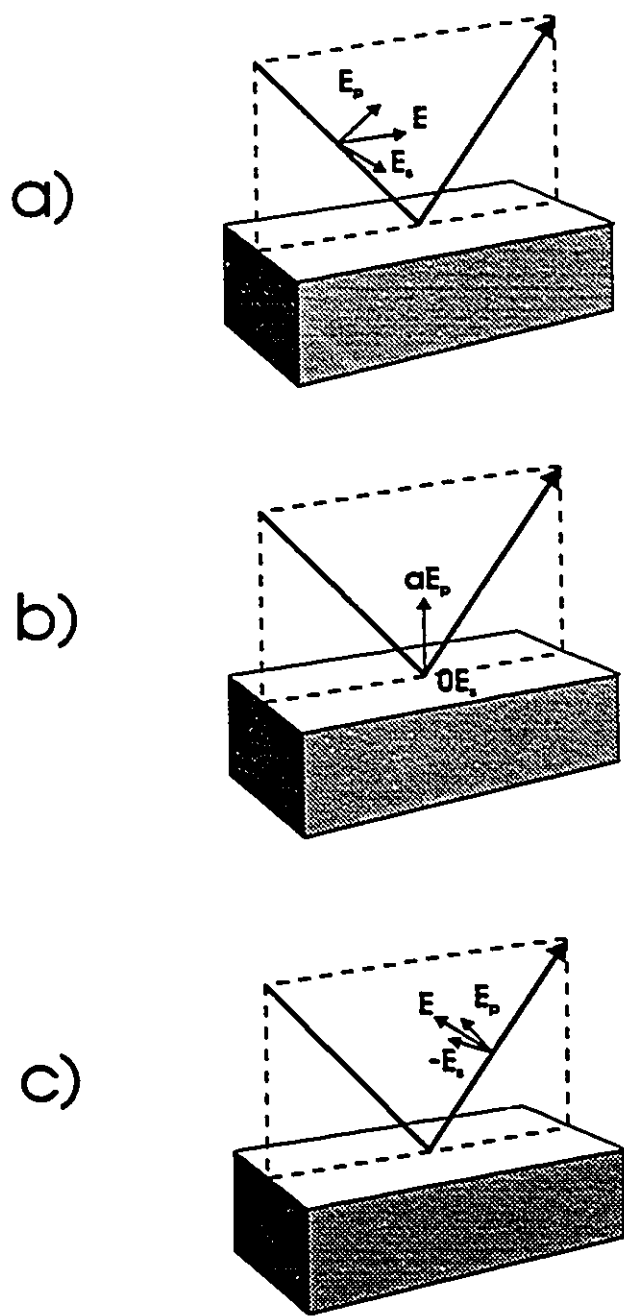
Figure 2.6: The polarization effects associated with RAIR spectroscopy.
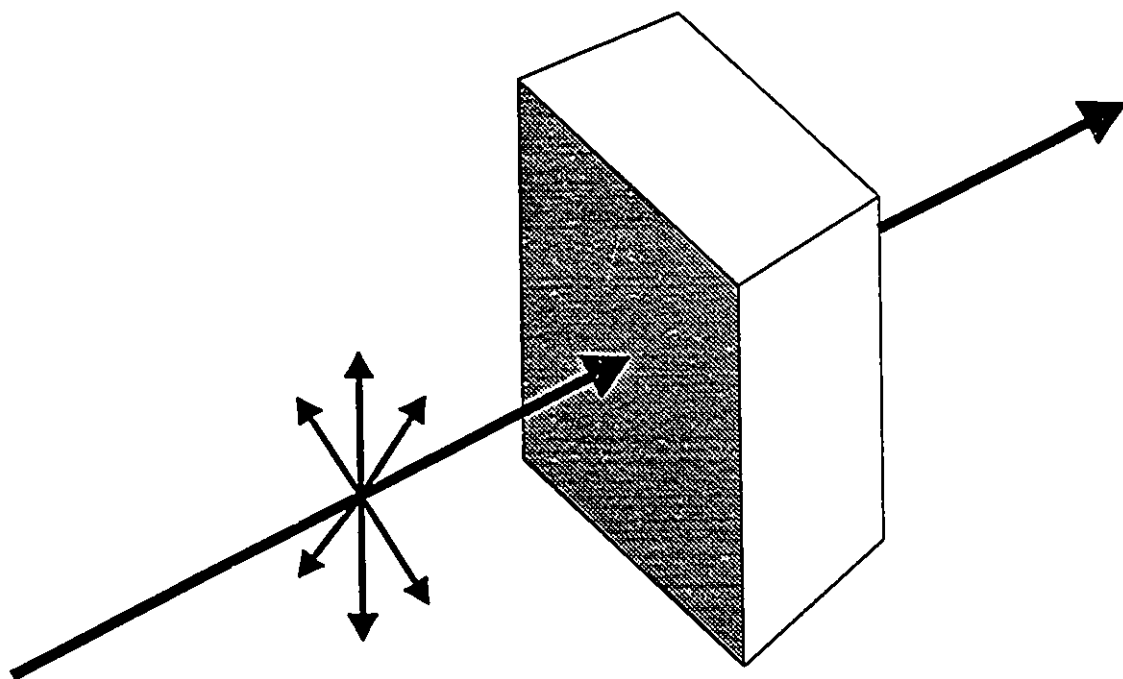
Figure 2.7:   The polarization effects associated with transmission infrared spectroscopy of LB monolayers. The polarization always resides in the plane of the monolayer.

reflection. When the light beam is reflected off the surface, a 180° phase change in the polarization takes place. For P polarized light, this results in constructive interference on the surface, hence an increase in the magnitude of the electric field interacting with the sample. For S polarized light, this phase change leads to the cancelling of the electric field during reflection. Therefore, no electric field exists at the surface for s-polarization. In the RAIRS experiments only the P-polarization component of the incident light can interact with the adsorbate, and the surface selection rules lead to the observation of molecular vibrations with a finite component of their dynamic dipole perpendicular to the metal surface [2.7,8].

The reverse trend exists for the transmission geometry. Regardless of polarization, the incident electric field always lies in the plane of the substrate. Only molecular vibrations with a finite component of their dynamic dipole parallel to the metal surface are detectable in this configuration. The net result of these selection rules is that strong bands in one configuration, say RAIR, will be weak in the other configuration.

It should also be pointed out that the angle of incidence is critical in the discussion of RAIR spectroscopy [2.9]. To maximize the electric field perpendicular to the substrate surface, a high incidence angle is desirable. The optimum incidence angle is 88° for a smooth metal surface [2.10,11].

The use of infrared spectroscopy allows the average molecular orientation in LB films to be determined. This involves a quantitative comparison of RAIR and transmission spectra, first demonstrated by Chollet [2.12] and improve by Takenaka [2.13] using Hansen's modification of the Fresnel equations as applied to stratified media [2.14]. A more detailed discussion involving the determination of molecular orientation and the enhancement factors associated with RAIR is given in *Chapter 4*.

Infrared Instrumentation

The infrared spectra were recorded using a Bomem DA3 Fourier transform infrared instrument (FT-IR) interfaced, through a high speed vector processor, to a PDP-11 minicomputer. The detector was a wide range MCD liquid nitrogen cooled detector. The reflection spectra were recorded by using a Spectra-tech variable angle reflectance accessory. Typical incidence angles were 75° and 80°. Angles slightly less than optimal were used to improve throughput of the system in order to improve the signal-to-noise ratio of the spectra. The infrared beam was polarized by using a Spectra-tech wire grid polarizer.

The spectra of the LB films (reflection and transmission) were typically recorded through the coaddition of 2000 interferograms, and processed using a fast Fourier transform (FFT) and using a Happ-Genzel function (HAMMING) for apodization. The selected apodization, one of seven choices in the Bomem software, provided the least distorted bands and produced only slight baseline ripple. Spectral resolution was 4 cm^{-1}. Bulk samples were dispersed in KBr pellets for IR characterization. The spectra of the KBr pellets were recorded through the coaddition of 128 scans and 1 cm^{-1} resolution. The sample box was purged with dry nitrogen, then evacuated to less than 1 torr before spectra were recorded. The spectra were imported into Spectra-Calc for data analysis.

Raman Spectroscopy and Instrumentation

Three different Raman instruments were used in different portions of this thesis work. Two spectrophotometers and a spectrograph were used to record Raman scattering and fluorescence. A Spex 1403 double beam spectrophotometer equipped with 1800 g/mm gratings and a water cooled Hamamatsu R928 photomultiplier tube interfaced with conventional photon counting electronics to an IBM microcomputer. Also, a Ramanor U-1000 spectrophotometer with similar photon detection electronics and equipped with a microscope attachment and an IBM microcomputer was used. The 488 and 514.5 nm laser lines of a Spectra-Physics argon ion laser was used as an excitation source. An S-1000 spectrograph equipped with a holographic notch filter, a liquid nitrogen cooled CCD detector and microscope attachment was also used. Typical recording conditions

for Raman scattering were 5 cm^{-1} band pass and 50 mW laser power on the sample. A liquid nitrogen cooled cold cell was used to record spectra for samples at temperatures as low as 92K. In order to prevent photodecomposition of LB samples, a spinning sample holder was used.

Fluorescence Spectroscopy

Steady state fluorescence was recorded using the two Raman spectrophotometers. Acquisition time was reduced and the spectral sampling interval was increased from 1 cm^{-1} to 10 cm^{-1}. The fluorescence of the LB films is sensitive to aggregation and the fluorescence can be used to measure energy transfer in these layers (see *Chapter 7*).

References - Chapter 2

[2.1]   Langmuir, I.; *J. Am. Chem. Soc.*, **1917**, *39*, 1848.

[2.2]   Langmuir, I.; *Trans. Faraday Soc.*, **1920**, *15*, 62.

[2.3]   Blodgett, K.; *J. Am. Chem. Soc.*, **1935**, *57*, 1007.

[2.4]   Hann, R.H. in *Langmuir-Blodgett Films*, ed. G.G. Roberts, Plenum Press, New York (1990) p 19.

[2.5]   Smith, T.; *Adv. Colloid Interface Sci.*, **1972**, *3*, 161-221.

[2.6]   Eckertova, L.; *Physics of Thin Films*, Plenum, New York (1986).

[2.7]   Hayden, B.E. in *Vibrational Spectroscopy of Molecules on Surfaces, Methods of Surface Characterization*, Yates, J.T.; Madey, T.E. Eds., Plenum Press, New York, 1987, Vol. 1, p 267.

[2.8]   Bradshaw, A.M.; Schweizer, E.; *Spectroscopy of Surfaces, Advances in Spectroscopy*, Clark, R.J.H.; Hester, R.E., Eds., John Wiley & Sons, N.Y., 1988, Vol. 16, p 413.

[2.9]   Greenler, R. in *CRC Critical Reviews in Solid State Sciences*, Schuele, D.E.; Hoffman, R.W., eds, Chemical Rubber Co., Cleveland, May, 1974, pp 420-425.

[2.10]   Greenler, R.G., *J. Chem. Phys.*, **1966**, *44*, 310.

[2.11]   Pritchard, J.; Sims, M.L., *Trans. Faraday Soc.*, **1970**, *66*, 427.

[2.12]   Chollet, P.A.; Messier, J.; Rosilio, C.; *J. Chem. Phys.*, **1976**, *64*, 1064.

[2.13]   Umemura, J.; Kamata, T.; Kawai, T. Takenaka, T.; *J. Phys. Chem.*, **1990**, *94*, 62.

[2.14]   Hansen, W.N., *J. Opt. Soc. Am.*, **1968**, *58*, 380.

Chapter 3:   General Spectroscopic Characteristics

Electronic Spectroscopy

It is known that polyaromatic compounds form aggregates in solution and in the solid state. Many such examples, such as naphthalene, anthracene, pyrene and perylene, have been reported in the literature [3.1-4]. Dye molecules, such as merocyanines [3.5], photo-merocyanines [3.6] and hemicyanines [3.7], also form aggregates. Aggregate formation may be characterized by electronic spectroscopy. The effect of the formation of ground state aggregates on the electronic spectra has been explained through molecular exciton theory [3.8,9] and a detailed description of this theory can be found in *Chapter 6*.

Molecular aggregates can be formed in the ground state as well as in the excited state. Such systems are called excimers when the aggregate consists of the same species and exciplexes when the system consists of more than one species [3.10]. The excimer, in the simplest case, can be considered an excited state dimer with no stable ground state. Hence, no absorption spectrum exists for the excimeric species, and the emission spectrum has unique characteristics. The excimer emission is characterized by a red shifted, broad and structureless band. Typical spectral shifts are on the order of one to two thousand wavenumbers with a bandwidth of a few hundred wavenumbers.

The early observations of excimer formation were made on solvated aromatic systems, such as perylene and anthanthrene in benzene [3.4]. The excimer formation is concentration and diffusion dependent. The higher the solute concentration or the lower the viscosity of the solvent, the greater the excimer emission and the lower the monomer emission [3.4,10].

Excimers have been observed for pyrene [3.11] and perylene crystals [3.1]. For perylene crystals, two polymorphs exist, the α and the β forms. The excimer emission is only observed for α-perylene crystal. The structural differences between the two polymorphs is quite distinct and is shown in *Figure 3.1.* The β-perylene has two molecules per unit cell with the ring planes at angles to each other. The α-perylene has
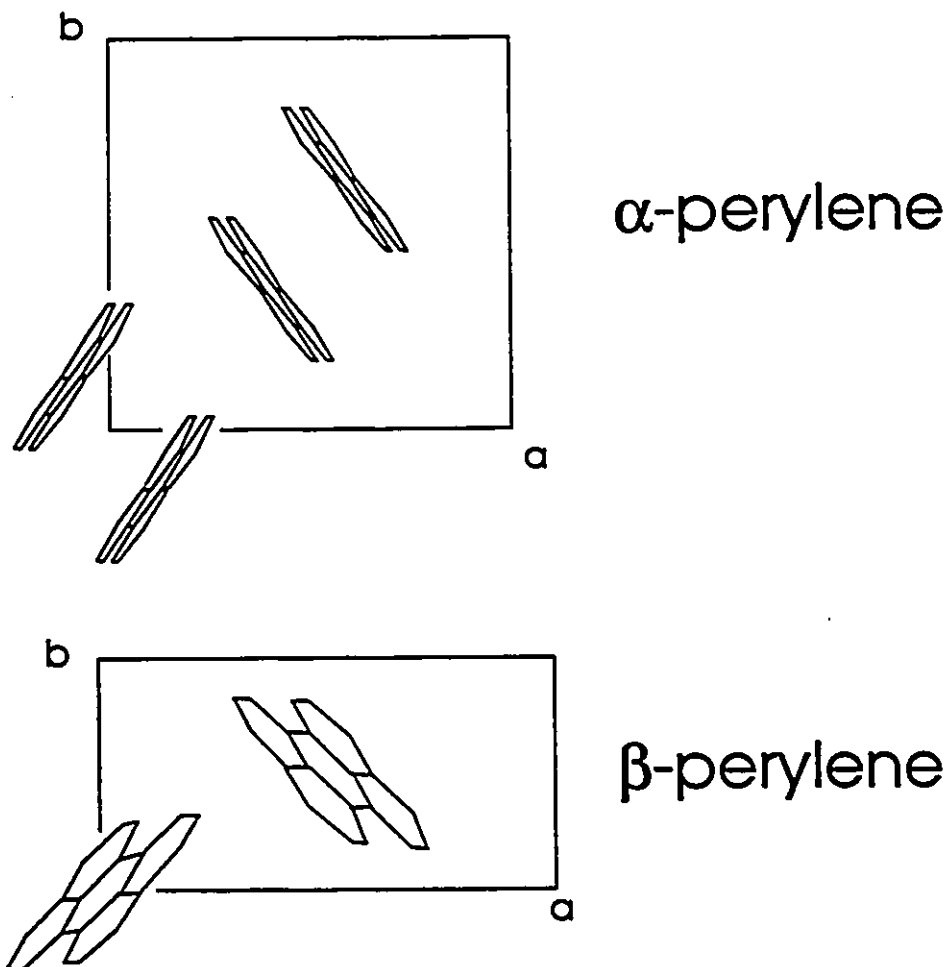
α-perylene

β-perylene

Figure 3.1: The two polymorphs of perylene crystals. a) α-perylene, b) β-perylene. View is looking along the c-axis at the ab plane.

two sandwich-pairs of molecules per unit cell. The sandwiches are arranged with their centres shifted by 0.09 nm along the long axis and 0.13 nm along the short axis [3.12]. It is this sandwich structure that facilitates excimer formation. Formation of excimers in monolayers has also been studied. In particular, fatty acid derivatives of pyrene [3.13-16] and perylene [3.17-19] have been transferred as LB monolayers and the excimer formation has been characterized.

As described in *Chapter 1*, X-ray crystal studies of symmetric PTCDs have shown that virtually all PTCDs exist in stacks, with parallel ring systems in the solid state and exhibit excimer-like emission [3.20-23]. The only exception to this trend is *N,N'*-Di(2,6-xylyl) perylene tetracarboxylic diimide (XPTCDX) [3.20,23]. The steric requirements of the methyl groups on the phenyl rings forces these rings to be nearly perpendicular to the perylene chromophore and prevent molecular stacking. As a result, only monomer-like emission is observed for crystals of this material. Therefore, the excimer emission arises from a stacked form of the material and monomer-like emission comes from non-stacked molecular arrangements.

Examples of the electronic spectra of PPTCDM and PPTCO are given in *Figures 3.2* and *3.3*. The top two spectra are of the material in solution and the bottom two were obtained from the material dispersed in a KBr pellet. The solution spectra of the two species are very similar and the fluorescence spectra are mirror images of the corresponding absorption spectra. They show the same vibronic patterns, as is expected for aromatic systems [3.10]. The spacing between the vibronic levels corresponds to the 1380 cm^{-1} band seen in the resonance Raman scattering (RRS) of the perylenes. The spectra of the same materials dispersed in KBr are dramatically different than those in solution. The spectra are very broad and shifted compared to the solution spectra. The fluorescence of the material dispersed in KBr pellets shows the characteristic excimer fluorescence. The other PTCDs and PTCOs studied in this thesis were similar to these examples. No excimer fluorescence was observed for the solution spectra, even when the solutions were saturated.
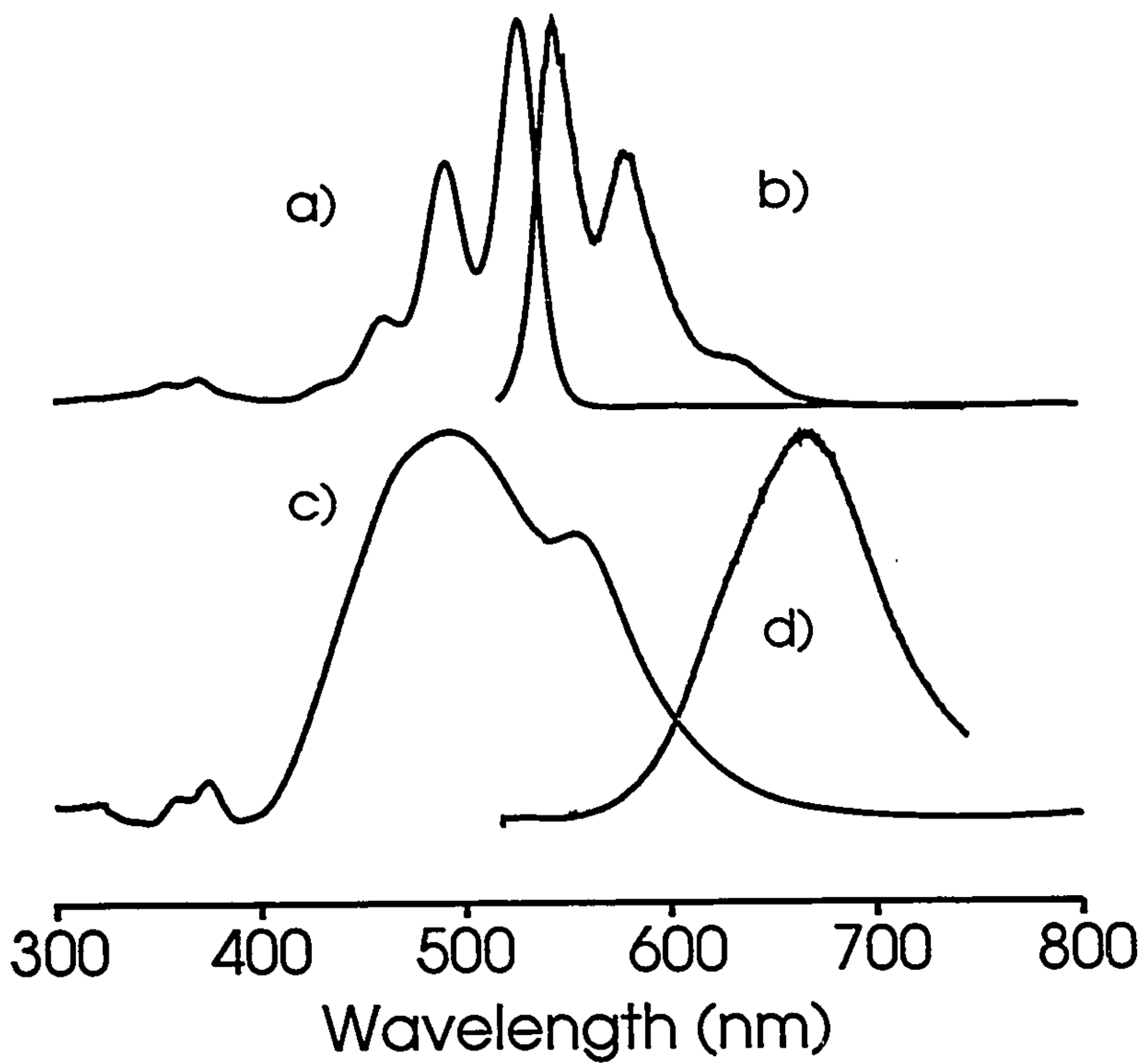
Figure 3.2: The electronic spectra of PPTCO: a) absorption and b) fluorescence of 1.95 ×10⁻⁵ M PPTCO in TFA/CHCl³ 5% and the c) absorption and d) fluorescence of PPTCO dispersed in a KBr pellet.
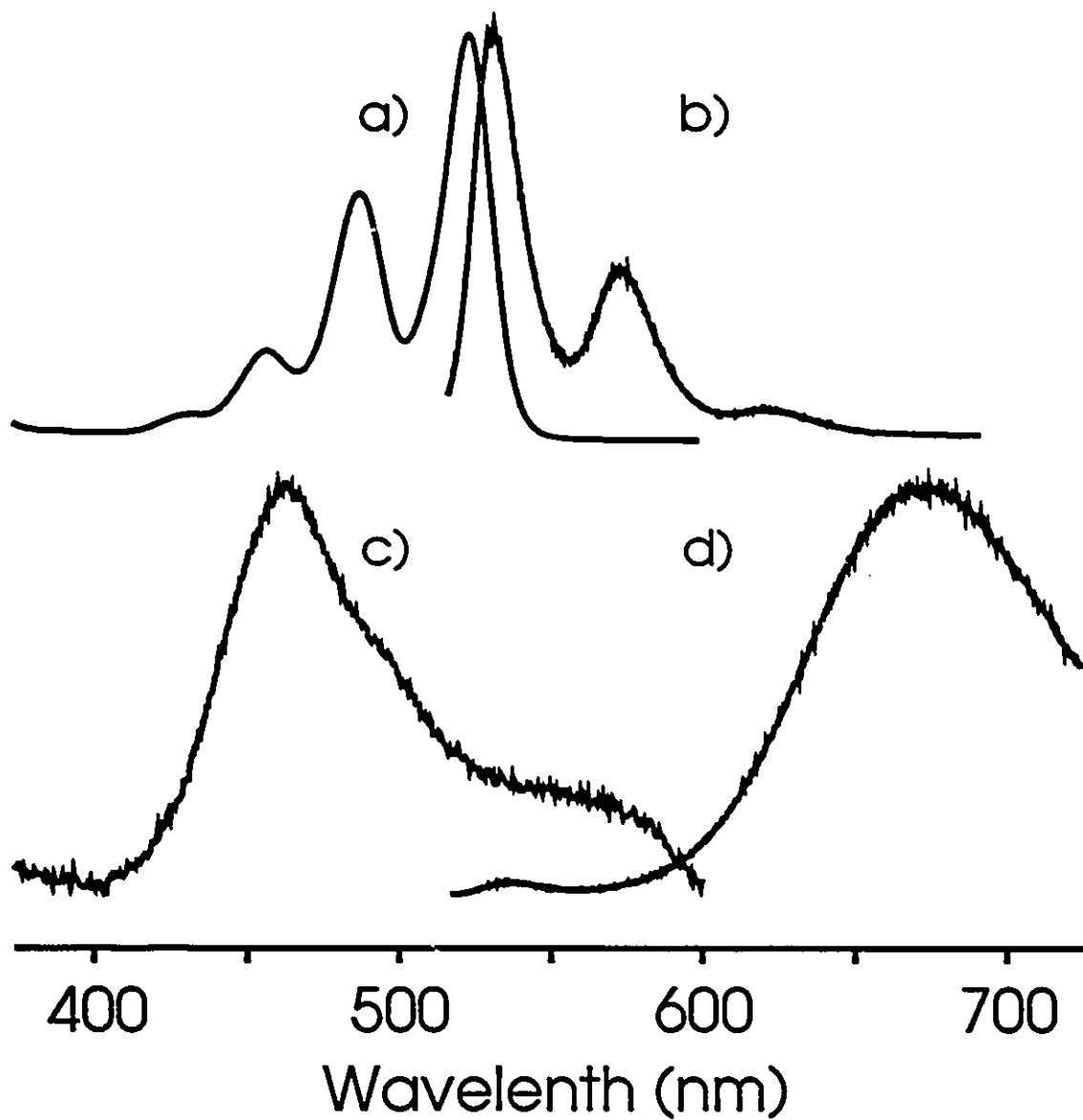
Figure 3.3: The electronic spectra of PPTCDM: a) absorption and b) fluorescence of 7.64 ×10⁻⁷ M PPTCDM in CHCl₃ and the c) absorption and d) fluorescence of PPTCDM dispersed in a KBr pellet.

Samples of XPTCDX were purchased from Aldrich and were studied without further purification. The electronic spectra for XPTCDX were recorded and are shown in *Figure 3.4*. The solution spectra were not different from to the other PTCDs and PTCOs in appearance. The spectra of the material in KBr pellets was a strong contrast to the other pellet spectra. The absorption spectrum had the same vibronic structure as the solution spectrum, but the spectrum was red shifted by about 700 cm^{-1} and broadened. The fluorescence of the pellet is very different from that of the other PTCDs. The spectrum is red shifted like the absorption spectrum, however, it is not sufficiently red shifted to be excimer emission. The fluorescence is also unusually structured compared to the solution spectra.

In order to elucidate the solution-like nature of the unusual fluorescence of XPTCDX seen in the pellet, an experiment in reabsorption of emitted light was conducted and compared to the KBr spectrum and to the spectrum of XPTCDX concentrated in $CHCl_3$. The $\nu_{0,0}$ band in the absorption spectra partially overlap with $\nu_{0,0}$ band in the fluorescence so reabsorption is a likely phenomenon in this situation. *Figure 3.5* shows the experimental setup to study reabsorption and *Figure 3.6* shows the resulting spectra. The first spectrum is of XPTCDX at 1.34×10^{-5} M in chloroform. A second sample cuvette was placed between the first cuvette and the collection optics of the spectrophotometer. The excitation light (514.5 nm) probed the first cuvette only. In the second case, the emitted light from the first cuvette had to pass through the same sample solution in the second cuvette. Reabsorption caused the $\nu_{0,0}$ fluorescence band to be reduced in intensity (refer to *Figure 3.6b*). A similar effect is observed when the concentration of XPTCDX is 1.34×10^{-4} M and is shown in *Figure 3.6c*. This solution was too concentrated to obtain absorption spectra. The fluorescence of XPTCDX dispersed in KBr is shown for comparison. Based on these observations, the unusual structure seen in the fluorescence of XPTCDX dispersed in KBr arises from a solution-like emission distorted by reabsorption.
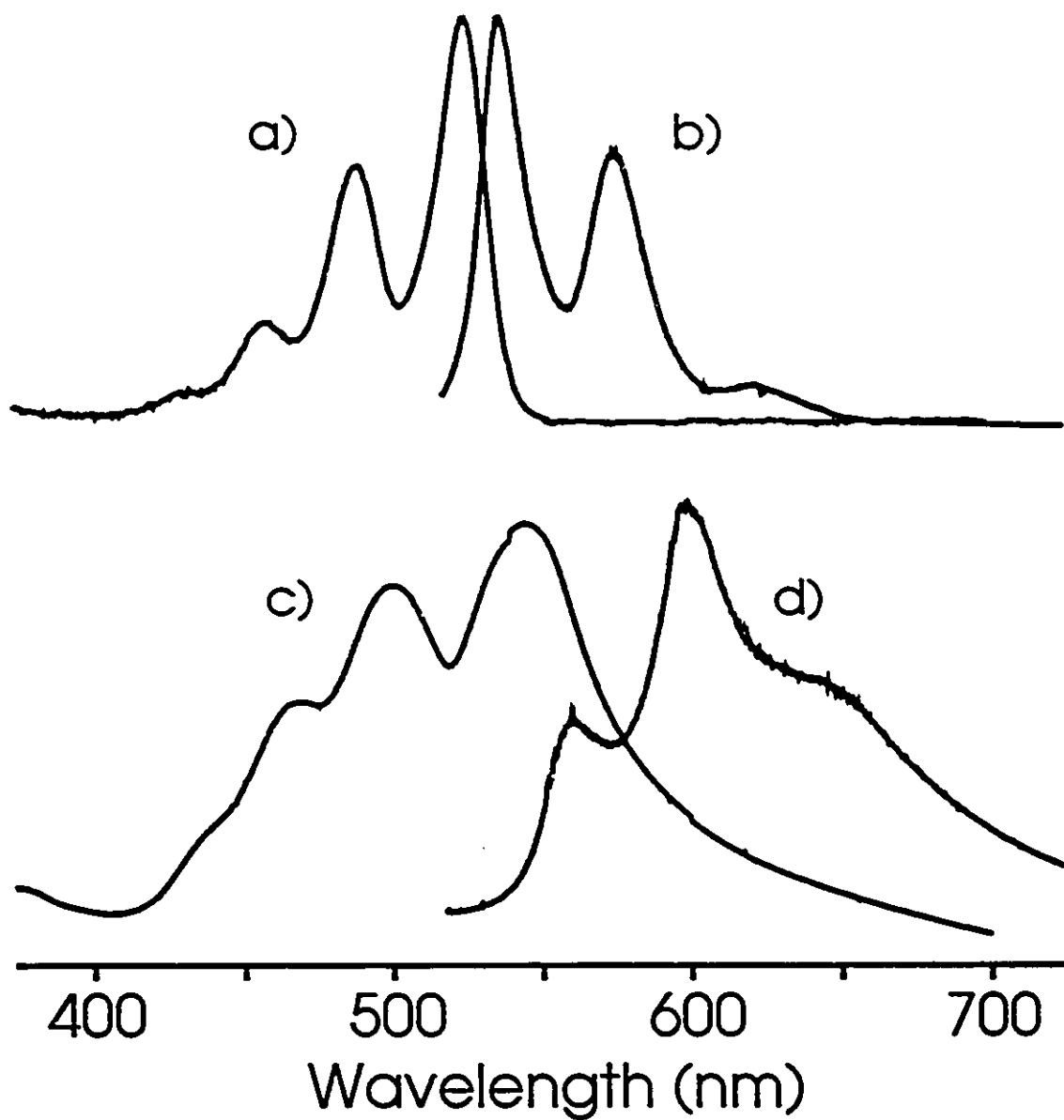
Figure 3.4: The electronic spectra of XPTCDX: a) absorption and b) fluorescence of 4.02 ×10⁻⁶ M XPTCDX in CHCl₃ and the c) absorption and d) fluorescence of XPTCDX dispersed in a KBr pellet.
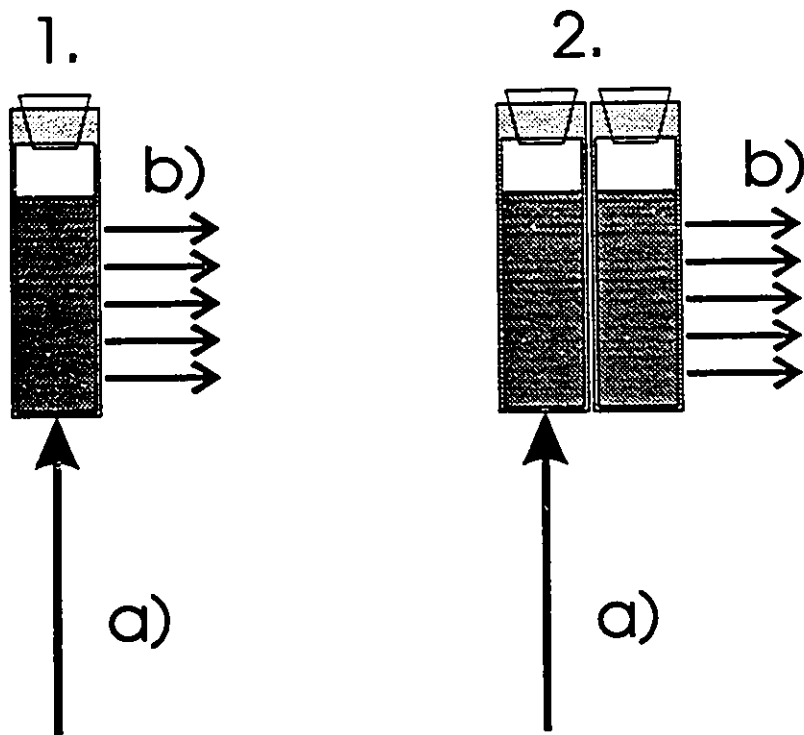
Figure 3.5:   The experimental set up to test reabsorption. The exciting light, a), probes one cuvette only. A second cuvette containing the same solution as the first is placed between the first cuvette and the collection optics of the instrument, forcing the emitted light, b), to pass through the second cuvette.
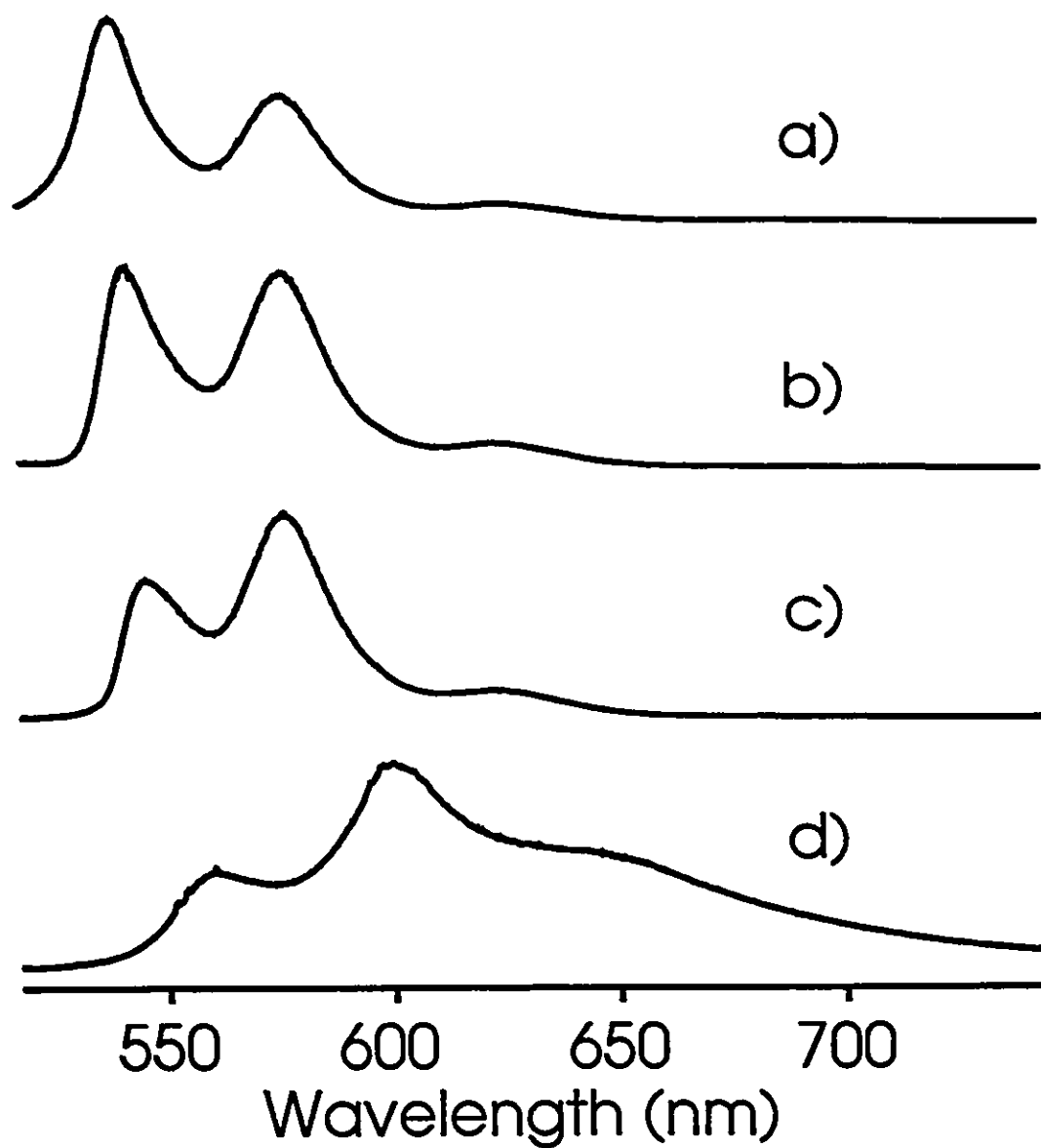
Figure 3.6: The spectra of XPTCDX from the reabsorption experiment: a) the fluorescence of 1.34×10^{-5} M XPTCDX in $CHCl_3$, b) same sample as a) but with the intervening cuvette, c) the fluorescence of 1.34×10^{-4} M XPTCDX in $CHCl_3$, d) the fluorescence from XPTCX dispersed in a KBr pellet.

When the PTCDs and PTCOs are incorporated into LB systems, monomer-like emission and excimer emission can be observed. Virtually all the materials show excimer emission. The implications for the structure of the film with respect to excimer emission are discussed in *Chapter 5* and, to a lesser extent, *Chapter 6*. A summary of excimer emission energy is given in *Table 1*. This table gives the position of the maximum of the excimer emission band observed in neat LB monolayers. Some monolayers showed a second excimer emission in the form of a shoulder at slightly higher energy than the strongest excimer emission and this may correspond to a more loosely bound excimer state *[3.24]*. LB fabrication was attempted for XPTCDX, however, this material did not form quality monolayers. The material would not transfer to solid substrates and the floating layer had a low collapse pressure.

Table 3.1: Excimer Emission Wavelength for LBs of PTCDs and PTCOs.

PTCDs	Wavelength (nm)	PTCOs	Wavelength (nm)
PPTCDM	624.2, 665.1	PrPTCO	660.0
PPTCDE	669.8	PPTCO	664.7
PPTCDPr	671.4	HPTCO	634.8, 672.3
HPTCDE	641.0, 687.0	PhPTCO	659.8
HPTCNH	649.0	HOPTCO	not observed

Vibrational Spectroscopy

The infrared spectra of the PTCDs and PTCOs were recorded for the materials dispersed in KBr pellets and as LB films on the appropriate substrates. The IR spectra of the LBs were used to determine the average molecular tilt of the chromophore. The orientation studies are elaborated in *Chapters 4* and *5*. Raman scattering of these materials could only be measured from monolayers on surface enhancing substrates such as silver island films *[3.25,26]*. The fluorescence of the perylenes overwhelms the scattering of the molecules and surface enhancing substrates, such as silver islands, quenches the fluorescence sufficiently for the SERRS to be recorded.

If the N and N' substituents are reduced to point-masses, then the point group of the PTCDs and PTCOs is C_{2v} *[3.27]*. This implies that all the bands, except the A_2 bands, will be visible in the infrared spectra. All vibrations should be visible in the Raman. Since the excitation wavelength used to obtain the Raman scattering is in resonance with the optical transition of the perylene, vibrational modes associated with the chromophore are selectively enhanced *[3.26]*. The observed infrared and SERRS bands are tabulated in *Appendix I*.

The most dominant features of the infrared spectra are the carbonyl stretching modes. For the diimides, only two C=O stretches are observed at 1656 and 1695 cm^{-1} *[3.28]*. These two bands are present in the PTCOs, but two more bands at 1737 and 1770 cm^{-1} are also present. The four C=O stretches seen in the spectra of perylene dianhydride (PTCDA) *[3.29]* are clustered closely together around 1770 cm^{-1}. When the infrared spectra of the PTCOs in LB films are recorded in the transmission and reflection geometries, the band at 1770 cm^{-1} can be resolved into two components at 1764 and 1776 cm^{-1}. Hence, these two bands correspond to the anhydride C=O stretches. The 1737 cm^{-1} band is not seen in the spectra of the PTCDs, nor in the spectrum of PTCDA. In perylene itself, a combination band, arising from out-of-plane fundamentals, is present at 1730 cm^{-1} *[3.30]*. The band observed at 1737 cm^{-1} may be a combination band with increased intensity due to Fermi resonance with the C=O stretches. The vibrational assignment of perylene was used to help in assigning the vibrations of the PTCOs and

PTCDs *[3.30-32]*.

Low Temperature Spectra

It has been shown that the excimer emission depends on temperature where the excimer fluorescence diminishes with decreasing temperature *[3.33]*. Spectra were measured at room, liquid nitrogen and liquid helium temperatures and the effects upon the monomer-like and excimer emissions were noted. The temperature dependence found for the fluorescence of the monolayers was compared to that of the α-perylene crystal. SERRS was also measured with laser excitation at 514.5 nm and 488 nm, in resonance with the electronic absorption of both compounds. Comparative studies of bandwidth and relative intensities of vibrational fundamentals were made to investigate the aggregation in the mixed LB layers.

Experimental Details for Low Temperature Studies

LB monolayers of HPTCO and arachidic acid were prepared at 25°C as per *Chapter 2.* Mixed monolayers were prepared by mixing 10 equivalents of arachidic acid (AA) with 1 equivalent of either HPTCO or HPTCDE in chloroform. Monomer-like and excimer emissions of HPTCO and HPTCDE have been observed on LB layers of these materials and mixing these materials with arachidic acid promotes monomer-like emission *[3.34,35].* In the mixed monolayers, isolated monomers may be considered to be dissolved in the arachidic acid and islands of PTCD may also exist. The isotherms of the mixed monolayers are given in *Figure 3.7.* In general shape, the isotherms resemble those of arachidic acid *[3.36],* however, the liquid region of HPTCDE and the limiting areas do not correspond to either the arachidic acid, or to the perylenes. The observed isotherms are not the result of the weighted addition of the isotherms of the components. Hence, mixing of the materials, to some degree, has occurred. Silver islands, 6 nm thick, were prepared by vacuum evaporation. Low temperature measurements were carried out in a liquid helium cryostat and in a liquid nitrogen variable temperature Raman cell. Measurements at He, temperatures were carried using a 0.8 double monochromator, with photomultiplier and multichannel analyzer detection systems. The photon counting electronics were interfaced to an IBM personal computer. LB measurements were carried
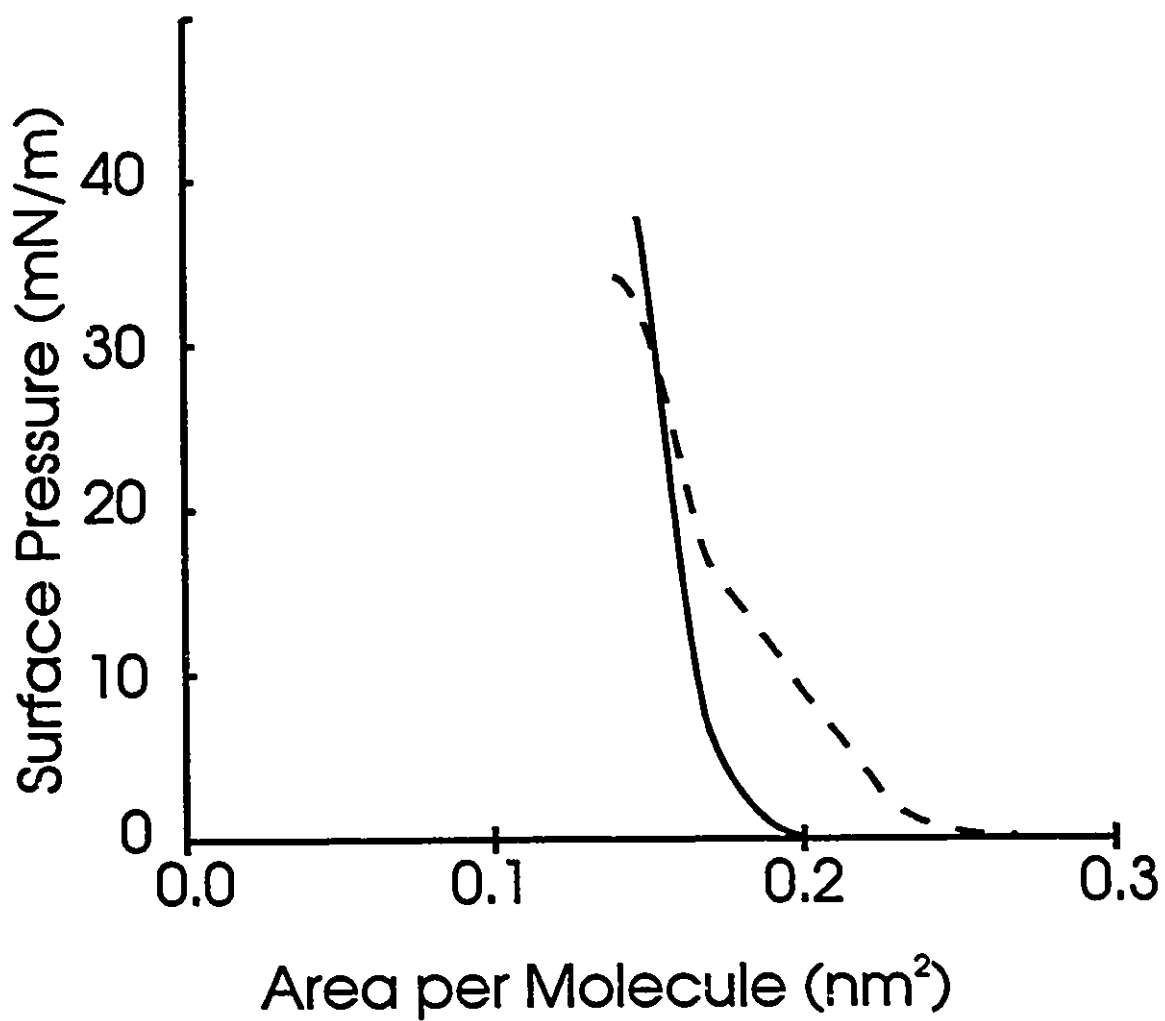
Figure 3.7: The isotherms of HPTCO (solid curve) and HPTCDE (dashed curve) mixed in a 1:10 ratio with arachidic acid.

out using a 90 degree geometry. The diameter of the excitation beam spot on the sample was 0.5 mm. No correction of the spectra for detection sensitivity was made. The 488 nm and 514.5 nm lines of the Ar$^+$ laser were used. Raman shifts and fluorescence were also measured with a Spex-1403 double monochromator and a Ramanor U-1000 with microscope attachment. For data analysis, all files were imported to Spectra Calc™ software available from Galactic Industries Corp.

Fluorescence of LB layers at Low Temperature

The SERRS spectra of a mixed LB monolayer obtained at room temperature and at 4.2 K are shown in *Figure 3.8*. These spectra contain strong fluorescence from the LBs. At room temperature, two bands are evident and the high frequency component at 536 nm is attributed to the monomer emission. At temperatures below 35 K, a new band appears in the emission spectrum of α-perylene *[3.33]*. This band has been named the Y emission of perylene and is the precursor to excimer formation *[3.19,33]*. Typically, this Y-state emission is only observed at very low temperatures and replaces the excimer emission *[3.1,33,37]*. The excimer formation is a thermally activated process involving configurational relaxation, originating from the Y-state *[3.18,19,33]*.

The relative intensity of the monomer band decreases in the low temperature spectra of mixed LB monolayers on Ag island films and a new band at 570 nm appears. This new band may correspond to a state similar to the Y-state seen in α-perylene. As discussed previously, the fluorescence spectrum of neat LB layers on glass (at 298 K) is completed dominated by the excimer fluorescence. At liquid helium temperature, four components can be used to fit the fluorescence background of the SERRS spectrum shown in *Figure 3.8*. The four Gaussians used in the fitting were centred at 571, 622, 647 and 678 nm. Notably, after two freeze/thaw cycles, the strong bands centred at 622 nm and 570 nm was substantially reduced, and the fluorescence was mainly due to the excimer formation (678 nm and 647 nm). Similar effects have been observed on annealed LBs of PTCOs and are discussed in detail in *Chapter 5*. The fluorescence spectrum of neat LB layers on glass and the spectrum showed in *Figure 3.8* contain a
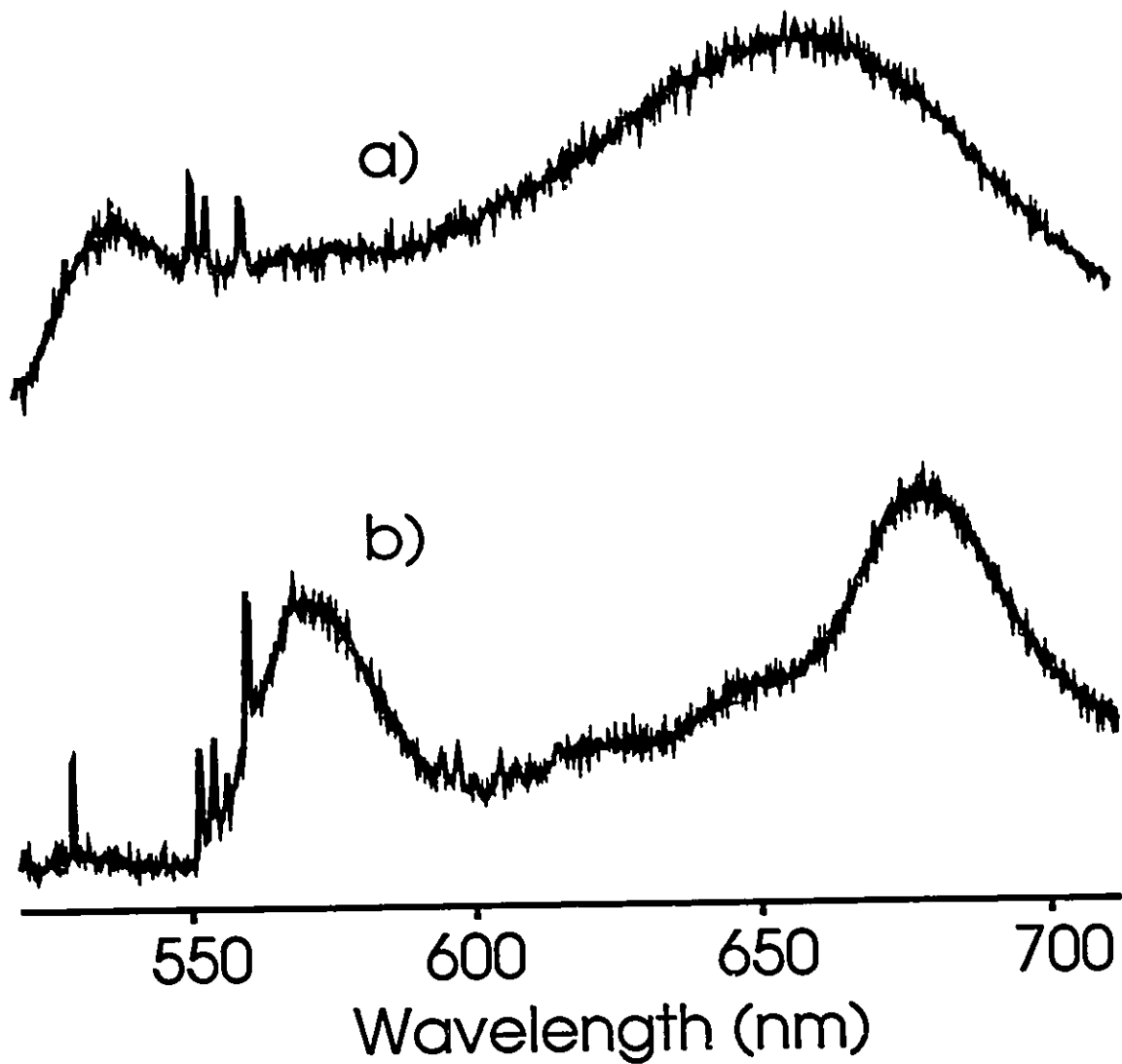
Figure 3.8. Fluorescence spectra of a single mixed LB layer, arachidic acid:HPTCO, on a 6 nm Ag island film at 293 K and 4.2 K.

broad structureless band centred at 654 nm. The FWHH is 2400 cm^{-1}. The low temperature spectra have shown that there are at least two overlapping emissions in this signal, centred at 647 nm and 678 nm. Similar results were obtained for a mixed LB layer of HPTCDE on Ag. The SERRS spectrum of HPTCDE at 4.2 K and the SERRS spectrum of HPTCO after two freeze/thaw cycles are shown in *Figure 3.9*. The fluorescence of an LB of HPTCDE on glass at room temperature can be fitted with three components centred at 534nm (monomer), 568 nm and a broad band at 661 nm respectively. However, the low temperature spectrum at 4.2 K shown in *Figure 3.9* was well fitted with three Gaussians centred at 573 nm, 641 nm and 687 nm, in agreement with the observed emissions of HPTCO. The broad band of the excimer emission at room temperature was also resolved into two bands (641 nm and 687 nm) as in HPTCO case. However, the relative intensity of the components was reversed.

Assuming that molecular arrangement and excimer formation in the solid is favoured by a molecular arrangement that maximizes the stacking between two perylene rings, it is believed that the geometrical organization of aggregates facilitates the formation of a Y-state (573 nm) and two distinct excimers (641 and 687) in both the HPTCDE and HPTCO molecules. The latter interpretation was also supported by the spectra of HPTCDE obtained at 4.2 K with the 488 nm excitation laser line. It was found that the relative intensity of the two excimer bands was different from that obtained with the 514.5 nm laser line. The results confirmed that the two bands originated from different emitters.
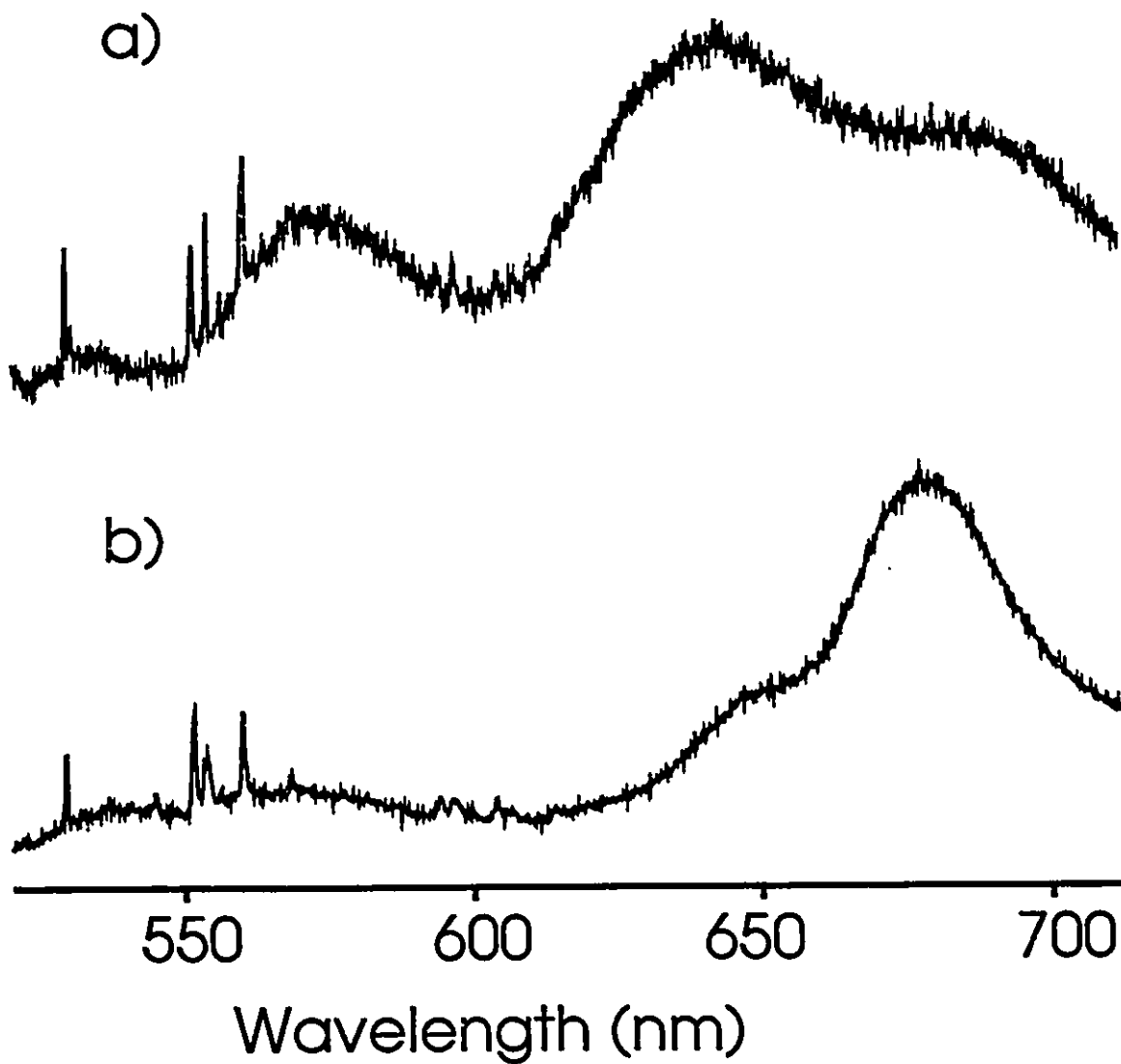
Figure 3.9. Fluorescence of a mixed LB of HPTCDE on Ag at 4.2 K, and of the HPTCO mixed LB after two freeze/thaw cycles.

Surface-Enhanced Resonant Raman Spectra

The SERRS spectra obtained at room temperature, liquid nitrogen and liquid helium temperatures for the mixed HPTCO LB layer are given in *Figure 3.10*. The discussion here is restricted to the characteristic bands in the region of ring stretching vibrations as shown in *Figure 3.11*, and the 543 cm^{-1} Raman band observed at liquid helium temperature. The FWHH of the 543 cm^{-1} band decreased with temperature from 20 cm^{-1} at room temperature to 12 cm^{-1} at 93 K and 11 cm^{-1} at liquid helium temperature. The latter band is symmetric in shape and has only one component. SERRS spectra of HPTCO on colloidal silver *[3.38]*, which is probably due to monomers adsorbed on the silver surface, gave a 540 cm^{-1} band with a FWHH of 11 cm^{-1}. The 1292 cm^{-1} and 1306 cm^{-1} bands of HPTCO and HPTCDE, shown in *Figure 3.11*, were fitted using two components for each case. Notably, the SERRS spectrum of HPTCO on Ag sols showed two bands, at 1289 and 1306 cm^{-1}, that were better resolved than in the low temperature spectrum. Therefore, the FWHH obtained at the liquid helium temperature are probably broadened as a result of aggregation in the monolayer. Two components centred at 1362 cm^{-1} and 1385 cm^{-1} were also required to fit the perylene stretching vibrational band (see *Figure 3.11*). However, for HPTCDE the first component was very weak and the two maxima were found at 1376 cm^{-1} and 1385 cm^{-1}. The C=C stretching vibration was also deconvoluted with two components at 1575 cm^{-1} and 1592 cm^{-1} (1590 cm^{-1} for HPTCDE). Notably, in the spectrum of the HPTCO on colloidal silver there is a strong band at 1570 cm^{-1} with a very weak shoulder at higher energy. Before drawing the conclusions, it is helpful to point out the similarity between the above described spectral changes and what is known from perylene spectra. The intensity of the two components in the doublets of perylene (1369-1380 cm^{-1} and 1574-1581 cm^{-1}) are comparable in frozen solutions of perylene. Hochstrasser and Nyi *[3.24]* found that one of the components became prominent in the low temperature spectrum of α-perylene crystal: 1574 cm^{-1} was four time more intense than the 1581 cm^{-1} band, and the 1380 cm^{-1} band had twice the intensity of the 1369 cm^{-1} vibration. In HPTCO the 1383 cm^{-1} has about three times the intensity of the 1362 cm^{-1} band, and the 1575 cm^{-1} is two times stronger

than the 1592 cm^{-1} component. The intensity pattern observed for HPTCDE bands does not follow the perylene pattern of relative intensities. The similarity in the spectral behaviour of HPTCO LB monolayers and the α-crystal of perylene support the assumption of an LB structure with geometrically aligned dimer units. The fluorescence spectra (*Figures 3.8* and *3.9*) also support the latter argument, and indicate that the freeze/thaw cycling process helped to increased the alignment with a predominant molecular organization (of the α-perylene type). However, the weak fluorescence band from a second emitter (see *Figures 3.8* and *3.9*) is also indicative of at least a second molecular arrangement in the monolayers. Fluorescence and SERRS spectra of HPTCDE allow one to conclude that the molecular alignment of the α-perylene type is not preferred in dimers and higher aggregates of the HPTCDE monolayer. It can be concluded that the fluorescence spectrum of HPTCDE (see *Figure 3.9*) is brought about by a distinct geometrical arrangement that favours the formation of a "second" emitter given the band centred at 687 nm. A different molecular arrangement than in the α-perylene crystal is partially supported by the crystal structure of EPTCDE *[3.21,23]*. This molecule arranges in twisted stacks. It may be possible that the presence of the ethyl group in HPTCDE may causes structural arrangements not seen in the other PTCDs or PTCOs.
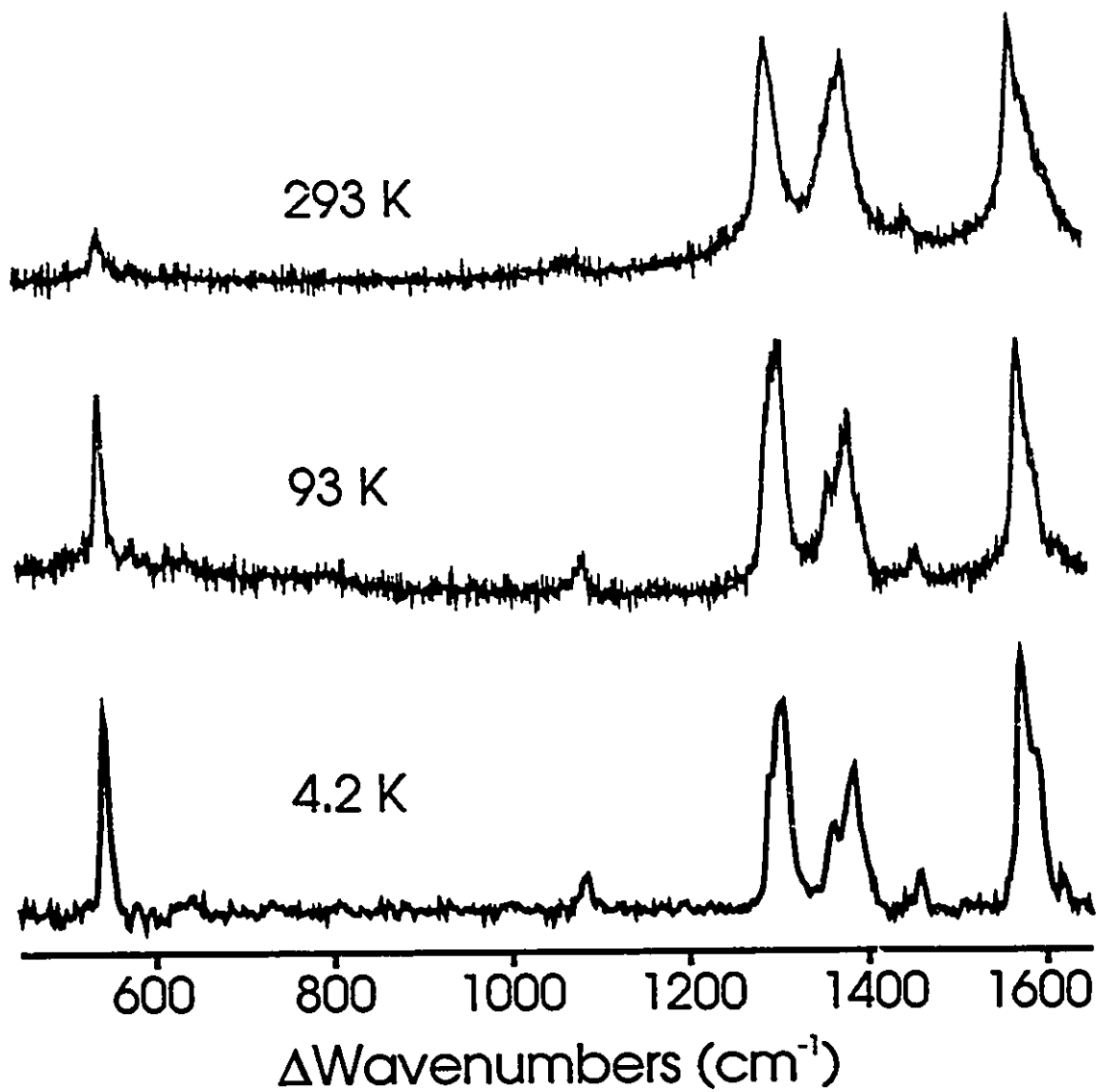
Figure 3.10: SERRS spectra of one mixed LB of HPTCO at 298 K, 93 K and liquid helium temperature.

a)

b)

ΔWavenumbers (cm^{-1})
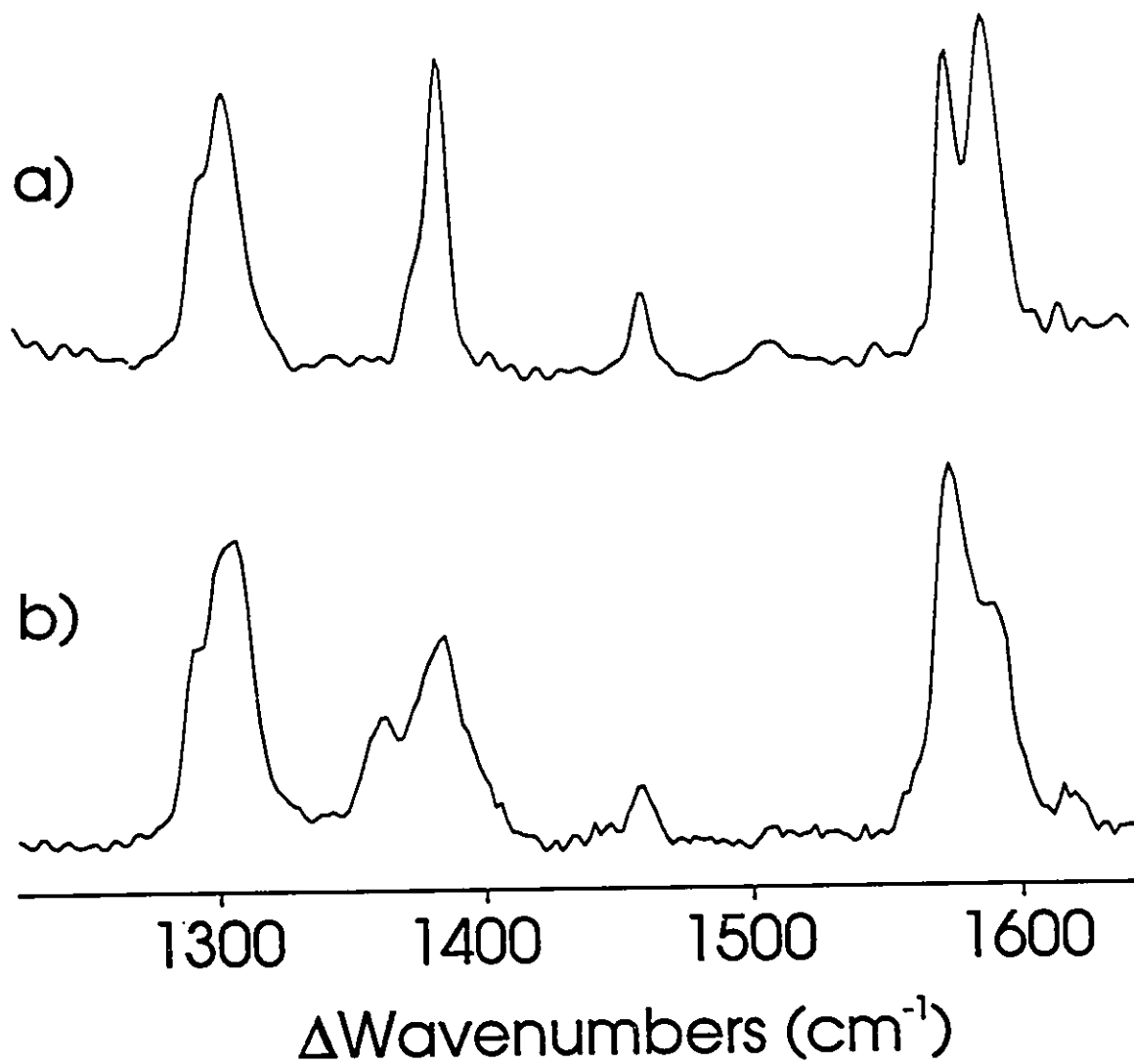
Figure 3.11:   Low temperature SERRS spectra of a) HPTCDE and b) HPTCO in the region of the ring stretching vibrations.

52

[3.1] Tanaka, J. *Bull. Chem. Soc. Japan* 1963, *36*, 1237.

[3.2] Azumi, T.; McGlynn, S.P. *J. Chem. Phys.* 1964, *41*, 3131.

[3.3] Azumi, T.; McGlynn, S.P. *J. Chem. Phys.* 1965, *42*, 1675.

[3.4] Birks, J.B.; Christophorou, L.G. *Proc. R. Soc. Lond.* 1963, *A277*, 571.

[3.5] Kajikawa, K.; Takezoe, H.; Fukuda, A. *Jpn. J. Appl. Phys.* 1991, *30*, L1525.

[3.6] Ando, E.; Suzuki, M.; Moriyama, K.; Morimoto, K. *Thin Solid Films* 1989, *178*, 103.

[3.7] Hertz, A.H. *Photogr. Sci. Eng.* 1974, *18*, 323.

[3.8] Kasha, M. in *Physical Processes in Radiation Biology* Augenstien, L.; Mason, R., Rosenberg, B., eds., Academic Press, New York, 1964, p 17.

[3.9] Czikkdely, V.; Forsterling, H.D.; Kuhn, H. *Chem. Phys. Let.* 1970, *6*, 207.

[3.10] Birks, J.B. *Photophysics of Aromatic Molecules*, Wiley-Interscience, Toronto, 1970.

[3.11] Tomura, M.; Takahashi, Y. *J. Phys. Soc. Jap.* 1971, *31*, 797.

[3.12] Warshel, A.; Huler, E. *Chem. Phys.* 1974, *6*, 463.

[3.13] Grieser, F.; Thistlethwaite, P.J.; Urquhart, R.S. *Chem. Phys. Let.* 1987, *141*, 108.

[3.14] Yamazaki, I.; Tamai, N.; Yamazak, T. *J. Phys. Chem.* 1987, *91*, 3572.

[3.15] Yamazaki, T.; Tamai, N.; Yamazaki, I. *Chem. Phys. Let.* 1986, *124*, 326.

[3.16] Kinnunen, P; Tulkki, A.; Lemmetyinen, H.; Paakkola, J.; Virtanen, J. *Chem. Phys. Let.* 1987, *136*, 539.

[3.17] Vitukhnovsky, A.G.; Sluch, M.I.; Warren, J.G.; Petty, M.C. *Chem. Phys. Let.* 1990, *173*, 425.

[3.18] Mahrt, J; Willig, F.; Storck, W.; Kietzmann, R.; Schwarzburg, K.; Tufts, B.; Trosken, B. *J. Phys. Chem.* 1994, *98*, 1888.

[3.19] Weiss, D.; Kietzmann, R.; Mahrt, J.; Tufts, B.; Storck, W.; Willig, F.; *J. Phys. Chem.*, 1992, *96*, 5320-5325.

[3.20] Graser, F.; Hadicke, E. *Liebigs Ann. Chem.* **1980**, 1994.

[3.21] Graser, F.; Hadicke, E. *Liebigs Ann. Chem.* **1984**, 483.

[3.22] Hadicke, E.; Graser, F. *Acta Cryst.* **1986**, *C42*, 189.

[3.23] Hadicke, E.; Graser, F. *Acta Cryst.* **1986**, *C42*, 195.

[3.24] Hochstrasser, R.M.; Nyi, C.A. *J. Chem. Phys.* **1980**, *72*, 2591.

[3.25] Moskovits, M. *Rev. Mod. Phys.* **1985**, *57*, 783.

[3.26] Aroca, R., Kovacs, G. in *Vibrational Spectra and Structure*, Durig, J.R., ed., Elsevier, Amsterdam, 1991.

[3.27] Cotton, F.A. *Chemical Applications of Group Theory*, 2nd *Ed.*, Wiley-Interscience, Toronto, 1971.

[3.28] Popovic, Z.D.; Loutfy, R.O.; Hor, A.M. *Can. J. Chem.* **1985**, *63*, 134.

[3.29] Akers, K.; Aroca, R.; Hor, A.M.; Loutfy, R.O. *J. Phys. Chem.* **1987**, *91*, 2954.

[3.30] Ambrosino, F.; Califano, S. *Spectroch. Acta* **1965**, *21*, 1401.

[3.31] Babkov, L.M.; Kovner, M.A.; Rents, V.B. *Opt. Spectrosc.* **1973**, *34*, 354.

[3.32] Baranov, A.V. *Opt. Spectrosc.* **1985**, *59*, 326.

[3.33] Walker, B.; Port, H.; Wolf H.C. *Chem. Phys.* **1985**, *92*, 177.

[3.34] von Freydorf, E.; Kinder, J.; Michel-Beyerle, M. *Chem. Phys.* **1978**, *27*, 199.

[3.34] Aroca, R.; Johnson, E. *SPIE Vol.1336 Raman and Luminescence Spectroscopies in Technology II* **1990**, 291.

[3.35] Johnson, E.; Aroca, R. *J. Mol. Struct.* **1993**, *293*, 331.

[3.36] Petty, M.C. in *Langmuir-Blodgett Films*, Roberts, G.G. Ed., Plenum Press, NY, 1990.

[3.37] Sallach, J.; Aroca R., unpublished data.

Chapter 4:   The Effect of Intermolecular and Molecule/Subphase Interactions on the Average Molecular Orientation of PTCDs in LB Films

Introduction

The structure of LB films can be influenced by several factors such as molecule-molecule interactions, molecule-subphase interactions and molecule substrate interactions. As discussed in *Chapter 2*, the classic molecules often used to prepare LB films are amphiphilic molecules like long chain fatty acids. Amphiphiles interact with the water subphase during the formation of the floating Langmuir layer, thereby reducing the surface tension of water. The surface pressure/area isotherm (π-A) is the difference between the surface tension of water and that of the water with the floating layer *[4.2]*, where A is the area per molecule on the water surface. Langmuir monolayers with well defined surface pressure/area isotherms of non-amphiphilic molecules *[4.1]* and polymers *[4.2]* have also been obtained *[4.3]*. For amphiphiles, the interaction of the molecular hydrophilic end with the subphase would be a determining factor in the molecular orientation of the Langmuir layer. For non-amphiphilic molecules the structure of the organized floating layer would be largely determined by the intermolecular interactions within the layer.

Six of the PTCDs studied may be described as having differing degrees of relative amphiphilicity. The more amphiphilic perylenes will experience a greater interaction with the aqueous subphase; the degree of this interaction could play a significant role in determining the molecular alignment. For the chosen dyes, evidence of π-π intermolecular interaction is present in their electronic absorption and emission spectra. It was therefore important to examine the outcome of molecular orientation of LB films formed under similar conditions for the perylene derivatives chosen. The observation of meaningful results using transmission and reflection-absorption IR spectroscopies was in itself evidence of organization in LB films fabricated on Ge, ZnS and smooth silver films. Notably, the formation of an organized LB film on amorphous surfaces has also been recently revealed by atomic force microscopy *[4.4]*.

Experimental Details

The starting materials were kindly provided by Professor Nagao from the University of Tokyo. The six molecules, shown in *Figure 4.1*, were N-pentyl N'-R perylenetetracarboxylic diimide [R = -CH$_3$ (PPTCDM), -C$_2$H$_5$ (PPTCDE) and -C$_3$H$_7$ (PPTCDPr)] and N-hexyl N'-ethyl perylenetetracarboxylic diimide. The two monosubstituted molecules were N-hexyl, perylenetetracarboxylic monoimide (HPTCO) and N-hexylperylenetetracarboxylic diimide (HPTCNH). LB monolayers of the various perylene derivatives were prepared at 15°C using the procedures outlined in *Chapter 2*. The spreading solvent was HPLC grade chloroform and Milli-Q purified water with a measured resistivity of 18.2 MΩcm was used as the subphase. π-A isotherms were recorded at a compression rate of 10^3 nm^{2}molecule^{-1}s^{-1} and are given in *Figure 4.2*. Multilayers were transferred to IR transparent substrates (ZnS, Ge) and smooth silver films. The latter substrate was used for RAIR spectroscopy. The 110 nm thick smooth silver films were also prepared as per Chapter 2. LB films were transferred at a constant surface pressure of 25 mN/m. The substrate was moved vertically through the gas-liquid interface at a rate of 0.06 mm/s. LB films of the more amphiphilic perylenes were transferred via Y-deposition and transfer ratios ca. 1.2 were measured (to Ge, ZnS and Ag). Only 1 LB was transferred to smooth silver for HPTCNH. Its low solubility required the spreading of about 50 mL of solution in order to prepare 1 LB. Since the infrared windows have considerably smaller area than glass slides, more monolayers could be transferred to these substrates. For the other PTCDs, up to 4 monolayers were transferred to smooth Ag substrates. 15-30 LBs were transferred to the IR transmission substrates. For non-amphiphilic molecules, a multilayer assembly of PPTCDM on ZnS was formed by Y-deposition with a nearly 1.0 transfer ratio. Acceptable transfer for PPTCDE, HPTCDE and PPTCDPr to ZnS was attained exclusively by Z-deposition. The Langmuir monolayer of all four compounds was transferrable to the smooth silver film solely by Z-deposition.

Infrared spectra were obtained for LBs deposited on ZnS and Ge (transmission geometry) and for LBs deposited on 110 nm Ag (reflection geometry). An incidence
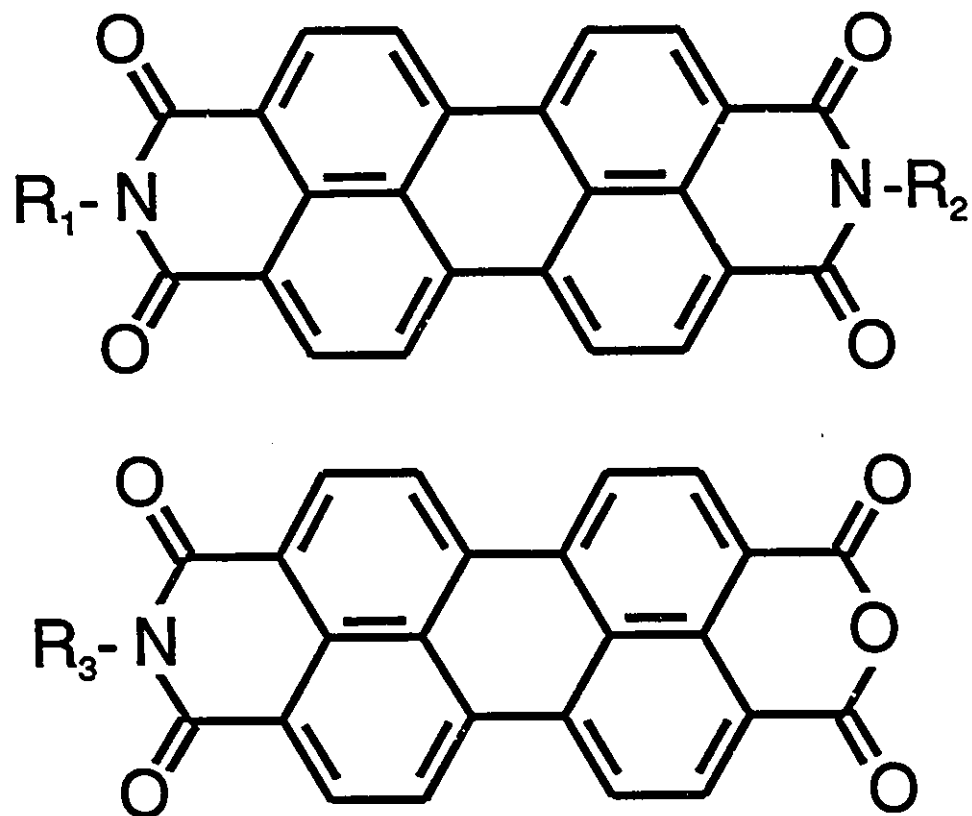
Figure 4.1. Structure of the perylene derivatives studied in this chapter.
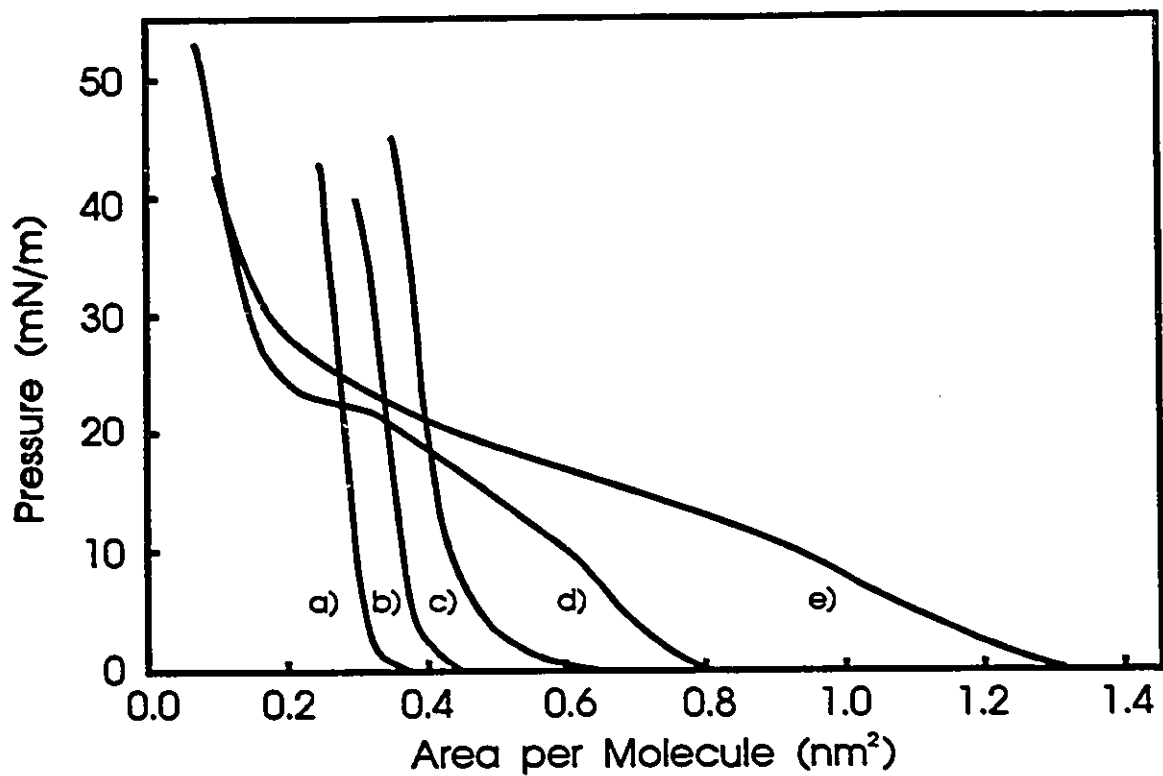
Figure 4.2. π-A isotherms for five of the PTCDs. a) PPTCDM, b) PPTCDE, c) PPTCDPr, d) HPTCO, and e) HPTCNH. The isotherm of HPTCDE is indistinguishable from that of PPTCDE.

angle of 75° to the surface normal was used in all RAIR spectra.

Results and Discussion
Langmuir Monolayers

The π-A isotherms given in *Figure 4.2* provide a striking illustration of the difference in the formation of the compressed floating monolayer at the water subphase. The isotherms for the four di-substituted imides (PPTCDM, PPTCDE, HPTCDE and PPTCDPr) are dominated by the low compressibility region, practically, the exclusive formation of a solid phase. Moreover, the limiting areas associated with these molecules increased by 0.06 to 0.07 nm² per molecule as the substituent's length is increased by one carbon atom. Therefore, the pressure sensed in recording these isotherms arises primarily from the compression of any given molecule against its neighbours.

The isotherms for the two mono-substituted perylenes are a strong contrast to the previous three molecules. These two molecules show a very evident liquid expanded phase at low pressures. However, at higher pressures, a solid phase for all materials is observed. The limiting area for this phase is about 0.06 to 0.07 nm² per molecule smaller than the limiting area of PPTCDM. In other words, the limiting areas observed for the mono-substituted chromophores are the same as the extrapolated limiting areas for the di-substituted imide with a chain length of zero carbons. The presence of a hexyl or a pentyl or hexyl group on the opposite end of the perylene chromophore does not seem to influence the isotherms.

The fact that the di-substituted imides do not show any liquid expanded region may be considered an indication of early molecular alignment of these molecules on the water surface. HPTCNH interacts strongly with the water subphase. The pressure associated with the liquid expanded region for these molecules could be due to strong, amphiphilic interaction at the monolayer/water interface. Moreover, HPTCNH interacts more than HPTCO since the onset of pressure for HPTCNH occurs at areas greater than for HPTCO and that the imide hydrogen facilitates more hydrogen bonding to the water subphase.

When the imide becomes substituted (which is the case for PPTCDM, PPTCDE

and PPTCDPr), its hydrogen bonding ability is lost and the alkyl substituent shields the imide nitrogen from the subphase. Therefore, only the solid phase is observed in their isotherms and these materials may be considered less amphiphilic that HPTCNH and HPTCO. The increase in the length of the carbon chain seems to change the packing between the molecules in the film, but does not seem to affect the area of the chromophore. The presence of either a hexyl or a pentyl group on the opposite imide does not seem to affect the isotherms, presumably because these chains are pointing into the air on the side of the molecules facing away from the subphase.

The solid phase limiting areas for the five perylenes is shown in *Table 4.1*. The isotherm of HPTCDE is indistinguishable from the isotherm of PPTCDE and was omitted for clarity. The small area per molecule obtained from the π-A isotherms eliminates a flat-on molecular organization of the chromophore plane in the floating layer. The chromophore plane could be in an edge-on or a head-on orientation. For comparison with the observed limiting areas, the calculated area of the chromophore projected onto the substrate plane (according to the angles found in the IR work which is discussed in the next section) has been included in *Table 4.1*. Since the projected areas do not include contributions from the alkyl chains in each molecule, it becomes even more striking that the limiting areas are smaller than the projected areas. This indicates that there must be significant chromophore overlap in the molecular organization or molecular stacking due to aromatic-aromatic interaction.

Table 4.1. Experimentally determined limiting molecular areas from π-A measurements and the corresponding projected molecular area given by spectroscopic techniques.

Molecule	Molecular Limiting Area (nm^2)	Molecular Projected Area (nm^2)
PPTCDM	0.31	0.63
PPTCDE	0.38	0.89
HPTCDE	0.38	0.91
PPTCDPr	0.44	0.51
HPTCO	0.24	0.42
HPTCNH	0.27	0.77

Molecular Orientation in the Langmuir-Blodgett Monolayers

First, a discussion of the vibrational assignment of the stretching vibrations occurring in the plane of the chromophore is necessary. Characteristic in-plane fundamental modes are: benzene C=C, carbonyl C=O and imide C-N stretching vibrations. In the parent perylene molecule, the highest C=C stretching frequency (1606 cm^{-1}) changes the dipole moment along the short axis of the perylene chromophore, while the stretching mode at 1592 cm^{-1} changes the dipole moment along the long molecular axis [4.5,6]. Similarly, the stretching vibrations of the two carbonyls of the imide group at 1656 cm^{-1} and 1696 cm^{-1} correspond to the in-plane (chromophore plane) and were assigned to the anti-symmetric carbonyl stretching and to the symmetric carbonyl stretching, respectively. These stretching modes can be seen in *Figure 4.3*. To illustrate the results, the spectra of all five molecules are given in *Figures 4.4-8*. The assignment of the high frequency band to the symmetric stretching vibration is uncommon. In five-membered ring compounds, such as phthalimide, the symmetric C=O stretch is higher than the anti-symmetric stretch [4.7]. However, there is no evidence that the assignment would hold for conjugated six-membered rings. The strong fluorescence of the PTCD molecules, and the small scattering cross-section of the carbonyl stretching modes, prevented a direct measurement of the depolarization ratio in solution. Searching for supporting evidence, we use a naphthalene-1-8-dicarboxylic anhydride as a model compound, and measured the depolarization ratios of the two carbonyl frequencies observed in the Raman. Although the signals were very weak, it was clearly evident that the high frequency band was polarized, thereby supporting its assignment to the symmetric stretching vibration. The transition moment for the anti-symmetric vibration is directed along the short axis of the chromophore, while that of the symmetric vibration is along the long chromophore axis.

For HPTCO there are two distinct groups of C=O frequencies. The carbonyl stretching vibrations of the imide group are observed at lower frequencies and the C=O stretches of the anhydride group [4.8] are seen above 1700 cm^{-1} as shown in *Figure 4.4*. The carbonyl modes have a large value of the dipole moment derivative.

Anti-Symmetric

1656 cm^{-1}

Symmetric

1696 cm^{-1}
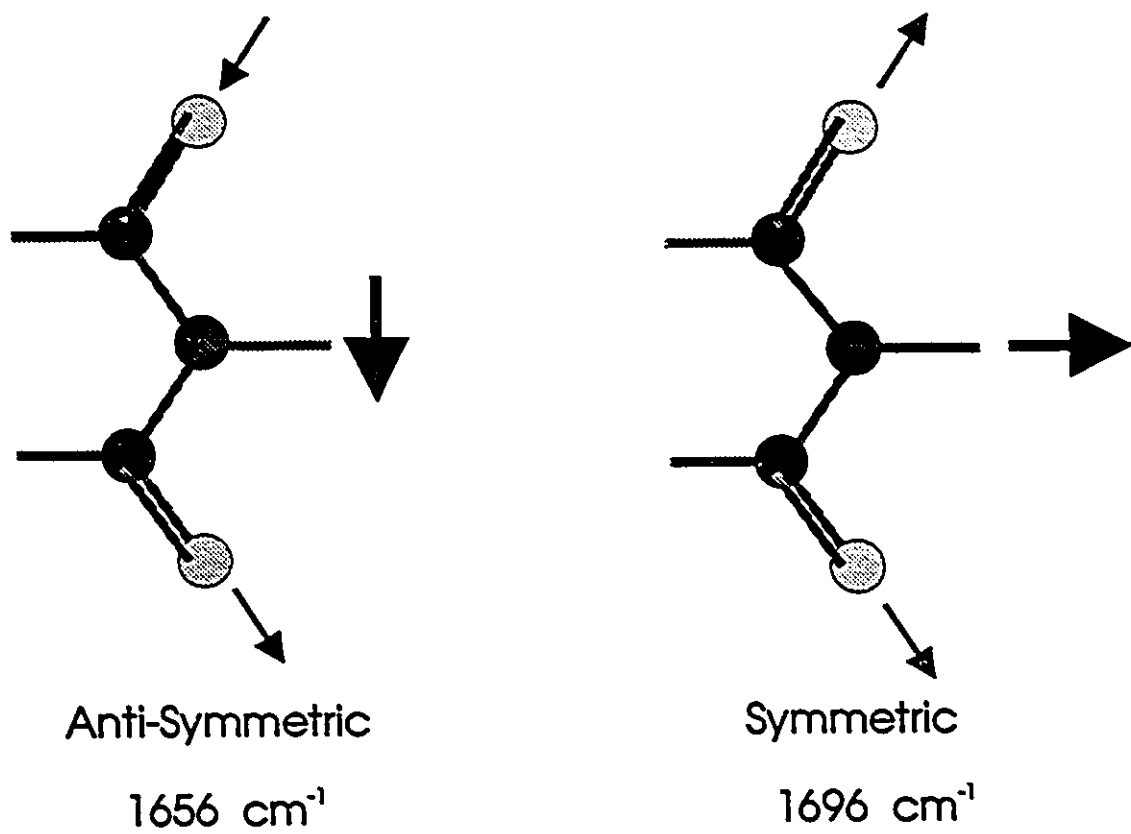
Figure 4.3.   The two imide carbonyl stretching modes and their respective net change in dipole moments are illustrated.
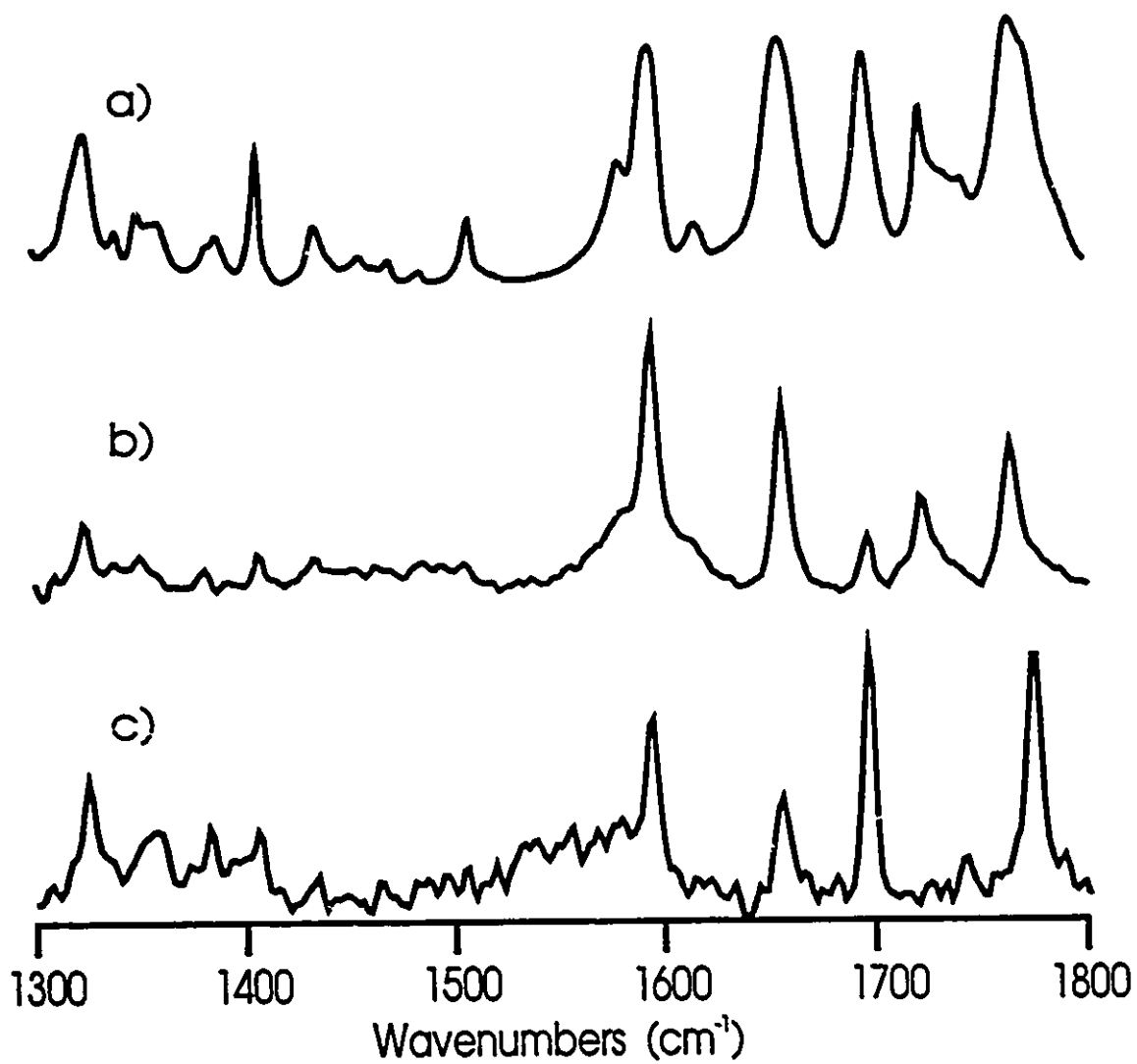
Figure 4.4.   FT-IR spectra of HPTCO in a) KBr pellet, b) LB film of 60 monolayers
on Ge, c) RAIRS of 3 LB monolayers on 110 nm Ag.
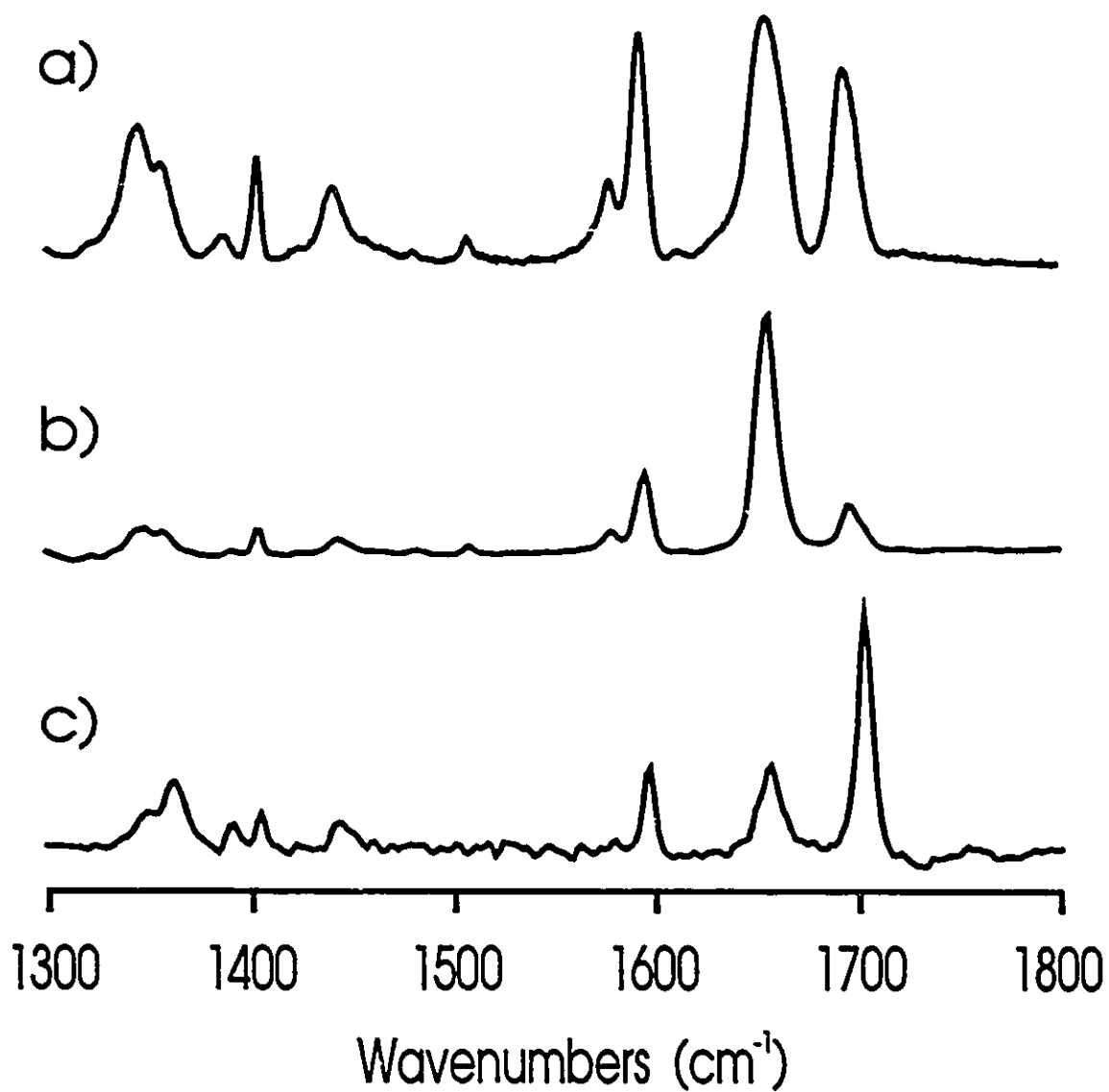
Figure 4.5.   Absorption FT-IR spectra of PPTCDM in a) KBr pellet, b) of 20 LB
monolayer on ZnS and c) of 4 LB layers on 110 nm Ag film.
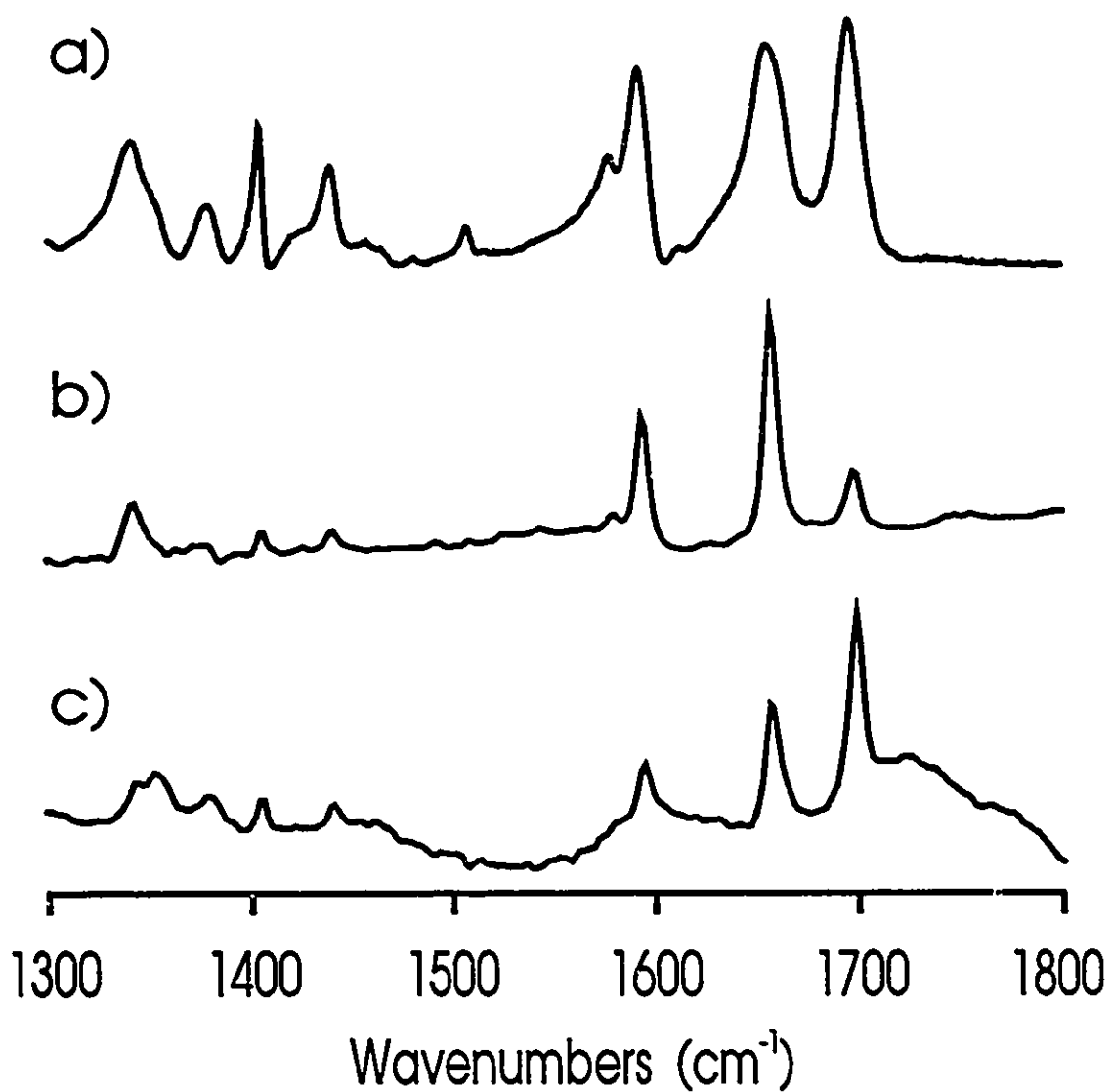
Figure 4.6. Absorption FT-IR spectra of PPTCDE in a) KBr pellet, b) of 20 LB monolayer on ZnS and c) of 4 LB layers on 110 nm Ag film.
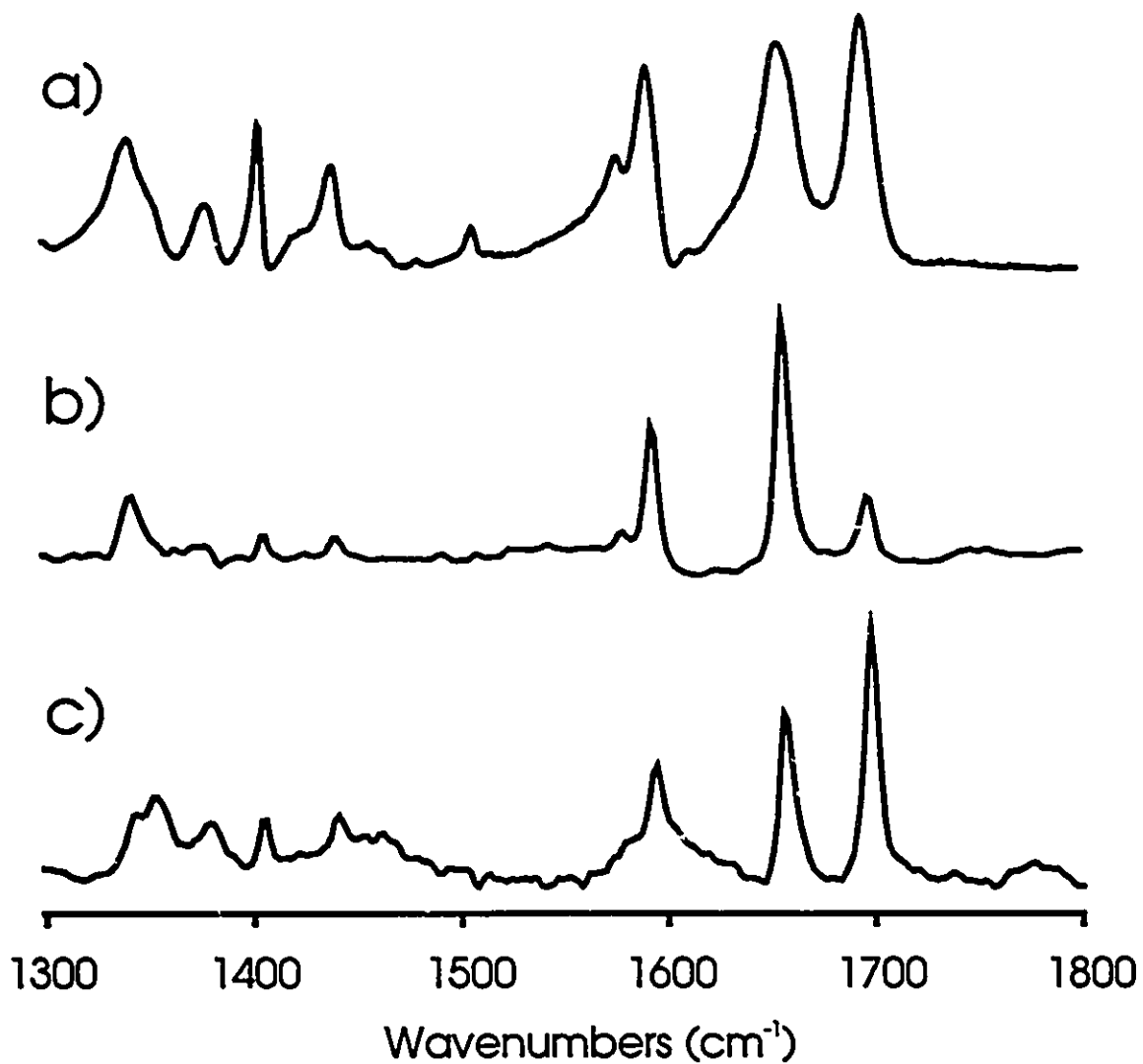
Figure 4.7. Absorption FT-IR spectra of PPTCDPr in a) KBr pellet, b) of 20 LB monolayer on ZnS and c) of 4 LB layers on 110 nm Ag film.
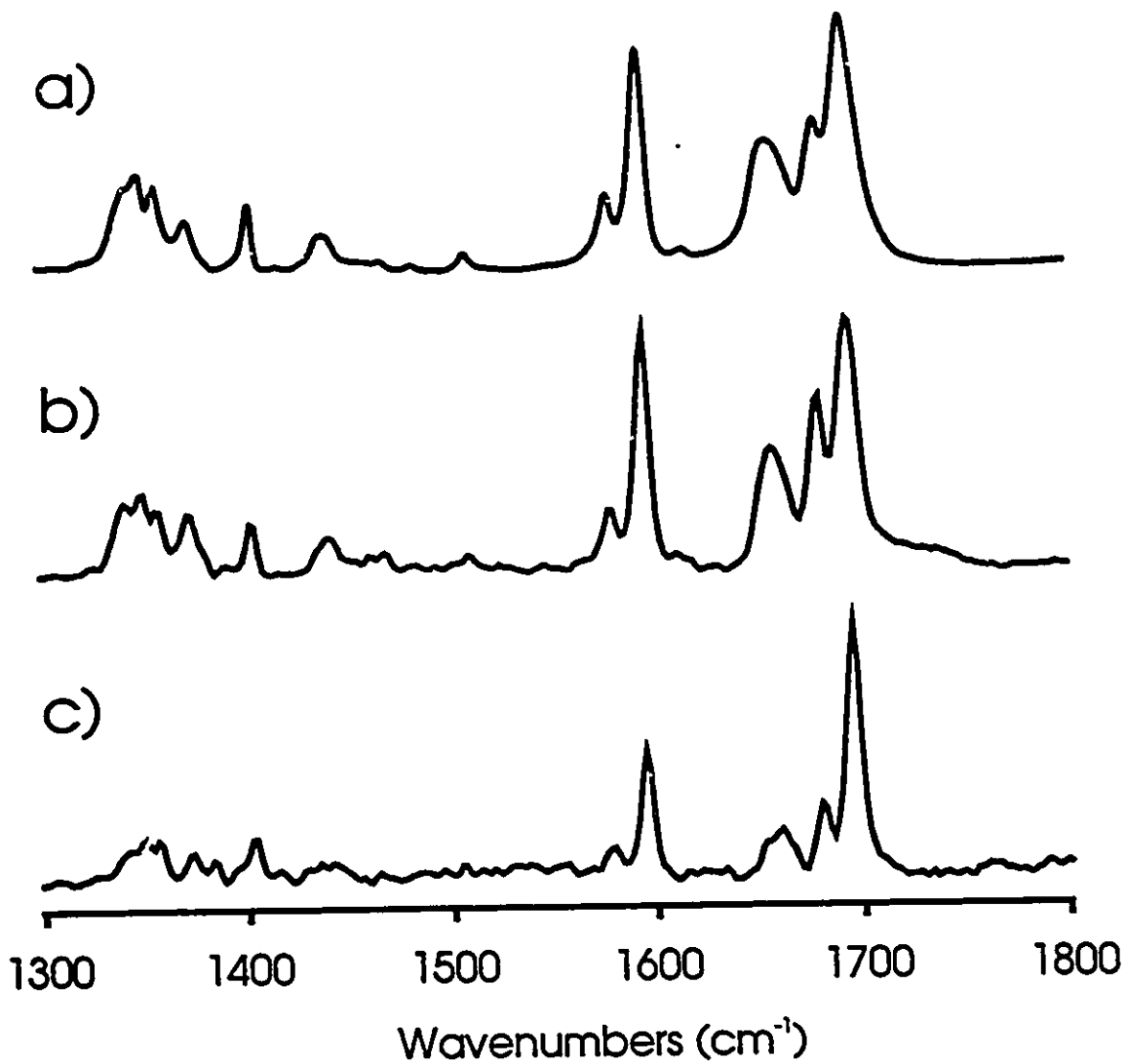
Figure 4.8. Absorption FT-IR spectra of HPTCNH in a) KBr pellet, b) of 22 LB monolayer on Ge and c) of 1 LB layer on 110 nm Ag film.

Correspondingly, they are observed with strong relative intensity in the infrared spectrum. The relative intensities of the C=O stretches would provide information about the molecular orientation of the perylene tetracarboxylic chromophore in LB films deposited on Ge, ZnS and smooth Ag surfaces.

The infrared spectra of HPTCNH are shown in *Figure 4.8*. The imide carbonyl region is identical with the other diimides, except for the appearance of a new band at 1679 cm^{-1}. This band has been assigned the C=O symmetric imide stretch due to hydrogen bonding between the N-H carbonyl of one molecule and the N-H hydrogen of a different PTCD. This band was not used in determining molecular orientation. Further discussion of this hydrogen bonding is given in *Chapter 6*.

For our discussion the substrate surface will be defined as the x-y plane. In transmission IR, the propagation direction is along the z axis and the electric field component is therefore parallel to the substrate surface. The IR spectrum of the sample dispersed in a KBr pellet is shown at the top of *Figures 4.4-8*. In the KBr pellet a random molecular orientation is assumed. The transmission spectra of an LB film deposited onto ZnS (less amphiphilic molecules) or Ge (amphiphilic molecules) are shown as spectrum b) in the *Figures 4.4-8*. The LB was transferred at 25 mN/m. Assuming a molecular organization with the planar chromophore lying flat on the x-y surface, a strong interaction between the electric field (E_x or E_y) and the transition moments (μ_x and μ_y) of both C=O stretching vibrations is expected. However, the relative intensity of the higher frequency C=O stretching mode decreased in the transmission spectrum of the LB samples. In HPTCO, as it can be seen in *Figure 4.4-b*, two high frequency vibrations were seen with an increase in relative intensity in RAIRS, while the opposite holds for the low frequency C=O modes in the transmission geometry. The results exclude a flat-on orientation of the chromophore moiety and may be rationalised in terms of a tilted or head-on organization of the chromophore on the Ag, ZnS and Ge surfaces. A perfect edge-on organization would lead to the disappearance of the C=O stretching vibration with a transition moment along the short axis (since μ_z would coincide with the normal to the surface). The symmetric C=O

vibration (the band observed at 1696 cm^{-1}) which generates a change in the dipole moment along the long axis (parallel to substrate normal, z), appears greatly reduced in the transmission LB spectra, evidence of an end-on orientation. The last spectrum (c) in the *Figures 4.4-8* illustrates the results obtained by a single reflection-absorption infrared experiment recorded at an incident angle of 75°. In the RAIRS experiments only the E_z (P-polarization) component of the incident light can interact with the adsorbate, and the surface selection rules lead to the manifestation of molecular vibrations with a finite component of their dynamic dipole perpendicular to the metal surface *[4.9,10]*. The RAIRS spectra showed a reverse trend when compared to the transmission spectra. In the frame of reference of the previous discussion, the relative intensity of the C=O mode along the long axis (z) is enhanced in the RAIRS spectrum. The result supports the end-on orientation, where the long axis also forms an angle (< 90°) with the normal to the metal surface. In conclusion, the transmission and reflection spectroscopic data show that the tilted molecular orientation (that is implied at the transfer surface pressure of 25 mN/m) was preserved during the transfer of the monolayer to all three solid substrates.

Since different substrates were used in this work, it was necessary to examine the effects that these different substrates have on the molecular orientation in the film. The infrared spectra were recorded for a variety of multilayer thicknesses for LBs transferred to the three different substrates used (Ge, ZnS and Ag). The absorbances of the peaks in the 1550 to 1800 cm^{-1} range varied linearly with the number of transferred monolayers. Moreover, the relative absorbances of these same peaks did not change with respect to the number of monolayers transferred. The absorbances observed in the spectra of LBs deposited on Ge were identical to those in the spectra of LBs deposited on ZnS. Therefore, for the three substrates used here, the molecular orientation depends very little on the nature of the substrate or on the number of layers in the LB film.

Calculation of the tilt angles.

Molecular orientation in Langmuir-Blodgett multilayers can be determined from the combined infrared spectral data obtained in a transmission geometry and in a reflection-absorption geometry. This approach has been recently demonstrated by Umemura et al. *[4.11]* using LB monolayers of cadmium stearate. The calculations are based on the formalism developed for the optical properties of thin multilayer films *[4.12]*. The quantity of interest that can be evaluated with this method is the tilt angle, ϕ, formed between the direction of the dynamic dipole moment and the normal to the surface of the film. The angle can be extracted from Equation 1,

$$A_T/A_R = \sin^2\phi \,/\, (2m_z \cos^2\phi + m_x \sin^2\phi) \qquad (4.1)$$

where A_T and A_R are transmission and reflection absorbances, normalized with respect to the number of LB layers, and m_z and m_x are the enhancement factors for light polarized normal to the surface (z direction) and parallel to the surface (x or y direction). In the RAIRS experiments, no detectable intensity was obtained for incident radiation polarized parallel to the film surface. Therefore, $m_x << m_z$ is a reasonable assumption and (4.1) becomes:

$$A_T/A_R = \tan^2\phi \,/\, 2m_z \qquad (4.2)$$

From this expression, the tilt angle can be readily calculated.

The most arduous task is the determination of m_z. The value of m_z is estimated from the hypothetical ratio of A_R/A_T which is theoretically determined for isotropic LB films according to Hansen's work *[4.12]*. The determination of the enhancement factors was performed using Math-Cad for Windows, a commercially available mathematical spreadsheet type program. A sample calculation using Math-Cad is given in *Appendix II*. The document is the hard copy of the actual spreadsheet used.

The value of m_z depends on several factors including the incident angle of

radiation, the thickness of the LB matrix, the complex index of refraction of the infrared transparent substrate (transmission geometry) and that of the metal (reflection geometry).

Values for m_z determined by Umemura *et al.* *[4.11]* were successfully verified using Mathcad for Windows. The same method was subsequently applied to calculate values for m_z involving our experimental conditions. The tilt of the carbon chain for arachidic acid was determined experimentally and was similar to the tilt angles determined by Umemura *et al.* *[4.11]*. The calculated tilt angles (measured in degrees from the surface normal) for all perylene derivatives studied here are listed in *Table 4.2*.

The first column of tilt angles corresponds to the high frequency $C=C$ stretching which, in the parent perylene, has a transition moment aligned parallel to the short axis of the molecule *[4.5]*. Based on this assignment, any other vibration whose transition moment is parallel to the short axis of the molecule should produced similar tilt angles to the ones observed for the 1593 cm^{-1} band. As can be seen in Table 2, the 1656 cm^{-1} band has comparable tilt angles to the 1593 cm^{-1} band whereas the tilt angles for the 1696 cm^{-1} band are considerably different from the other two bands. The calculations for the $C=O$ stretching vibration at 1656 cm^{-1}, with a dynamic dipole moment along the short axis of the chromophore, give the angle between the short axis and the normal to the surface. The third column gives the angle between the long axis of the chromophore and the normal to the surface. The spatial arrangement determined for PPTCDM on the surface is depicted in *Figure 4.9*. The calculated angles indicate that the molecular arrangements in the LB films are very similar. Therefore, molecule-subphase interactions were not the dominant driving force behind the structure of the monolayers studied. Instead, the results may be rationalized in terms of a predominant contribution of the aromatic-aromatic interactions to the stabilization of the two dimensional layer. Evidence for these interactions arises from the observation of excimer formation of these and similar perylene diimides in LB films *[4.13,14]*.

Table 4.2. Tilt angles (given in degrees) between the surface normal and the transition moments of the 1593 cm^{-1}, 1656 cm^{-1} and 1696 cm^{-1} bands.

Molecule	Tilt Angle (1593 cm^{-1} transition moment)	Tilt Angle (1656 cm^{-1} transition moment)	Tilt Angle (1696 cm^{-1} transition moment)
PPTCDM	65	75	40
PPTCDE	77	78	58
HPTCDE	76	80	60
PPTCDPr	68	63	41
HPTCO	60	64	36
HPTCNH	62	65	56
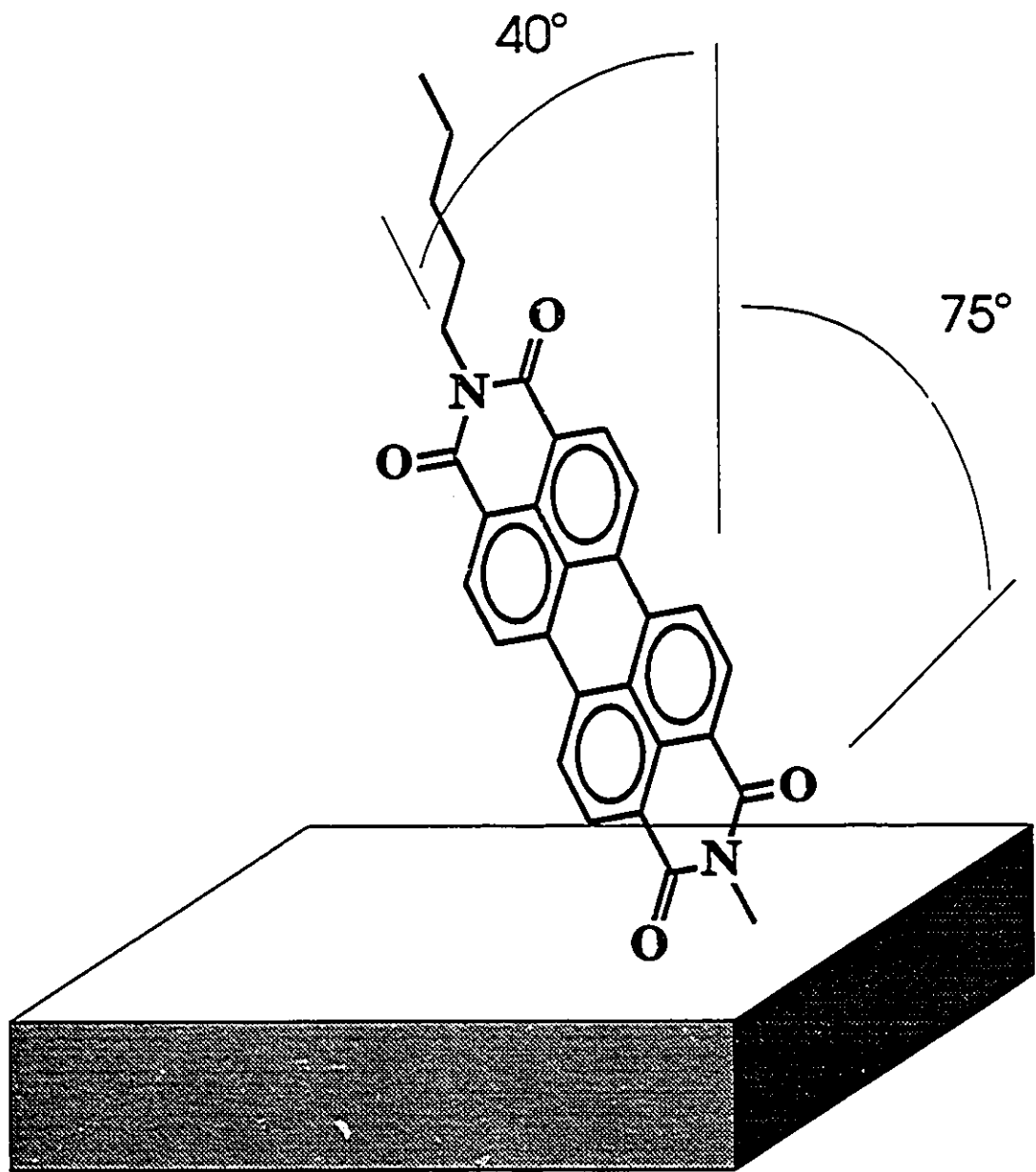
Figure 4.9.   Representation of the molecular orientation determined by transmission and RAIRS experiments for PPTCDM.

Once ϕ was established, then the expected projected area occupied by a single molecule on the substrate was calculated and listed in *Table 4.1*. Using the tilt angles for the long and short molecular axes, the area of the projection of the chromophore onto the substrate surface was estimated. PC model calculations supplied a chromophore geometry which was approximately rectangular with a length of 1.29 nm (distance between nitrogens of the imide groups) and a width of 0.84 nm (distance between hydrogens of the perylene moiety).

There are two serious concerns when applying this model to a determination of molecular orientation. First of all, the orientation on the reflection absorption substrate needs to be the same as the orientation on the transmission substrates. A qualitative comparison of carbonyl bands seen in the reflection absorption and the transmission spectra can be used as an indicator for different orientations in the different LB systems. Weak bands in the RAIR spectra are relatively stronger in the transmission spectra and weak bands in the transmission spectra are relatively stronger in the RAIR spectra. According to our qualitative discussion preceding the calculation of molecular tilt angles, these trends are observed. Therefore, it is sound to assume that the molecular orientation is similar in the two systems.

Secondly, it should be emphasized that this work reports the average molecular tilt in LB films. In order to achieve good signal to noise ratios for our LB systems, the spectra of multilayers were recorded. However, the transfer ratios for the deposition of each layer in the multilayered systems were identical. Therefore, we do not expect significant deviation from the determined tilt angles.

Chapter Summary

Floating and Langmuir-Blodgett monolayers of molecules with varying amphiphilic character and with a common π system chromophore were prepared. Molecular orientation in LB films was similar for all six perylene tetracarboxylics studied. The observed molecular orientation for each material was independent of the substrate (Ge, ZnS and Ag) used and the number of layers transferred. A nearly end-on orientation with a long axis tilted angle of ca. 40 degrees was calculated. It is concluded that molecular organization is mainly determined by π-π interactions, given the similar structures observed for the LB films of five different perylene derivatives studied and regardless of substrates used. The influence of π-π interactions is explored in *Chapter 6.*

References - Chapter 4

[4.1] Ulman, A.; *Ultrathin Organic Films*, Academic Press, Inc. N.Y., 1991.

[4.2] R.A. Hann in *Langmuir-Blodgett Films*, G. Roberts, Ed., Plenum Press, N.Y., 1990.

[4.3] Kumaki, J.; *Macromolecules*, 1988, *21*, 749.

[4.4] Meyer, E.; Howald, L.; Overney, R.M.; Heinzelmann, H.; Frommer, J.; Guntherodt, H.J.; Wagner, T.; Schier, H.; Roth, S.; *Nature*, 1991, *349*, 398.

[4.5] Ambrosino, F.; Califano, S.; *Spectrochim. Acta.*, 1965, *21*, 1401.

[4.6] Hochstrasser, R.M.; Nyi, C.A.; *J. Chem. Phys.*, 1980, *72*, 2591.

[4.7] Hase, Y.; *J. Mol. Struct.*, 1978, *48*, 33.

[4.8] Akers, K; Aroca, R.; Hor, A.M.; Loutfy, R.O.; *J. Phys. Chem.*, 1987, *91*, 2954.

[4.9] Hayden, B.E. in *Vibrational Spectroscopy of Molecules on Surfaces, Methods of Surface Characterization*, Yates, J.T.; Madey, T.E. Eds., Plenum Press, New York, 1987, Vol. 1, p 267.

[4.10] Bradshaw, A.M.; Schweizer, E.; *Spectroscopy of Surfaces, Advances in Spectroscopy*, Clark, R.J.H.; Hester, R.E., Eds., John Wiley & Sons, N.Y., 1988, Vol. 16, p 413.

[4.11] Umemura, J.; Kamata, T.; Kawai, T.; Takenaka, T.; *J. Phys. Chem.*, 1990, *94*, 62.

[4.12] Hansen, W.N.; *J. Opt. Soc. Am.*, 1968, *58*, 380.

[4.13] Johnson, E.; Aroca, R.; Pahapill, J.; *Journal of Molecular Structure*, 1993, *293*, 331.

[4.14] Johnson, E.; Aroca, R.; Nagao, Y.; *J. Phys. Chem.*, 1991, *95*, 8840.

Chapter 5: Spectroscopic Properties and Packing of Langmuir-Blodgett Monolayers of Perylene Tetracarboxylic Anhydrides

Introduction

In this chapter, a series of perylene tetracarboxylic anhydrides have been spread as Langmuir monolayers and transferred as Langmuir-Blodgett films to a variety of solid substrates. The structures of the species studied are given in *Figure 5.1*. The substituents on the imide nitrogen are R = propyl for PrPTCO, pentyl for PPTCO, 2-phenylethyl for PhPTCO and 6-hydroxyhexyl for HOPTCO. The objectives of this work were the spectroscopic characterization of these four PTCOs, the formation of floating Langmuir layers and the fabrication of LB films of these materials by transferring the floating layers to solid substrates. These materials are particularly interesting because this is the first attempt at forming films of PTCOs with functionalized side chains. The ultimate aim of this chapter is to determine the effect these side chains upon the film structure and stability, and to resolve which derivative provides the best quality film. The only perylenetetracarboxylic monoimide previously characterized as a LB film is N-hexyl PTCO (HPTCO) *[5.1]*, but this chapter represents the first comparison of a series of PTCOs fabricated into LB films.

The structure of the film plays an important role in the potential application of the films. Therefore, it is important to find derivatives of the perylene tetracarboxylic chromophore that yield films with consistent and reproducible structure. For practical applications, such structures should also be as durable and as simple to produce as possible.

Perylene dyes are known to form aggregates in the ground and excited states *[5.2-4]*. Hence electronic spectroscopy such as UV-visible absorption and steady state fluorescence are ideal tools to study perylene aggregates. Transmission and reflection absorption infrared (RAIR) spectroscopy supplements the observed electronic data by providing insight into molecular orientation.
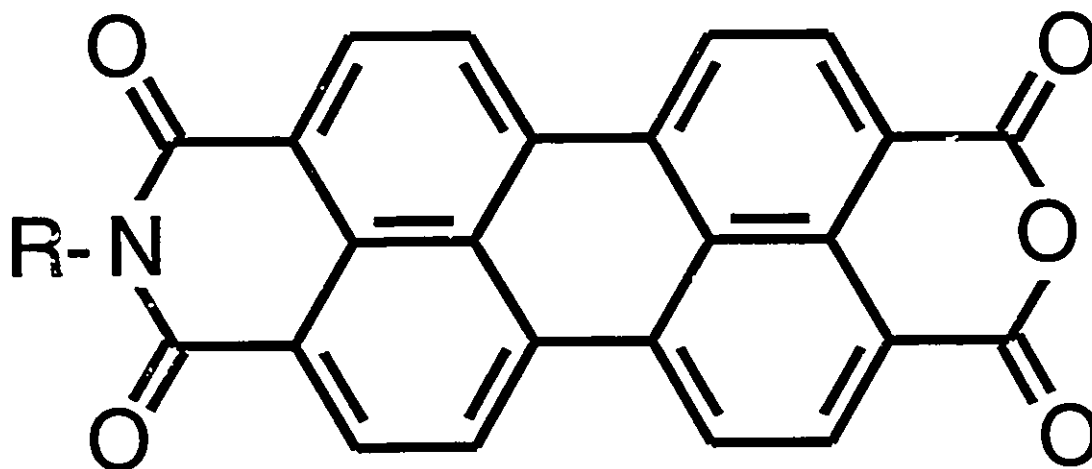
Figure 5.1:   The structure of the four PTCOs studied. PrPTCO, R = propyl; PPTCO,
                R = pentyl; PhPTCO, R = 2-phenylethyl; HOPTCO, R = 6-
                hydroxyhexyl.

It is of particular interest to study the effects of different side chains upon the aggregation phenomenon. It has been learned that the colour of the solid material depends upon intermolecular arrangement *[5.5,6]* for N,N' symmetric diimides and that theoretical modelling of polymorphs of perylene tetracarboxylics has been attempted *[5.7]*. The substituents of the imide nitrogens influence intermolecular structure and ring system overlap. The effect of deposition technique and film annealing were also studied.

Experimental Details

The synthesis and purification of these perylene compounds were performed by Dr. Jim Duff at the Xerox Research Centre of Canada. LB monolayers were prepared as per *Chapter 2*. The spreading solvent was 10% Trifluoroacetic acid in chloroform. Pure chloroform was attempted, but these perylene derivatives were exceptionally insoluble in this solvent. Purified water was used as the subphase. Pressure/area isotherms were recorded at a compression rate of $0.325 \ mm^2 s^{-1}$. The isotherms were recorded at 15 and 25°C. Monolayer transfer, through Z and Y deposition, was attempted for these materials. However, the resulting floating layers (except for PPTCO) were very rigid and could only transferred via horizontal deposition. Transfer pressure was 20 mN/m in all cases. Multilayers (up to 10 LBs) as well as single monolayers were transferred. For all successful transfers, the transfer ratio was near unity. LB film quality was assessed by optical microscopy using a x100 objective lens. On this scale, the films appeared homogeneous. Only a few pinholes were observed, as well as cracks in the films near the edges of the substrates.

For spectroscopic characterization, the LBs were transferred to appropriate substrates. For visible absorption and fluorescence work, the substrates were Corning 7059 glass slides. For infrared characterization, the substrates were polished zinc sulphide windows for transmission work and 100 nm of smooth silver on glass for RAIR spectroscopy. Silver islands, 6 nm mass thickness, were also used for SERS, and SERRS. The silver films were prepared as per *Chapter 2*. Before transfer was attempted, the substrates were cleaned ultrasonically in water, then chloroform and were dried in a stream of high purity nitrogen. The spectroscopic instrumentation and techniques have already been described in *Chapter 2*.

Results

Langmuir and Langmuir-Blodgett Layers

The isotherms were recorded at 15 and 25°C. Each perylene showed a slight increase in limiting area with an increase in temperature. There was also a minor change in collapse pressure with increasing temperature. The only exception was PhPTCO. There was no change in limiting area and an increase in collapse pressure with increasing temperature. The shape of the π-A curves did not change within the 10°C temperature interval. The pressure/area isotherms recorded at 25°C for the four perylenes studied are shown in *Figure 5.2* and the isotherm data is listed in *Table 5.1*.

Transfer of the floating layers was then attempted to a variety of solid substrates. The only successful vertical transfer was achieved for PPTCO, by the Z deposition, to glass slides and smooth silver at 25°C. Therefore, horizontal transfer was used for all of the perylenes studied. Monolayers of PPTCO transferred by different methods were compared spectroscopically in order to investigate the effect of deposition technique upon the LB formed.
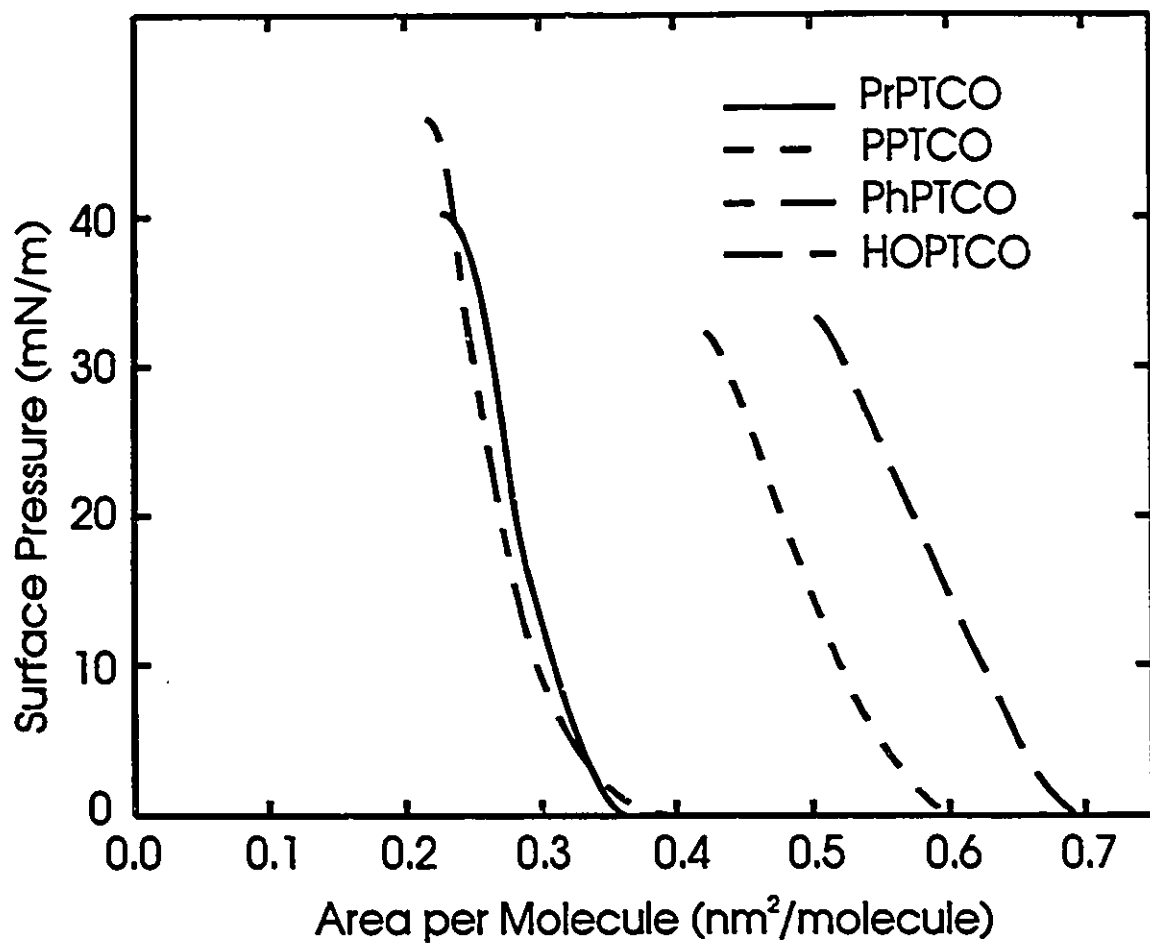
Figure 5.2: The pressure/area isotherms at 25°C of the four PTCOs studied.

Table 5.1: Isotherm Data

Molecule	15°C		25°C	
	Limiting Area (nm²/molecule)	Collapse Pressure (mN/m)	Limiting Area (nm²/molecule)	Collapse Pressure (mN/m)
PrPTCO	0.28	50	0.32	45
PPTCO	0.48	33	0.56	32
PhPTCO	0.31	43	0.31	47
HOPTCO	0.60	38	0.68	34

Electronic Spectra

The absorbance and steady state fluorescence spectra of dyes and pigments can reveal much about the nature of the aggregation of such materials *[5.8-10]*. The visible absorption of the PTCOs was recorded and were all virtually identical. They all exhibited the characteristic vibronic structure associated with aromatic hydrocarbons, with a ν_{0-0} transition at 529 nm. Since the solvent used (for LB work) is 10% TFA in $CHCl_3$, the spectra are red shifted compared to those obtained in pure $CHCl_3$ *[5.11]* due to the increase in solvent polarity *[5.12]*. The fluorescence spectra of the same solutions yielded a mirror image of the absorption spectrum, giving no indication of aggregation in solution.

Once the PTCOs were transferred to solid substrates, the absorption and emission spectra were dramatically different. *Figure 5.3* illustrates the absorption and emission of the solution and of 1 LB on glass for PPTCO. The absorption spectrum of 1 LB and that of the material dispersed in a KBr pellet are similar, and are split into two broad peaks. The blue shifted component, at 483 nm, is considerably stronger than the red shifted component at 552 nm. Such a splitting pattern is generally indicative of H aggregation for such chromophores *[5.8-10]*. The absorbance spectra of the four PTCOs studied show the same splitting pattern. Moreover, the relative intensities of the two components and the magnitude of the splitting are invariant for the four perylenes. The emission spectrum of 1 LB of PPTCO contains two interesting features. First of all, the two bands at 542 and 586 nm correspond well with the bands of the solution spectrum, thereby indicating the presence of a monomer-like emission of PPTCO in the LB. The broad, red shifted band at 663 nm is characteristic of excimer formation in LB films of perylene tetracarboxylic derivatives.

The emission spectra of the LBs are different from each other and are illustrated in *Figure 5.4*. Each film exhibits different relative quantities of monomer-like and excimer emission. The LB of HOPTCO shows primarily monomer-like emission and that of PhPTCO contains mostly excimer emission. The spectra of PrPTCO and PPTCO show a mixture of monomer-like and excimer emission.
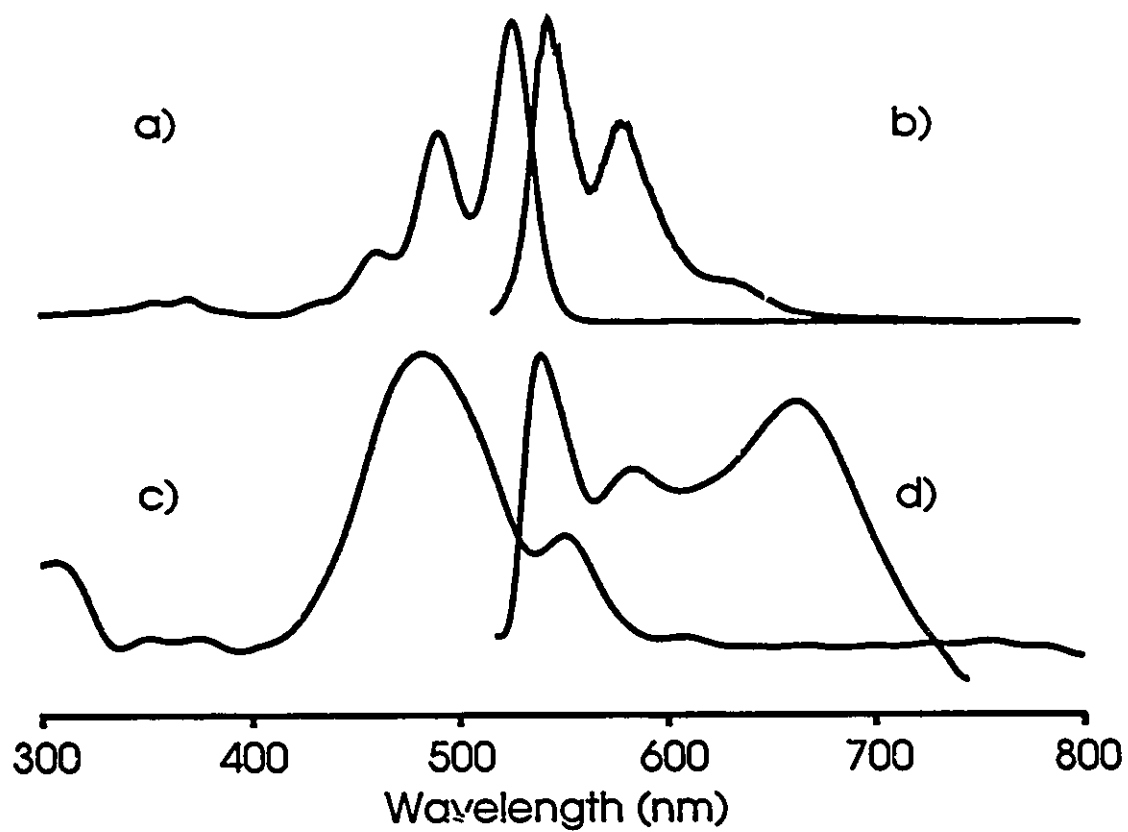
Figure 5.3:   The electronic spectra of PPTCO: a) absorption in solution, b) emission in solution, c) absorption of 1 LB, d) emission of 1 LB. Y axis units are arbitrary.
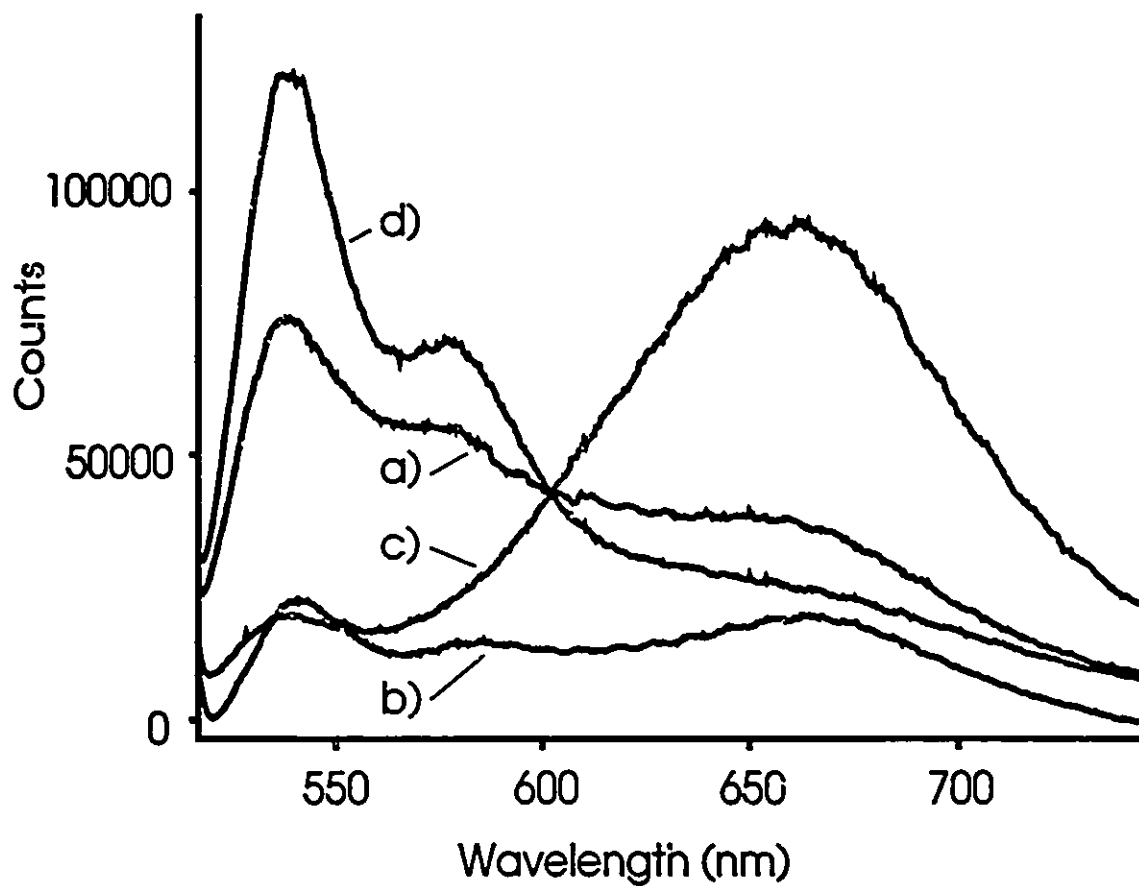
Figure 5.4:   The emission spectra of 1 LB of each of the PTCOs studied. a) PrPTCO,
b) PPTCO, c) PhPTCO, d) HOPTCO.

Infrared Spectra

The observed fingerprint infrared frequencies for the PTCOs dispersed in KBr are given in *Appendix I* and the spectra are shown in *Figure 5.5*. All four spectra differed very little. The spectra of PPTCO and PrPTCO are virtually identical. PhPTCO can be differentiated from the former two by the presence of the weak C=C aromatic stretch at 1498 cm^{-1} and the presence of a C-H aromatic stretch at 3024 cm^{-1} that does not exist in the other three spectra. The most distinguishable feature of the HOPTCO infrared is the broad, hydrogen bonded O-H stretch at 3362 cm^{-1}.

The characteristic (in plane) benzene C=C stretching vibrations of the perylene ring were observed for all four molecules at 1507, 1580 and 1595 cm^{-1}. In the parent perylene molecule, the highest C=C stretching frequency at 1606 cm^{-1} has a change in dipole moment parallel to the short molecular axis *[5.13]*. Four strong carbonyl stretching vibrations exist for each PTCO. At 1656 and 1696 cm^{-1} are the anti-symmetric and symmetric C=O stretches, respectively. The anhydride C=O stretches appear at about 1764 and 1776 cm^{-1} for the anti-symmetric and symmetric modes, respectively. The four anhydride C=O stretches of the dianhydride, PTCDA, are also clustered close together *[5.14]*. The two PTCO anhydride bands overlap significantly in the KBr spectrum, but are revealed as two bands in the two LB spectra. The change in dipole moment associated for these carbonyl stretches is parallel to the short molecular axis for the antisymmetric modes and parallel to the long molecular axis for the symmetric modes. Using this information as a frame of reference, it is now possible to elucidate the average molecular orientation of the chromophore in the LB film by a comparison of transmission and RAIR infrared spectra. The comparison of the imide C=O stretches have been used to qualitatively *[5.15,16]* and quantitatively *[5.17]* to evaluate orientation for perylene tetracarboxylic diimides in LB films.

The average molecular orientation can be determined by inspecting changes in the band intensities in the spectra of 1 LB in the transmission geometry and in the reflection geometry. In the transmission case, the polarization of the incident radiation is parallel to the substrate surface. Therefore, only vibrations with a transition dipole moment
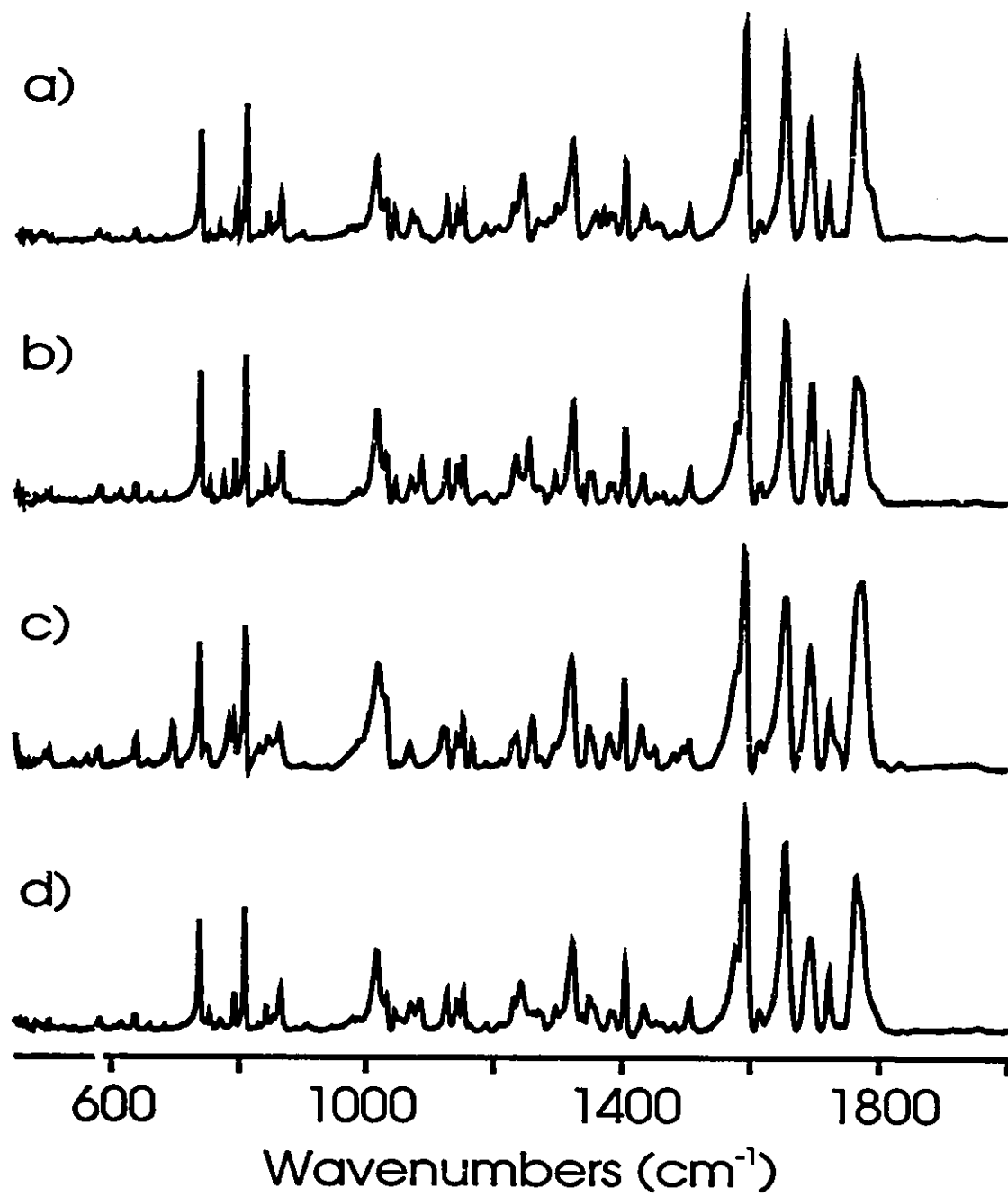
Figure 5.5: The infrared spectra of the four PTCOs dispersed in KBr pellets. a) PrPTCO, b) PPTCO, c) PhPTCO, d) HOPTCO.

parallel to the substrate surface will be active. Vibrations perpendicular to the substrate surface will be silent. The opposite case exists for the reflection geometry. Here, surface selection rules operate [5.18]. The intensities of vibrational modes with a dynamic dipole perpendicular to the surface are enhanced and those modes parallel to the surface are suppressed. The infrared spectra of the carbonyl region of PPTCO and HOPTCO are given in *Figures 5.6* and *7*. Spectrum a) is the material dispersed in a KBr pellet, which is assumed equivalent to a random spatial molecular orientation. Spectra b) and c) are the transmission and reflection spectra, respectively. The orientation trends regarding the imide carbonyl stretching intensities are the same for the four compounds studied. In the transmission case, the 1656 cm⁻¹ band is more intense than the 1696 cm⁻¹ band. The reverse trend is true for the RAIR spectra. Since the 1656 cm⁻¹ band is polarized along the short molecular axis, then the short molecular axis must be tilted closer to the substrate plane than the long molecular axis. Since both bands are visible in both spectra, the short molecular axis is not parallel to the substrate surface, nor is the long molecular axis completely perpendicular to the substrate surface.

The only unforeseen absorbance in the LB spectra is the appearance of an additional band at 1788 cm⁻¹ in the two HOPTCO spectra. Since this band does not appear in the LB spectra of the other three PTCOs and it is absent in the KBr pellet spectrum of HOPTCO, it can be concluded that this is the TFA ester of HOPTCO. There was some concern that in the TFA/CHCl₃ solvent system, the TFA could react with the anhydride portion of the PTCO. No changes in the infrared spectra support this. Moreover, it is also known that the perylene tetracarboxylic anhydrides are exceptionally stable [5.12] due to conjugation with the perylene ring system. Hence, the LBs of HOPTCO prepared are actually LBs of the HOPTCO-TFA ester, where the ester link is through the hydroxy function on the hexyl side chain and this band corresponds to the carbonyl of the ester of trifluoroacetic acid.

Average molecular orientation can be evaluated quantitatively by comparing the transmission and RAIR spectra of the same material [5.19]. This approach has also been used successfully on other perylene tetracarboxylic derivatives [5.17]. In order for this
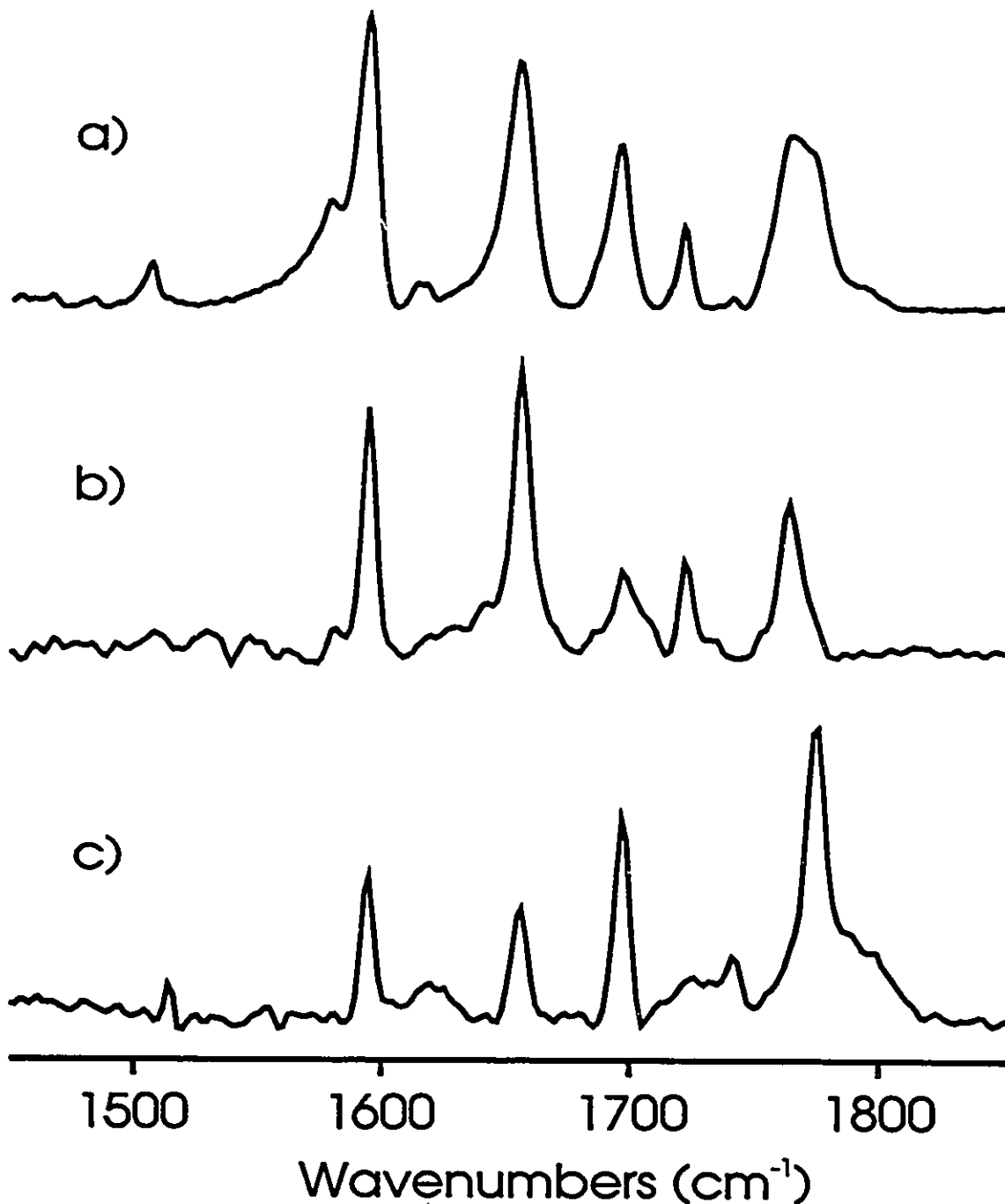
Figure 5.6:   The infrared spectra of the carbonyl region of PPTCO. a) dispersed in
KBr pellet, b) transmission on ZnS, c) RAIR on smooth silver.
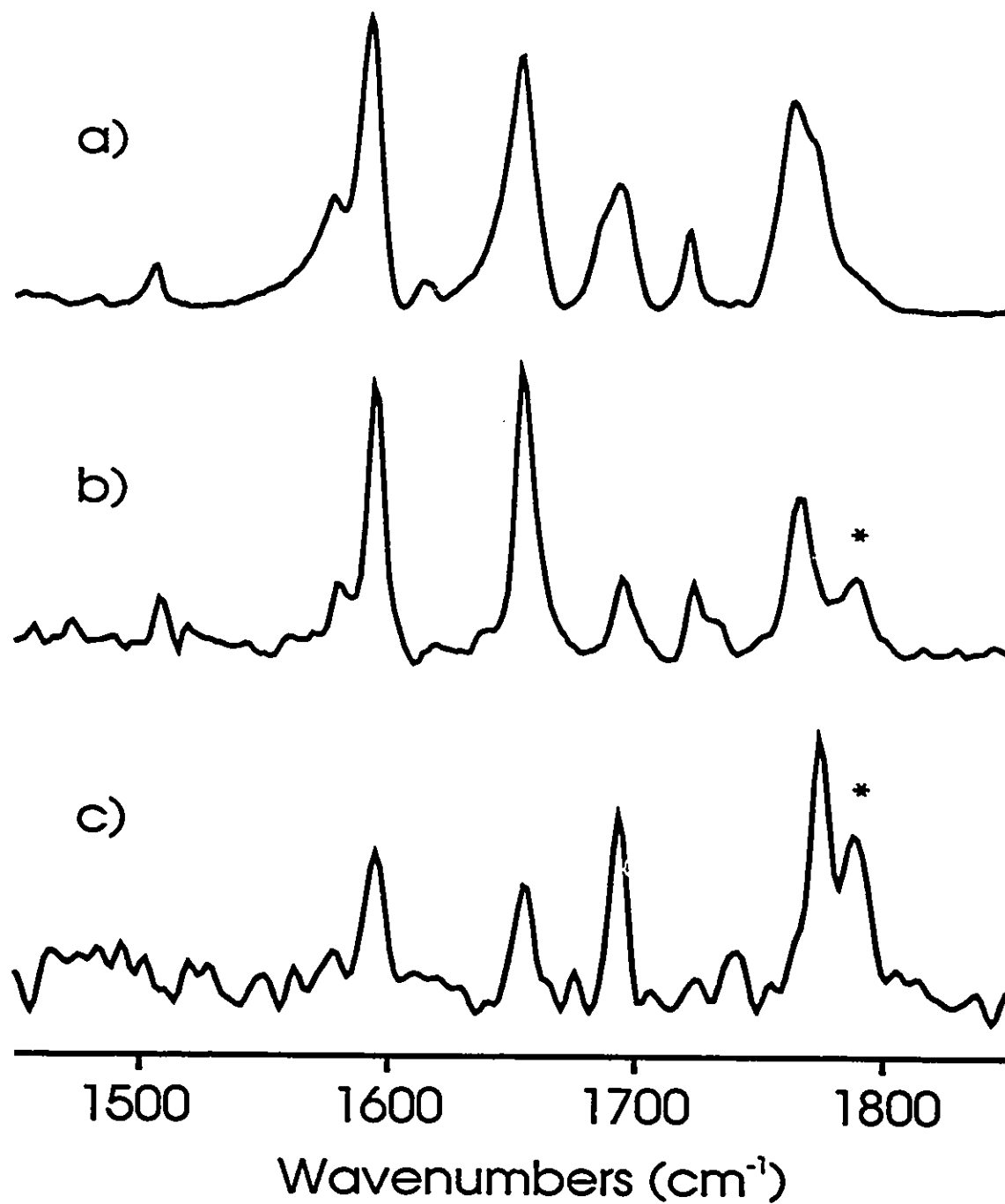
Figure 5.7:   The infrared spectra of the carbonyl region of HOPTCO. a) dispersed in
KBr pellet, b) transmission on ZnS, c) RAIR on smooth silver. The *
indicates appearance of 1788 cm⁻¹ band.

method to be successful, several criteria need to be met. First of all, uniaxial molecular orientation must exist. This was demonstrated by measuring the transmission spectra at various polarization angles. No change in intensity was observed. Secondly, the orientation on the transmission substrate needs to be reproduced on the RAIR substrate. Both the ZnS and the smooth silver are hydrophobic according to the contact angle the air/water interface when the substrate is dipped perpendicular into the subphase. Since horizontal deposition was performed, there is less likelihood of molecular rearrangement upon transfer. The preceding qualitative discussion of molecular orientation is indicative of similar, if not identical, average molecular orientation. The calculated tilt angles for the long and short molecular axes are given in *Table 5.2*. As can be seen from the calculated tilt values, the tilt angle of the short axis calculated from the 1595 and the 1656 cm^{-1} bands are within a few degrees of each other. All four PTCO's have the same average molecular orientation.

Table 5.2: Average Chromophore Orientation for the PTCOs

Molecule	Chromophore Axis Tilt Angle (in ° from surface normal)		
	Short Axis (1596 cm^{-1} band)	Short Axis (1656 cm^{-1} band)	Long Axis (1696 cm^{-1} band)
PrPTCO	77	75	57
PPTCO	72	76	63
PhPTCO	77	76	61
HOPTCO	73	76	59

Raman Spectra

The strong fluorescence of PTCO compounds overwhelms the Raman spectrum from bulk samples. Surface enhanced resonance Raman (SERRS) spectra was the only Raman spectra obtained from the LB on silver islands. The resonance Raman effect selectively enhanced vibrations associated with the chromophore several orders of magnitude above that of other bands. In order to observe the weaker SERS bands, different experimental conditions were needed so no direct comparison of band intensity was possible. The observed SERRS frequencies for the four PTCOs studies are listed in Appendix I, and *Figure 5.8* shows the PPTCO SERRS spectrum. The SERRS spectra are dominated by three very prominent bands in the 1300-1600 cm^{-1}. Most of the bands listed in the SERRS table of PPTCOs in the Appendix are not discernible in *Figure 5.8*. In order to observe these bands, large acquisition times were required and 50 spectra were coadded. Even the carbonyl stretches, very weak in the Raman, were observed and the correct stretching mode could be assigned based on intensity. Totally symmetric vibrations are more intense than anti-symmetric ones. From our spectra, the 1696 cm^{-1} imide stretch and the 1770 cm^{-1} anhydride stretch are the more intense carbonyl vibrations. Hence, these are the symmetric stretches.
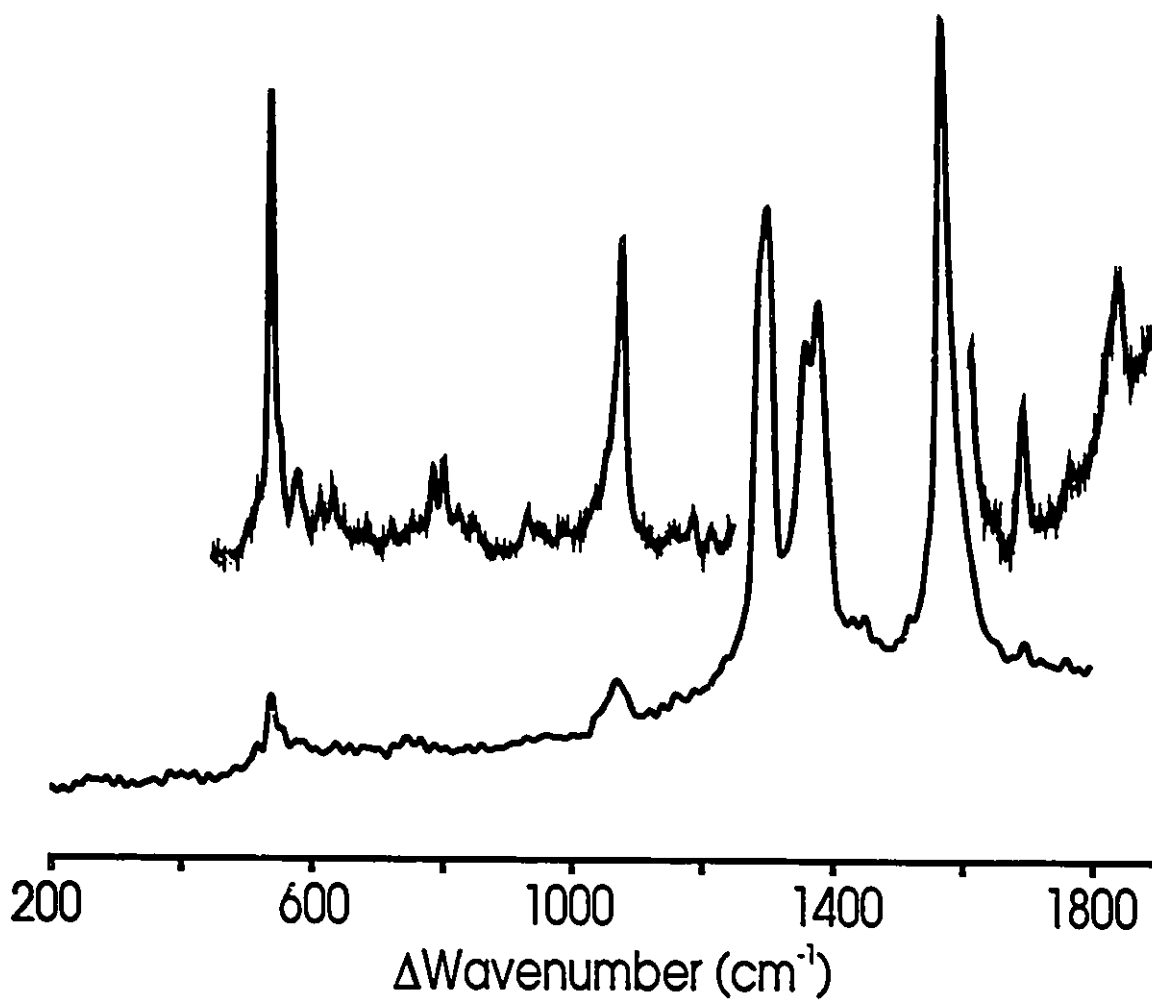
Figure 5.8: The SERRS spectra of PPTCO. Inset regions contain weaker bands that could only be detected with different instrument conditions (see text).

Comparison of Deposition Techniques

PPTCO was the only material that could be effectively transferred by Z deposition and horizontal deposition to glass slides. Important structural differences between films transferred by these two techniques are expected. In Z deposition, the hydrophillic end (presumably the anhydride portion of the PTCO) of the molecule faces toward the substrate after transfer. For horizontal deposition, the hydrophilic portion faces away from the substrate and when transfer takes place, the monolayer does not have to undergo a 90° change in direction as in the case for vertical deposition techniques. The horizontally deposited films should be inverted compared to the Z deposited films. However, the RAIR spectra of the two films showed very little difference in relative intensities, implying similar chromophore tilting.

The absorption and emission spectra of the two films gave the most contrasting results. The absorption spectra are shown in *Figure 5.9*. The film deposited by horizontal deposition has a lower absorbance than the film deposited by Z deposition. The Z deposited film was normalized since this system had a monolayer on both sides of the substrate and the horizontally deposited film had only 1 LB on one side only. Since the transfer ratios were about unity in both cases, the same quantity of material was transferred to a given substrate. The horizontally deposited film was annealed at 200°C for one hour and the absorption spectrum was again recorded. After annealing, the absorbance had increased and the spectrum became directly superimposible upon the spectrum of the Z-deposited film, as can be seen in *Figure 5.9*. There was no change in the absorption of the Z deposited film after annealing.

A similar trend can be seen in the fluorescence spectra of these two films. *Figure 5.10* shows the emission spectrum of a) the Z deposited film and b) the horizontally deposited film. Both spectra show monomer-like and excimer fluorescence, indicating structures with monomer-like emission and excimer emission exist in the films. The Z deposited film has a stronger excimer emission than monomer and the horizontally deposited film has a stronger monomer-like emission. Again, the Z deposited film was normalized to account for the presence of a second LB on the backside of the slide. After annealing, both samples showed a sharp reduction in the monomer-like emission, but a
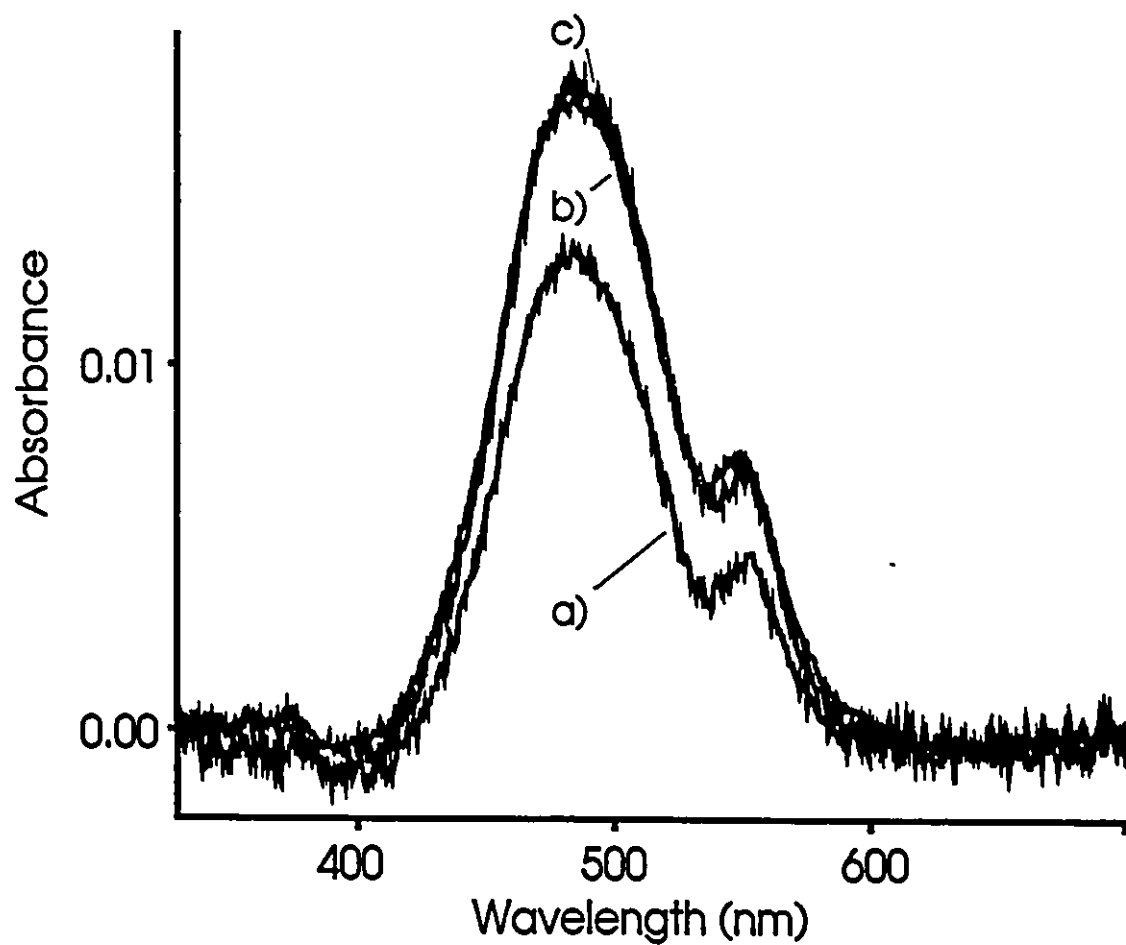
Figure 5.9: The absorbance of 1 LB of PPTCO a) by horizontal deposition, b) by Z deposition and c) by horizontal deposition after annealing.
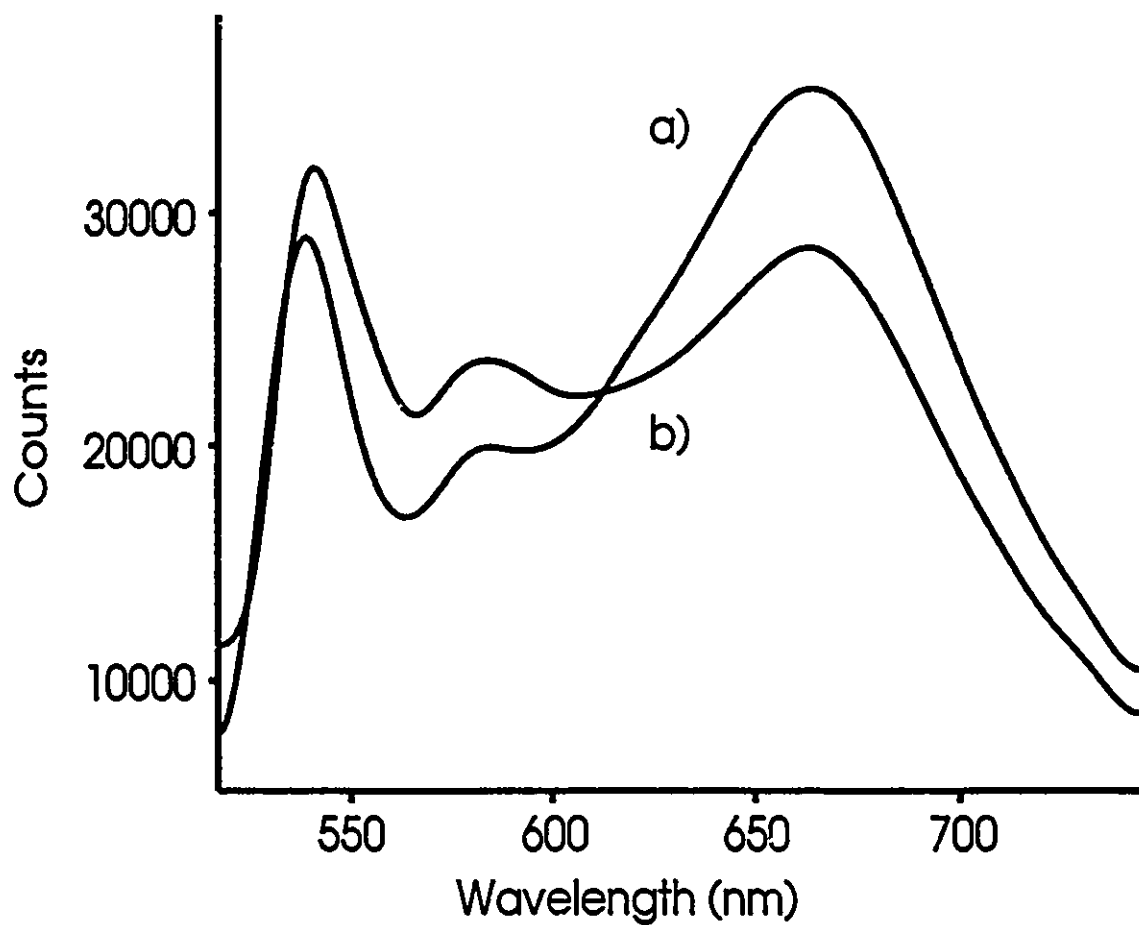
Figure 5.10:   The emission of 1 LB of PPTCO a) by Z deposition and b) by horizontal deposition.

negligible increase in excimer fluorescence. *Figure 5.11* illustrates these changes in emission after annealing.

The other PTCOs, transferred solely by horizontal deposition, were also annealed. Two LBs, PrPTCO and HOPTCO, showed the same trends in their absorption spectra as PPTCO. After annealing, the absorbance increased for these two compounds. On the other hand, PhPTCO had the same absorption before and after annealing. Moreover, the absorbance of PhPTCO before annealing was the same magnitude as the others after annealing. Also, PhPTCO was the only PTCO that showed almost exclusively excimer emission before annealing.

In order to investigate structural changes responsible for changes in the electronic spectra, the RAIR samples were also annealed. Absorbances in the IR underwent very small increases, but these changes were on the same scale as the signal to noise ratio for the spectra, so nothing conclusive can be determined from these spectra. Essentially, the IR spectra indicated that the average molecular tilt did not change after annealing.
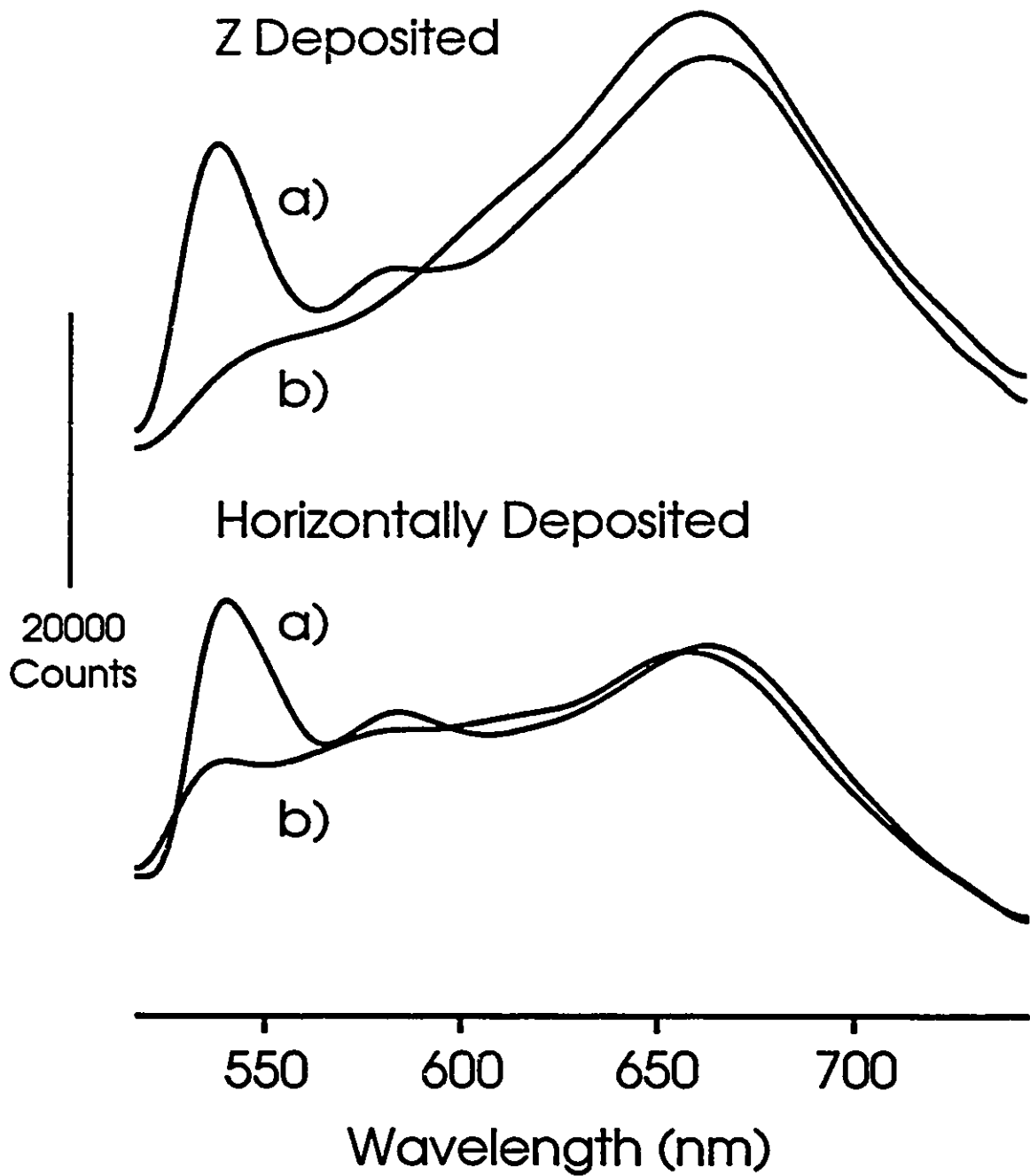
Figure 5.11: The emission spectra of 1 LB of PPTCO by different deposition techniques. a) before annealing and b) after annealing.

Discussion

Even though all four PTCOs share similar tilt angles, these angles are considerably greater than those determined for the N-hexyl PTCO (HPTCO) [5.17]. However, HPTCO was spread from pure chloroform and was deposited through Z deposition so it is not expected that the tilt angles should be the same. Also, the absorption spectra of the PTCOs studied were remarkably similar. The splitting observed is indicative of H-aggregate formation and can be explained through molecular exciton theory using either the point dipole approximation [5.20] or the far more accurate extended dipole approximation [5.8,9,21]. The extended dipole model has been applied to PTCDs in *Chapter 6* in order to elucidate intermolecular geometry. Since the band positions and splitting for all four PTCOs is identical, then it can generally be assumed that all four chromophores exist in very similar electrostatic environments. This is also supported by the similarity in chromophore tilt angles.

The changes in the absorption and fluorescence spectra reveal changes in the structure of the LB films. The relationship between fluorescence and crystal structure of perylene and perylene tetracarboxylics is given in *Chapter 3*. The excimer emission arises from a stacked form of the material and monomer-like emission comes from non-stacked molecular arrangements. The emission spectra of the LB's, as in *Figure 5.4*, show a mixture of monomer-like and excimer emission. When these films are annealed, there is a dramatic decrease in monomer-like emission, but a very small increase in excimer emission. The monomer emission is known to have a quantum yield orders of magnitude greater than aggregate emission [5.12]. Therefore, the transferred films contain a mixture of two different film structures. The annealing of the films transforms the non-stacked structure into the stacked structure. It has also been shown that excimer formation in LB films of perylene derivatives is extremely sensitive to small changes in intermolecular geometry [5.23,24]. Hence, it is possible to have similar absorption spectra and different emission spectra.

The different deposition techniques performed for PPTCO also yield interesting insights into the fabricated LBs. Each deposition technique results in a different mixture

of stacked and non-stacked forms. However, the RAIR spectroscopy shows that the tilt of the chromophore is similar in both films, yet one film is upside-down compared to the other. Therefore, intermolecular interactions must play a significant role in determining film organization. The greatest difference between these films is in their electronic spectra. The Z deposited film shows a stronger absorbance and more intense excimer emission than the horizontally deposited film. After annealing the horizontally deposited film, its absorption spectrum became identical in absorbance to the Z deposited film. Therefore, when a PTCO monolayer undergoes Z deposition, the change in film direction during transfer results in a greater quantity of the material to be in a stacked form. Annealing the horizontally deposited film transforms non-stacked structures into stacked structures, thereby creating a film similar in structure to the film formed during Z deposition. This means that the stacked form is thermodynamically more stable and that the monomer emission has a higher quantum yield than the excimer.

Extending this reasoning to the other three PTCOs illustrates interesting properties of these films. PrPTCO is similar to PPTCO in that a mix of two structures exist in the film and annealing promotes stacking. On the other hand, HOPTCO monolayers (which are really HOPTCO-TFA ester monolayers), exhibit strictly monomer-like emission, yet maintain the same absorption spectra as the other PTCOs. After annealing, the absorbance increases, yet there is no decrease in monomer emission, nor is there the appearance of excimers. The esterification of HOPTCO may have formed a molecule that has difficulty forming stacked structures. Since HOPTCO exhibits similar tilt angles compared to the other three PTCOs and the LB technique results in oriented films with the hydrophilic, anhydride portion of the molecule facing toward the water subphase, the molecules will be in an electrostatic environment similar to the other PTCOs and little difference in the absorption spectra will be observed.

The most interesting result concerns PhPTCO. First of all, this PTCO experienced the smallest changes in its isotherm with a change in temperature. Its absorption spectrum before and after annealing was identical and as strong as the post-annealing spectra of the other PTCOs. Before annealing, the emission spectrum of PhPTCO was dominated by excimer fluorescence and virtually no monomer fluorescence was present. After

annealing, there was no change in the emission spectrum. This indicates that PhPTCO has the strongest preference for a stacked structure compared to the other three PTCOs studied n this work. The presence of the phenyl group on the N substituent may provide additional π-π interactions that help PhPTCO stack more efficiently than other PTCOs. The X-ray determined structure for the analogous diimide, N,N'-di(2-phenylethyl) perylene tetracarboxylic diimide (PhPTCDPh), shows the phenyl groups stacking as well as the perylene chromophores [5.5].

Chapter Summary

The four PTCOs studied have been successfully spread as floating Langmuir layers and transferred, via horizontal deposition, to solid substrates. Characteristic vibrational frequencies were observed and assigned in the Raman and infrared spectra. All LBs formed have similar average molecular orientation, but the role of the N-substituent played a significant role determining the structure of these films. The HOPTCO-TFA ester was the most resistant to stacking and PhPTCO formed stacks most readily. Annealing experiments have shown that the stacked structure is thermodynamically preferred and that vertical deposition forces a molecular rearrangement that also produces the favoured, stacked form. The PhPTCO derivative yielded the most consistently stacked structure of the four LB films prepared.

References - Chapter 5

[5.1] Aroca, R.; Johnson, E.; *SPIE, Raman and Luminescence Spectroscopies in Technology II*, 1990, *1336*, 291-298.

[5.2] Florsheimer, M.; Mohwald, H.; *Thin Solid Films*, 1988, *159*, 115

[5.3] Law, K.Y.; Chen, C.C.; *J. Phys. Chem.*, 1989, *93*, 2533.

[5.4] Aroca, R. Guhathakurta-Ghosh, U.; Loutfy, R.; Nagao, Y.; *Spectrocim. Acta, A.*, 1990, *46*, 717.

[5.5] Graser, F.; Hadicke, E.; *Leibigs Ann. Chem.*, 1980, 1994-2011.

[5.6] Graser, F.; Hadicke, E.; *Leibigs Ann. Chem.*, 1984, 483-494.

[5.7] McKerrow, A.J.; Buncel, E.; Kazmaier, P.M.; *Can. J. Chem.*, 1993, *71*, 390-398.

[5.8] Czikklely, V.; Forsterling, H.D.; Khun, H.; *Chem. Phys. Let.*, 1970, *6*, 207-210.

[5.9] Czikklely, V.; Forsterling, H.D.; Khun, H.; *Chem. Phys. Let.*, 1970, *6*, 11-14.

[5.10] Herz, A.H., *Photographic Sci. Eng.*, 1974, *18*, 323-335.

[5.12] Ford, W.; *J. Photochem.*, 1986, *34*, 43-54.

[5.11] Johnson, E.; Aroca, R.; *Appl. Spectrosc.* submitted

[5.13] Ambrosino, F.; Califano, S.; *Spectrochim. Acta*, 1965, *21*, 1401.

[5.14] Akers, K.; Aroca, R.; Hor, A.M.; Loutfy, R.O. *J. Phys. Chem.* 1987, *91*, 2954.

[5.15] Aroca, R.; Maiti, A.K., Nagao, Y.; *J. Raman Spectrosc.*, 1993, *24*, 227-232.

[5.16] Aroca, R.; Maiti, A.K., Nagao, Y.; *J. Raman Spectrosc.*, 1993, *24*, 351-356.

[5.17] Aroca, R.; Johnson, E.; Maiti, A.K., *Appl. Spectrosc.*, submitted

[5.18] Hayden, B.E. in *Vibrational Spectroscopy of Molecules on Surfaces, Methods of Surface Characterization*, Yates, J.T.; Madey, T.E., Eds, Plenum Press, New York (1987) p267.

[5.19] Umemura, J.; Kamata, T.; Kawai, T.; Takenaka, T.; *J. Phys. Chem.*, 1990, *94*, 62-67.

[5.20] Kasha, M. in *Physical Processes in Radiation Biology*, Augenstein, L.; Mason, R.; Rosenberg, B., eds., Academic Press, New York (1964) p17-42.

[5.21] Nagamura, T.; Kamata, S.; *J. Photochem. Photobiol. A: Chem.*, **1990**, *55*, 187-196.

[5.22] Tanaka, J.; *Bull. Chem. Soc. Japan*, **1963**, *36*, 1237-1249.

[5.23] Weiss, D.; Kietzmann, R.; Mahrt, J.; Tufts, B.; Storck, W.; Willig, F.; *J. Phys. Chem.*, **1992**, *96*, 5320-5325.

[5.24] Mahrt., J.; Willig, F.; Storck, W.; Weiss, D.; Kietzmann, R.; Schwarzburg, K.; Tufts, B.; Trosken, B. *J. Phys. Chem.* **1994**, *98*, 1888.

Chapter 6: Molecular Orientation and Stacking of Perylenetetracarboxylic Diimide Derivatives in Langmuir-Blodgett Monolayers

Introduction

In the previous two chapters, the average molecular tilt of various PTCDs and PTCOs was determined through infrared spectroscopy. The next step in elucidating the structure of LB films of PTCDs involves determining intermolecular order. The degree of molecular overlap in a series of PTCD derivatives can determined by using Kuhn's extended dipole model *[6.1]* and spectral data in the visible region. The structures thus obtained were then compared with the x-ray structures of similar PTCDs reported in the literature.

The molecular structure *[6.2,3]* and crystal packing *[6.4,5]* of various symmetric PTCD derivatives have been determined via X-ray crystallography. A qualitative interpretation of colour *[6.4,5]* and fluorescence *[6.6]* based on molecular packing has been attempted for some derivatives. No information about intermolecular packing for PTCD's in LB films has been reported to date. Since the optical and electronic properties of PTCD's can depend upon intermolecular arrangement, it is important to study the structural characteristics of these materials incorporated into ultrathin films.

A brief overview of the previous spectroscopic characterizations of PTCD and PTCO LBs described in *Chapter 4 and 5* is presented here. In addition to the infrared determination of chromophore tilting, intermolecular interactions leading to excimer formation have also been observed for these materials *[6.7,8]*. It is proposed that stacking of PTCD's is the primary intermolecular organization in the six PTCD's deposited as LB films. The species studied were PPTCDM, PPTCDE, PPTCDPr, HPTCO, HPTCNH and HPTCDE.

Information regarding intermolecular organization can be extracted from intermolecular effects observed in the optical spectra of the PTCD's. All six PTCD's exhibit exciton splitting with an intense hypsochromic component which indicates H aggregate formation, possibly originating from some type of pin cushion arrangement of

the transition dipoles in the LB films [6.9]. Since the long chromophore axis, which is coincident with the transition dipole moment of the symmetric C=O imide stretching vibration of the PTCD systems, is not parallel to the plane of the film, a suitable arrangement of transition moments permitting H aggregation is facilitated. Since all of these films exhibit excimer emission, the chromophores must be arranged with parallel and overlapping ring systems in a manner analogous with the excimer forming α-perylene crystal [6.10]. The geometric constraints that exist in two dimensional system, such as LB films, for perylene materials simplifies the determination of intermolecular geometry. By applying the extended dipole model developed by Kuhn [6.1], the intermolecular geometry for PTCD LB systems can be determined.

Molecular Exciton Theory and Intermolecular Geometry

Application of molecular exciton theory to the observed visible absorption spectra is used to elucidate molecular organization. Michael Kasha *[6.11]* introduced the point-dipole approximation to describe the spectroscopic shifts and splittings observed for dye aggregates. The point-dipole model represents the transition dipoles associated with the optical transition as points. When two such point-dipoles are close together, they interact, electrostatically, and cause splitting of the energy levels of the involved transitions. This model was subsequently applied to monomolecular lamellar systems *[6.12]*. Detailed reviews of Kasha's molecular exciton theory are an excellent summary of his work *[6.13,14]*. *Figure 6.1* is a simple energy level diagram representing the observed splitting for a dimer system. Normally, one of the two states in *Figure 6.1* is allowed and the other is forbidden. In addition to the splitting, small van der Waals interactions can provide some stabilization energy, so the splitting is not symmetrical about the unsplit state.

The most interesting aspect of the point-dipole model is its ability to quickly but qualitatively predict band shifts and splits. The point-dipole can be represented as a vector (i.e. representing the direction and orientation of the transition dipole in question). In order to predict band shifts and splits, two vectors (in the case of a simple dimer) are arranged as the molecular system is arranged. Simple vector addition is then performed. *Figure 6.2* represents this concept. Here, the point dipoles are represented by arrows with one end representing one charge, the other end the opposite charge. If a favourable electrostatic arrangement exist (*Figures 6.2a,d*), like a head to tail arrangement, then the observed band is red shifted. A blue shifted situation arises from an unfavourable arrangement (*Figures 6.2b,c*). These are the extreme cases. Intermediary cases will result in band splitting. *Figure 6.2e* illustrates one of many such arrangements. The intensity of the observed transition can also be predicted via vector addition. The magnitude of the resulting vector represents the magnitude of the observed intensity. For example, *Figures 6.2b and d* have no resulting vector, hence the transition will be weak. These vector concepts are also applicable to aggregates in monolayers. When describing the spectra
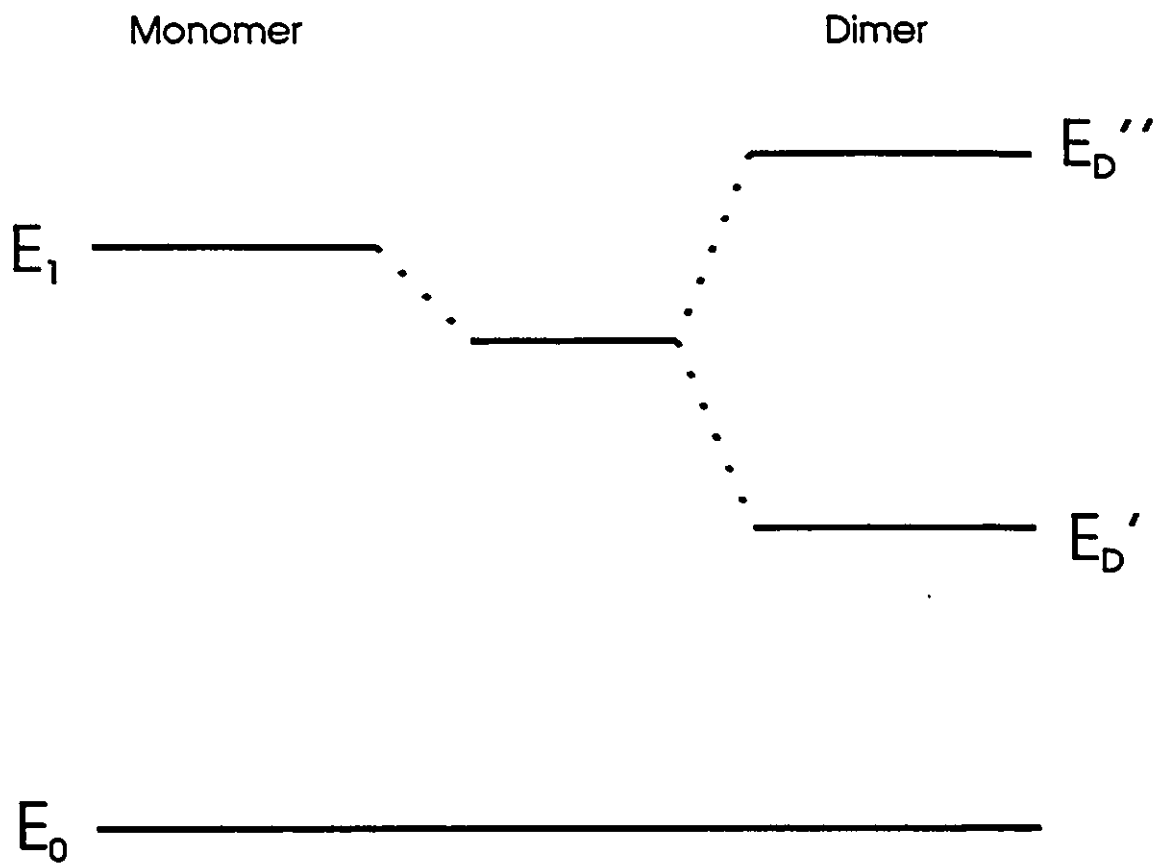
Figure 6.1: Simple energy level diagram illustrating the molecular exciton splitting for an isolated dimer.
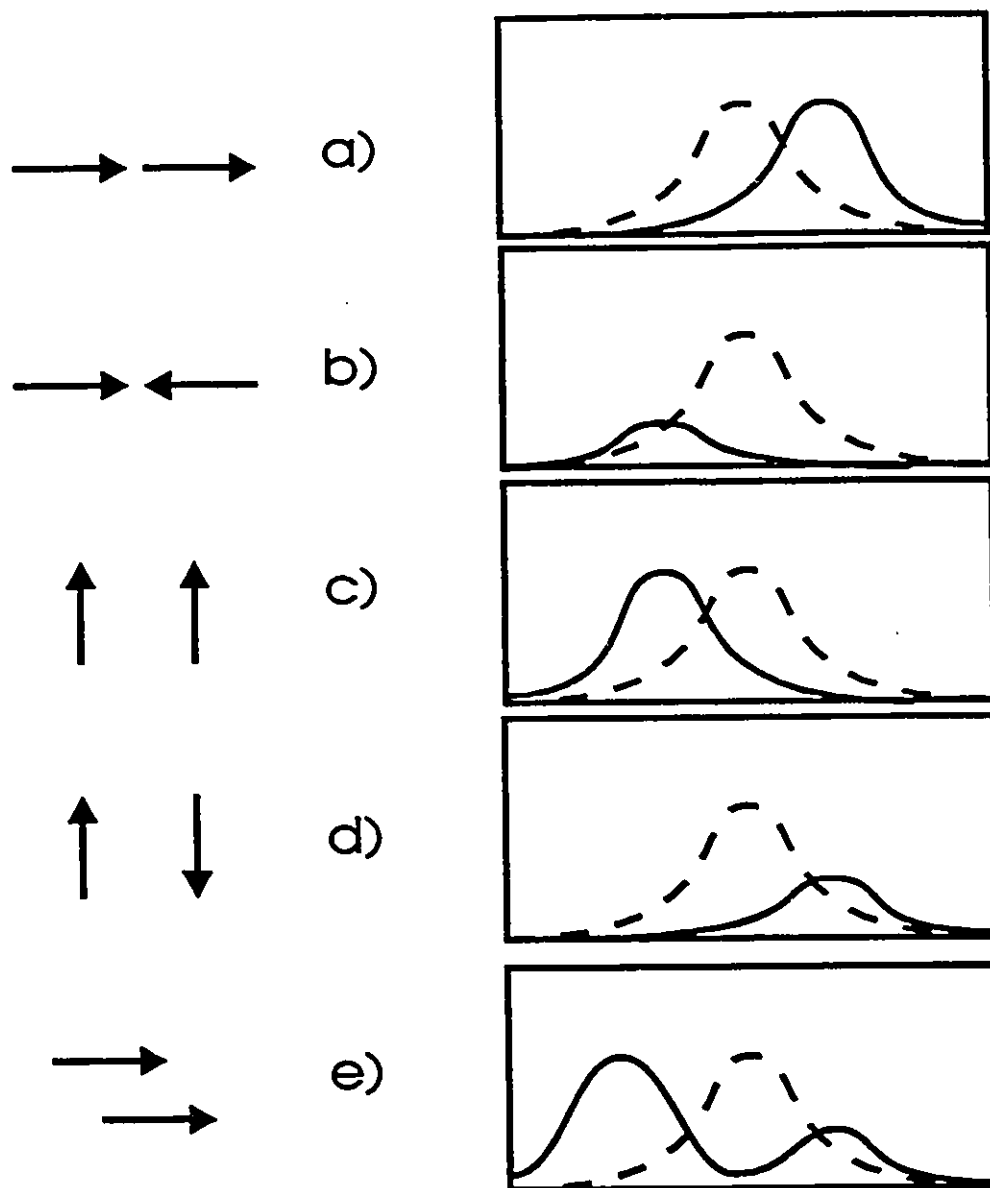
Figure 6.2:   The vector aspects of the point-dipole approximation are illustrated here. The absorption spectra are drawn so higher energy is on the left side of the spectrum. The dashed curve represents the spectrum of the unsplit transition.

of aggregates, the terms J aggregate and H aggregate are frequently used. An H-aggregate is an aggregate with a strong, broad blue shifted component in its absorption spectrum. A J aggregate has a strong, red shifted component and the fluorescence from this system nearly overlaps the shifted absorption band [6.15].

The point-dipole approximation is very good at predicting, qualitatively, shifts and splits in visible absorption spectra. However, it lacks quantitative accuracy. At molecular separation distances found in LB films, the extended dipole model offers superior accuracy [6.16], with similar basic concepts as the point-dipole approximation. Instead of using a simple vector to describe the transition dipole, a dipole is modeled by separating partial charges, $+\epsilon$ and $-\epsilon$, by a distance, l. In addition to head to head and tail to tail interactions, as in the point dipole model, the effect of cross terms is included in the extended dipole model. Reference 16 also contains a comparison of the accuracies of the point-dipole and the extended dipole models with computations using the one dimensional electron gas model for branched π-electron systems [6.17]. From Kuhn's work, the extended dipole model produced results very similar to those obtained from quantum chemical calculations. The point dipole model produced poor results. At large separation distances, around 50 A, the point-dipole and the extended dipole models give similar results.

The extended dipole model, as described by Kuhn [6.1,16,18], determines the transition energy for an intermolecular dimer as:

$$\Delta E' = \Delta E \pm 2J_{12} \tag{6.1}$$

where ΔE is the transition energy for the monomer, $\Delta E'$ is the transition energy of the dimer and J_{12} represents the interaction integral between two monomers. J_{12} can be determined from the extended dipole model:

$$J_{12} = \epsilon^2/D(1/a_1 + 1/a_2 - 1/a_3 - 1/a_4) \tag{6.2}$$

112

where the molecule is embedded in a dielectric medium, D (assumed to be 2.5 for hydrocarbons *[6.19]*). The geometric terms, a_1 through a_4, are illustrated in *Figure 6.3*.

The molecule is considered to be a dipole of length l and charges $+\epsilon$ and $-\epsilon$. In our case, the dipole length is assumed to be the length of the long chromophore axis. Crystal data for several symmetric PTCDs indicates the distance between the two imide nitrogens varies in the 11.34 to 11.43 Å range *[6.5]*. At this time, no crystal data exists for asymmetric PTCDs, so l has been taken as 11.4 Å. The transition dipole moment, M, is given by l and charge, ϵ:

$$M = \epsilon l \tag{6.3}$$

The tilt angle of the long molecular axis for each PTCD was determined in *Chapter 4* and are repeated in *Table 6.1*. Since excimer emission is observed for all six PTCDs, a parallel arrangement of the chromophore rings is a reasonable expectation. The separation between the ring systems is taken to be about 3.45 Å *[6.4]*. Based on these geometric conditions and that the molecules are placed in an essentially 2 dimensional arrangement, then the placement of one molecule with respect to the other can be determined if the interaction energy (i.e. J_{12}) is known. The structure must involve parallel, overlapping ring systems where the rings are separated by a fixed distance. Therefore, the intermolecular geometry calculations are reduced to determining the displacement of one molecule, in the substrate plane, parallel to its neighbouring molecule.

Thus far, the extended dipole model pertains to molecular dimers. It is important to note that in an LB assembly molecules do not exist as isolated dimers. One molecule will experience interactions from many neighbours. Therefore, it is necessary to sum the Columbic interactions of all translationally equivalent dipoles *[6.20]*. Then, Equation 6.1 becomes:

$$\Delta E' = \Delta E \pm 2\Sigma J_{12} \tag{6.4}$$

113
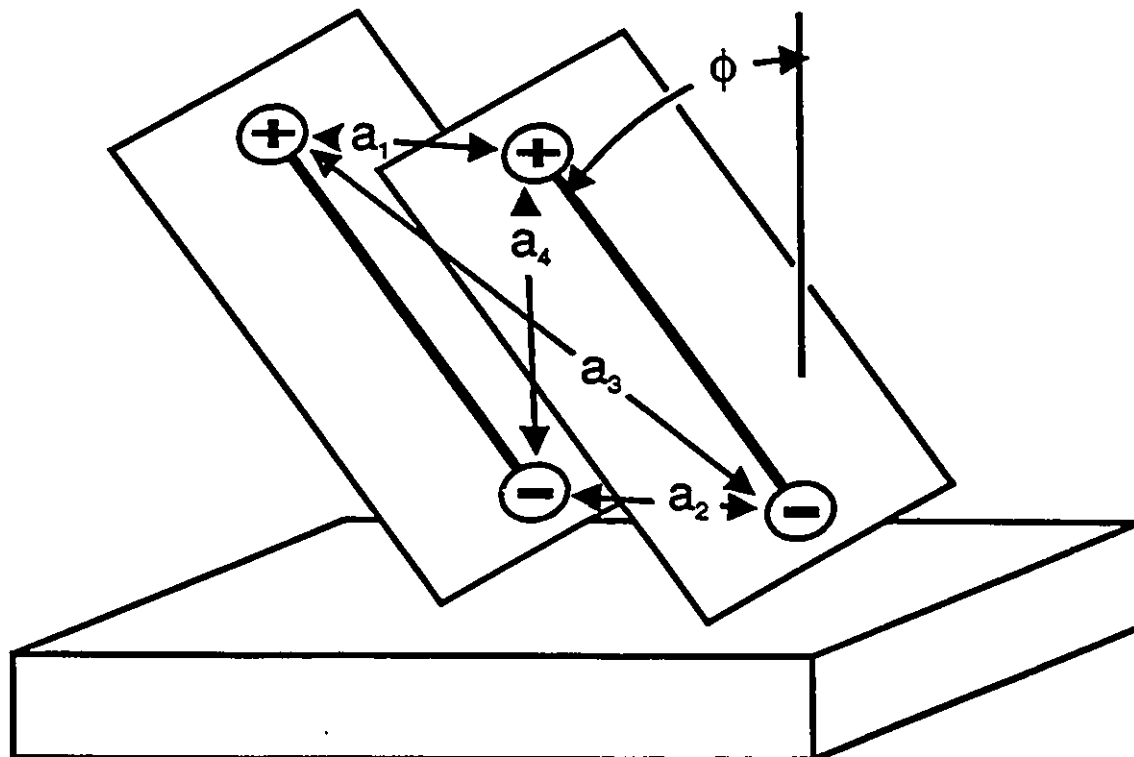
Figure 6.3: This figure illustrates the nature of the intermolecular geometry as discussed in the text. The angle ϕ represents the average angle between the long molecular axis and the normal to the substrate. The distances between $\epsilon+$ and $\epsilon-$ (a_1 through a_4) correspond to the geometric terms used in Equation 6.2. The length of each dipole is l. In this figure, the parent chromophores are represented by parallel rectangles. This is a required geometry due to the observed excimer emission. The assignment of + and - to the shown dipoles is arbitrary. An accurate assignment (i.e. + up or down with respect to the substrate) is not required in the calculations.

Table 6.1: PTCD information used to calculate molecular organization

Molecule	ϕ_{vl}	ϕ_{ul}	$\nu_{0\text{-}0}$	f	$2J_{12}$
	(degrees)	(degrees)	(cm^{-1})		(cm^{-1})
PPTCDM	40	75	19030	.39	1780
PPTCDE	58	78	19030	.44	1940
PPTCDPr	41	63	19030	.44	1550
HPTCO	36	64	19170	.16	1330
HPTCNH	56	65	19060	.17	1810
HPTCDE	60	80	19030	.49	1760

A value for J_{12} can obtained from the visible absorption spectra of the LBs deposited onto a transparent substrate. In order to deduce intermolecular geometry, the geometric portion of Equation 2 must be solved. Normally, this would involve determining four unknowns (a_1 through to a_4), thereby requiring a system of four equations. It is possible to reduce the dependence from four variables to one by applying the three constraints imposed by the system studied. These three constraints are:

(1) the known tilt of the transition dipole moment with respect to the substrate,

(2) parallel, overlapping ring systems dictated by observed excimer emission and

(3) the LB film restricts the molecules to a two dimensional plane.

Based upon these constraints, the geometric terms in equation 6.2, a_1 through to a_4, can be reduced to a single variable dependence. When a value for J_{12} is obtained, it will be possible to use this derived expression to deduce the intermolecular geometry of the PTCD chromophores.

Let the normal to the substrate plane be assigned the z axis and the substrate surface be defined as the x-y plane. Let v_1 and u_1 be vectors representing the long and short axes of molecule, $M1$, respectively. The angles that v_1 and u_1 make with the z axis are ϕ_{v1} and ϕ_{u1}, respectively. These are the tilt angles previously determined via FT-IR spectroscopy. Now, let $M1$ be placed on the surface such that v_1 lies in the y-z plane (refer to *Figure 6.4*). Then place u_1 so that the x and y components of u_1 (u_{1x} and u_{1y}) are less than zero (both molecular axes are drawn from the origin). The molecular plane, defined by u_1 and v_1, will intersect the x-y plane in a line defined as:

$$y = mx + b_1. \qquad (6.5)$$

Since this line contains the origin, $b_1 = 0$ and (5) becomes:

$$y = mx \qquad (6.6)$$

116
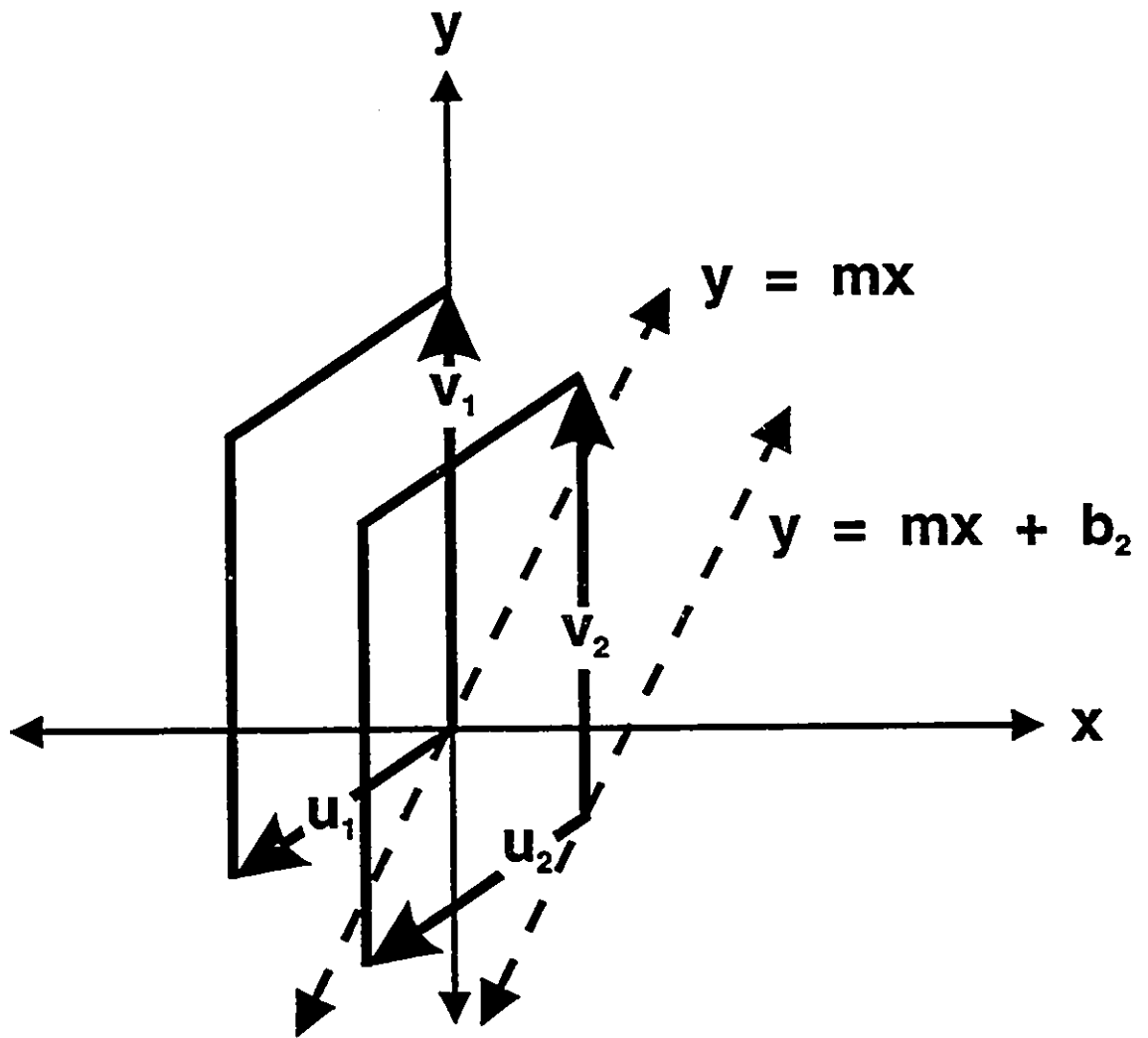
Figure 6.4: The geometric quantities used to define equations 6.5 through 6.8 are shown here.

where m is the slope of the line. The second molecule, *M2*, also forms a line of intersection that is parallel to (6.6) and has the form:

$$y = mx + b_2 \tag{6.7}$$

M2 is placed on the x-y plane so that $b_2 < b_1$ (i.e. $b_2 < 0$). By using the vectors $\mathbf{u_1}$ and $\mathbf{v_1}$, an expression for the slope, m, of these lines can be derived in terms of ϕ_{v1} and ϕ_{u1} and the form of this expression can be seen in the appropriate Math-Cad document in *Appendix II*. Now, the four quantities a_1 to a_4 can be expressed in terms of m and b_2:

$$a_1^2 = x^2 + (mx+b_2)^2 \tag{6.8a}$$

$$a_2^2 = x^2 + (mx+b_2)^2 \tag{6.8b}$$

$$a_3^2 = (v_{2x} + x)^2 + (v_{2y} + mx + b)^2 + v_{1z}^2 \tag{6.8c}$$

$$a_4^2 = (v_{1x} - x)^2 + (v_{1y} - mx - b)^2 + v_{:z}^2 \tag{6.8d}$$

When J_{12} is determined experimentally, it is now possible to determine the placement of one molecule with respect to the other by using equations 6.4 and 6.8a-d and solving for x.

Experimental Details

The six PTCD samples were kindly provided by Professor Nagao from the University of Tokyo. A description of LB monolayer preparation of these perylene derivatives can be found in *Chapter 4*. Preparation conditions are identical. Y-deposition was attempted, but the transfer ratio (TR) in the downward dipping direction was nearly zero, and the TR in the upward direction was slightly greater than unity. Therefore, the films underwent Z deposition. Materials were transferred to clean, glass slides. Multilayers of most of the materials could be prepared, except for HPTCDE. The first layer lifted off the substrate when the slide was dipped downward the second time. Single LB layers were investigated in this work in order to simplify the calculations by eliminating contributions from adjacent layers. The quality of the LB films was inspected by optical microscopy and, on this scale, no significant defects were visible. All of the films appeared smooth and homogeneous. The visible absorption spectra were recorded on a Response spectrophotometer interfaced to an IBM microcomputer. Math Cad for Windows was used to deduce intermolecular geometry.

Molecular modelling of the chromophore was carried out using Hyper Chem on a Silicon Graphics Workstation. The structure was minimized using the MM2 program and the orbital symmetry of the HOMO and LUMO of the chromophore was determined through Extended Hückel. *Figure 6.8* represents the general shape of the HOMO of the PTCD chromophore.

Results

Visible Absorption Spectra

Figure 6.5 shows the visible absorption spectra of five of the PTCD's studied for this chapter. Superimposed on the absorption spectra of the LB films is the solution spectra of the same dye. The broad and intense blue shifted band observed in all six films indicates H aggregate formation. The extended dipole model permits a splitting of the observed absorption bands, with one component significantly more intense than the other due to geometric considerations. In this work, a weaker, red shifted component is visible. The value for $2J_{12}$ was measured from the visible absorption spectra of the LB films. The value of $2J_{12}$ is one half the energy difference between the red shifted and blue shifted maxima. The mid point between these two maxima does not correspond to the v_{0-0} transition seen in the solution spectra. This apparent discrepancy arises from small energy changes of the unsplit excited state due to Van der Waals interactions.

All of the observed spectra are similar except for HPTCNH. The observed absorption spectrum of the LB shows an intense red shifted component in addition to the blue shifted component seen in the other LB's. HPTCNH forms hydrogen bonded dimers in solutions as dilute as 10^{-6} M. The effect of concentration upon this red shifted component is shown in *Figure 6.6*. The absorbance of the dimer band drops much more quickly with respect to the monomer bands. These hydrogen bonded dimers, formed between the imide hydrogen of one molecule and a carbonyl of a second molecule, as indicated by shifting in the C=O stretching bands in the infrared (refer to *Chapter 4* for spectra), are responsible for the red shifted absorption band. The hydrogen bonding is also present in the LBs of HPTCNH since the 1679 cm^{-1} band persists in the transmission IR and the RAIR spectra of the LB. Two bands can be curve fitted to this red shifted component of HPTCNH, one of which corresponds to the weak red shifted component seen in the other PTCD's.In the LB layer, both red shifted and blue shifted bands are present, indicating a mixture of aggregate and hydrogen bonded dimer forms. In our analysis of HPTCNH, only data from the blue shifted band was used.
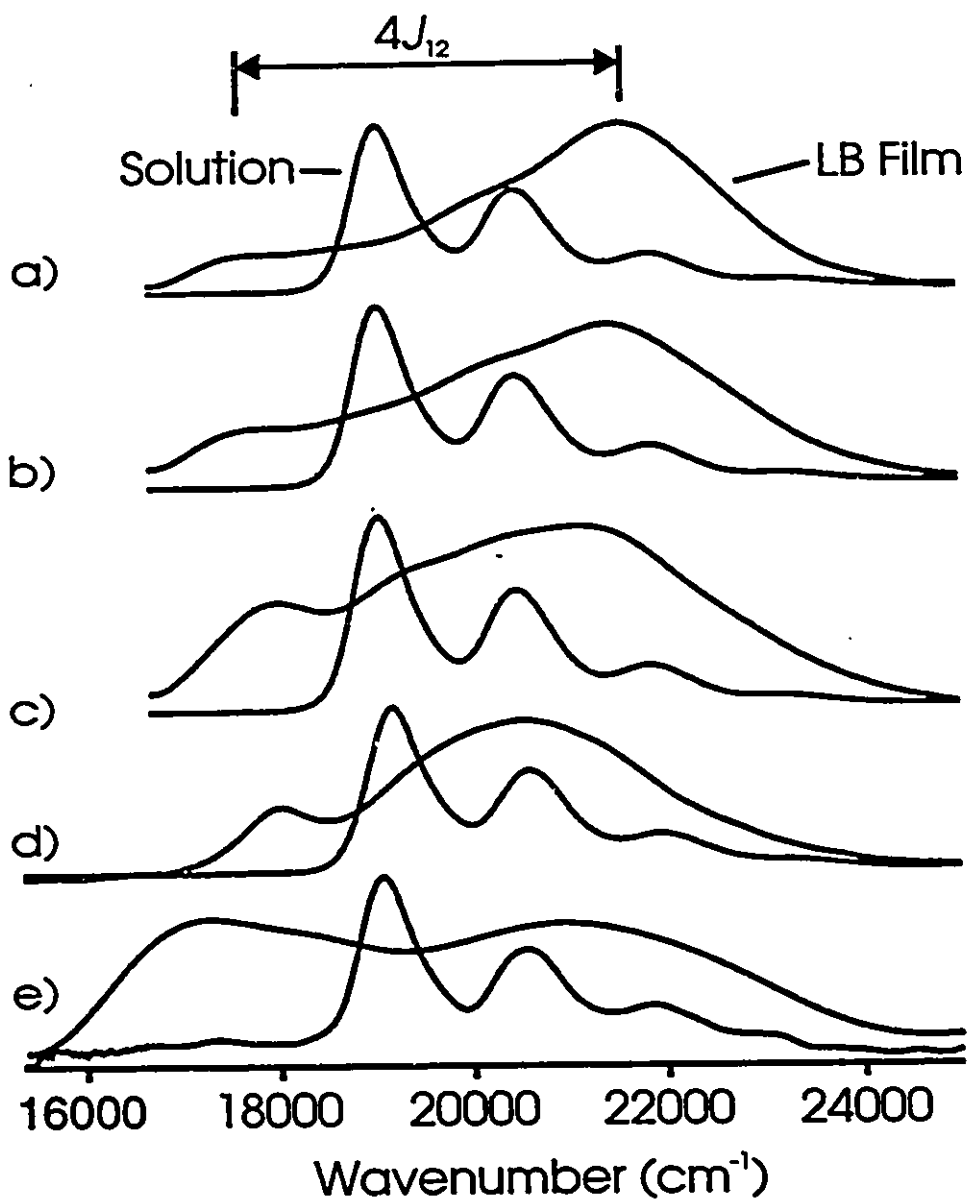
Figure 6.5: The absorption spectra of the PTCD's studied are displayed: PPTCDM (a), PPTCDE (b), PPTCDPr (c), HPTCO (d), HPTCNH (e). The solution spectra are superimposed upon the LB spectra and the shift used for $2J_{12}$ is indicated.
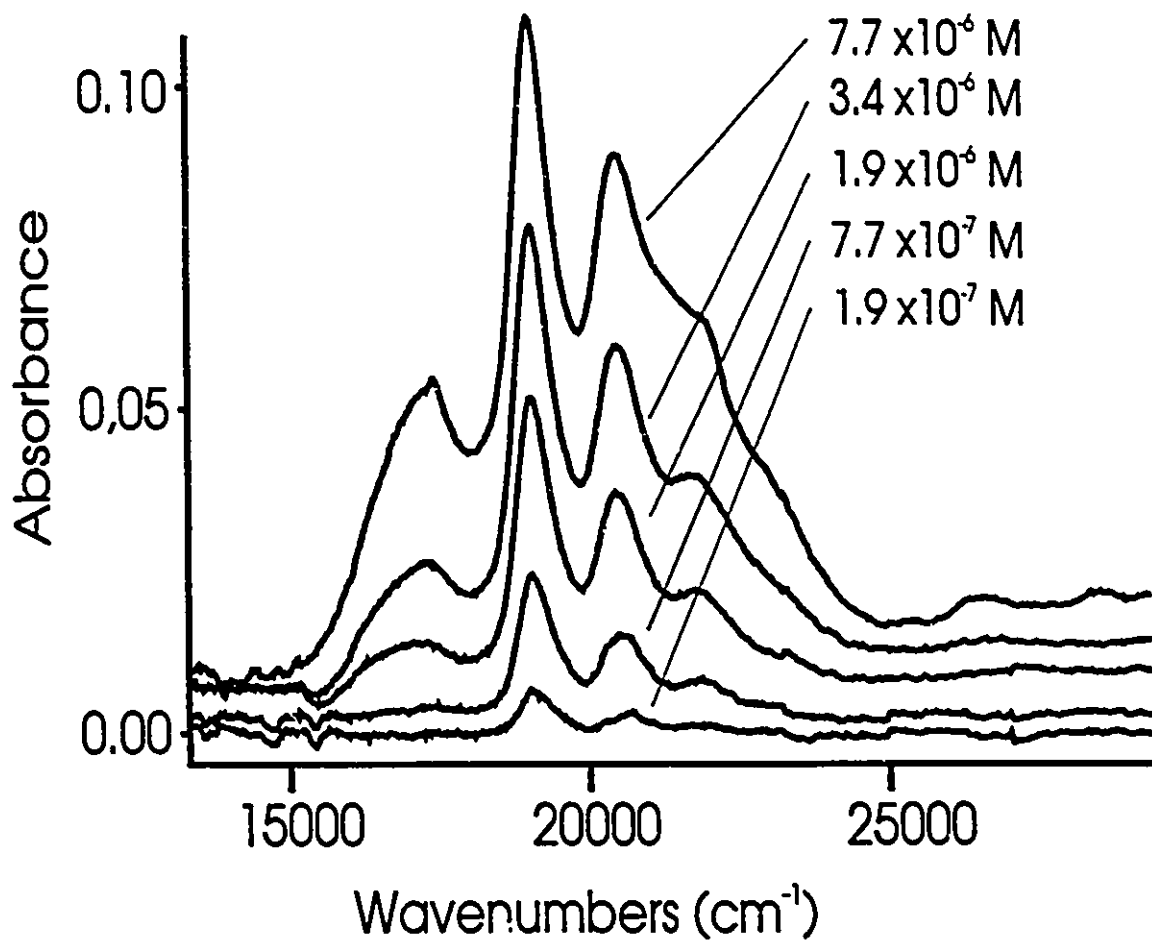
Figure 6.6:   The absorption spectra of HPTCNH at various concentrations.

The general structure of the LB film has been elucidated through infrared spectroscopy [6.21]. The LB film shows no dichroism when probed in the transmission geometry. Therefore, on a macroscopic scale, a uniaxial molecular orientation exists. Reflection absorption infrared spectra have revealed a mean molecular tilt in the LB layers. The tilt angle of the long and short axes of the chromophore have been determined and these values are listed in *Table 6.1*. The long molecular axis is coincident with the electronic transition moment of the chromophore, hence the orientation of this dynamic dipole is also known.

It is important to note that a mean molecular tilt exists in spite of the lack of dichroism in the molecular plane. Therefore, any intermolecular organization is restricted to patches of aggregation and each of these patches possesses a different axial orientation.

In order to utilize Equation 6.4, it is necessary to determine the magnitude, M, of the transition dipole moment for the isolated chromophore. M can be calculated from the chromophore's oscillator strength, f.

$$f = 4.33 \times 10^{-9} \int \epsilon_{\nu}\, d\nu \tag{6.9}$$

where ϵ_{ν} is the extinction coefficient at frequency ν. From this, M can be calculated:

$$M = f/(4.704 \times 1029\ \nu 0\text{-}0) \tag{6.10}$$

where $\nu_{0\text{-}0}$ is the 0-0 transition energy (in cm^{-1}). *Table 6.1* summarizes the data used to determine the molecular organization.

By using this data and combining Equation 6.4 with 6.8a-d, a value for x is found. Equation 6.7 will give the corresponding y value. These x,y values give the translation of one molecule with respect to its neighbour. Equation 6.4 involves the summation of all columbic interactions experienced by the molecule in question. In our case, the columbic interactions of ten neighbours in a stack on either side of a PTCD were included in the calculations. *Table 6.2* lists the x,y displacement of molecule 2 with respect to molecule 1. Simply changing the signs of these values would give the position

Table 6.2: Displacement of one molecule to its neighbour with respect to the coordinate system used to describe the monolayer on the substrate. X and Y values are those that were solved from Eq. 6.4 and 6.8a-d. Values are given to the nearest 0.5 Å.

Molecule	X Translation	Y Translation
	(Å)	(Å)
PPTCDM	2.5	-3.5
PPTCDE	5.0	-4.5
PPTCDPr	4.0	-1.5
HPTCO	3.0	-2.0
HPTCNH	4.5	-3.0
HPTCDE	5.5	-4.5

of the neighbouring molecule on the other side of molecule 1.

Another useful way to display the intermolecular geometry involves the shift of one molecule in the stack with respect to its neighbour. This is illustrated in *Figure 6.7*. Molecule 2 is laterally displaced compared to molecule 1. The x and y shifts (with respect to the plane defined by the short and long molecular axes, respectively) is given in *Table 6.3*. The % overlap of the chromophores is also given.
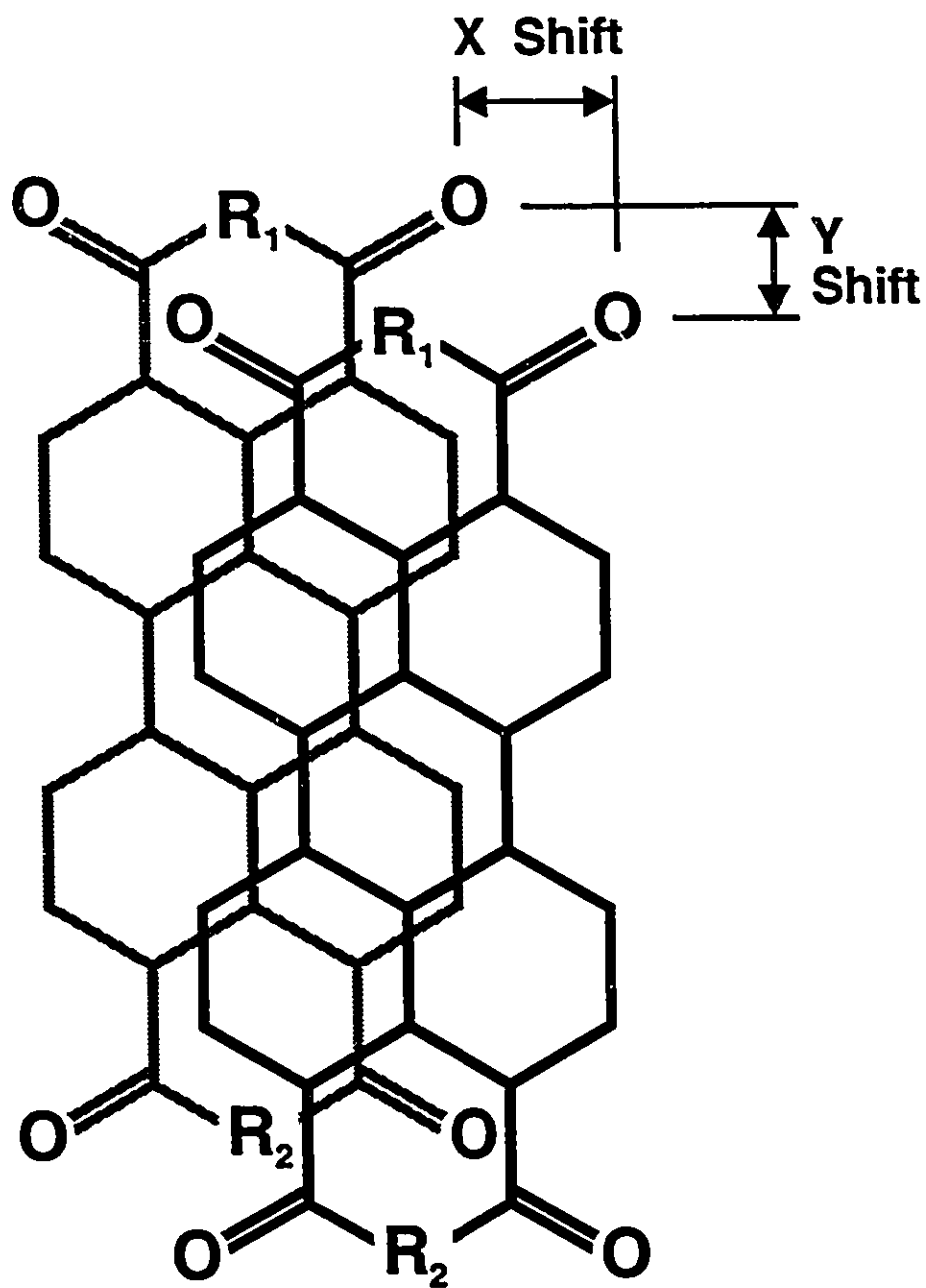
Figure 6.7.   This figure shows the lateral shift of one PTCD with respect to its neighbour. Values for the x and y shifts are given in Table 3.

Table 6.3: Shift of one molecular plane to that of the neighbouring plane. X and Y shifts are given with respect to the molecular frame of reference as shown in Figure 6.5. Values are given to the nearest 0.5 Å.

Molecule	X Shift	Y Shift	% Overlap
	(Å)	(Å)	
PPTCDM	1.5	-2.0	60
PPTCDE	4.0	-3.5	10
PPTCDPr	2.0	-1.0	55
HPTCO	1.0	-1.0	70
HPTCNH	3.0	-2.0	33
HPTCDE	4.5	-4.0	5.0

Discussion

The displacement of one molecule with respect to its neighbour can be expressed as % overlap. In this case, the % overlap refers to the ratio of the area overlapped on one chromophore by its neighbour to the overall area of the chromophore. The chromophore area is again approximated as a rectangle 11.4 Å by 4.8 Å *[6.5]*. The length is taken as the imide nitrogen to imide nitrogen distance and the width as the distance between opposite carbons across the perylene moiety.

The % overlap determined here compares favourably well with the molecular overlap observed from X-ray data. For a series of symmetric PTCD's, Graser and Hadicke *[6.5]* report % overlap values ranging from 9.2 to 55.6 per cent. Most of our PTCD's fall into this range. Two molecules, PPTCDE and HPTCDE, yielded exceptionally small molecular overlaps. Even though these geometric overlaps are small, overlap between the conjugated π systems may still be large. Extended Hückle calculations for the HOMO were performed in order to gain some insight into the shape and spatial distribution of this orbital. The crystal structure of EPTCDE indicates the molecules are arranged in twisted stacks *[6.3,5]*. As discussed in *Chapter 3*, the molecular arrangement of HPTCDE in mixed LBs differs from that of an α-perylene type of structure. Since both ethyl-containing PTCDs yielded such small overlaps, it is possible that the long axes of the molecules are not parallel to each other. This would cause the calculations used here to give spurious results.

The Extended Hückel calculations revealed regions of one orbital phase imbedded in a sea of opposite phase and were arranged in a hexagonal pattern. *Figure 6.8* is a cartoon of the HOMO that illustrates the general orbital phasing. Extended Hückel was performed for a variety of molecules. The relative orbital phasing is virtually identical between the diimide and the imide/anhydride. Also, substitution on the imide nitrogens did not alter the relative orbital phasing.

After a pictorial representation of the HOMO was deduced, the molecules were overlapped as per the values in *Table 3* and these results are shown in *Figure 6.9*. The phase of the overlapping HOMOs was then examined and two patterns emerged. For
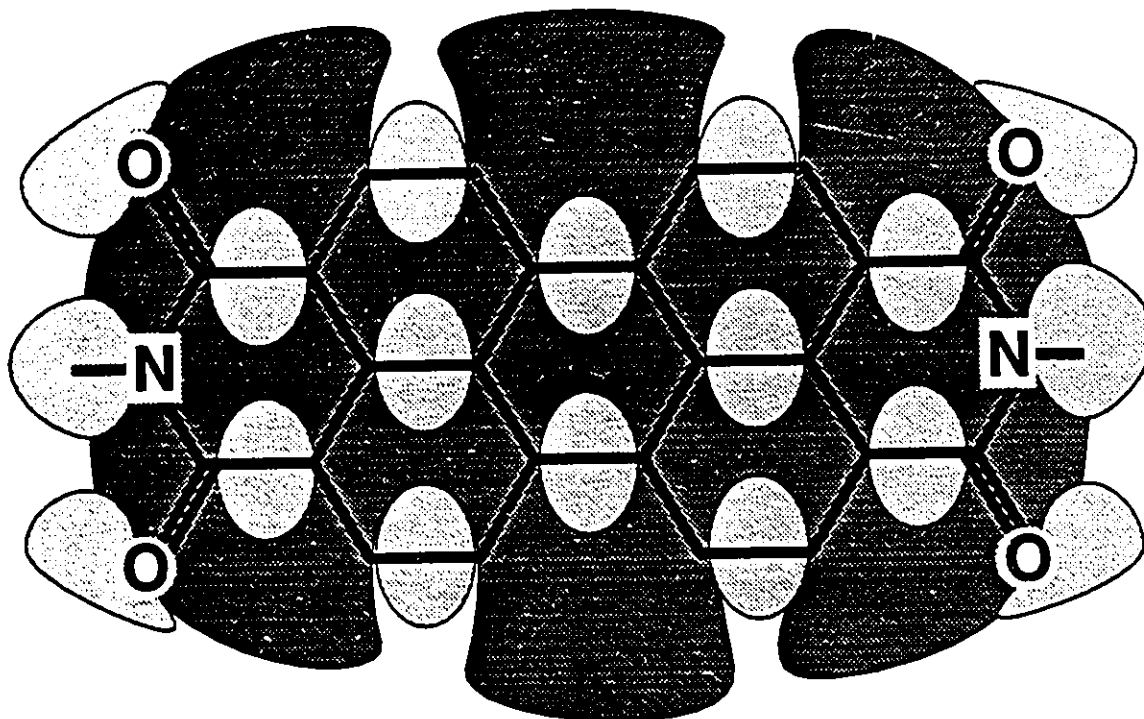
Figure 6.8. The HOMO of the PTCD chromophore is shown here. Regions of different shading indicate regions of opposite orbital symmetry.

PPTCDM

HPTCO
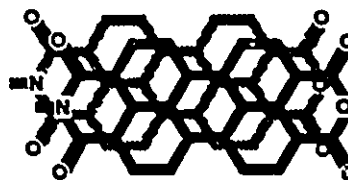
PPTCDE
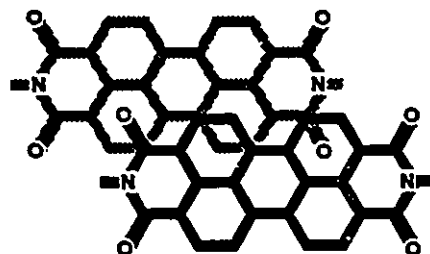
HPTCNH
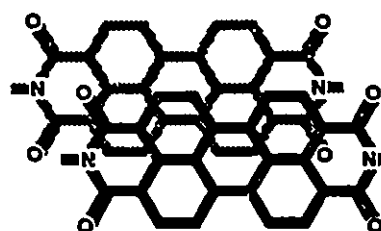
PPTCDPr
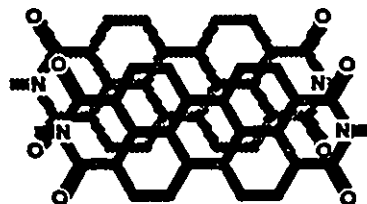
HPTCDE
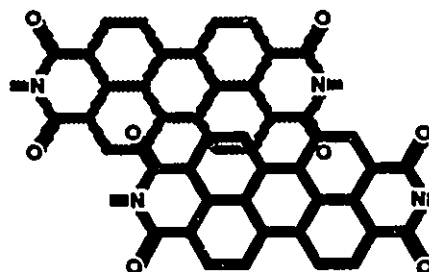
Figure 6.9. Overlap between two adjacent PTCD's. PPTCDM (a), PPTCDE (b), PPTCDPr (c), HPTCO (d), HPTCNH (e), HPTCDE (f) are shown here.

130

PTCDM, an almost direct overlap of regions of equivalent phase occurred. This implies a highly stable arrangement of chromophores. For the other derivatives, a diagonal pattern of phasing appeared. The embedded phase regions of one molecule aligned, in a alternating diagonal pattern, with the embedded phase regions of its neighbour. This gives antibonding character to the system. However, the other symmetry region extends beyond the embedded symmetry and forms the periphery of the chromophore system. The net effect is a more favourable than non-favourable molecular overlap. Moreover, the fact that the HOMO extends well past the carbon skeleton of the PTCD's shows that there is still significant overlap for the two ethyl diimides. The Extended Hückle results were also applied to the structures obtained from X-ray diffraction. The patterns of HOMO overlap are virtually identical to those obtained from our experiments.

The greatest source of error in the calculations using the Kuhn's extended dipole model involves the summation of Coulumbic interactions (Equation 4). Only the interactions between transition dipole moments in a single stack were included in the computations. Interactions from dipoles in adjacent stacks were not included for two reasons. First of all, the spacing between the stacks is unknown. Secondly, displacement of one stack along its length to another stack is also unknown. However, in the LB film, it is conceivable that there may be significant deviation in the lengthwise displacement of one stack to another. This would lead to greater broadening in the observed absorption spectra rather than to a change in the observed band shifts.

Imperfections in the film can also have a significant effect on the immediate electrostatic environment of the PTCD's. However, the area probed by the spectrophotometer was several square centimetres. Hence, imperfections will not have a measurable effect on the observed spectra.

Since there is a strong correlation between the stacking geometry determined in this paper and the stacking observed from X-ray diffraction data, the suggested structures are reasonable. The Hückel calculations for the HOMO provide additional support for favourable intermolecular interactions in the stacks.

Since the only significant difference between the PTCDs studied involves the alkyl side groups, they must play a significant role in the packing of the materials. However,

the geometry of these chains could not be accurately determined since these molecules are asymmetric. Side chain orientation could not be obtained from FT-IR measurements since the two side chains may have different orientations and their contributions to the observable CH stretching modes could not be separated from each other.

A similar study of stacking of the PTCOs is described in *Chapter 5*. Unfortunately, these materials did not exhibit pure excimer formation, so a plane parallel arrangement could not be assumed. The calculations were attempted for these systems, but the results were meaningless.

Chapter Summary

Langmuir-Blodgett films of perylene tetracarboxylic diimides were used as model systems to study intermolecular packing. The molecular organization in two dimensional systems was interpreted using Kuhn's extended dipole model. Observed exciton splitting and molecular orientation in the LB films were used to deduce overlapping and intermolecular structure. Present results compare favourably with reported X-ray data of similar compounds.

References - Chapter 6

[6.1] Czikklely, V.; Forsterling, H.D.; Kuhn, H., *Chem. Phys. Let.*, **1970**, *6*, 11.

[6.2] Hadicke, E.; Graser, F., *Acta Cryst.*, **1986**, *C42*, 189.

[6.3] Hadicke, E.; Graser, F., *Acta Cryst.*, **1986**, *C42*, 195.

[6.4] Graser, F.; Hadicke, E., *Liebigs Ann. Chem.*, **1980**, 1994.

[6.5] Graser, F.; Hadicke, E., *Liebigs Ann. Chem.*, **1984**, 483.

[6.6] Langhals, H.; Demmig, S.; Potrawa, T., *J. Prakt. Chem.*, **1991** *333*, 733.

[6.7] Aroca, R.; Guhathakurta-Ghosh, U.; Loutfy, R.O.; Nagao, Y., *Spectrochim. Acta*, **1990**, *46A*, 717.

[6.8] Johnson, E.; Aroca, R.; Pahapill, Y., *J. Mol. Struct.*, **1993**, *293*, 331.

[6.9] Hochstrasser, R.M.; Kasha, M., *Photochem. Photobiol.*, **1964**, *3*, 317.

[6.10] Tanaka, J.; *Bull. Chem. Soc. Japan*, **1963**, *36*, 1237.

[6.11] Kasha, M., *Radiation Research*, **1963**, *20*, 55.

[6.12] Hochstrasser, R.M.; Kasha, M., *Photochem. Photobiol.*, **1964**, *3*, 317.

[6.13] Kasha. M. in *Physical Processes in Radiation Biology*, Augenstein, L.; Mason, R.; Rosenberg, B., eds, Academic Press, N.Y. (1964) p17-42.

[6.14] Kasha, M. in *NATO Advanced Study Series*, Bartolo, B.D.D., ed., Plenum Press, N.Y. (1976) p337-363.

[6.15] Hertz, A., *Photogr. Sci. Eng.*, **1974**, *18*, 323.

[6.16] Czikklely, V.; Forsterling, H.D.; Kuhn, H., *Chem. Phys. Let.*, **1970**, *6*, 207.

[6.17] Forsterling, H.D.; Huber, W.; Kuhn, H.; Martin, H.H.; Schweig, A.; Seeiing, F.F.; Stratmann, W. in *Optische Anregung organischer System*, Verlag Chemie, Weinheim (1966) p55.

[6.18] Czikkely, V.; Dreizler, G.; Forsterlng, H.D.; Kuhn, H.; Sondermann, J., Z. *Naturforsch. Teil A.*, **1969**, *24*, 1821.

[6.19] Nagamura, T.; Kamata, S., *J. Photochem. Photobiol. A: Chem.*, **1990**, *55*, 187.

[6.20] Ando, E.; Miyazaki, J.; Morimoto, K.; Nakahara, H.; Fukuda, K., *Thin Solid Films*, **1985**, *133*, 21.

[6.21] Aroca, R.; Johnson, E.; Maiti, A.K. "Molecular orientation in Langmuir-Blodgett Monolayers of Perylenetetracarboxylic Diimide Derivatives: Part 1," *Appl. Spectrosc.*, submitted.

Chapter 7: Energy Transfer Between Langmuir-Blodgett Monolayers of Organic Dyes

Introduction

In the preceding chapters, the spectroscopic and structural properties of several PTCD and PTCO species have been studied. As mentioned in *Chapter 1*, these materials have a wide range of potential applications. This includes a role in an energy transfer system. In order to demonstrate this application, both a PTCO and a PTCD are incorporated into energy transfer systems and the properties of these systems are explored.

Langmuir-Blodgett monolayers of strongly absorbing and fluorescent dyes represent an important type of model system where the increase and direction of photon absorption can be studied. The non-trivial transfer of electronic excitation energy between well separated molecules occurs before the emission takes place. Förster's dipole theory of energy transfer predicts that when the corresponding optical transitions in both molecules are allowed, the probability of ET decreases with the sixth power of the distance *[7.1]*. A parallel can be drawn between the trivial and non-trivial ET between molecules and the transfer of power in the far zone and the near zone fields of oscillating dipoles in classical electrodynamics *[7.2]*. Hans Kuhn *[7.3]* applied the dipole-dipole model to a number of practical systems with restricted geometries. In particular, he derived the basic equations for the luminescence quenching of a dipole emitter by a monolayer of oriented dipoles. The latter approach has been used by several groups to explain the results for the distance dependence of non-trivial ET between well separated monomolecular layers *[7.4-6]*. Recently, the dynamics of the Förster-type energy transfer in organic systems of restricted geometries has been reviewed by Yamazaki et al.*[7.7]*. There exist, however, a very limited amount of data for energy transfer between neat layers of strongly absorbing dye molecules. Only very recently, Penner reported steady state energy transfer for donor and acceptor layers of concentrated J-aggregated cyanine dyes *[7.5]*. In this chapter, the excimer emissions of two perylene derivatives (HPTCDE and HPTCO) that were in resonance with the red absorption of lutetium bis-

135

phthalocyanine (LuPc$_2$), structure given in *Figure 7.1*, were used to study the distance dependence of the energy transfer between LB layers. The separation between the two dye layers was controlled by interposing fatty acid layers. A critical discussion of the results and Kuhn's model is presented. The possibility of a competitive quenching from electron transfer processes has also been examined experimentally, and the perylene-phthalocyanine interactions were followed for a two perylene derivatives.
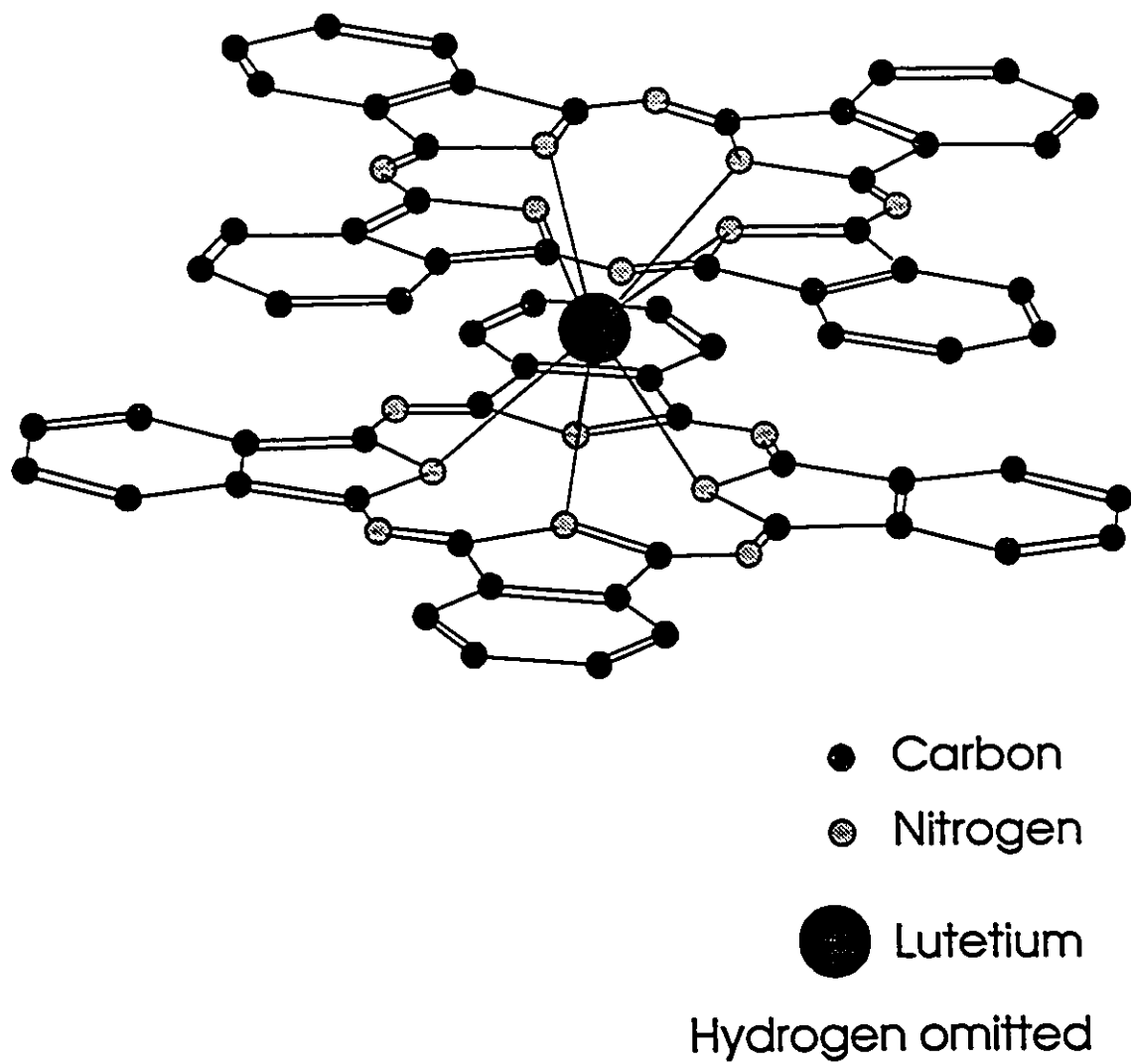
Figure 7.1: The structure of LuPc$_2$. Hydrogen atoms are omitted for clarity.

Experimental Details

The spectroscopic characterization of $LuPc_2$ have been reported [7,8] in the literature and has not been repeated in this thesis. LB monolayers of HPCTDE, HPTCO and $LuPc_2$ were prepared at 25°C, and transferred to Corning 7059 glass slides, and glass slides coated with LB monolayers of arachidic acid. The arachidic acid was used as a spacing layer between the perylene (donor) layer and the diphthalocyanine (acceptor) layer. LB preparation was identical to that given in Chapter 2. Monolayers of arachidic acid were transferred by Z or Y type deposition at constant pressure, to Corning 7059 glass slides. Monolayers of $LuPc_2$ were transferred at 10 mN/m. In all cases, the transfer ratio was near unity.

Care was taken in the deposition order of the three materials used. $LuPc_2$ was the first layer deposited. On top of that, the arachidic acid spacers were deposited and, lastly, the perylene layer was transferred. The area of the slide coated was different for each layer as can be seen in *Figure 7.2* so a step-like architecture is obtained. In this figure, the perylene layer covers the greatest area of the slide. The portion where the perylene is in direct contact with the substrate acts as a reference layer (I_o, see below). The next portion has the perylene and the $LuPc_2$ in direct contact and the two dyes are separated by an arachidic acid spacer layer in the third portion of the sample slide.

Spectra Physics model 2020 Kr^+ and Ar^+ ion lasers were used. Typical spectral bandpass and laser power were 5 cm^{-1} and 200 mW respectively. Raman shifts and steady state fluorescence were measured with a Spex-1403 double monochromator and the Ramanor U-100 with microscope attachment. Electronic absorption spectra were recorded on a Response UV-VIS spectrophotometer interface with an IBM PC computer.
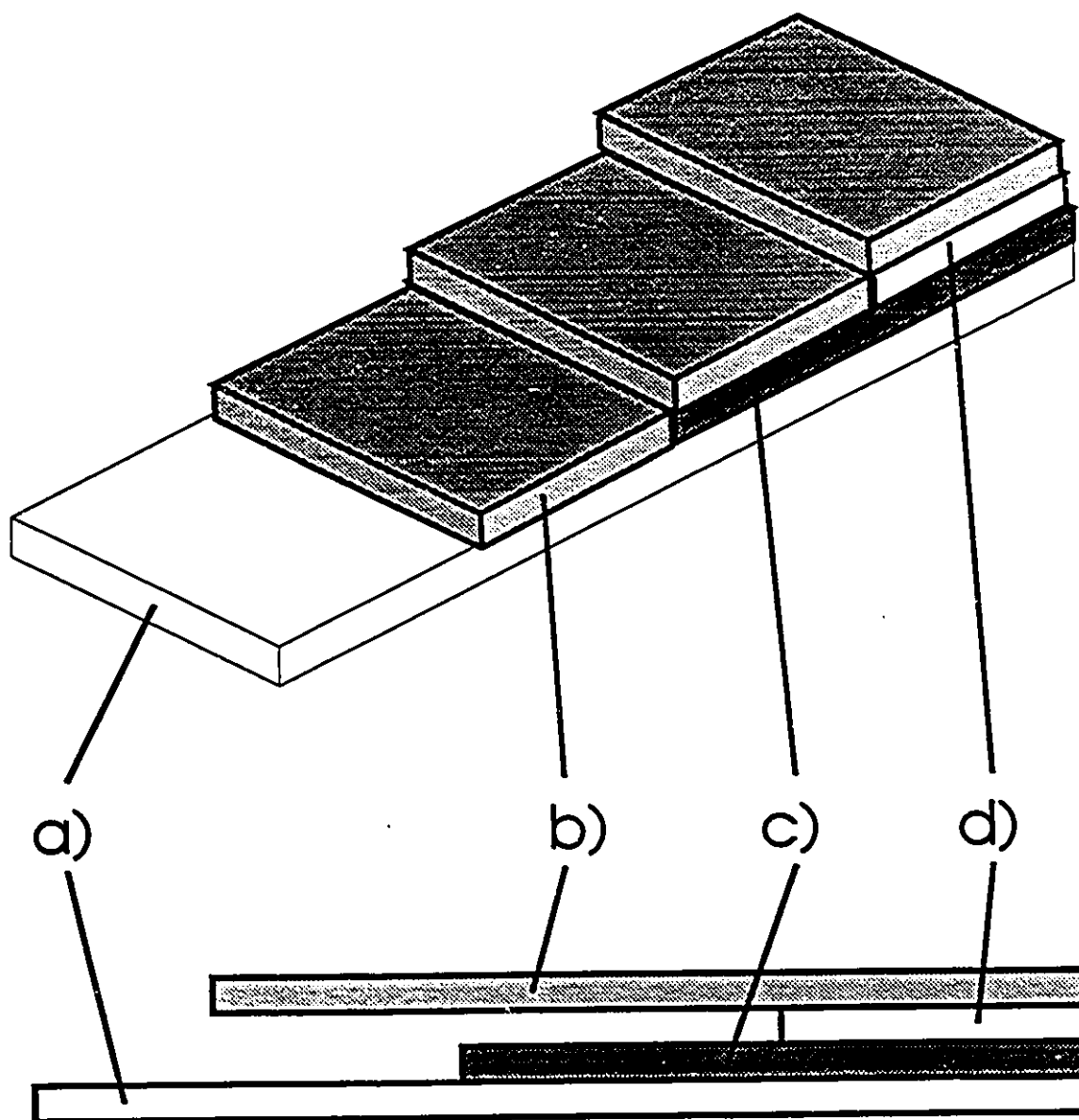
Figure 7.2: The architecture of the energy transfer system prepared by the LB technique. The components of the system are the glass substrate a), the perylene donor layer b), the $LuPc_2$ acceptor layer c), and an arachidic acid spacer layer d).

Results and Discussion

Electronic Spectra and Excimer Emission

The electronic absorption spectrum of $LuPc_2$ in a 1:1 molar ratio of HPTCDE and $LuPc_2$ in $CHCl_3$, and the fluorescence spectrum of HPTCDE in the same solution are shown in *Figure 7.3*. A dip in the 650-680 nm region of the emission spectrum of HPTCDE is due to trivial and non-trivial energy transfer between the two dye molecules. It can be seen that the molecular monomer emission of perylene and perylene derivatives does not have a strong fluorescence band in resonance with the absorption Q (666 nm) band of the $LuPc_2$. However, perylene and perylene derivatives show the excimer band about 5000 cm^{-1} to the red of the lowest absorption band [7.9,10]. The strong excimer emission in the 650 nm region is observed in crystal, thin solid evaporated films, pellets and LB layers of perylene derivatives [7.11].

It is the strong excimer emission of perylene derivatives in LB monolayers, which is in resonance with the Q-absorption band of the $LuPc_2$ molecule, that was used to monitor the energy transfer between the two LB monolayers. Typical results of steady state measurements of the excimer fluorescence of an HPTCDE LB monolayer of the neat material and separated from one LB of $LuPc_2$ by arachidic acid monolayers (represented by AA) are illustrated in *Figure 7.4*. The emitter monolayer was facing the collection optics to avoid the contribution of trivial emission-absorption transfer in the intensity measurements.
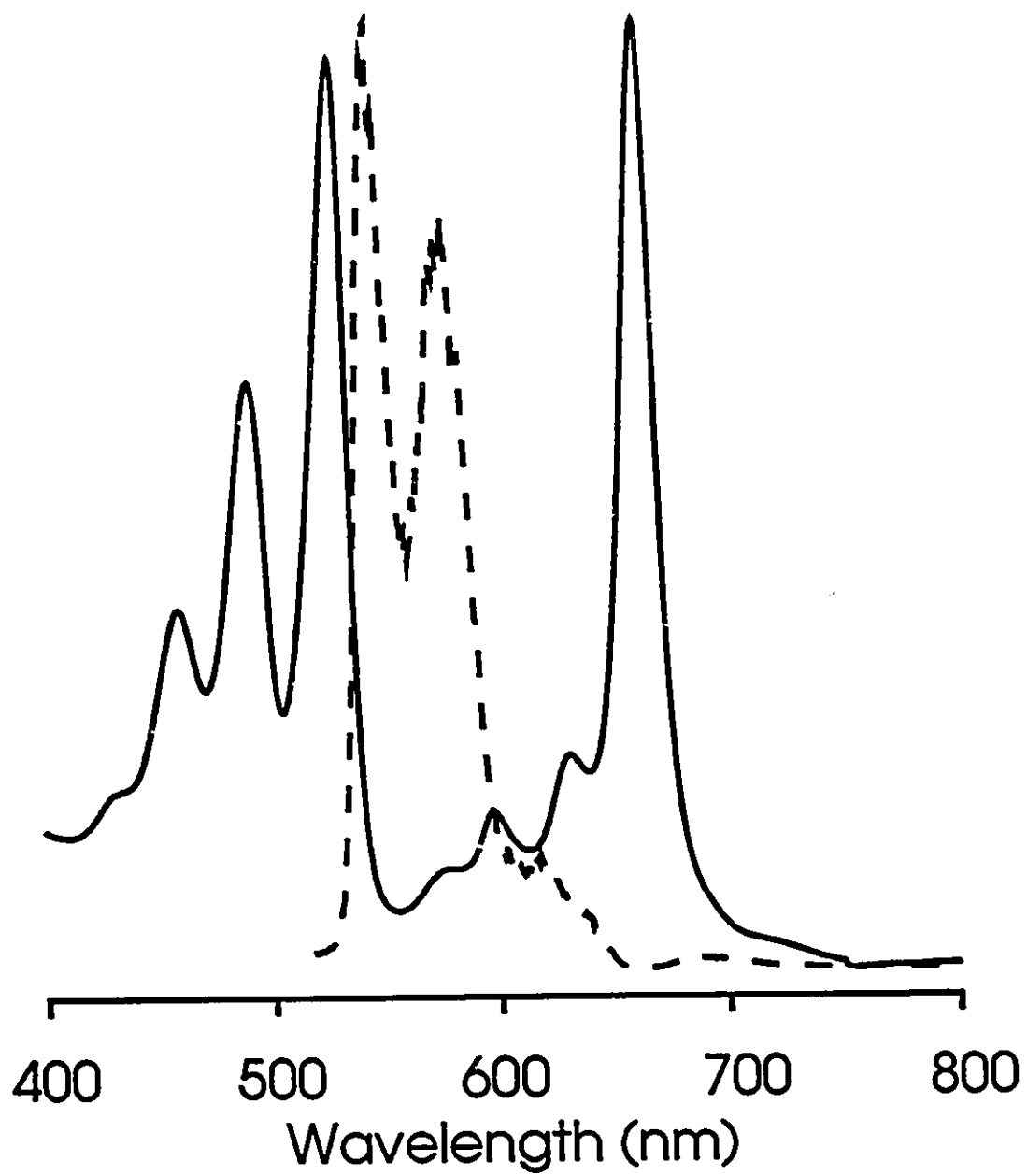
Figure 7.3:   Absorption spectrum (solid line) and fluorescence spectrum (dashed line)
of LuPc₂ and HPTCDE in a 1:1 molar ratio in CHCl₃.
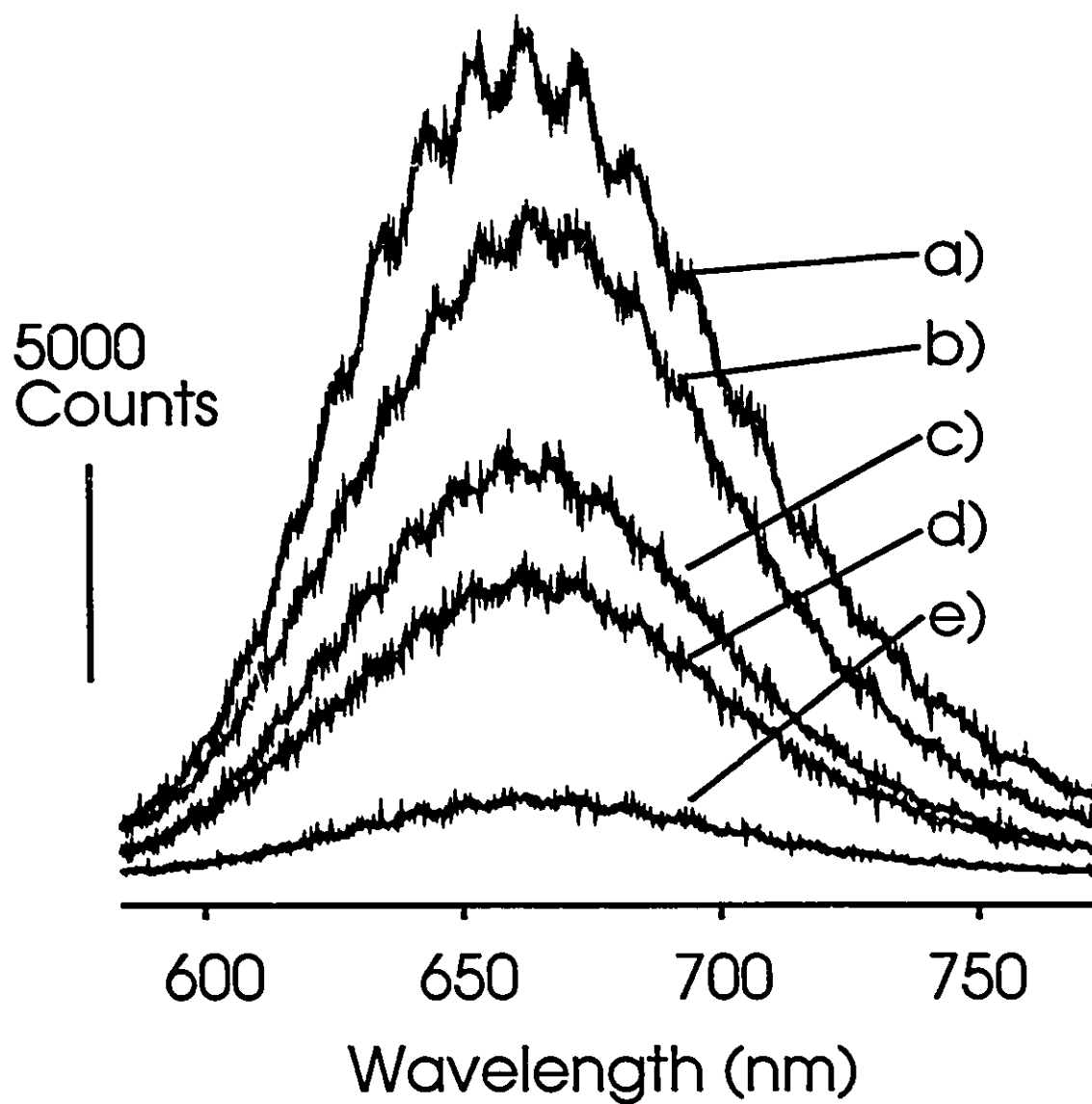
Figure 7.4:   Fluorescence intensity of the HPTCDE excimer emission in a
HPTCO/AA/LuPc$_2$ energy transfer system. a) reference spectrum, b) 4,
c) 3, d) 2 and e) 1 spacer layer of arachidic acid.

Distance Dependence of the Energy Transfer

The $LuPc_2$ monolayer is the acceptor layer and the perylene derivative forms the donor layer. The physical model in the Förster's dipole theory of energy transfer is a donor monolayer of point dipoles interacting with an acceptor layer of dipoles, in a case where the corresponding electronic transitions are allowed. The limitations of the model have been recently discussed by Chang [7.12]. It was found that the Förster dipole approximation for energy transfer would be applicable for donor-acceptor distances large compared to their sizes and when an angular average of the dipolar orientations may be taken. The latter condition implies that the approximation would not be suitable for ordered layers if the rotational relaxation time is greater than the fluorescence lifetime.

The quenching of luminescence of a dipole emitter in the donor layer by absorbing dipoles in the acceptor layer is proportional to the power of the electric field. In Kuhn's model, the emitter is an oscillating dipole perpendicular to the donor layer plane located at a distance d from the acceptor layer with dipoles parallel to the layer plane [7.3]. The power of the classical field contains three terms proportional to r^{-2}, r^{-4} and r^{-6}, that after integration to calculate the power absorbed, produces Kuhn's equation for the distance dependence of the energy transfer:

$$q/q_d = 1 + (d_o/d)^4 + \eta(d_o/d)^2 \tag{7.1}$$

where q is the quantum yield of the emitter in the absence of the acceptor layer, and q_d is the quantum yield for an acceptor layer at a distance d. d_o is the critical transfer distance, or distance where the energy transfer and deactivation through other paths are equal. A simplification of the equation (7.1) is obtained by dropping the quadratic dependence, and the energy transfer decreases as the fourth power of the interlayer separation [7.5]. Application of the former equation to the interpretation of experimental data has not always been successful and Fromherz and Reinbold [7.13] have found that the dependence of the energy transfer on the distance of the dye layers, for their experiments, was better fit by a cubic power.

In summary, the information accumulated on ET between LB monolayers seems to indicate:

a) the fourth power term in equation (1) may not provide a good fitting of the experimental results,

b) the most significant ET between LB layers (d_o values) take place on a scale of 10 nm.

One set of LB samples for the present study were prepared by Z deposition of the acceptor layer, spacer and donor monolayer. A second set of samples was prepared by Z deposition of the acceptor and donor layer, and Y deposition of the spacer layer. The thickness of one spacer layer was estimated to be 2.5 nm, and in the case of Y deposition 5 nm. For the case of adjacent donor-acceptor layers a 1.2 nm separation between the point dipoles was assumed. The results of the ET experiments for HPTCDE/LuPc$_2$ and HPTCO/LuPc$_2$ are presented in *Figures 7.5 and 6* respectively. The equation (7.1) gave the best fit for the present set of experimental points. The critical distance values obtained are given in *Table 7.1*, where the results produced by the fourth power fitting are also included for comparison.

The d_o values given by Khun's full equation gave results in agreement with Formherz and Reinbold *[7.13]* who reported d_o values between 6.2 and 6.4 nm for their monomethin-oxacyanine-monomethin-thiacyanine system. The fourth power approximation seems to overestimate the critical transfer distance. The η coefficient, which depends strongly on molecular orientation, changes considerably for the two molecules 1 for HPTCDE and 3 for HPTCO. In this respect it would interesting to carry out experiments with LB monolayers fabricated with well defined molecular orientations to study the orientational effect on the energy transfer measurements.

It would be very interesting to include a discussion of the role of molecular orientation in energy transfer. However, the structural data regarding HPTCO and HPTCDE do not reveal information regarding the orientation of the transition dipole associated with excimer emission. Without this portion of critical information, it is not possible to quantitatively involve chromophore orientation into Equation 7.1.

Table 7.1: Energy Transfer Parameters

	Khun's Full Equation (equation 7.1)		Power = 4 term only
	d_o (Å)	η	d_o (Å)
HPTCDE	65	1	81
HPTCO	58	3	108
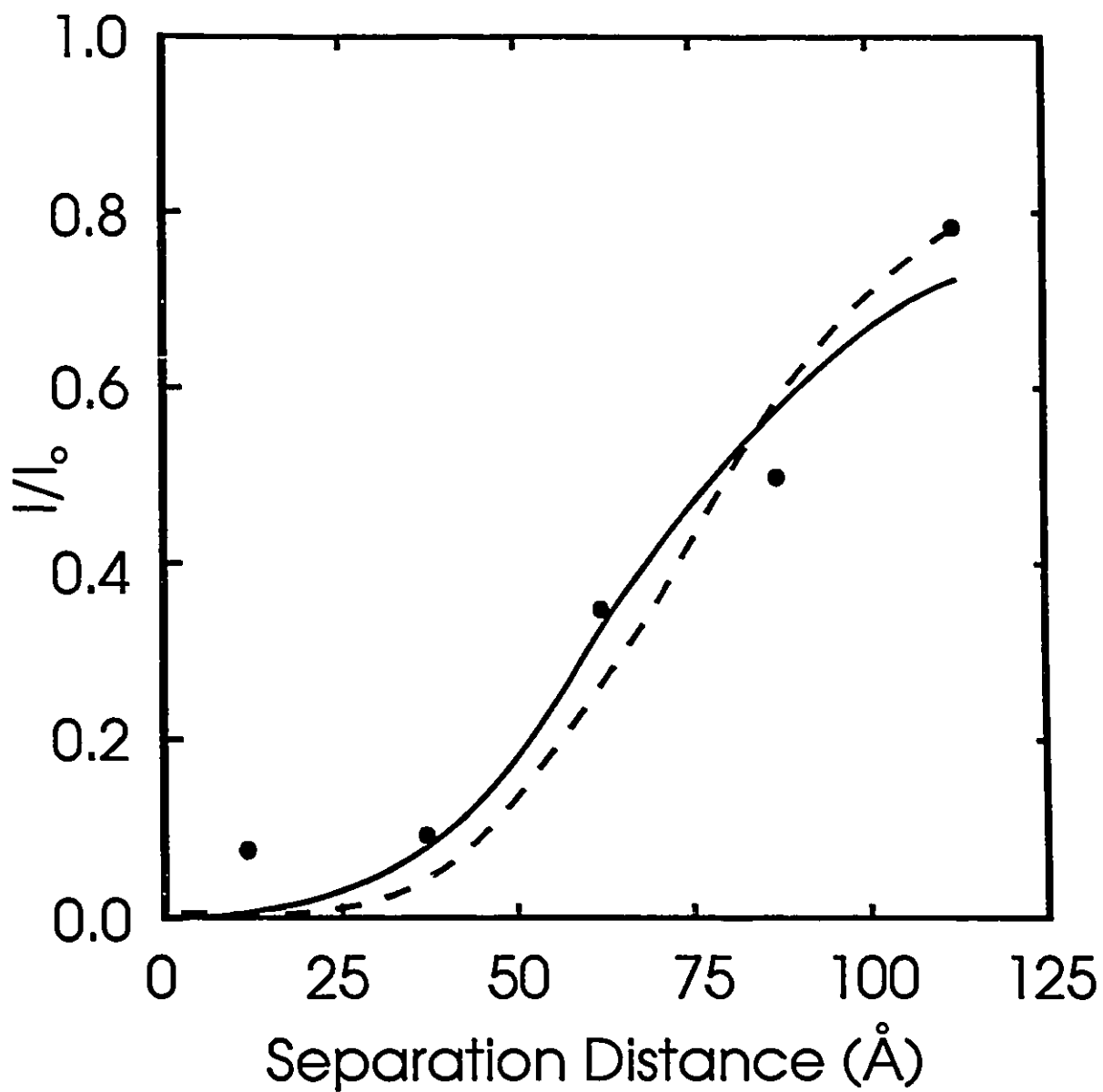
Figure 7.5:   Fluorescence intensity ratio I/I_o of the HPTCDE excimer emission as a function of the distance from one LB of neat $LuPc_2$. Dashed curve, fitted using power = 4 term only, solid curve fitted using equation 7.1

Figure 7.6: Fluorescence intensity ratio I/I_0 of the HPTCO excimer emission as a function of the distance from one LB of neat LuPc$_2$. Dashed curve, fitted using power = 4 term only, solid curve fitted using equation 7.1

Electron transfer versus energy transfer

In order to distinguish electron transfer from energy transfer, the Q-band absorption of $LuPc_2$ was studied. Solutions with different relative concentrations of HPTCO, HPTCDE and $LuPc_2$ were prepared. The solution containing $LuPc_2$ mixed with HPTCDE showed no changes in any of the absorption bands of either component. However, at a high relative concentration of HPTCO with $LuPc_2$, a new band at 700 nm appears (see *Figure 7.7a*). This new band corresponds to the Q-band of oxidized $LuPc_2$ *[7.14]*. The 700 nm band was not observed for a HPTCO/$LuPc_2$ bilayer assembly or any other LB assemblies used in this study of energy transfer. The latter results would indicate that electron transfer complex formed between $LuPc_2$ and HPTCO has geometric requirements which are not satisfied by the molecular arrangement in the LB films.

The mixed solution of HPTCO/$LuPc_2$ in $CHCl_3$ was unique in forming aggregates that precipitated out of solution. This reaction is limited to the perylene derivatives containing an anhydride group, and was not observed in a series of solutions of perylene dicarboximide derivatives and $LuPc_2$. The absorption spectra of the solution and that of the precipitate are shown in *Figure 7.7*. In solution the absorptions of the HPTCO and $LuPc_2$ are clearly observed. The Q-band of $LuPc_2$ showed the presence of the 700 nm band which corresponds to the oxidized form of $LuPc_2$. The spectrum of the precipitate indicated the formation of an aggregate with very broad bands of the phthalocyanine unit and an a weak absorption in the spectral region of the HPTCO. The nature of the aggregate is not known.

In another set of experiments, an aliquot of an aqueous solution containing the strong electron acceptor 1,1'-diheptyl-4,4'-bipyridinium dibromide (HBP) *[7.15]* was spread over 1 LB of $LuPc_2$. After the solvent had evaporated, the absorption spectrum of this slide was recorded. Again, no bands corresponding to either the reduced or oxidized form of $LuPc_2$ were observed. In conclusion, there was no evidence of electron transfer for the HPTCDE/$LuPc_2$ system. The HPTCO and $LuPc_2$ formed, in solution, aggregates or a charge transfer complex that contains oxidized $LuPc_2$. However, the formation of aggregates or the oxidation of $LuPc_2$ was not observed in LB bilayers with
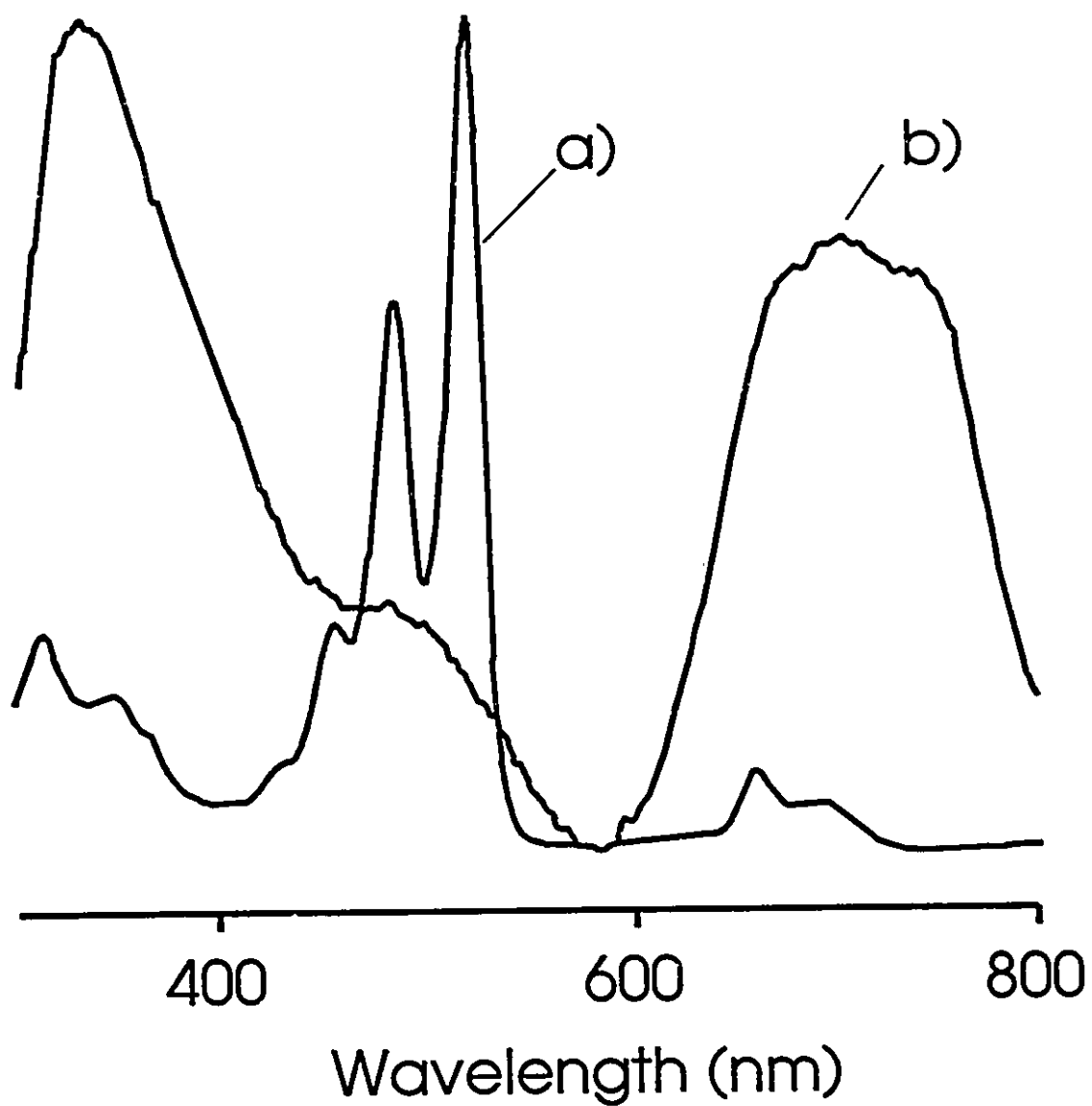
Figure 7.7: Absorption spectrum of the HPTCO-LuPc$_2$ mixture in CHCl$_3$, a), and absorption spectrum of the precipitate obtained from reacting mixture, b).

adjacent LB monolayer of each dye. Furthermore, the quenching of HPTCO for the latter system was less effective than in the HPTCDE/LuPc₂ case (see *Figures 7.5* and *6*), ruling out the extra quenching due to electron transfer.

Chapter Summary

An important new system of perylene-phthalocyanine dyes has been used for energy transfer studies involving the excimer emission of the perylene derivative. The critical distance observed for energy transfer in the new systems indicated that the ET occurs mainly on the 10 nm scale, which is in agreement with previous observations with different dyes. The possibility of electron transfer contributions to the fluorescence quenching was found to be negligible. Further studies of energy transfer between LB monolayers with well defined molecular orientation could help to clear up the limitations of the dipole theory.

References - Chapter 7

[7.1] Förster, T., *Discussions Far. Soc.*, **1959**, *27*, 7.

[7.2] Clayton, R.P.; Syed, A.N., *Introduction to Electromagnetic Fields*, McGraw-Hill, **1987**.

[7.3] Kuhn, H., *J. Chem. Phys.*, **1970**, *53*, 101.

[7.4] Kuhn, H.; D. Mobius, D.; Bucher, H., in *Physical Methods of Chemistry*, Weissberger, A.; Rossiter, W.B., Eds., Vol I, part IIIB, Wiley, New York **1972**, pp. 577-702.

[7.5] T.L. Penner, *Thin Solid Films*, **1988**, *160*, 241.

[7.6] Clavijo, R.E.; Aroca, R., *XII International Conference on Raman Spectroscopy*, Durig, J.R., Sullivan, J.F., Editors. John Wiley & Sons, Chichester, 1990, p.256.

[7.7] Yamazaki, I.; Tamai, N.; Yamazaki, T., *J. Phys. Chem.*, **1990**, *94*, 516.

[7.8] Aroca, R.; Clavijo, R.E.; Jennings, C.A.; Kovacs, G.J.; Duff, J.M.; Loutfy, R.O., *Spectrochim. Acta*, **1989**, *45A*, 957.

[7.9] Birks, J.B., *Photophysics of Aromatics Molecules*, John Wiley & Sons Ltd., London **1970**.

[7.10] Hochstrasser, R.M.; Nyi, C.A., *J. Chem. Phys.*, **1980**, *72*, 2591.

[7.11] Aroca, R.; Guhathakurta-Ghosh, U.; Loutfy, R.O., Nagao, Y., *Spectrochim. Acta*, **1990**, *46A*, 717.

[7.12] Chang, J.C. *J. Chem. Phys.* **1977**, *67*, 3901.

[7.13] Fromherz, P.; Reinbold, G. *Thin Solid Films* **1988**, *160*, 347.

[7.14] Corker, G.A.; Grant, B.; Clecak, N.J. *J. Electrochem. Soc.* **1979**, *126*, 1339.

[7.15] Steiger, R.; Zbiden, F., *J. Imaging Sci.*, **1988**, *32*, 64.

Chapter 8: Surface Enhanced Infrared Spectroscopy of Monolayers

Introduction

Surface enhanced Raman scattering (SERS) is a well documented and investigated phenomenon and is an established analytical technique for adsorbates on surfaces and interfaces [8.1,2]. The nature of the enhancement mechanism has been firmly established as electromagnetic in origin. In special circumstances, other effects, such as resonance Raman scattering (RRS) [8.3] or chemisorption [8.4] can have a multiplicative effect upon the SERS signal. The application of SERS to the study of Langmuir-Blodgett (LB) monolayers in the visible region has also been extended to the near infrared region where enhancement, using the 1064 nm laser excitation, has been observed in Fourier transform Raman spectroscopy [8.5].

The surface enhancement of infrared spectra was first observed and investigated by Hartstein [8.6] using gold or silver islands. This work centred on attenuated total reflection techniques. Recently, Osawa et al. have reported surface enhanced infrared in the reflection absorption geometry (SEIRRA) [8.7] and in the transmission geometry (SEIR) [8.8,9], however, the nature and the mechanism(s) of this enhancement have not been completely clarified.

In order to fully use the SEIR phenomenon and close the circle of Raman and infrared enhanced vibrational spectroscopy, a study of the properties of the infrared enhancement was initiated. This chapter contains the first set of experimental results in the investigation of the distance dependence of the enhancement factor. The effects of the incidence angle, the nature of the substrate and the enhancing metal are also investigated. A brief discussion of physical models proposed in the literature is given in light of the new information acquired. It is also demonstrated that the same substrates used in SEIR and SEIRRA spectroscopy are enhancers of the Raman scattering.

Physical model

The simulation of the observed SEIRRA and SEIR spectra was performed by modelling the metal islands and LB layers as a composite film *[8.7]*. The sample, modelled as a composite film, has a complex index of refraction, n_2 sandwiched between two semiinfinite regions ($n_1 = 1$, vacuum and n_3, the support substrate of the composite layer *[8.7,8]*).

In order to determine the spectroscopic behaviour of the composite layer, the silver island films were modelled as oblate ellipsoids. The effective dielectric constant for the composite layer could be determined by using the Maxwell-Garnett (MG) model:

$$\epsilon_{MG} = \epsilon_h (3 + 2F\alpha)/(3 - F\alpha) \tag{8.1}$$

or by the Bruggeman (BR) model:

$$\epsilon_{BR} = \epsilon_h [3(1-F)+F\alpha]/[3(1-F)-2F\alpha] \tag{8.2}$$

where ϵ_h is the dielectric constant of the host medium, F is the packing factor of the metal island film defined as d_{mass}/d_{opt} and α is the polarizability of the metal particles.

The polarizability is calculated according to Equation 8.3 *[8.8]*:

$$\alpha_{\parallel,\perp} = \{[(\epsilon_d-1)[\epsilon_m L_1 + \epsilon_d(1-L_1)] + Q(\epsilon_m-\epsilon_d)[\epsilon_d(1-L_2) + L_2]]/$$
$$[[\epsilon_d L_2 + \epsilon_d(1-L_1)] + Q(\epsilon_m-\epsilon_d)(\epsilon_d-1)L_2(1-L_2)]\}_{\parallel,\perp} \tag{8.3}$$

Here, Q represents the volume ratio (V_1/V_2) of the metal particles without and with the LB film present. The depolarization ratios, L_1 and L_2, depend upon the aspect ratios for the metal particles *[8.10]*. The dielectric constants of the organic layer and the metal particles are given by ϵ_d and ϵ_m, respectively. The dielectric constants for the silver islands is

given by *[8.11]*:

$$\epsilon_\infty = 1 - [\omega_p^2/(\omega(\omega+i/\tau))] \tag{8.4}$$

where ω_p is the plasma frequency (1.38×10^{16} s^{-1}) and τ is the relaxation time (3.1×10^{-14} s) of bulk silver.

The strongest band observed in the SEIR and SEIRRA spectra is at 1592 cm^{-1} and is the band model in this work. The absorbance calculations require the complex dielectric constant of the organic monolayer. The values associated with the 1592 cm^{-1} band (between 1400 and 1800 cm^{-1}) were determined following the method used by Osawa *et. al. [8.8]*. The SEIRRA spectra were simulated using the equations of Mielczarski and Yoon *[8.12]*. The optical constants for glass and silicon were taken from reference *[8.13]*.

Experimental Details

The preparation of the monolayers of PhPTCO has been described in *Chapter 5* and is not repeated here. LB films were transferred to a variety of substrates in order to explore the surface enhanced vibrational phenomena. The films deposited onto silver island coated substrates were viewed through an optical microscope under x100 power. The films appeared homogeneous and no large scale defects were visible at this magnification.

In order to study SEIR spectroscopy in a transmission geometry, 6 nm (mass thickness) of silver was evaporated onto polished CaF_2 windows (Wilmad). Substrates used for SEIR reflection/absorption (SEIRRA) spectroscopy were similarly prepared by vacuum evaporation of 6 nm of silver, gold or copper onto Corning 7059 glass slides held at 200°C. The same silver coated glass slides were also used to investigate the SERS spectra of Ph-PTCO.

The distance dependence of the SEIR and SEIRRA phenomena was investigated by depositing spacer layers of arachidic acid (AA) between the metal film and the Ph-PTCO monolayer. An initial Z-deposited AA film, with several subsequent Y-deposited layers produced systems with 0, 1, 3, 5 and 7 spacer layers. The AA was transferred at 25°C, 30 mN/m and at 0.6 mm/s using a Lauda Filmlift FL-1. Transfer ratios were 1.0 in all cases.

Infrared spectra were recorded using a Bomem DA3 interferometer equipped with a MCT wide range detector. A Spectra-tech variable angle reflectance accessory was used to record SEIRRA spectra. Polarized spectra were obtained using a Spectra-tech wire grid polarizer. All spectral data were transferred to an IBM microcomputer and were analyzed using Spectra Calc. Math Cad for Windows was used to model calculations of surface enhanced infrared spectroscopy using classical electromagnetic theory and a Math Cad document for these calculations can be found in *Appendix II*.

In order to show that the prepared enhancing substrates were suitable for both infrared and Raman work, the Raman scattering of 1 LB of PhPTCO on silver islands was also recorded. Laser excitation at 514.5 nm was provided by an argon ion laser. The spectra were recorded in the back-scattering configuration.

Results and Discussion

Langmuir and Langmuir-Blodgett Layers

The isotherm recorded for Ph-PTCO is shown in *Figure 5.2* of *Chapter 5*. A discussion of the π-A isotherms are also found in *Chapter 5* and are not repeated here. The films were exceptionally rigid and could only be transferred through horizontal deposition. A good transfer ratio, near one, was achieved in all cases.

The silver islands were characterized by atomic force microscopy. The silver particles were sufficiently homogeneous so they could be approximated as oblate ellipsoids with a 21 nm short axis parallel to the surface normal and a radius, perpendicular to the substrate surface, of 46 nm. The mass thickness was 6 nm, thereby yielding a packing factor of about 0.3. The AFM image of the silver particles on glass is given in *Figure 8.1*.

Infrared and surface-enhanced infrared spectra

The infrared spectra of the 1500-1850 cm^{-1} region of Ph-PTCO dispersed in a KBr pellet is shown in *Figure 8.2*. In this spectrum, five bands are dominant and their assignments, based on previous work *[8.14,15]*, are given in Table 8.1. It is changes in relative intensity of these five bands that are used to investigate the SEIR and SEIRRA phenomena. The shoulders seen in these spectra were not analyzed.

Table 8.1: Characteristic PTCO Bands in the 1550 to 1800 cm^{-1} Region

Infrared Band (cm^{-1})	Assignment
1592	naphthalene ring stretch
1656	anti-symmetric imide carbonyl stretch
1694	symmetric imide carbonyl stretch
1724	anti-symmetric anhydride carbonyl stretch
1765	symmetric anhydride carbonyl stretch
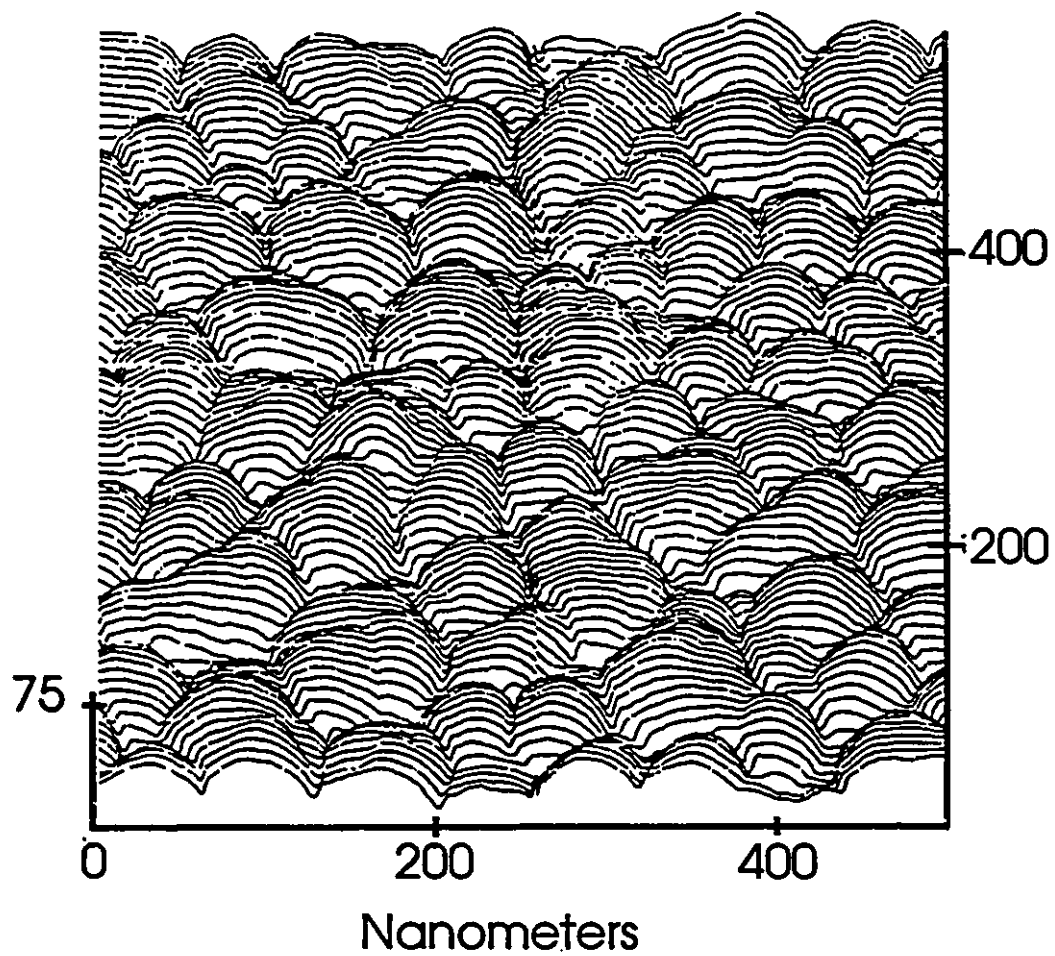
Figure 8.1: The AFM image of 6 nm (mass thickness) of silver evaporated onto Corning 7059 glass slides.
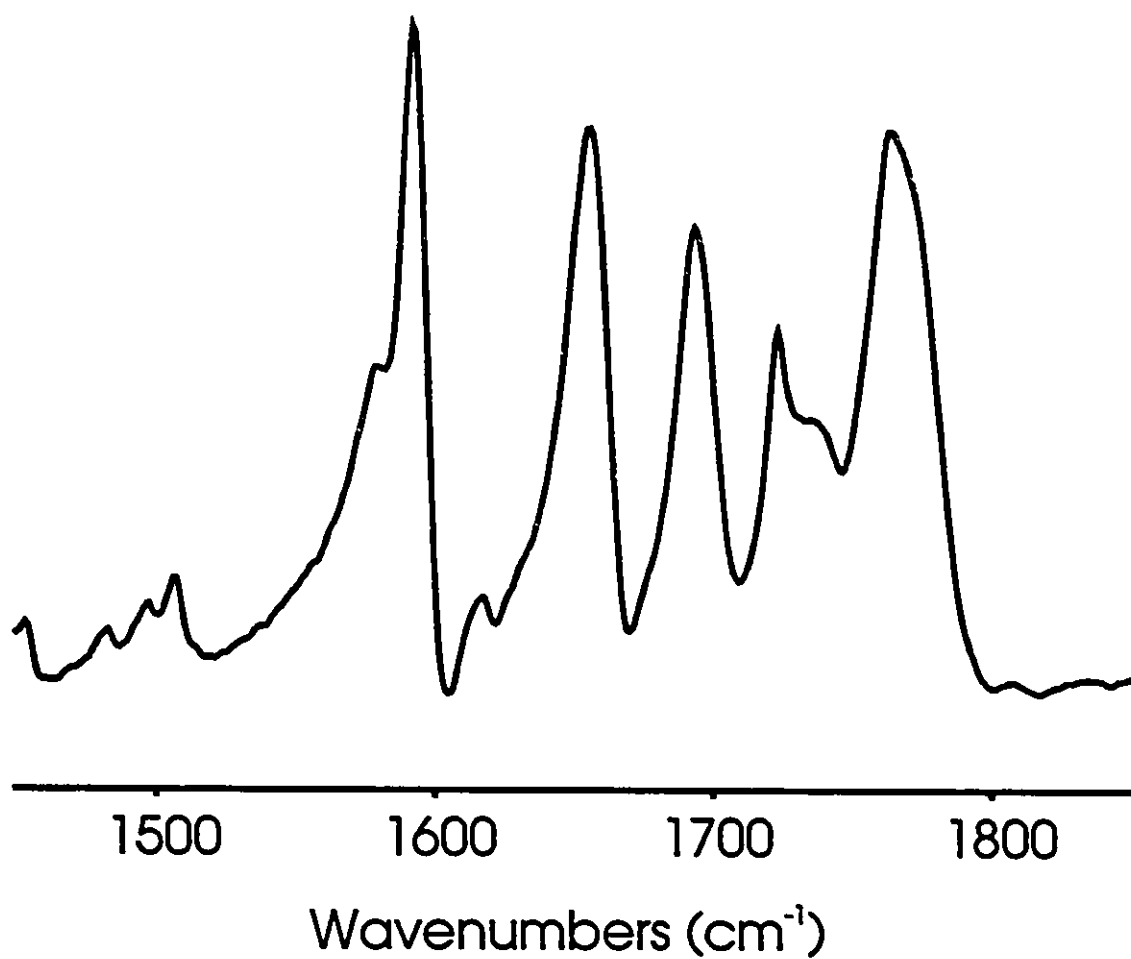
Figure 8.2: The IR of the carbonyl region of PhPTCO dispersed in a KBr pellet.

The surface enhanced spectra were recorded in the reflection mode (SEIRRA) and in the transmission mode (SEIR) for 1 LB of Ph-PTCO on silver islands on silicon wafers (Ag/Si). The SEIRRA spectra were obtained for monolayers of this material on Ag/glass, Au/glass and Cu/glass. The SEIR spectra were obtained using Ag/CaF_2 and Ag/Si.

In all cases, the observed reflectances ($-\log(R/R_o)$) in SEIRRA were negative, whereas SEIR spectra always yielded positive signals. *Figure 8.3* shows the SEIRRA spectrum of 1 LB of PhPTCO on Ag/glass superimposed on the reflection/absorption spectrum of 2 LBs on smooth silver on glass. Based on the calculations of Takenaka *et al. [8.16]*, the reflection/absorption spectrum has an enhancement factor of 4.6. The magnitude of the enhancement factor for the SEIRRA spectrum, compared to an unenhanced spectrum, is estimated to be about 30. Also note the negative glass bands below about 1500 cm^{-1}.

The effect of light polarization upon the excitation of the SEIRRA spectra was investigated. In both S and P polarized spectra, the observed bands were negative. A poor signal to noise ratio was obtained for S-polarization compared to P-polarization. The P-polarized spectra were virtually superimposible upon the spectra obtained with natural light.

Angle Dependence

The SEIRRA spectra were recorded at different angles of incidence for one LB on Ag/glass and are plotted in *Figure 8.4a*. In these spectra, all of the observed bands have negative reflectances and the magnitude of the reflectance increases with decreasing angle of incidence. The spectrum recorded at an angle of incidence of 35° gave the most intense signal, which was about 4.5 times as intense as the signal obtained at 75° incidence. Based on the enhancement factor determined from the reflection/absorption spectrum in *Figure 8.3*, the overall enhancement factor for this spectrum is about 135.

The angle dependence of the enhancement was also investigated for Ag/Si. *Figure 8.4b* illustrates these spectra. Again, the more intense signals were obtained far from grazing angles of incidence, with maximum enhancement observed at 45°. The spectra
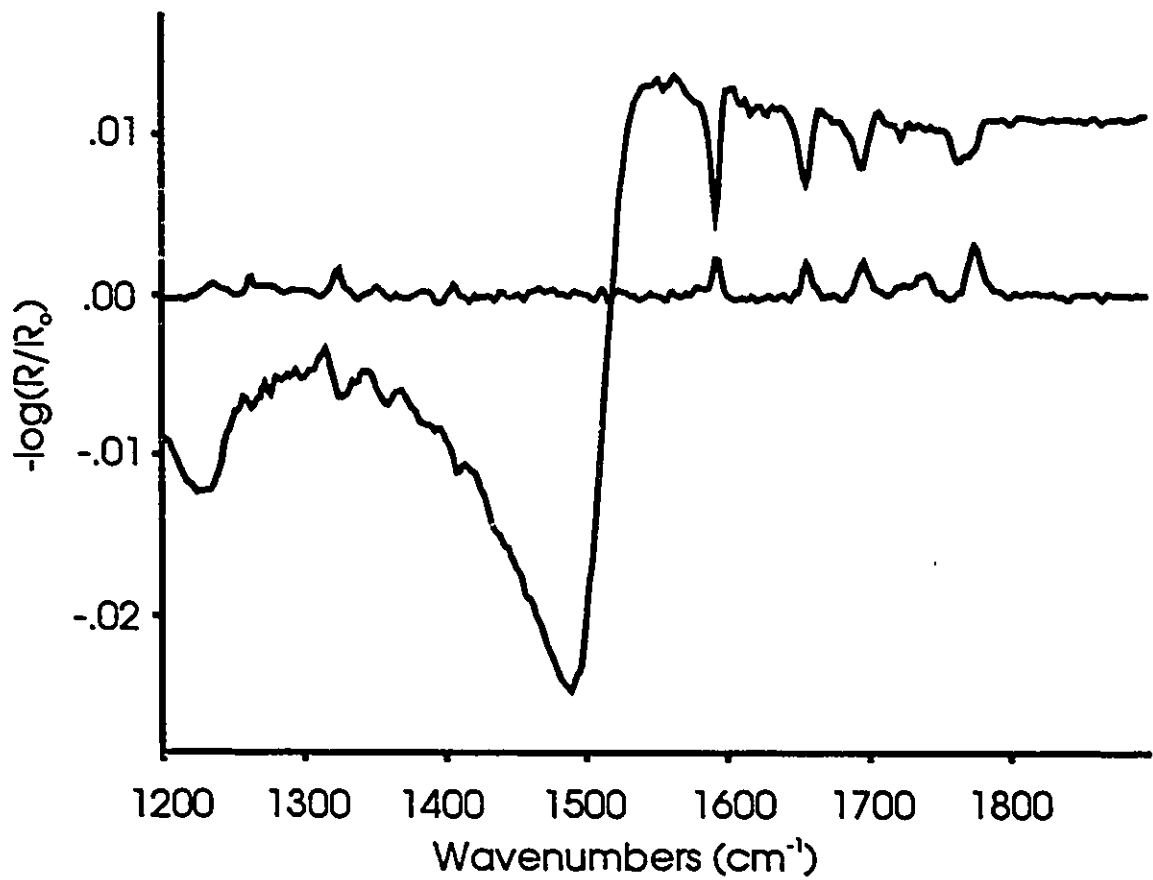
Figure 8.3: A comparison of SEIRRA (upper trace) of 1 LB and RAIR spectra (lower trace) of 2 LBs of PhPTCO. Angle of incidence was 75°, and deposition conditions were identical in both cases.
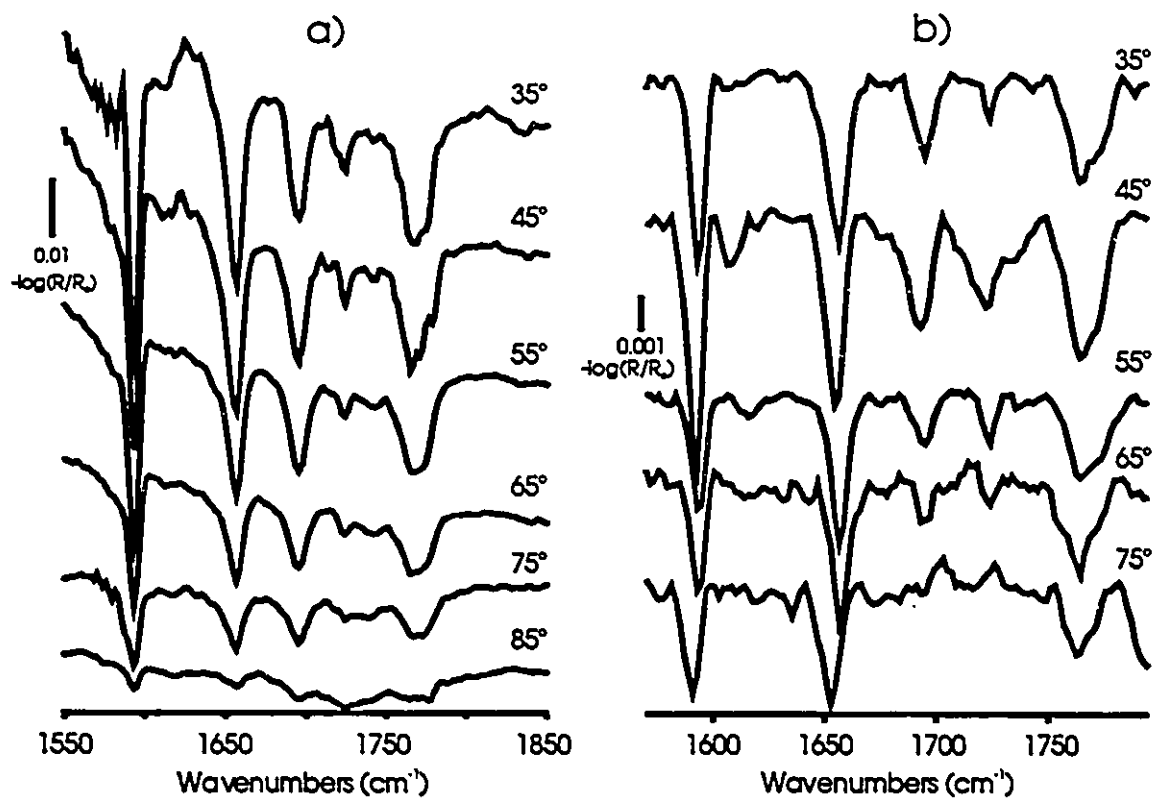
Figure 8.4:   The angle dependence of 1 LB of PhPTCO on 6 nm silver islands a) on glass b) on silicon.

obtained of 1 LB on Ag/Si were about an order of magnitude weaker than the comparable spectra obtained on Ag/glass.

The simulated angle dependent spectra in *Figure 8.5* are similar to the results of Nishikawa *et al.[8.8]*, but do not correspond well to the observed experimental results. The simulated spectra all yield negative absorbances, except for the spectrum calculated for 55° angle of incidence. The magnitude of the absorbances generally decreased with increasing incidence angle. The only exception occurred between 35° and 45° where the former was less intense than the latter. The simulated absorptions were similar in magnitude to those of the observed spectra.

The relative intensities of the SEIR spectra were compared with the relative intensities of the SEIRRA spectra. The transmission geometry spectrum and the SEIRRA spectrum (35° incidence) of 1 LB of PhPTCO on silver islands are shown in *Figure 8.6*. No change in relative intensities exists between the two spectra. The choice of silicon or calcium fluoride did not significantly alter the observed absorbances for the transmission case. The magnitude of the enhancement in the SEIRRA case are about 3.5 times the enhancement of the SEIR spectra.

The reflection/absorption spectrum of a single LB of PhPTCO on glass or silicon was attempted, as well as the transmission spectrum of 1 LB on calcium fluoride or on silicon. The IR signals in the 1500-1850 cm^{-1} region were not observed in any of these cases, therefore, the presence of the metal island films is responsible for the observed infrared intensities.

Metals other than silver also provided enhancement of the infrared absorption. Metals island films of gold or copper, also gave SEIRRA spectra of PhPTCO. As with the case of silver, all of the observed absorption bands were negative for PhPTCO on gold or copper islands. The enhancement was an order of magnitude smaller in both cases than it was for silver. There was a smaller variation of the absorption magnitude in the angle dependence for these metals, but the same trends associated with silver held for copper or gold.
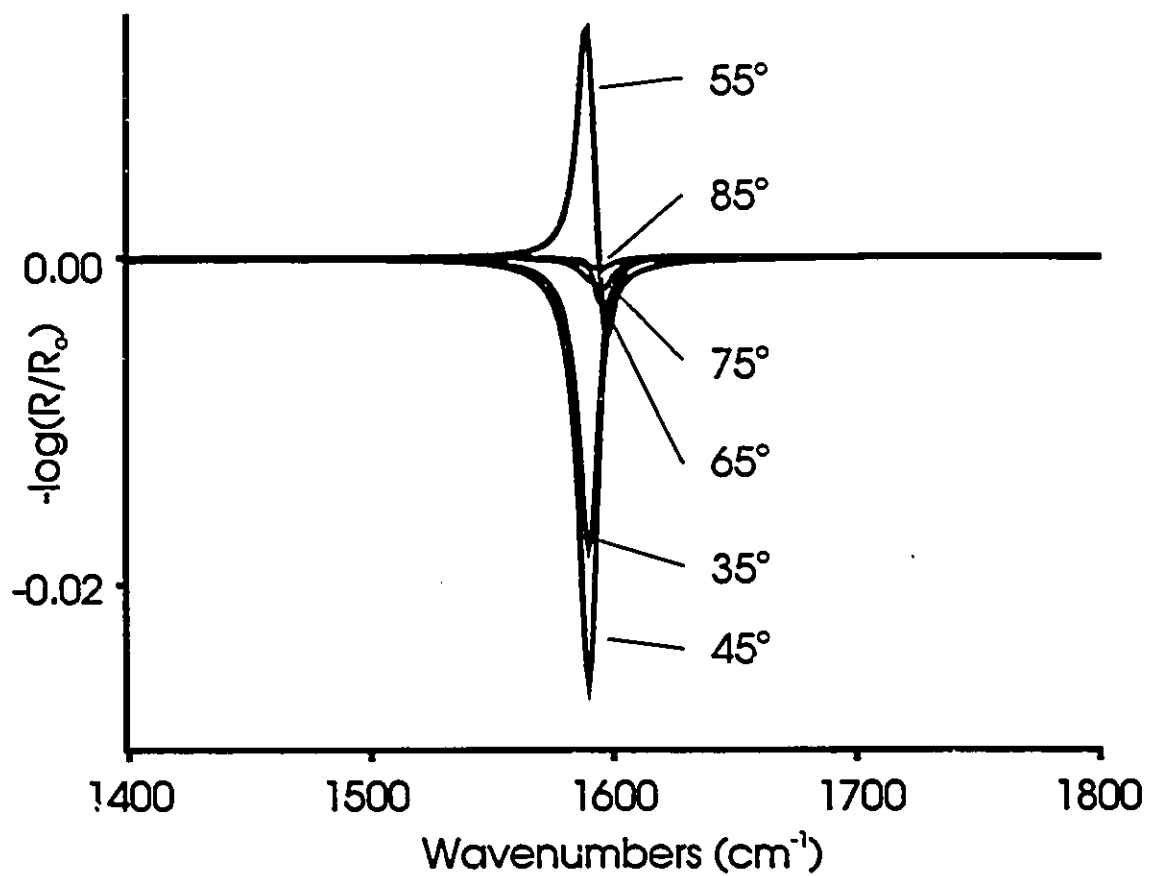
Figure 8.5: The simulated angle dependent absorption of the 1592 cm⁻¹ band using the Maxwell-Garnett model of the silver island film.

a)

b)

0.01

1600   1650   1700   1750

Wavenumbers (cm⁻¹)
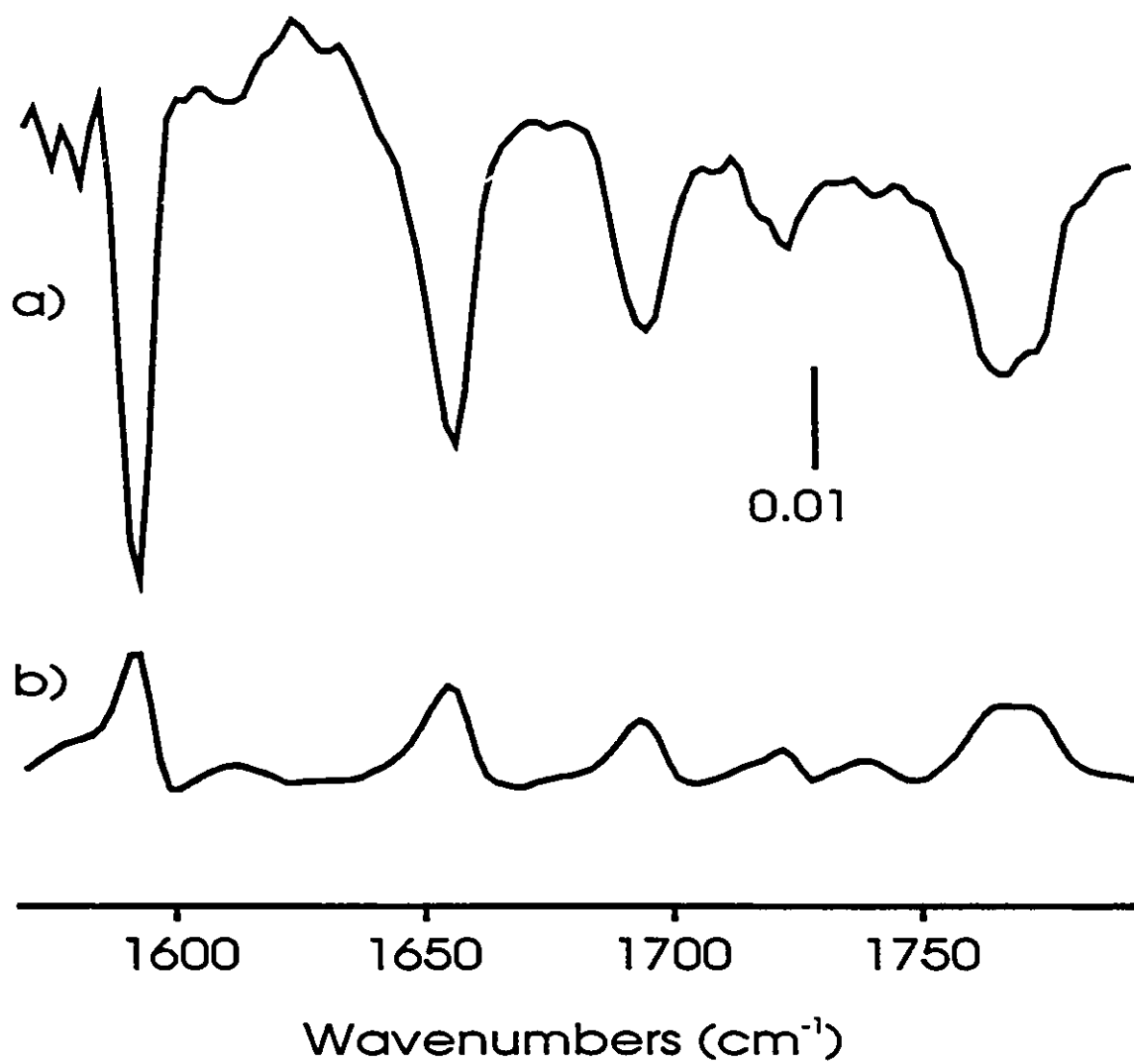
Figure 8.6:   Comparison of the magnitudes of SEIRRA (a) and SEIR (b) spectra.

164

Distance dependence of surface-enhance infrared spectra

The distance dependence of the enhancement factor in SERS is a fundamental property of the electromagnetic enhancement mechanism [8.3]. Therefore, the distance dependence of the SEIR and SEIRRA phenomena was investigated. A varying number of arachidic acid (AA) spacer layers were deposited onto the surface enhancing substrate before deposition of the probe PhPTCO LB layer. Each arachidic acid layer provides a 2.5 nm (approx.) thick spacer separating the silver islands and the probe layer. By plotting the magnitude of the absorbance in the SEIRRA and SEIR spectra versus the number of AA spacer layers, the distance dependence of the surface enhancing phenomenon can be observed.

The distance dependence of SEIRRA is illustrated in *Figure 8.7*. The region above 1700 cm^{-1} was omitted due to overlap with the arachidic acid carbonyl stretching vibration. The integrated absorption intensity of the 1592 cm^{-1} PhPTCO band is plotted versus the number of arachidic acid layers in *Figure 8.8b*. The error bars associated with each data point give the statistical uncertainties in determining the area of the 1592 cm^{-1} band in each spectrum and the absorbances were multiplied by -1 to gave positive values. From this data, the surface enhancing phenomenon is most efficient well within 5 nm of the surface. Farther from the surface, the signal diminishes considerably. The distance dependence SEIR spectra are given in *Figure 8.9*. The wavenumber region is broader than in *Figure 8.7* and the arachidic acid carbonyl band can be seen to grow in absorbance with respect to the number of spacer layers. However, this increase is not linear. Rather, absorbance increased more slowly with increases in the number of arachidic acid layers. This occurs because the arachidic acid layers closer to the silver islands experience greater enhancement than those farther away. At 7 spacer layers, the arachidic acid carbonyl is the dominant feature of the spectrum.

The distance dependence for SEIRRA was also simulated using the composite layer model. The calculated spectra were determined for different layer thicknesses and the difference between these two spectra was taken in order to determine the absorbance of a single layer at various distances from the metal particles. The SEIRRA distance
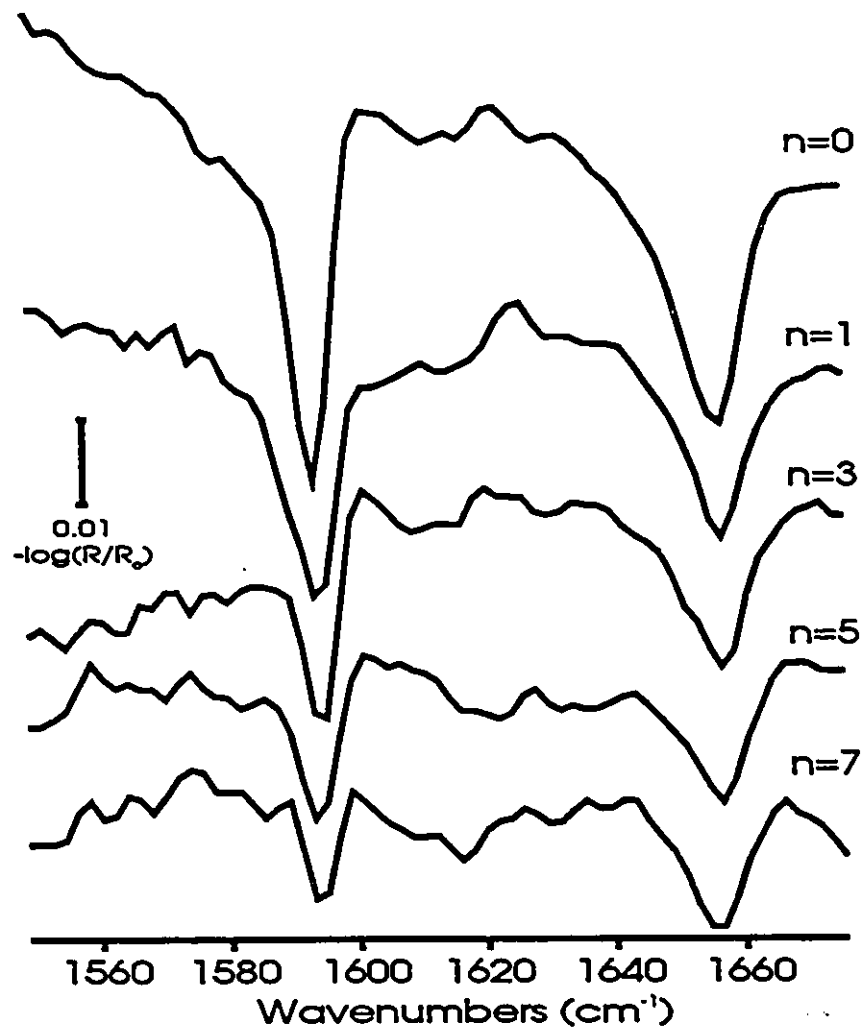
Figure 8.7: The distance dependence of SEIRRA spectra recorded at 45° incidence (n is the number of AA spacer layers).
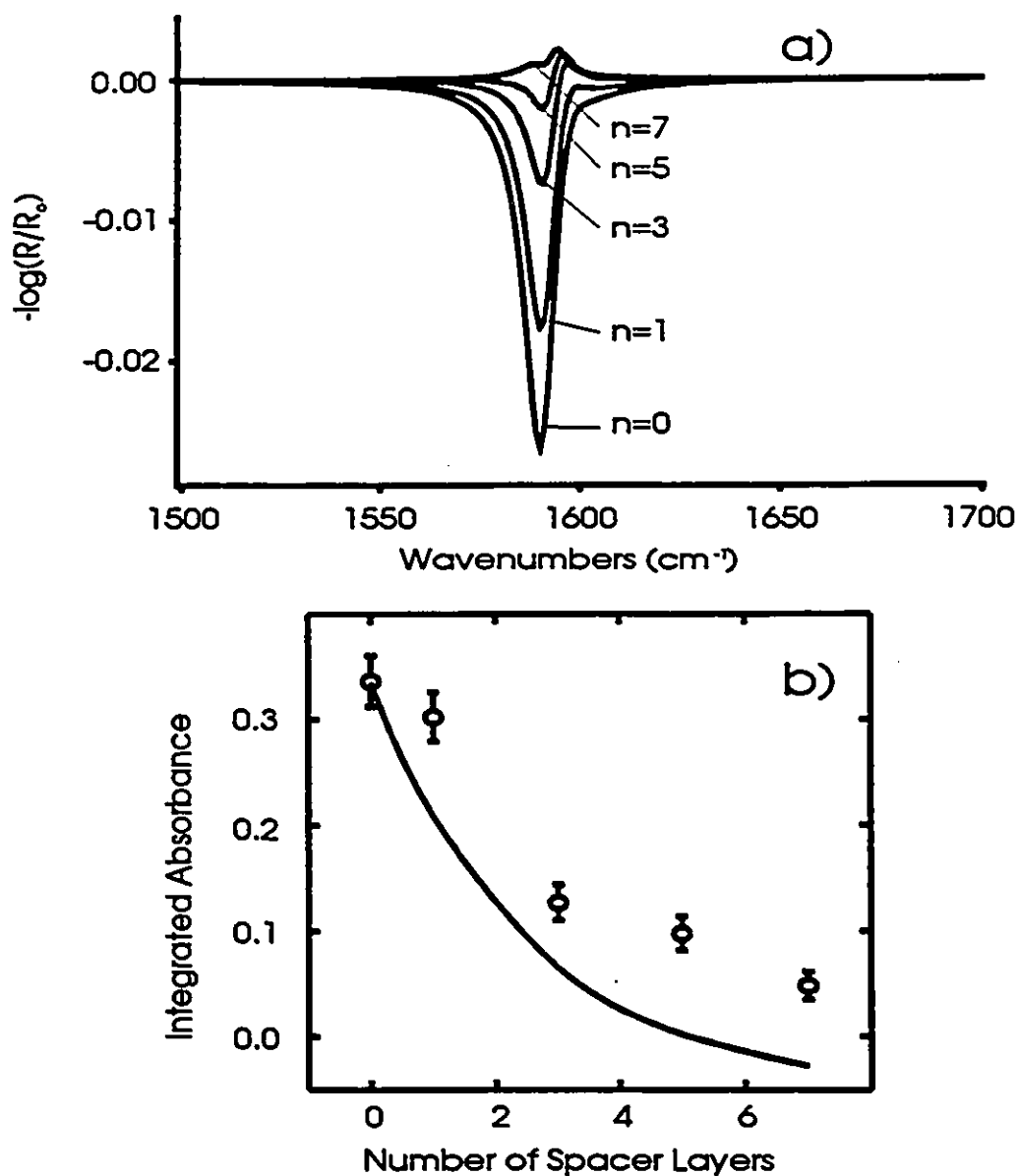
Figure 8.8: a) The simulated distance dependence SEIRRA spectra of 1 LB of PhPTCO on 6nm Ag on glass at 45° incidence angle; n is the number of arachidic acid spacer layers. b) Plot of the simulated distance dependence for the negative of the integrated absorbance for 1 LB of PhPTCO on silver islands. The experimental negative of the integrated absorbances are plotted for comparison with the theoretical curve (solid line).
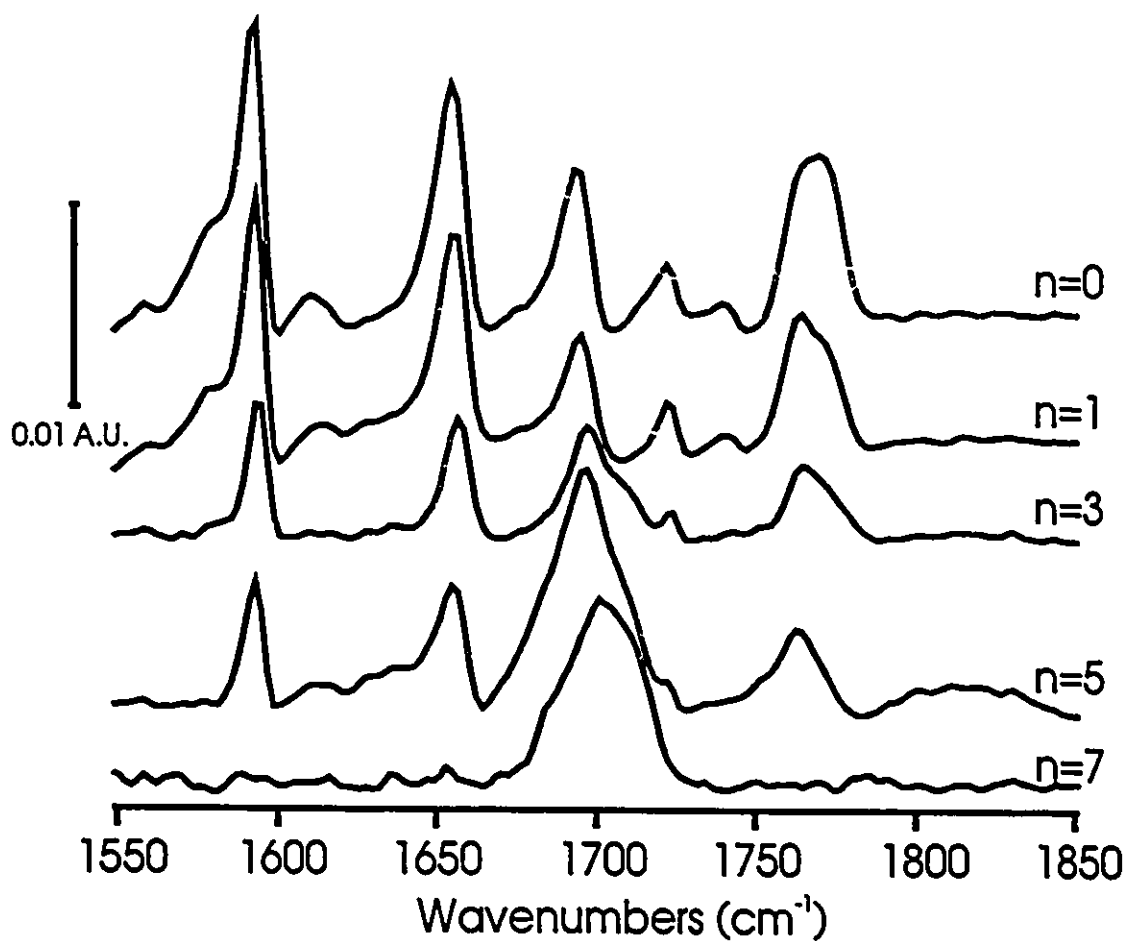
Figure 8.9: The distance dependence of SEIR spectra (n is the number of AA spacer layers) for 1 LB of PhPTCO on 6nm Ag on calcium fluoride.

dependence was calculated for 1 LB of PhPTCO, separated from silver islands on glass by various numbers of arachidic acid spacer layers. The simulated spectra are illustrated in *Figure 8.8a*. As the number of spacer layers, n, increases, the magnitude of the absorption decreases. Unlike the experimentally observed distance dependence, the magnitude of the simulated absorbances decreases much more rapidly. The curve shown in *Figure 8.8b* is a plot of the integrated absorbance for the simulated distance dependence. The experimentally observed values also plotted for comparison. For no spacer layers, the calculated integrated absorbance is virtually identical to the observed value. As the number of spacer layers increases, the calculated values drop off much more quickly than the experimental ones.

The most striking feature of the angle dependent spectra of 1 LB of PhPTCO on silver islands on either glass or silicon, involves the relative intensities of the observed carbonyl bands. Remarkably, the relative intensities are unaltered with changing angle of incidence. Moreover, the pattern of relative intensities is very similar to that seen in the KBr pellet. It has been established in previous chapters and in the literature that perylene tetracarboxylics do form organized LB films on a variety of substrates *[8.14,15]*. In such films, the short molecular axis is tilted much farther from the surface normal than the long molecular axis. Moreover, the 1656 cm^{-1} and 1694 cm^{-1} imide stretches are polarized along the short and long molecular axes, respectively. *Figure 8.10* is a comparison of transmission and reflection/absorption infrared of PhPTCO multilayers. The spectra have been normalized with respect to the number of monolayers present. A comparison of relative intensities between these two spectra clearly demonstrate that some level of organization exists. A detailed evaluation of organization is beyond the scope of this report. A quantitative evaluation of LB organization for PhPTCO, and several other perylene imide/anhydride compounds, is currently under preparation *[8.17]*. Since the SEIRRA and SEIR spectra do not show any change in relative absorbance and closely resemble the relative absorbances of the spectrum of the KBr pellet, the surface enhanced spectra must undergo a depolarization mechanism similar to the SERS phenomenon. This is supported by the observation that these films
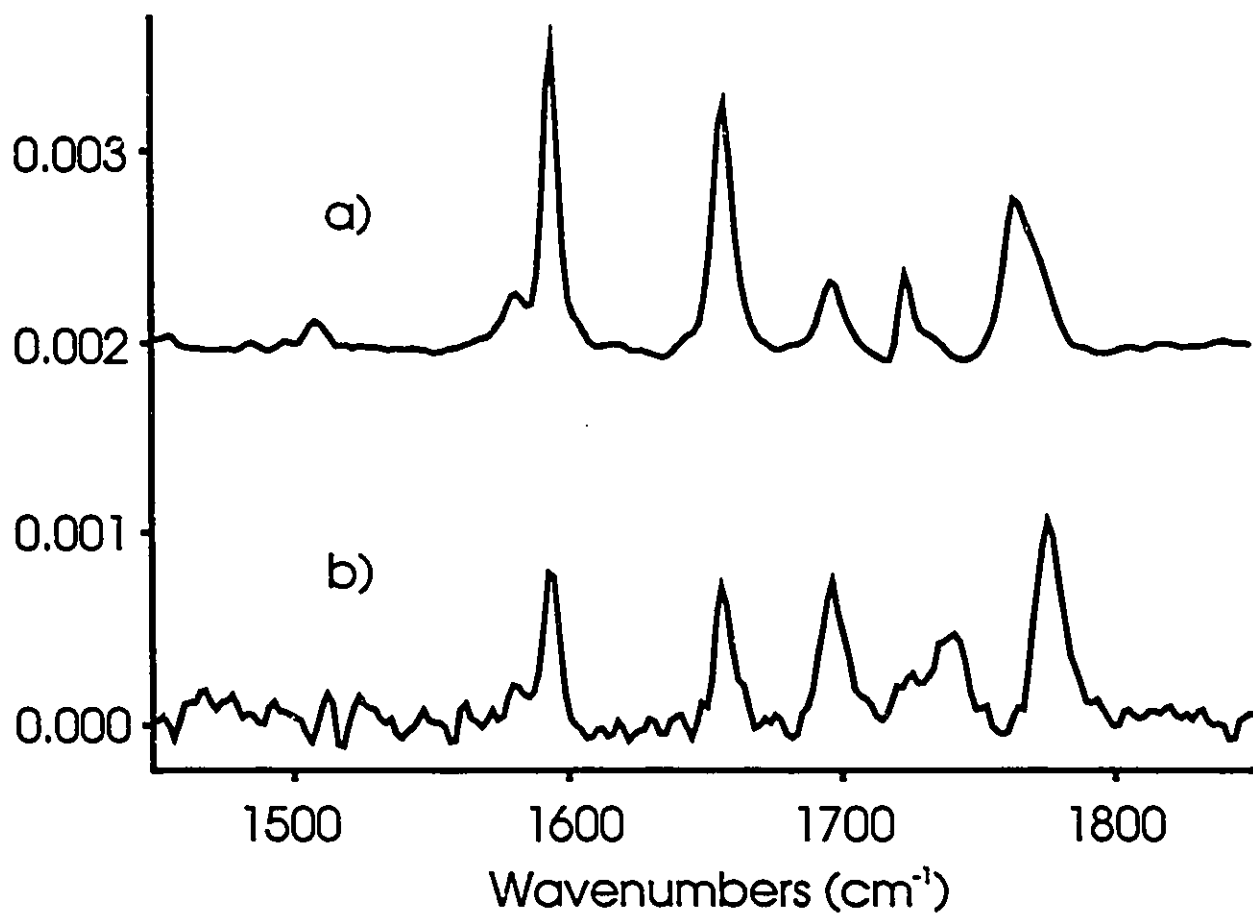
Figure 8.10: The normalized transmission (a) and reflection/absorption (b) spectra of PhPTCO. Y-axis units are absorbance for the transmission spectrum and -log(R/R$_o$) for the reflection spectrum.

do exhibit organization detectable by other infrared experiments.

A strong analogy with the SERS effect can be made with the SEIRRA and SEIR phenomenon. It is likely that the local electromagnetic field associated with the metal islands is responsible for the observed enhancements in absorbances. Since the plasmon resonances in infrared region are very weak, the enhancement would be a small fraction of that expected in the visible region.

The observation of negative absorbances could be associated with emission properties of the metal island film. If this were the correct mechanism, then all the observed spectra should be negative and of similar magnitude when using the same metal islands, however, the absorbances for the SEIR spectra are positive. Therefore, the positive or negative absorbance must be a function of the substrate under the metal islands. For example, the exact same metal islands and LB films were prepared on glass and on silicon, however, there is an order of magnitude difference in the observed SEIRRA spectra for these two substrates. Calculations simulating the SEIRRA phenomenon also predict negative absorbances and the composite layer model does not involve plasmon emission.

The angle dependence yielded interesting results. The calculated results give an anomalous positive absorbance at 55°. This may have resulted since this incident angle is near the pseudo-Brewster angle determined from the chosen optical constants [8.13] for glass. The term pseudo-Brewster angle is used since glass is an absorbing medium in the infrared spectral region. The actual slides, Corning 7059 glass, are specially prepared to give very smooth surfaces. It is possible that these slides have a different index of refraction that those published and that has lead to the discrepancies between the observed and simulated spectra.

The distance dependence studies support an electromagnetic mechanism for surface enhanced infrared spectroscopy. Further, the strongest absorbance is achieved close to the metal islands, a clear indication that the metal islands are primarily responsible for the observed enhancement. It should be pointed out that no spectra could be obtained for a single LB without the presence of the metal islands. Finally, the surface roughness plays a distinct role in the SEIRRA spectra and they differ remarkably from

171

the RAIR spectra of a monolayer on smooth silver.

The composite layer model predicts the highest enhancement very near the metal islands. As the distance between the metal islands and the probe monolayer is increased, the predicted absorbance drops off much more quickly than the experimental values. At large separations (7 arachidic acid spacer layers) the modeled absorbance changes sign from negative to positive. At this point, unenhanced absorption becomes a strong competitor with the negative enhance signal. This causes the more rapid decrease in absorbance magnitude in the modelled spectra. Moreover, the modelled spectra, at large separations, are quite asymmetric and begin to gain a slight positive shoulder. This will result in slightly lower integrated absorbances than those used to plot the curve in *Figure 8.7.*

The distance dependence results have implications regarding potential quantitative analysis of samples using SEIR or SEIRRA techniques. At greater than monolayer coverage, quantitative aspects of the signal intensity become compromised because components far from the surface will contribute differently to the observed intensity than components directly adjacent to the enhancing metal.

The SEIRRA phenomenon was also observed for three other PTCOs on silver islands on glass. *Figure 8.11* shows the SEIRRA spectra of 1 LB of PrPTCO, PPTCO, PhPTCO and HOPTCO on silver islands at 75° incidence angle. The magnitude of the observed absorbances and the relative intensities were similar.
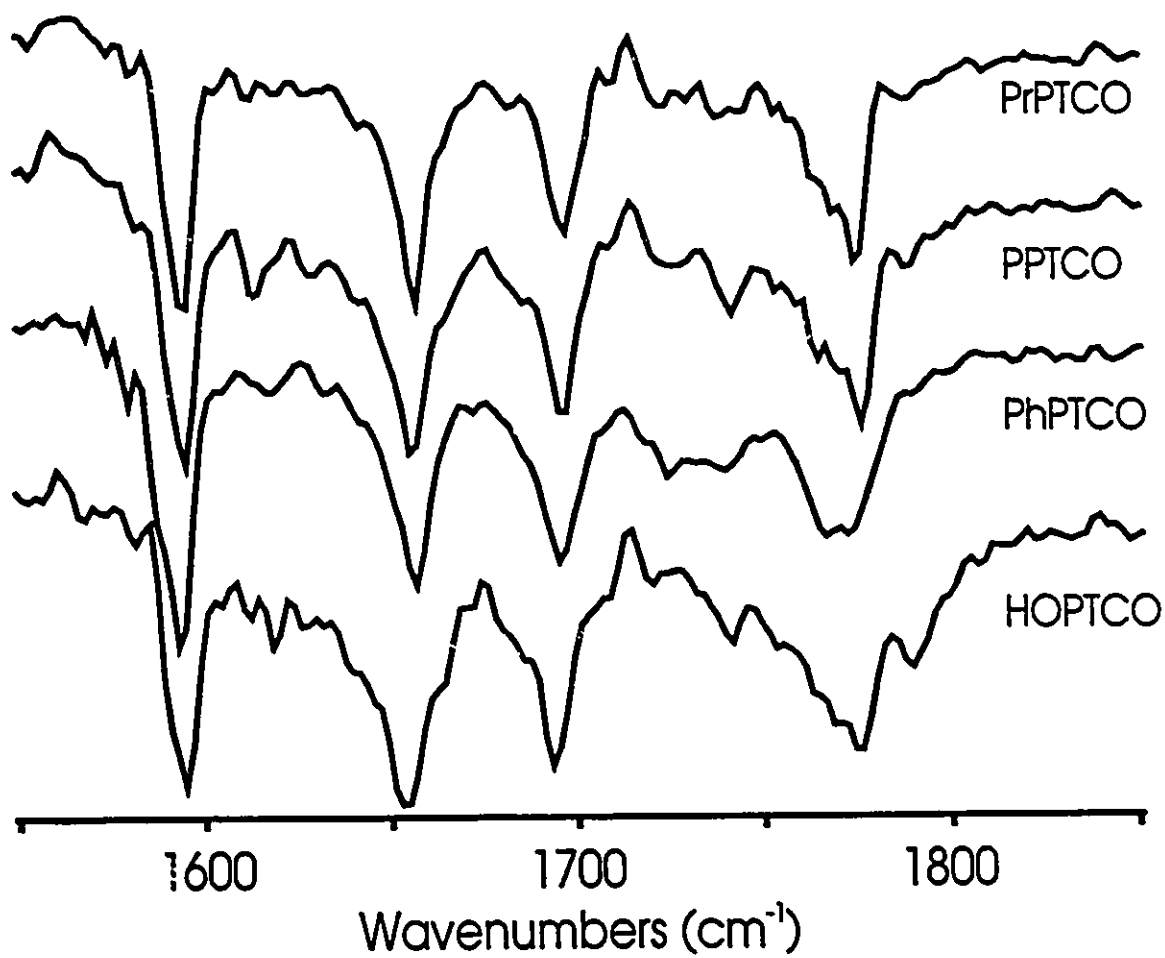
Figure 8.11: The SIERRA spectra of four PTCOs.

Raman Spectra

The substrates used in the SEIRRA experiments also produced surface enhanced Raman spectra of these monolayers. *Figure 8.12* shows the SERS spectrum of the carbonyl region of PhPTCO. Spectrum a) is the surface enhanced resonance Raman (SERRS) spectrum of PhPTCO. In this case, the surface plasmons of the substrate and the molecular absorption are in resonance with the excitation laser, causing enhancement from surface and resonance effects. The bands observed in SERRS are associated primarily with the chromophore portion of the molecule. Spectrum b) shows the carbonyl region of the same sample. Since the carbonyl bands are not associated with the chromophore, they experience only surface enhancement and are about two orders of magnitude weaker than the SERRS bands in a). The strong band at 1845 cm^{-1} is an overtone from a SERRS active band, hence is more intense than the carbonyl vibrations. It should also be noted that this is the first direct observation of the carbonyl stretching vibrations of perylene tetracarboxylic molecules in the inelastic light scattering spectrum.
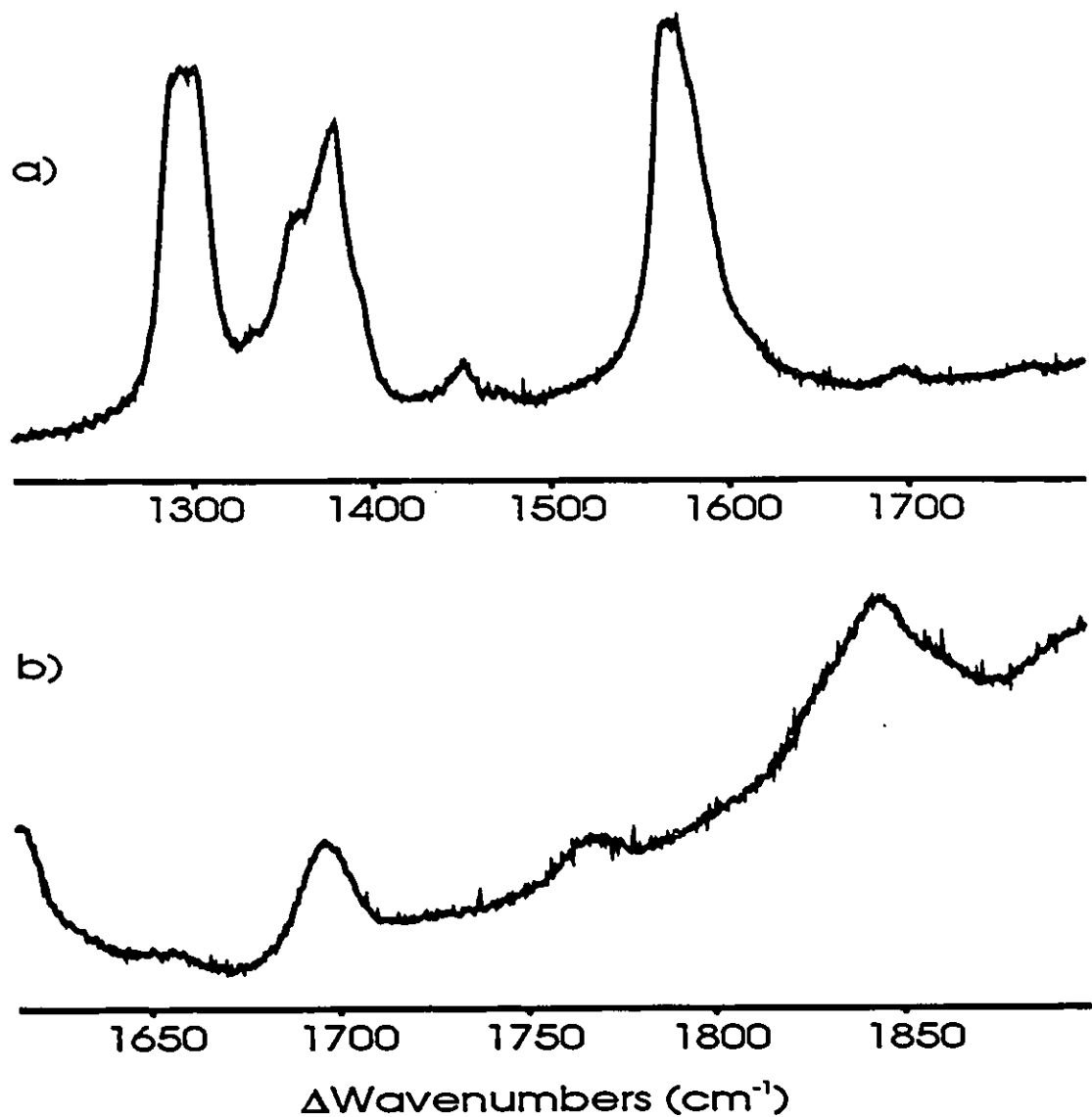
Figure 8.12: The Raman spectra collected from 1 LB of PhPTCO on 6 nm silver islands on glass. a) the SERRS spectrum of the finger print region, b) the SERS spectrum of the carbonyl region.

Chapter Summary

The properties of the surface enhanced infrared effect have been studied using Langmuir-Blodgett monolayers of a perylene tetracarboxylic diimide transferred to a variety of substrates coated with metal island films. Out of gold, copper and silver, silver islands on glass gave the greatest enhancement. The magnitude of the transmission SEIR spectra was independent of the host substrate (i.e. calcium fluoride and silicon). The observed SEIRRA spectra was simulated using a composite layer model and the angle dependence of these spectra can be obtained. The distance dependence of the SEIRRA spectra can also be modelled. The model seems to be reliable for distances close to the enhancing media (within 5 nm), but becomes less reliable at large separations. Finally, it has been shown that a single sample can be prepared to achieve the complete surface enhanced vibrational characterization (SERS and SEIR) of a perylene tetracarboxylic diimide.

References - Chapter 8

[8.1] *Surface Enhanced Raman Scattering*, Chang, R.K.; Furtak, T.E., eds., Plenum, New York, 1982.

[8.2] Moskovits, M. *Rev. Mod. Phys.* **1985**, *57*, 783.

[8.3] Aroca, R., Kovacs, G. in *Vibrational Spectra and Structure*, Durig, J.R., ed., Elsevier, Amsterdam, 1991.

[8.4] Otto, A. *Surf. Sci.* **1980**, *57*, 309.

[8.5] Jennings, C.A., Kovacs, G.J., Aroca, R. *Langmuir* **1993**, *9*, 2151.

[8.6] Hartstein, A.; Kirtley, J.R.; Tsang, J.C. *Phys. Rev. Let.* **1980**, *45*, 201.

[8.7] Nishikawa, Y.; Fujiwara, K.; Ataka, K.; Osawa, M. *Anal. Chem.* **1993**, *65*, 556.

[8.8] Osawa, M.; Ataka, K.; Yoshii, K.; Nishikawa, Y. *Appl. Spectrosc.* **1993**, *47*, 1497.

[8.9] Nishikawa, Y.; Fujiwara, K.; Shima, T. *Appl. Spectrosc.* **1991**, *45*, 747.

[8.10] Stoner, E.C. *Philos. Mag. 7* **1945**, *36*, 803.

[8.11] Johnson, M.R.; Christy, R.W. *Phys. Rev. B* **1972**, *6*, 4370.

[8.12] Mielczarsk, J.A.; Yoon, R.H. *J. Phys. Chem.* **1989**, *93*, 2034.

[8.13] Philipp, H.R., *Handbook of Optical Constants of Solids*, Palik, E.D., ed., Academic Press, N.Y., 1985, p749-762.

[8.14] Aroca, R.; Johnson, E.; Maiti, A. *Appl. Spectrosc.* (submitted)

[8.15] Maiti, A.K.; Aroca, R.; Nagao, Y. *J. Raman Spectrosc.* **1993**, *24*, 351.

[8.16] Umemura, J.; Kamata, T.; Kawai, T.; Takenaka, T. *J. Phys. Chem.* **1990**, *94*, 62.

[8.17] Aroca, R.; Johnson, E., unpublished data

Conclusions

A selection of ten perylene tetracarboxylic derivatives have been fabricated into Langmuir-Blodgett monolayer assemblies. The vibrational and electronic spectroscopic characterization of these monolayer systems was accomplished. This spectroscopic information was used to help elucidate the average molecular orientation and molecular structure. It was found, through infrared spectroscopy, that the short chromophore axis was tilted more than the long chromophore axis. Molecular exciton theory accounted for the observed spectral shifts in the LB films and the extended dipole model was used to deduce intermolecular structure. The materials formed stacked structures in the LB films. These stacks exist in patches since there is no observed dichroism in the plane of the LBs.

The structure of the films plays a very significant role in the observed spectroscopic properties. Even though the same chromophore moiety exists in each material studied, the role of the imide nitrogen substituents plays a significant role in the determination of LB structure. Hence, these substituents are the driving force behind molecular organization in these systems. The 2-phenylethyl PTCO produced structures that formed a structure that yields primarily excimer emission. The TFA ester of HOPTCO formed a structure similar to β-perylene, since only monomer-like emission was observed. The LBs of the other PTCOs and PTCDs exhibited varying quantities of monomer-like and excimer emission.

Two materials, HPTCO and HPTCDE, were used to demonstrate energy transfer in LB systems. The distance dependence of these systems was inspected and the energy transfer, to a diphthalocyanine monolayer, occurs on the 10 nm scale. Even though redox reactions can take place between diphthalocyanines and PTCOs, none was observed in the LB systems, presumably because the required geometry does not exist in the LB architecture.

The properties of the surface enhanced infrared effect have been studied using Langmuir-Blodgett monolayers of N-2-phenylethyl perylene tetracarboxylic diimide transferred to a variety of substrates coated with metal island films. The angle dependence and distance dependence of surface enhanced infrared spectroscopy in the

178

reflection and transmission geometries was investigated. Silver islands on glass provided the strongest enhancement, with optimal enhancement occurring within 5 nm of the enhancing media. Other metals, such as gold and copper, also exhibit surface enhancing properties, but not nearly as strong as silver.

Appendix I: Observed Vibrational Frequencies of PTCOs and PTCDs

Infrared Frequencies

The following tables of infrared frequencies were obtained from the material dispersed in a KFr pellet. Frequencies are given in wavenumbers and relative intensities are given as a percentage of the intensity of the strongest band observed for the given species. Band assignements were made through comparison with previously published analysis of the spectrum of perylene and perylene tetracarboxylics (see *Chapter 3* for references).

Abbreviations

alk. = alkyl, anhyd. = anhydride, bend. = bending, per. = perylene, str. = stretching, wag. = wagging.

PrPTCO		PPTCO		PhPTCO		HOPTCO		Assignment
Band (cm^{-1})		Band (cm^{-1})		Band (cm^{-1})		Band (cm^{-1})		
578	2	581	6	581	7	582	4	Alkyl def.
		614	4					Per. def.
636	3	637	7	639	12	638	5	Alkyl def.
		661	3					
		685	2	697	18			
739	51	739	61	739	57	739	51	Per. wag
752	2	754	8	750	9	754	7	
769	5					771	4	
775	2	776	10	785	20			
796	16	794	20	793	20	794	16	Alkyl wag
810	63	810	69	810	65	810	57	Per. wag
				832	9			
845	11	843	14	846	13	843	10	Per. wag
855	5							C-H bend (alk.)
865	19	866	22	864	17	866	18	Per. wag

180

899	2							
972	4	981	3	980	7	980	5	Per. ring
				989	11			
1016	37	1017	43	1019	47	1017	36	C-H bend (alk.)
1031	17	1032	21			1033	15	C-H bend (alk.)
1044	13	1046	9			1046	8	C-H bend (alk.)
1070	11	1070	10	1068	10	1070	12	C-H bend (alk.)
1078	8							C-H bend (alk.)
		1087	18			1086	13	C-H bend (alk.)
				1121	17			C-H bend (per.)
1126	15	1127	18	1125	17	1127	17	C-H bend (per.)
1143	12	1144	16	1143	15	1143	13	C-H bend (alk.)
1152	18	1153	20	1152	22	1153	17	C-H bend (alk.)
				1167	11			C-H bend (per.)
1186	5	1188	3					C-H bend (per.)
1231	16			1231	12	1232	14	C-H bend (alk.)
		1235	21	1236	15			C-H bend (alk.)
1245	29					1243	21	C-H bend (alk.)
		1256	27	1261	22			C-H bend (per.)
1269	8	1277	5	1274	4	1272	8	C-H bend (alk.)
1298	15	1296	12	1295	10	1297	10	C-H bend (alk.)
1323	46	1324	47	1322	50	1323	41	C-N str.
		1338	6					
		1348	13	1349	18	1349	15	C-N str.
1360	12	1354	13					
1371	12							
1382	11	1381	8	1381	15	1382	7	per. ring str.
1387	10	1387	7			1388	8	C-H bend (alk.)
1406	35	1406	35	1405	41	1406	30	per. ring str.
1435	14	1433	12	1431	19	1435	11	
1461	6	1467	3	1453	9			CH2 scissoring
				1483	6			
				1498	9			C=C phenyl str.
1506	13	1507	14	1506	12	1507	13	C=C per. str.
		1556	7			1556	7	C=C per. str.
1579	34	1580	36	1580	44	1579	38	C=C per. str.
1595	100	1595	100	1593	100	1594	100	C=C per. str.

1615	7	1615	7	1617	12	1615	9	C=C per. str.
		1618	7					
1656	92	1656	84	1656	79	1656	87	C=O imide str.
1694	54	1697	55	1694	55	1694	42	C=O imide str.
1722	22	1722	27	1724	28	1723	26	C=O anhyd. str.
1767	83	1766	58	1773	86	1766	72	C=O anhyd. str.
1787	23	1794	7					
		2853	4			2854	11	CH2 str.
2872	4	2874	3					CH3 FR
2897	3							C-H str. (alk.)
2933	5	2929	8			2928	15	CH2 str.
2956	8	2955	9	2956	5	2950	8	C-H Str. (alk.)
				3024	4			C-H str. (phenyl)
3067	4	3069	1	3064	5	3070	5	C-H str. (per.)
3098	4	3105	1	3105	3	3099	5	C-H str. (per.)
						3362	13	O-H str.

HPTCO		HPTCNH		HPTCDE		Assignment
Band (cm⁻¹)		Band (cm⁻¹)		Band (cm⁻¹)		
739	93	734	7			per. wag.
		743	27			per. wag.
746	8	749	6	746	29	per. wag.
754	13					
759	6	756	4			
769	8					
794	34	795	16	794	9	alk. wag.
810	100	811	48	810	49	per. wag.
843	15			846	6	per. wag.
854	7	853	8	854	7	C-H bend alk.
867	29	860	5			per. wag.
981	6	982	4			per. ring
1019	61					C-H bend, alk.
1032	33					C-H bend, alk.
1046	13					C-H bend, alk.
1071	13			1074	8	C-H bend, alk.
1088	22	1090	7	1095	6	C-H bend, alk.
1127	27	1129	3	1127	2	C-H bend, per.
1143	20					C-H bend, alk.
1153	26					C-H bend, alk.
		1159	3	1157	4	C-H bend, alk.
1175	3			1176	5	C-H bend, per.
1183	4	1183	8	1178	6	C-H bend, per.
1190	2					
1212	3					
1233	24					C-O-C stretch
1250	42	1248	9	1255	25	C-H bend, per.
1273	13					
1279	18	1276	30			
1297	14					
1323	52					C-N stretch
1339	17	1342	34	1341	53	C-N stretch
1350	23	1349	39			C-N stretch

1359	20	1356	35	1358	sh	C-N stretch
1383	11	1372	20	1378	sh	C-H bend, alk.
1387	15					C-H bend, alk.
1406	45	1403	26	1404	31	ring str.
				1424	2	ring str.
1434	18	1439	14	1441	24	ring str.
1456	7			1457	8	CH2 scissoring
1508	20	1509	6	1507	7	C=C per. str.
1580	41	1579	29	1579	27	C=C per. str.
1595	82	1594	88	1594	81	C=C per. str.
1616	18	1615	7	1610	9	C=C per. str.
1656	84	1656	50	1657	100	C=O imide str.
		1679	58			C=O imide str. (H-bonded)
1697	79	1692	100	1696	89	C=O imide str.
1723	60					
1742	34					
1766	91					C=O anhyd. str.
2854	13	2859	10	2856	7	C-H str., alk.
2873	8			2873	6	C-H str., alk.
2926	18	2906	5			C-H str., alk.
		2919	7			C-H str., alk.
		2932	8	2930	13	C-H str., alk.
2953	16	2952	9	2956	11	C-H str., alk.
3037	3	3034	7			C-H str., aryl.
		3040	8			C-H str., aryl.
3073	5	3059	8			C-H str., aryl.
		3157	6			N-H str. (H-bonded)

184

PPTCDM		PPTCDE		PPTCDPr		Assignment
Band (cm^{-1})		Band (cm^{-1})		Band (cm^{-1})		
621	6			631	13	alk. def.
745	44	746	62	747	65	per. wag.
794	15	794	17	793	24	alk. wag.
		802	12			alk. wag.
810	55	810	81	810	73	per. wag.
847	8	847	17			per. wag
		852	11	850	24	C-H alk. bend
863	7	864	10			per. wag.
		874	7			C-H alk. bend
		978	3			per. ring
1014	8			1012	7	C-H alk. bend
1035	11					C-H alk. bend
		1040	6			C-H alk. bend
1057	15	1074	21	1079	20	C-H alk. bend
1093	12	1091	15	1089	17	C-H alk. bend
1123	4	1124	7			C-H per. bend
1155	7	1155	7	1155	8	C-H alk. bend
1178	12	1177	17	1177	12	C-H per. bend
1243	14			1245	25	C-H alk. bend
1257	12	1254	33			C-H per. bend
1288	31					C-H alk. bend
		1300	4			C-H alk. bend
1345	54	1340	78	1341	49	C-N str.
1356	39	1358	36			C-N str.
		1372	29			C-H alk. bend
1386	9	1379	18	1378	22	C-H alk. bend
1403	40	1403	56	1404	53	per. ring str.

1423	sh					per. ring str.
1441	29	1440	44	1439	39	per. ring str.
		1455	15	1463	4	per. ring str.
1507	8	1507	10	1507	13	per. ring str.
1578	32	1578	41	1578	43	C=C per. str.
1593	93	1593	91	1592	80	C=C per. str.
1611	4	1611	5	1612	4	C=C per. str.
1656	100	1656	100	1656	90	C=O imide str.
1694	78	1696	99	1696	100	C=O imide str.
2853	7	2854	11	2860	8	C-H alk. str.
		2870	10	2873	8	C-H alk. str.
		2909	sh			C-H alk. str.
2930	12	2933	17	2929	13	C-H alk. str.
2955	13	2954	17	2957	14	C-H alk. str.
				3065	2	C-H aryl. str.
3075	3	3079	2	3079	2	C-H aryl. str.
3097	3					C-H aryl. str.

SERRS Frequencies

The SERRS frequencies for HPTCO, HPTCDE, HPTCNH, PPTCDM, PPTCDE, PPTCDPr were recorded using the 1403 Spex monochromator and 514.5 nm Ar$^+$ ion laser excitation. The measured Raman shifts were measured using Δwavenumbers (cm^{-1}). The SERRS of PrPTCO, PPTCO, PhPTCO and HOPTCO were measured using a S-1000 spectrograph equipped with a liquid nitrogent cooled CCD detector. The superior sensitivity of this instrument allowed the observation of very weak Raman bands not detected with the other instrument. The 514.5 nm laser line was also used.

Abbreviations

vw = very weak, w = weak, m = medium, s = strong, vs = very strong, br = broad, sh = shoulder

PPTCO		PrPTCO		PhPTCO		HOPTCO	
Band (cm^{-1})		Band (cm^{-1})		Band (cm^{-1})		Band (cm^{-1})	
539	m	539	m	538	m	539	m
552	sh	551	sh	553	sh		
574	vw		vw				
580	vw	579	vw	581	vw	579	vw
589	vw						
612	vw						
615	vw	615	vw			616	vw
633	vw	633	vw	629	vw		
636	vw					635	vw
		683	vw				
		725	vw	724	vw	725	vw
		756	vw			757	vw
787	vw	787	vw	786	vw	787	vw
802	w	802	w	801	w	802	w
				819	w		
828	w	829	w				
855	vw	849	vw	852	vw	852	vw
		890	vw				
934	vw	936	vw	936	vw	931	vw

						957	vw
				993	vw		
		1000	vw				
1057	sh	1055	sh	1057	sh		
1081	m	1081	m	1079	m	1080	m
1191	w	1190	w	1190	w	1190	w
		1220	vw			1220	vw
1290	vs	1290	vs	1294	vs	1289	vs
1305	vs	1304	vs	1302	vs	1304	vs
1333	vs	1334	vs			1333	vs
1358	vs	1358	vs	1359	vs	1358	vs
1379	vs	1379	vs	1380	vs	1378	vs
1453	w	1452	w	1452	w	1453	w
		1475	w				
1574	vs	1569	vs	1566	vs	1570	vs
			.	1572	sh		
1615	vw					1616	vw
1655	vw	1656	vw	1655	vw	1653	vw
1697	w	1698	w	1697	w	1697	w
		1732	vw	.			
1769	w	1770	w	1768	w	1796	w
		1830	vw				
1844	w	1845	w	1845	w	1844	w

HPTCO		HPTCDE		HPTCNH	
Band (cm⁻¹)		Band (cm⁻¹)		Band (cm⁻¹)	
237	w,br	236	w,br	236	w,br
543	m	548	m		
555	sh			560	w
579	vw	586	w		
632	vw			620	vw
		1065	w		
1080	w	1079	sh	1073	sh
		1247	vw	1245	vw
		1293	vs	1292	vs
1297	vs	1297	vs		
		1300	vs		
		1310	sh		
1373	sh	1373	sh		
1377	sh	1378	vs	1380	vs
1383	vs	1382	vs		
		1388	sh		
		1393	sh		
		1397	sh	1400	sh
1453	w	1451	w,br	1455	w,br
		1560	sh	1547	sh
1573	vs	1572	vs	1573	vs
1586	sh,br	1584	vs	1582	sh
		1592	sh	1592	sh
		1604	vs		
1612	sh,br	1612	sh		

PPTCDM		PPTCDE		PPTCDPr	
Band (cm⁻¹)		Band (cm⁻¹)		Band (cm⁻¹)	
551	m	551	m	554	m
587	vw	584	vw	584	vw
660	vw	659	vw	660	vw
1074	vw	1072	vw	1075	vw
1236	sh	1236	sh	1238	sh
1294	vs	1295	vs	1293	vs
1382	vs	1379	vs	1381	vs
1454	sh	1455	sh	1455	sh
1523	sh	1520	sh		
1572	vs	1571	vs	1574	vs
1580	vs	1581	vs	1582	vs
1612	sh	1611	sh	1611	sh

Appendix II - Math Cad Documents

This Appendix is a compilation of the Math Cad documents used to perform the calculations in this work. The items calculated were the reflection/absorption enhancement factors used to calculate molecular orienta'ion in *Chapter 4* and *5*, the intermolecular geometry from the extended dipole model in *Chapter 6* and the simulated SEIRRA spectra in *Chapter 8*. These documents are hard copies of the actual spreadsheets used and illustrate the calculations used in the respective chapters.

ORIGIN = 1

Reflection/Absorption Enhancement Factors: Determination

Definition of Variables

$h2 := 17.5 \cdot 10^{-7}$ —— Film Thickness (cm)

$v := 2900$ —— Wavenumber (cm-1)

$n1 := 1$ —— air, refractive index

$n2a := 1.5 + 0i$ —— reference, refractive index

$n2b := 1.5 + 0.1i$ —— sample film, refractive index

$n3 := 2.455$ —— substrate, ZnS, refractive index

$\theta1 := 0 \cdot deg$ —— Incidence angle

$$\theta2\alpha := Re\left[asin\left[\frac{n1 \cdot sin[\theta1]}{n2a} \right] \right]$$

$$\theta2\beta := Re\left[asin\left[\frac{n1 \cdot sin[\theta1]}{n2b} \right] \right]$$

$$q1 := \frac{cos[\theta1]}{n1}$$

$$q2a := \frac{cos[\theta2\alpha]}{n2a}$$

$$q2b := \frac{cos[\theta2\beta]}{n2b}$$

$$\theta3\alpha := asin\left[\frac{n2a \cdot sin[\theta2\alpha]}{n3} \right]$$

$$\theta3\beta := asin\left[\frac{n2b \cdot sin[\theta2\beta]}{n3} \right]$$

$$q3a := \frac{cos[\theta3\alpha]}{n3}$$

$$q3b := \frac{cos[\theta3\beta]}{n3}$$

$$B2a := 2 \cdot \pi \cdot v \cdot h2 \cdot n2a \cdot \cos[\theta 2\alpha]$$

$$Ma := \begin{bmatrix} \cos(B2a) & -\left[\dfrac{i}{q2a}\right] \cdot \sin(B2a) \\ -i \cdot q2a \cdot \sin(B2a) & \cos(B2a) \end{bmatrix}$$

$$B2b := 2 \cdot \pi \cdot v \cdot h2 \cdot n2b \cdot \cos[\theta 2\beta]$$

$$Mb := \begin{bmatrix} \cos(B2b) & -\left[\dfrac{i}{q2b}\right] \cdot \sin(B2b) \\ -i \cdot q2b \cdot \sin(B2b) & \cos(B2b) \end{bmatrix}$$

Transmittance of Film

$$Ta := Re\left[\dfrac{\cos[\theta 3\alpha]}{n3}\right] \cdot \left[\left\| \dfrac{2 \cdot q1}{\left[Ma_{1,1} + Ma_{1,2} \cdot q3a\right] \cdot q1 + \left[Ma_{2,1} + Ma_{2,2} \cdot q3a\right]} \right\|\right]^2$$

$$Ta = 0.82298$$

$$Tb := Re\left[\dfrac{\cos[\theta 3\beta]}{n3}\right] \cdot \left[\left\| \dfrac{2 \cdot q1}{\left[Mb_{1,1} + Mb_{1,2} \cdot q3b\right] \cdot q1 + \left[Mb_{2,1} + Mb_{2,2} \cdot q3b\right]} \right\|\right]^2$$

$$Tb = 0.81844$$

$$Af := \log\left[\dfrac{Ta}{Tb}\right]$$

$$Af = 0.0024 \qquad \text{——Absorbance of Film}$$

Reflection from Film Coated Substrate

$n1 := 1 + 0i$

$n2a := 1.5 + 0i$

$n2b := 1.5 + .1i$

$n3 := 0.62 + 25.1i$ —— metal substrate

$\theta1 := 85 \cdot deg$ —— incidence angle

    —— converted to radians

$\theta1 = 1.48353$

Angle changes according to Snell's Law

$$\theta2\alpha := asin\left[\frac{n1 \cdot sin[\theta1]}{n2a}\right]$$

$$\theta2\beta := asin\left[\frac{n1 \cdot sin[\theta1]}{n2b}\right]$$

$$\theta3\alpha := asin\left[\frac{n2a \cdot sin[\theta2\beta]}{n3}\right]$$

$$\theta3\beta := asin\left[\frac{n2b \cdot sin[\theta2\beta]}{n3}\right]$$

Calculation of Q's:

$$q1 := \frac{cos[\theta1]}{n1}$$

$$q2a := \frac{cos[\theta2\alpha]}{n2a}$$

$$q2b := \frac{cos[\theta2\beta]}{n2b}$$

$$q3a := \frac{cos[\theta3\alpha]}{n3}$$

$$q3b := \frac{cos[\theta3\beta]}{n3}$$

Determine M matrices for reference (a) and sample (b) cases:

$$B2a := 2 \cdot \pi \cdot v \cdot h2 \cdot n2a \cdot \cos[\theta2\alpha]$$

$$B2b := 2 \cdot \pi \cdot v \cdot h2 \cdot n2b \cdot \cos[\theta2\beta]$$

$$Ma := \begin{bmatrix} \cos(B2a) & -\left[\dfrac{i}{q2a}\right] \cdot \sin(B2a) \\ -i \cdot q2a \cdot \sin(B2a) & \cos(B2a) \end{bmatrix}$$

$$Mb := \begin{bmatrix} \cos(B2b) & -\left[\dfrac{i}{q2b}\right] \cdot \sin(B2b) \\ -i \cdot q2b \cdot \sin(B2b) & \cos(B2b) \end{bmatrix}$$

Reflectance of Film

$$Ra := \left[\left| \dfrac{\left[Ma_{1,1} + Ma_{1,2} \cdot q3a\right] \cdot q1 - \left[Ma_{2,1} + Ma_{2,2} \cdot q3a\right]}{\left[Ma_{1,1} + Ma_{1,2} \cdot q3a\right] \cdot q1 + \left[Ma_{2,1} + Ma_{2,2} \cdot q3a\right]} \right| \right]^2$$

$$Rb := \left[\left| \dfrac{\left[Mb_{1,1} + Mb_{1,2} \cdot q3b\right] \cdot q1 - \left[Mb_{2,1} + Mb_{2,2} \cdot q3b\right]}{\left[Mb_{1,1} + Mb_{1,2} \cdot q3b\right] \cdot q1 + \left[Mb_{2,1} + Mb_{2,2} \cdot q3b\right]} \right| \right]^2$$

The calculated reflectances are:

$$Ra = 0.96899 \qquad Rb = 0.91245$$

$$\frac{Ra}{Rb} = 1.06197$$

$$Ar := \log\left[\frac{Ra}{Rb}\right]$$

$$Ar = 0.02611$$

$$\frac{Ar}{At} = 10.86399 \qquad = \text{The sum of enhancement factors, } mz + mx$$

Exciton Splitting in Aggregates: Extended Dipole Approach

Parallel Diopies Confined to a Plane:

Molecule: PPTCDM

$\phi := 40 \cdot deg$ — tilt

$v := 1.14 \cdot 10^{-7}$ — length

Long Molecular Axis

$\psi := 75 \cdot deg$ — tilt

$u := 0.836 \cdot 10^{-7}$ — length

Short Molecular Axis

$$v1 := \begin{bmatrix} 0 \\ v \cdot \sin[\phi] \\ v \cdot \cos[\phi] \end{bmatrix}$$

Vector representing long transition axis of molecule 1

$$u := \frac{\cos[\psi]}{\cos[\phi] \cdot \sqrt{\left|1 - \left[\frac{\cos[\psi]}{\sin[\phi]}\right]^2\right|}} \cdot \left[\left[\frac{\cos[\phi]}{\sin[\phi]}\right]^2 + \sin[\phi]\right]$$

$$u1 := \begin{bmatrix} -u \cdot \sqrt{\left|1 - \left[\frac{\cos[\psi]}{\sin[\phi]}\right]^2\right|} \\ -u \cdot \cos[\psi] \cdot \frac{\cos[\phi]}{\sin[\phi]} \\ u \cdot \cos[\psi] \end{bmatrix}$$

Vector representing short axis of Molecule 1

$$v1 \times u1 = \begin{bmatrix} 3.837 \cdot 10^{-15} \\ -6.683 \cdot 10^{-15} \\ 5.607 \cdot 10^{-15} \end{bmatrix}$$

$N := v1 \times u1$ **Vector normal to uv plane**

Other Important Physical Quantities

$M := 4.319 \cdot 10^{-35}$
Magnitude of the square of the Transition Dipole Moment

$e := \dfrac{\sqrt{M}}{v}$
Charge on Transition Dipole (e.s.u.)

$D := 2.5$
Dielectric constant of surrounding medium

$E := 7.0631 \cdot 10^{-13}$
Observed Splitting Energy (ergs)

$x := 0 \cdot 10^{-7}$
Initial Guesses for x and b

$space := 3.45 \cdot 10^{-8}$
space between neighbouring molecules

$j := 1 .. 25$
number of neighbouring molecules in the stack

Set Up Find routine

Given

$$E = \frac{8 \cdot e^2}{D} \cdot \sum_j \left[\frac{2}{\sqrt{(j \cdot x)^2 + \left[m \cdot j \cdot x + j \cdot \left[\dfrac{|N| \cdot space - x \cdot N_0 - m \cdot x \cdot N_1}{N_1} \right] \right]^2}} \right.$$

$$+ 0 - \frac{1}{\sqrt{\left[v1_0 + j \cdot x \right]^2 + \left[v1_1 + m \cdot j \cdot x + j \cdot \left[\dfrac{|N| \cdot space - x \cdot N_0 - m \cdot x \cdot N_1}{N_1} \right] \right]^2 + \left[v1_2 \right]^2}}$$

$$-(1)$$

$$\left. + \frac{1}{\sqrt{\left[v1_0 - j \cdot x \right]^2 + \left[v1_1 - m \cdot j \cdot x - j \cdot \left[\dfrac{|N| \cdot space - x \cdot N_0 - m \cdot x \cdot N_1}{N_1} \right] \right]^2 + \left[v1_2 \right]^2}} \right]$$

$z := Find(x)$

$$y := m \cdot z + \left[\frac{|N| \cdot space - z \cdot N_0 - m \cdot z \cdot N_1}{N_1} \right]$$

Find the distance, D, between molecular planes and
compare with given value:

$$b := \frac{|N| \cdot space - z \cdot N_0 - m \cdot z \cdot N_1}{N_1}$$

$$spacer := \frac{|z \cdot N_0 + y \cdot N_1|}{|N|}$$

$m = 0.761$

$$r = \begin{bmatrix} z \\ y \\ 0 \end{bmatrix} \qquad r = \begin{bmatrix} 2.712 \cdot 10^{-8} \\ -3.363 \cdot 10^{-8} \\ 0 \end{bmatrix} \qquad |r| = 4.32 \cdot 10^{-8}$$

$space = 3.45 \cdot 10^{-8}$ $\qquad$ $spacer = 3.45 \cdot 10^{-8}$

Determine Displacement of one molecule with respect to the other:

$$xshift := \frac{r \cdot u1}{|u|} \qquad yshift := \frac{r \cdot v1}{|v|}$$

$xshift = -1.445 \cdot 10^{-8}$ $\qquad$ $yshift = -2.162 \cdot 10^{-8}$

$$\sqrt{xshift^2 + yshift^2 + space^2} = 4.32 \cdot 10^{-8}$$

$$|r| = 4.32 \cdot 10^{-8}$$

$$r = \begin{bmatrix} 2.712 \cdot 10^{-8} \\ -3.363 \cdot 10^{-8} \\ 0 \end{bmatrix}$$

Calculation of Polarizability of Composite Layer

ORIGIN := 1

b := 1.. 926   Set up wavenumber range

w_b := b + 1074

angle := 35·deg   Incidence angle

naway := 1.5   refractive index away from absorption band
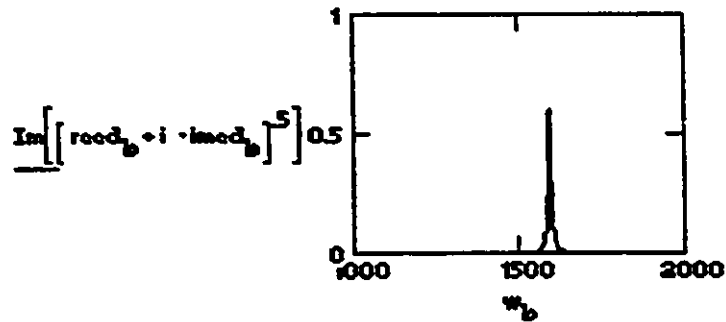
read in dielectric constant of organic layer

$reed_b$:= READPRN(reed)   real component

$imed_b$:= READPRN(imed)   imaginary component

Plot of imaginary portion of refractive index of organic layer

$$Im\left[\left(reed_b + i \cdot imed_b\right)^{.5}\right]$$

Load Dielectric Constants

reem := READPRN(reem)   Real and imaginary componets of
imem := READPRN(imem)   silver being read in

ed := reed + i ·imed

em_b := $reem_{b+1}$ + i ·$imem_{b+1}$

Aspect Ratios - Parallel Polarization

$l1 := .421837$

$l2 := .4177075$

N.B.: 1 refers to particles without organic layer
and 2 refers to particles with organick layer

$a1 := 46$

$b1 := 21$

$mm1 := \dfrac{a1}{b1}$ — aspect ratio

$thick := 1.5$ — thickness of organic film

$a2 := a1 + thick$

$b2 := b1 + thick$

$mm1 = 2.19$

$mm2 := \dfrac{a2}{b2}$

$mm2 = 2.111$

$q := \dfrac{b1 \cdot a1^2}{b2 \cdot a2^2}$ — volume ratio

Calculations - Parallel Polarization

Polarizability:

$$\alpha_b := \left[\frac{\left[\left[ed_b - 1\right] \cdot \left[em_b \cdot l1 + ed_b \cdot (1-l1) + q \cdot \left[em_b - ed_b\right] \cdot \left[ed_b \cdot (1-l2) + l2\right]\right]\right]}{\left[\left[ed_b \cdot l2 + (1-l2)\right] \cdot \left[em_b \cdot l1 + ed_b \cdot (1-l1)\right] + q \cdot \left[em_b - ed_b\right] \cdot \left[ed_b - 1\right] \cdot l2 \cdot (1-l2)\right]} \right]$$

Calculation of composite Dielectric Constant
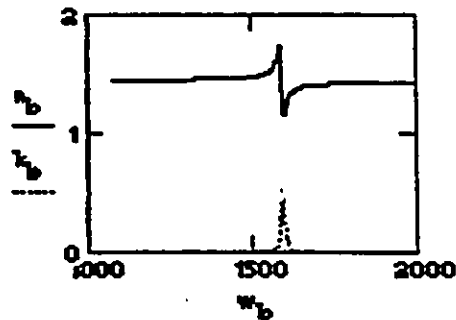
$eh := 1$

$f := .3$ — packing factor

$e2_b := eh \cdot \dfrac{\left[3 + 2 \cdot f \cdot \alpha_b\right]}{\left[3 - f \cdot \alpha_b\right]}$ — Maxwell-Garnet model for dielectric constant
of composite layer

200

Calculation of Refractive Indexes

$$n_b := \mathrm{Re}\left[\sqrt{e2_b}\right]$$

$$k_b := \mathrm{Im}\left[\sqrt{e2_b}\right]$$

$n1 := 1$ —— refractive index of vacuum

$h2 := thick \cdot 10^{-7}$ —— convert thickness to cm

$reglass := \mathrm{READPRN}(reglass)$

$imglass := \mathrm{READPRN}(imglass)$ —— read in refractive index of glass

$$n3_b := reglass_{b,2} + i \cdot imglass_{b,2}$$

$$e3_b := \left[\left[n3_b\right]^2 - n1 \cdot \sin(angle)^2\right]^{\frac{1}{2}}$$

Calculate Absorbances:

$$AS_b := \frac{-16 \cdot \pi}{\ln(10)} \cdot \left[\frac{\cos(angle)}{\left[n3_b\right]^2 - 1}\right] \cdot n_b \cdot k_b \cdot h2 \cdot w_b$$

$$APX_b := \frac{-16 \cdot \pi}{\ln(10)} \cdot \left[\frac{\cos(angle)}{\dfrac{\left[e3_b\right]^2}{\left[n3_b\right]^4} - \cos(angle)^2}\right] \cdot \left[\frac{-\left[e3_b\right]^2}{\left[n3_b\right]^4}\right] \cdot n_b \cdot k_b \cdot h2 \cdot w_b$$

Perpendicular Polarization Calculations

$l1 := .156326$

$l2 := .164585$

$$a_b := \left[\frac{\left[\left[ed_b - 1 \right] \cdot \left[cm_b \cdot l1 + ed_b \cdot (1-l1) + q \cdot \left[cm_b - ed_b \right] \cdot \left[ed_b \cdot (1-l2) + l2 \right]\right]\right]}{\left[\left[ed_b \cdot l2 + (1-l2) \right] \cdot \left[cm_b \cdot l1 + ed_b \cdot (1-l1) \right] + q \cdot \left[cm_b - ed_b \right] \cdot \left[ed_b - 1 \right] \cdot l2 \cdot (1-l}\right]$$

$$e2_b := eh \cdot \frac{-3 + 2 \cdot f \cdot a_b}{3 - f \cdot a_b}$$

$$n_b := Re\left[\sqrt{e2_b} \right]$$

$$k_b := Im\left[\sqrt{e2_b} \right]$$

Calculate Absorbance:

$$APZ_b := \frac{-16 \cdot x}{\ln(10)} \cdot \left[\frac{\cos(angle)}{\left[\frac{e3_b}{n3_b}\right]^4 - \cos(angle)^2} \right] \cdot \frac{\sin(angle)^2}{\left[\left[n_b\right]^2 + \left[k_b\right]^2\right]^2} \cdot n_b \cdot k_b \cdot h2 \cdot w_b$$

Plot Absorption - unpolarized light

$$\underline{APZ_b + APX_b + AS_b}$$
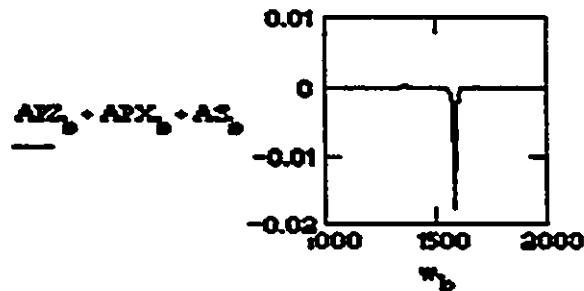
Generating Output Files

PRNPRECISION := 5

PRNCOLWIDTH := 15

output := augment(w, Re(APZ + APX + AS))

WRITEPRN(ssg45p) := output

Vita Auctoris

Eric G. Johnson

Eric Johnson was born on April 12, 1967 in Cooksville, Ontario. He graduated from Sandwich Secondary School in 1986 before attending the University of Windsor. In 1990, Eric graduated top of his class with an Honours Bachelor of Science with a major in Chemistry. He is currently a Doctor of Philosophy candidate at the University of Windsor and hopes to graduate in the fall of 1994.

Publications

10. Johnson, E.; Aroca, R., "Spectroscopic Properties and Packing of Langmuir-Blodgett Monolayers of Perylene Tetracarboxylic Anhydrides," *Langmuir*, submitted.

9. Johnson, E.; Aroca, R., "Surface Enhanced Spectroscopy of Monolayers," *J. Phys. Chem.*, submitted

8. Aroca, R; Johnson, E., "Molecular Orientation and Stacking of Perylenetetracarboxylic diimide Derivatives in Langmuir Blodgett monolayers: Part II," *Appl. Spectrosc.*, submitted.

7. Aroca, R; Johnson, E.; Maiti, A.K., "Molecular Orientation and Stacking of Perylenetetracarboxylic diimide Derivatives in Langmuir Blodgett monolayers: Part I," *Appl. Spectrosc.*, submitted.

6. Johnson, E.; Aroca, R.; Pahapill, J., "Low temperature SERRS and fluorescence spectra of a Langmuir-Blodgett monolayer of *N*-hexyl, perylenetetracarboxylic monoimide," *J. Mol. Struct.*, 1993, *293*, 331.

5. Aroca, R.; Johnson,E., "Vibrational Spectra and Structure of Langmuir-Blodgett Monolayers of Octa-Tert-Butyl Zirconium Bisphthalocyanine," *Langmuir*, 1992, 8, 3137.

4. Johnson, E.; Aroca, R., "Energy transfer between Langmuir-Blodgett monolayers", *Can. J. Chem.*, 1991, *69*, 1728.

3. Johnson, E.; Aroca, R.; Nagao, Y., "Electronic and vibrational spectra of films and Langmuir-Blodgett monolayers of *N*-Octyl-3,4-perylenedicarboximide", *J. Phys. Chem.*, **1991**, *95*, 8840.

2. Aroca, R.; Johnson, E.; Clavijo, R.E.; Nagao, Y., "Spectroscopic characterization of Langmuir-Blodgett films of electroactive organic materials" in *New Physical Problems in Electronic Materials*, N. Kirov and J. Marshall, Editors. World Scientific Publishing Co., Teaneck NJ, **1991**, 281-293.

1. Aroca, R. Johnson, E., "Surface enhanced fluorescence of aggregates in Langmuir-Blodgett monolayers," *SPIE Vol. 1336 Raman and Luminescence Spectroscopies in Technology II*, **1990**, 291.